

# Thermal Drawing of Polymer Nano-composites: Fluid Dynamic Analysis and Application to Novel Functional Fibers

Thèse N°9101

Présentée le 18 avril 2019

à la Faculté des sciences et techniques de l'ingénieur  
Laboratoire des fibres et matériaux photoniques  
Programme doctoral en science et génie des matériaux

pour l'obtention du grade de Docteur ès Sciences

par

**Alexis Gérald PAGE**

Acceptée sur proposition du jury

Prof. F. Stellacci, président du jury  
Prof. F. Sorin, directeur de thèse  
Prof. X. Jia, rapporteuse  
Dr S. Danto, rapporteur  
Prof. F. Gallaire, rapporteur

2019







# Acknowledgements

First of all, I am very grateful to my PhD advisor, Professor Fabien Sorin, who offered me to join his team recently formed. His passion for science and thoughtful ideas have been essential to the construction of my thesis. His enthusiasm, availability and care of the human being make him a great mentor, and I highly appreciate to work under his supervision.

I would like to express my gratitude to Prof. Xiaoting Jia, Prof. François Gallaire, Dr. Danto Sylvain and Prof. Francesco Stellacci for accepting to be the members of my thesis jury and taking the time to read and comment my thesis. I am also thankful to Dr. Stefano Mischler, Dr. Christopher Plummer and Dr. Yves Leterrier, who formed the committee of my candidacy exam and provided valuable advice.

Being a member of the FIMAP laboratory is a great experience. Thanks to Fabien and all my colleagues, a very friendly ambiance reigns in our working environment. Fruitful discussions and productive collaborations are well balanced with laughter and casual conversation in a relaxed but stimulating atmosphere. It was a pleasure to share the office with Dr. Tung Nguyen, Dr. Wei Yan and Inès Richard. I am very thankful to Anne Roy, who runs efficiently the administrative and logistic matters of the lab and is mindful of our well-being, and to all my other colleagues, Dr. Arthur Le Bris, Chie Kitano, Dr. Yunpeng Qu, Marco Volpi, Dr. Tapajyoti Das Gupta, Shahrzad Shadman, Nicola Bartolomei, Chaoqun Dong, Louis Martin-Monnier, Dr. Federica Sordo, Dr. Bastien Schyrr, Andreas Leber, William Esposito and Dr. Rajasundar Chandran. I would also like to thank our neighbors, first Prof. Michel Rappaz, Jean-Luc Desbiolles and the LSMX, then Prof. Michele Ceriotti and his COSMO team.

I am grateful to Dr. Yves Leterrier for sharing his expertise on rheology, and the LTC/LPAC laboratory for the use of their equipment, in particular Dr. Rajasundar Chandran for his frequent help. I had the chance to follow the excellent course taught by Prof. Craig Carter, and collaborate with Dr. Mathias Bechert and Prof. François Gallaire for a fruitful collaboration thanks to their expertise and advice. I wish to thank the members of CIME for their teaching on Electron Microscopy and their technical support: Dr. Duncan Alexander, Dr. Thomas La Grange, Dr. Marco Cantoni, Fabienne Bobard, Danièle Laub, Colette Vallotton and Grégoire Baroz. The ATMX and BM workshops, and Gilles Auric from the MX shop were very helpful. I am also thankful to Chrystelle Demierre, Anne Kolly and Sandra Roux for their assistance on the administrative side of the doctoral program.

It was a very interesting and instructive experience to be teaching assistant of the course Introduction to Materials Science of Professors Michel Rappaz, Véronique Michaud and Fabien Sorin, and to supervise students for their semester project. Many thanks to the students who contributed to this work: Pauline Malaurie, Ioannis Katrantzis, Vincent Vernay, Valentine Favrod, David Schmidt, Eleonore Wild and Jean-Baptiste Desbrest.

I would like to thank my housemates and all the friends I met in Lausanne or before coming to EPFL, with whom I shared great moments of fun, sport and adventures in the mountains.

Finally, I am grateful to my loving family. My parents have encouraged and supported me through all my studies, which have been successful thanks to their education and hard work. My brother sets an example of excellence and passion for science. I also thank my parents for giving me the passion for the mountains and letting me practice activities that they find scary. My thesis is dedicated to them.

# Abstract

The thermal drawing process is emerging as a versatile platform for the development of multimaterial fiber devices and advanced textiles for sensing, energy harvesting or medical applications, owing to the possibility to integrate insulators, conductors and various types of functional materials together in complex architectures. This field of research remains relatively recent and still has unexploited potential and unanswered questions. In particular, the lack of transparent conducting material compatible with thermal drawing has so far limited the development of optoelectronic fiber devices. It has indeed hindered the ability to fabricate the types of optoelectronic devices that require a transparent electrode, most notably photovoltaic cells.

Furthermore, conductive polymer composites based on carbon black have been utilized for years as an alternative to crystalline metals that can maintain finer geometries, crystalline metals being limited by capillary instabilities due to their low viscosity in the melted state during thermal drawing. However, the observation that the conductivity of composites depends on drawing conditions has thus far not been explained through an understanding of the underlying mechanism.

In this thesis, we investigate the production and thermal drawing of thermoplastic nanocomposites based on carbon black, but also on high aspect ratio conductive fillers such as silver nanowires and carbon nanotubes. The latter are indeed suitable to fabricate transparent conducting films, and we show that we can find appropriate compositions and drawing conditions to integrate them in multimaterial fibers. After looking into the thermal drawing of such composites in more details, we propose an advanced fluid dynamic analysis that accurately models the thermal drawing process, with new insights on the radial dependency of the axial velocity. We design a way to visualize the deformation in the neckdown region and show that our model compares well with the experimental observation. We use this model to further develop the theoretical approach to account for the influence of thermal drawing on the conductivity of nanocomposites. The impact of both the draw ratio and the radial position observed experimentally is explained quantitatively by the results of the model. Our approach can potentially be applied to other types of materials whose properties change under the deformation due to thermal drawing.

From these findings, we demonstrate a variety of novel composite-based fiber devices. We fabricated a functional photodetecting fiber using a transparent electrode made of a carbon nanotube composite, paving the way towards the development of novel optoelectronic fiber devices that integrate transparent electrodes. Moreover, we present a new type of touch sensing fiber device that relies on a freely moving conductive domain made of a carbon black nanocomposite. Such type of electronic fiber device is capable of both detecting a pressure applied and localizing it along its entire length. We can envision applications in soft electronics or healthcare with individual fiber devices or by embedding them in smart textiles.

## Keywords

Thermal Drawing, Multi-Material Fibers, Functional Fibers, Nanocomposites, Carbon Nanotubes, Transparent Conducting Electrodes, Fluid dynamics, Modeling, Electronic fibers devices, Optoelectronic fiber devices.

# Résumé

Le procédé d'étirage à chaud apparaît comme une plateforme polyvalente pour le développement de dispositifs à base de fibres multi-matériaux et de textiles perfectionnés pour des applications médicales, de détection ou de récupération d'énergie, grâce à la possibilité d'assembler en architectures complexes des matériaux isolants, conducteurs ou ayant divers types de propriétés fonctionnelles. Ce domaine de recherche étant relativement récent, son potentiel n'est pas totalement exploité et de nombreuses questions restent à résoudre. En particulier, l'absence de matériau transparent et conducteur compatible avec l'étirage à chaud limite le développement de dispositifs optoélectroniques à base de fibres. Pour cette raison, il est en effet impossible de fabriquer les types de dispositifs optoélectroniques qui nécessitent une électrode transparente, en particulier les cellules photovoltaïques.

Par ailleurs, les composites polymères conducteurs à base de noir de carbone sont utilisés depuis des années comme alternative aux métaux cristallins car ils peuvent conserver des formes précises, contrairement aux métaux cristallins qui sont limités par des instabilités capillaires dues à leur basse viscosité dans l'état liquide pendant l'étirage à chaud. Cependant, il a été observé que la conductivité des composites dépend des conditions d'étirage, mais cela n'a pas encore été expliqué par une description du mécanisme sous-jacent.

Dans cette thèse, nous étudions la fabrication et l'étirage à chaud de nanocomposites thermoplastiques à base de noir de carbone, mais également de nanoparticules à haut rapport d'aspect telles que des nanofils d'argent et des nanotubes de carbone. Ces derniers sont en effet adaptés à la réalisation de films transparents et conducteurs, et nous montrons que l'on peut déterminer des compositions et des conditions d'étirage appropriées pour les intégrer dans des fibres multi-matériaux. Après avoir étudié l'étirage à chaud de tels composites en détail, nous présentons une analyse avancée en dynamique des fluides qui modélise le procédé d'étirage à chaud de façon précise, apportant de nouvelles connaissances sur la variation radiale de la vitesse axiale. Nous élaborons une méthode de visualisation de la déformation dans la zone de rétrécissement et montrons que notre modèle concorde avec les observations expérimentales. Nous exploitons ensuite ce modèle pour développer une approche théorique qui représente l'influence de l'étirage à chaud sur la conductivité des nanocomposites. Les résultats du modèle rendent compte quantitativement de l'impact, observé expérimentalement, du taux d'étirage et de la position radiale. Notre approche pourra être appliquée à d'autres types de matériaux dont les propriétés sont affectées par la déformation due à l'étirage à chaud.

A partir de ces résultats, nous exposons une variété de dispositifs innovants à base de fibres. Nous avons fabriqué une fibre fonctionnelle photo-déTECTrice utilisant une électrode transparente faite d'un composite de nanotubes de carbone, ouvrant la voie au développement de dispositifs optoélectroniques novateurs à base de fibres qui intègrent des électrodes transparentes. De plus, nous présentons un nouveau type de fibre sensible au toucher qui repose sur l'utilisation d'une partie mobile et conductrice faite d'un nanocomposite de noir de carbone. Ce type de fibre électronique est capable de détecter une pression appliquée et de la localiser le long de la fibre. Il est possible d'envisager des applications dans les domaines de l'électronique flexible ou de la santé utilisant des fibres fonctionnelles individuellement ou en les incorporant à des textiles intelligents.

## Mots-clés

Etirage à chaud, Fibres Multi-matériaux, Fibres fonctionnelles, Nanocomposites, Nanotubes de Carbone, Electrodes Transparentes et Conductrices, Dynamique des Fluides, Modélisation, Fibres Electroniques, Fibres Optoélectroniques.

# List of Abbreviations and Symbols

AgNW	Silver Nanowire
CB	Carbon Black
CNT	Carbon Nanotube
DMA	Dynamic Mechanical Analysis
DMAc	Dimethylacetamide
DMSO	Dimethyl sulfoxide
EDX	Energy-dispersive X-ray spectroscopy
HDPE	High Density Polyethylene
ITO	Indium Tin Oxide
MEMF	Micro Electro-Mechanical Fiber
MEMS	Micro Electro-Mechanical System
MWCNT	Multi-Walled Carbon Nanotube
NMP	<i>N</i> -Methyl-2-pyrrolidone
PC	Polycarbonate
PDMS	Polydimethylsiloxane
PE	Polyethylene
PEI	Polyetherimide
PET	Polyethylene terephthalate
PMMA	Poly(methyl methacrylate)
PSu	Polysulfone
PTFE	Polytetrafluoroethylene (Teflon)
PVD	Physical Vapor Deposition
PVDF	Polyvinylidene fluoride
PVP	Polyvinylpyrrolidone

SEM	Scanning Electronic Microscopy
SWCNT	Single-Walled Carbon Nanotube
TEM	Transmission Electronic Microscopy
TGA	Thermogravimetric analysis
THF	Tetrahydrofuran
TPE	Thermoplastic elastomer
$a$	Parameter describing the breakage rate of the percolating network
$\alpha$	Fiber parameter
$\alpha^2$	Parameter for expansion of variables
$Bi$	Biot number
$c$	Critical exponent
$c_p$	Specific Heat Capacity
$Ca$	Capillary number
$\mathbf{D}$	Rate-of-deformation tensor
$Dr$	Draw-down ratio
$E_a$	Activation energy for viscosity
$\eta$	Viscosity
$\eta_{min}$	Viscosity at $T_{max}$
$Fr$	Froude number
$\gamma$	Surface tension
$\dot{\gamma}$	Shear rate
$G'$	Storage modulus
$G''$	Loss modulus
$h$	Heat transfer coefficient
$II_D$	Second scalar invariant of the rate-of-deformation tensor
$k$	Thermal conductivity

$L$	Length of a piece of material (Chapter 2 only) or Length of neckdown region
$m$	Exponent in kinetic equation
$\omega$	Angular frequency
$p$	Concentration or Pressure (in 4.1 only)
$p_e$	Effective concentration
$p_c$	Critical concentration
$p_{in}$	Initial effective concentration
$Pe$	Peclet number
$r$	Radial position in cylindrical coordinates
$\bar{R}$	Gas constant
$R$	Resistance (Chapter 2 and Chapter 5) or Preform-to-fiber radius
$R_0$	Preform radius
$R_s$	Sheet resistance
$Re$	Reynolds number
$\rho$	Resistivity (Chapter 2 and Chapter 5) or Density
$T$	Temperature or Transmittance
$T_{max}$	Maximum air temperature
$\Lambda$	First parameter for the Gaussian air temperature profile
$\Delta$	Second parameter for the Gaussian air temperature profile
$\tau$	Shear stress
$\boldsymbol{\tau}$	Extra stress tensor
$\theta$	Azimuth in cylindrical coordinates
$S$	Cross-sectional area
$\sigma$	Electrical conductivity
$\sigma_{DC}/\sigma_{op}$	Ratio of electrical to optical conductivity (Figure of Merit)
$\sigma_{in}$	Initial conductivity
$\boldsymbol{\sigma}$	Stress tensor

$St$	Stanton number
$u$	Radial velocity
$v$	Axial velocity
$\mathbf{v}$	Velocity vector
$v_{draw}$	Drawing speed
$v_{feed}$ or $v_0$	Feeding speed
$z$	Axial position in cylindrical coordinates

# Contents

<b>Acknowledgements</b> .....	<b>v</b>
<b>Abstract</b> .....	<b>vii</b>
<b>Keywords</b> .....	<b>viii</b>
<b>Résumé</b> .....	<b>ix</b>
<b>Mots-clés</b> .....	<b>x</b>
<b>List of Abbreviations and Symbols</b> .....	<b>xi</b>
<b>Contents</b> .....	<b>xv</b>
<b>Chapter 1 Introduction</b> .....	<b>17</b>
<b>Chapter 2 Fabrication and properties of conductive polymer nanocomposites</b> .....	<b>23</b>
2.1 Properties of conductive polymer nanocomposites .....	23
2.1.1 Motivation for the study of conductive polymer nanocomposites .....	23
2.1.2 General ideas and theoretical background on relevant properties .....	24
2.1.3 Properties to optimize for thermal drawing .....	33
2.2 Solution casting .....	34
2.2.1 Materials and preliminary experiments .....	34
2.2.2 PMMA/SWCNT nanocomposites: Fabrication, measurements and properties .....	37
2.3 Melt mixing of CB and CNT thermoplastic nanocomposites .....	48
2.3.1 State of the art .....	48
2.3.2 Experiments: Materials, fabrication process and measurements .....	54
2.3.3 Properties and interpretation .....	58
2.3.4 Discussion .....	64
<b>Chapter 3 Thermal drawing of conductive nanocomposites</b> .....	<b>65</b>
3.1 Description of the experimental process .....	65
3.1.1 Thermal drawing and fiber designs .....	65
3.1.2 Experimental process for the fabrication of the preforms .....	73
3.2 Thermal drawing of nanocomposites and resulting properties .....	76
3.2.1 Solution cast SWCNT composites .....	76
3.2.2 Melt-mixed MWCNT composites .....	77
3.2.3 Carbon Black composites .....	85
3.3 Discussion .....	89
3.3.1 Rheology and ability to draw MWCNT composites .....	89
3.3.2 Properties of MWCNT composites thermally drawn in fibers .....	90

<b>Chapter 4</b>	<b>Modeling thermal drawing and the conductivity of nanocomposites .....</b>	<b>93</b>
4.1	Modeling the thermal drawing process.....	94
4.1.1	Presentation of the model .....	94
4.1.2	Slender fiber approximation and expansion .....	101
4.1.3	Iterative and simultaneous implementations .....	107
4.1.4	Analytical solution for the velocity field at the first order .....	109
4.2	Results of the model.....	110
4.2.1	Parameter determination .....	110
4.2.2	Deformation of initially straight lines.....	111
4.2.3	Comparison of the two implementations .....	114
4.2.4	Velocity field and deformation rates.....	117
4.3	Modeling the conductivity of nanocomposites .....	120
4.3.1	Presentation of the model .....	120
4.3.2	Results of the model for conductivity .....	123
4.4	Discussion and summary .....	125
<b>Chapter 5</b>	<b>Applications .....</b>	<b>127</b>
5.1	Touch sensing fiber devices .....	127
5.1.1	Introduction .....	127
5.1.2	Multi-material micro-electromechanical fibers with bendable functional domains.....	129
5.1.3	Elastic multimaterial electronic fibers and devices via thermal drawing .....	140
5.2	Fiber devices employing a nanocomposite transparent electrode.....	145
5.2.1	Working principle .....	145
5.2.2	Fabrication of a photoconducting fiber device .....	146
<b>Chapter 6</b>	<b>Conclusion .....</b>	<b>151</b>
<b>References.....</b>	<b>.....</b>	<b>153</b>
<b>Curriculum Vitae.....</b>	<b>.....</b>	<b>162</b>

# Chapter 1 Introduction

The field of advanced functional fibers and textiles is experiencing an unprecedented development owing for a large part to recent scientific and technological breakthroughs in fiber processing. The thermal drawing process in particular, at the heart of the fabrication of telecommunication optical fibers, now allows for the fabrication of fibers with a large range of materials and functionalities. It consists in heating a macroscale preform, typically made out of glass or thermoplastics, to its softening temperature and pulling it to create a much thinner and longer fiber. A more comprehensive description of the process is given in Chapter 3. From simple glass-based step index structures, the design of optical fibers was expanded to photonic crystal and Bragg mirror fibers [1], [2]. Recently, this technique has also been used to make microstructured multi-material fibers that integrate optical, electronic and optoelectronic materials [1]–[3]. To make such fibers, the different materials are assembled in a macroscopic preform with a defined cross-sectional architecture, then the preform is thermally drawn into a fiber that ideally keeps the architecture of the preform, with dimensions reduced by a factor of up to two orders of magnitude. Such fibers can combine conducting, semiconducting and insulating materials in appropriate geometries to exhibit advanced functionalities [1], [4] making them promising building blocks for applications in optics but also soft electronics [5]–[8], optoelectronics [3], [5], [9], [10] or bioengineering [11], [12].

The thermal drawing process enables to create kilometers of fiber with sub-micron-thick layers, however it requires the materials used to be compatible in terms of viscosity at the temperature used. Various new functional materials have been shown to be compatible with the thermal drawing process in the last decade, which vastly increases the range of potential applications of multi-material fibers. All materials need to flow during drawing, but their viscosity should not change abruptly with temperature in order to be stable enough to be used as the fiber cladding or as thin films. Amorphous materials have this property and include insulating thermoplastics and semiconducting chalcogenides that have a glass transition temperature between room temperature and a few hundred degrees Celsius. Crystalline metals that melt during drawing can nevertheless be integrated in such fibers as electrodes, but as their viscosity is low no fine structure can be obtained due to fluid instabilities [13], and they have to be encapsulated by more viscous materials. To circumvent this issue, conductive thermoplastic nanocomposites based on carbon black (round carbon nanoparticles) [3], [5], [7] and carbon nanofibers [12] have been introduced as their viscosity can be in the appropriate range for thermal drawing, and they can serve as electrodes since they are conductive. However, the conductivity of these nanocomposites is far from that of metals, as the highest value reported is 20 S/m from a combination of carbon black and nanofibers and along the fiber direction [12], whereas it is typically of the order of  $10^7$  S/m for metals. Moreover, the conductivity of conductive nanocomposites is influenced by temperature and drawing speed, as mentioned by Gu et al. [7], but no detailed study of this phenomenon has been done so far.

An important use of conducting nanocomposites is for optoelectronic fibers [3], [10]. Various types of optoelectronic fiber devices have been created by employing the thermal drawing technique thanks to the possibility to arrange conducting, semiconducting and insulating materials in defined structures. In particular,

photodetecting fibers were realized, at first with a bulk semiconducting core as photosensitive element [14] (Figure 1 (a)). Then, their photosensitivity was enhanced by almost two orders of magnitude by employing a thin film configuration (Figure 1 (b)), which reduces the dark current due to the thick core of the fiber, whereas light only penetrates a thin layer [1]. In this case, the photosensitivity was increased by decreasing the thickness of the semiconducting region, but the distance between the electrodes is still large (several hundred  $\mu\text{m}$ ) even in the thin film configuration, and decreasing it would also improve the photosensitivity. Decreasing this distance to the film thickness would be possible with a planar sandwich structure in which light is transmitted through a transparent conducting electrode. Moreover, the possibility to introduce other interesting functionalities, such as light-to-electricity conversion, has so far been limited by the lack of transparent electrodes. It may be possible to perform post-drawing treatments to add a transparent electrode at the surface of a fiber, but this would be limiting in terms of scalability and possible architectures. Therefore, finding a way to integrate a transparent conducting layer in thermally drawn fibers would open vast opportunities to create novel and more performant optoelectronic fiber devices.

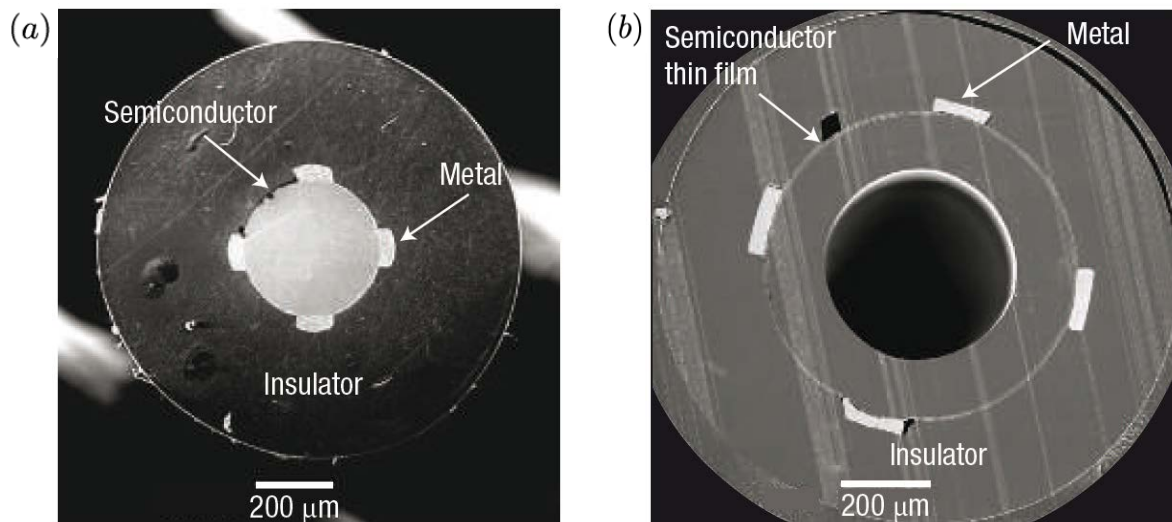


Figure 1. From [1], [14]. SEM pictures of the cross-section of photodetecting fibers made by thermal drawing (a) based on a thick semiconducting core; (b) based on a thin semiconducting film.

Transparent electrodes are essential in most optoelectronic devices such as solar cells, LCD displays, touch screens and OLEDs [15]. However, they are traditionally made of a metal oxide such as Indium Tin Oxide (ITO), which is a ceramic and incompatible with thermal drawing since it does not melt or soften at the temperatures typically employed. Fibers and fabrics made thanks to the thermal drawing process have some advantages over the traditional Silicon wafer process, being less energy-intensive, costly or limited in terms of size and shape [9], but the materials that can be used are inherently restricted. Flexibility is one of the attributes required in thermally drawn fibers, and the appeal for flexible and textile electronics seems to make it essential in the next generation of devices. Fortunately, this has recently driven substantial research on flexible transparent conducting films to find low-cost and performant alternatives to ITO. In particular, high aspect ratio conducting nanoparticles such as carbon nanotubes and silver nanowires have been shown to form a conducting network with so little material that conducting films based on them can be transparent even if the nanoparticles themselves are not. They can achieve a performance comparable to ITO in terms of

sheet resistance and transmittance [16], [17] and have been demonstrated to function as substitute in all the main types of electronic devices, reaching similar efficiencies [15].

Films based on nanoparticles can be materials made entirely from them, or nanocomposites comprising a matrix material and nanoparticles dispersed throughout the matrix. Compared to their counterparts made entirely of nanoparticles, the nanocomposites performance may be similar or much lower depending on their concentration and fabrication process [18]–[21]. Interestingly, nanocomposites based on carbon black have been proven to be compatible with thermal drawing and employed in various fiber devices, such as those shown in Figure 2. We are not aware of any study employing a carbon black nanocomposite as transparent electrode, likely because the performance would be too poor due to the low aspect ratio of the fillers. However, this suggests that thermoplastic nanocomposites based on carbon nanotubes or metal nanowires may be compatible with thermal drawing and suitable materials as transparent electrodes in multi-material fibers. This is the first reason driving the study, in this thesis, of the thermal drawing of polymer nanocomposites.

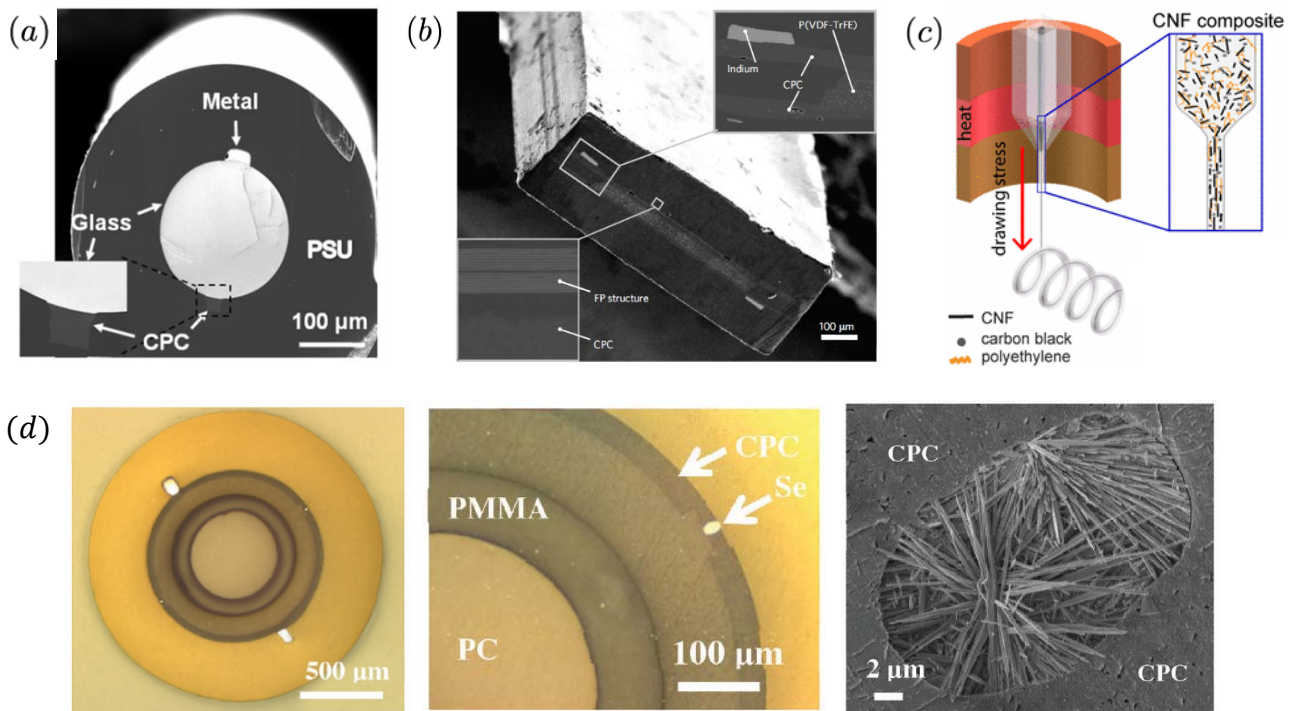


Figure 2. Fiber devices employing conductive polymer composites (CPC) based on carbon black, from [3], [5], [12], [22]. (a) Photodetecting fiber with spatial localization of incident optical beams along the fiber. (b) Piezoelectric-modulated optical fiber. (c) Neural probe with a hybrid carbon black/carbon nanofiber composite. (d) All-fiber integrated fluorescent system with a photodetecting component based on semiconducting nanowires at the tip of the fiber and a step index optical waveguide in the core.

The carbon black nanocomposites that have been employed for years in multimaterial fibers [3], [5], [7], [10] have a higher viscosity than the corresponding pure thermoplastic matrix, without preventing them from being compatible with thermal drawing. However, we observed that higher aspect ratio fillers have an effect on processability that can make them incompatible, even at relatively low concentration. Therefore, we

examined the mechanisms of dispersion and agglomeration of fillers to understand the impact of the different steps of the process and optimize the balance between processability and post-drawing properties. This enabled us to fabricate multi-material fibers that integrate a transparent conducting film made of a carbon nanotube composite. Although the optoelectronic properties are not sufficient for high performance applications, they are adequate for devices that simply require a functional transparent electrode. We realized a photodetecting fiber that indeed demonstrates the ability of such a carbon nanotube composite to work as transparent electrode in a thermally drawn optoelectronic fiber device.

Moreover, we also applied our knowledge on conducting nanocomposites to create a new type of touch sensing fiber device based on freely moving functional domains made of a carbon black nanocomposite. Thanks to processing of the electrical signal detected, the device is able not only to sense a pressure applied on the fiber but also to localize it along its entire length.

While working on improving the post-drawing conductivity of carbon black and compatible carbon nanotube composites, we observed that it strongly depends on drawing conditions, for a given composition. This effect has already been noticed for carbon black composites [7], but remained to be understood in detail. To explain it accurately, we developed a fluid dynamics analysis of the thermal drawing process. Our model takes into account the radial dependency of the axial velocity, whereas existing analytical models of the thermal drawing process assumed it to be independent of the radial position [11], [23], which is not sufficient to explain the experimental results. For the modeling of the conductivity during drawing, we utilized a kinetic equation that links the deformation undergone to the conductivity of nanocomposites [24].

The outline of the thesis is the following:

The mechanisms and properties of nanocomposites that are relevant in view of their intended use as transparent electrodes in thermally drawn fibers are presented in Chapter 2. We describe the experimental fabrication of carbon nanotube and silver nanowire nanocomposites by two different techniques, solution casting and melt-mixing. The resulting properties are interpreted in relation with the processing conditions. Useful knowledge on their influence is provided by previous research realized on conducting nanocomposites and reported in the literature. In particular, studies on the melt-mixing of carbon nanocomposites can be transposed to the context of thermal drawing since both techniques involve the deformation of the material in the melt.

In Chapter 3, we describe the experimental details of the different steps of the preform fabrication and the thermal drawing technique. We present the preform designs employed on one hand to study the compatibility of nanocomposites with thermal drawing, on the other hand to evaluate the post-drawing properties of compatible nanocomposites. The materials made by solution casting do not lead to interesting properties in fibers. However, carbon nanotube composites made by melt-mixing reach higher post-drawing conductivities than carbon black based composites and are successfully drawn as transparent conducting films in multimaterial fibers. We observe that the conductivity of nanocomposites decreases when increasing the draw ratio and the distance from the center of the fiber cross-section.

An advanced fluid dynamic analysis of the thermal drawing process is developed in Chapter 4. It enables to compute an accurate description of the velocity field in the neckdown region, which we verify by comparing the result of the model with an experimental visualization of the deformation. This visualization is realized

by incorporating thin sheets of a colored material in a transparent preform. We observe that material lines that are straight in the preform and perpendicular to the drawing direction deform during drawing, in a way that is well reproduced by the model. The knowledge of the deformation during drawing is then applied to quantitatively explain how the post drawing conductivity of nanocomposites depends on draw ratio and distance from the center of the fiber cross-section.

In Chapter 5, we present two different applications of conductive nanocomposites in thermally drawn fibers. The new type of touch sensing electronic fiber device mentioned above is described in detail. A first version is based on a rigid thermoplastic and an open structure, then an improved version has an elastic cladding material and a closed structure that make it more robust. Finally, we employ a carbon nanotube composite as transparent electrode in a photodetecting fiber. This optoelectronic fiber device uses a thick Selenium layer as photoconducting material and shows that the conducting nanocomposite is able to fulfill the role for which we developed it.



# Chapter 2 Fabrication and properties of conductive polymer nanocomposites

In this chapter, we identify the properties of conductive polymer nanocomposites that must be examined for their drawing in multimaterial fibers. We first introduce relevant ideas and theory on electrical, rheological and optical properties. Then we present the experimental work realized for the fabrication and characterization of conductive polymer nanocomposites, along with appropriate results from the literature.

## 2.1 Properties of conductive polymer nanocomposites

### 2.1.1 Motivation for the study of conductive polymer nanocomposites

As mentioned in the Introduction chapter, thermally drawn multimaterial fibers often employ thermoplastic nanocomposites with carbon-based fillers as electrode materials. They are indeed compatible with the thermal drawing process thanks to their thermoplastic properties and can be used in complex cross-sectional architectures. Unlike with metals which are liquid during drawing, architectures with small features sizes and electrical contacting of thin layers of functional materials can be achieved thanks to their high viscosity. This was for example shown for capacitor fibers [7] and with thin semiconducting [25] and piezoelectric [5] films.

Gu et al. [7] observed that the conductivity of a thermally drawn carbon black composite is lower when decreasing the temperature or increasing the speed. This loss of conductivity was qualitatively explained by a higher shear stress, due to a higher speed or a higher viscosity from a lower temperature, that causes a degradation of the conductive network of carbon black particles. To understand this phenomenon in more details, we need to know more about the nanocomposite itself, in particular how and why precisely its conductivity changes when it undergoes the type of deformation found in the drawing process.

Furthermore, the conductivity of carbon black nanocomposites is far from that of metals, which is of the order of  $10^7$  S/m. Nanocomposites based on high aspect ratio conductive nanoparticles reach higher conductivities than carbon black based ones, hence the interest in using them in thermally drawn fibers. For example with carbon nanotubes, the conductivity of a polypropylene composite with a loading of 5.3 wt% was 150 S/m [26], whereas it was 1000 S/m with 30 wt% in polycarbonate [27] and  $7 \times 10^3$  S/m in polystyrene with 82 wt% [28]. As is emphasized here, the concentration of fillers is a crucial factor, and for a given nanocomposite under fixed fabrication parameters the conductivity understandably increases monotonically with loading. Moreover, unlike carbon black, carbon nanotubes, graphene and silver nanowires were shown

to be fillers from which transparent conducting nanocomposite films can be fabricated [18]–[20] and functional optoelectronic devices such as a solar cell were demonstrated using them [29].

We refer here only to nanocomposites in which the matrix is a thermoplastic polymer, because thermoset composites and films made purely of nanoparticles are not expected to be compatible with thermal drawing. Thermoplastics have adequate rheological properties, but when filling them with nanoparticles these can drastically change and prevent the resulting nanocomposites from being drawn, as will be shown in Chapter 3. The nanoscale size of the particles indeed means a very large interfacial area; therefore, the interactions particle-matrix and particle-particle can have a large impact on the properties of the composite. Therefore, their rheological properties must be examined in order to optimize their ability to be drawn.

The properties and processability of the nanocomposites not only depend on the intrinsic properties and concentration of the fillers, but also on their dispersion, which is dictated by the fabrication technique employed. Commonly, polymers and nanoparticles are produced separately, then the fillers are dispersed in the matrix. However, the method used can lead to breaking, bundling and a distribution that prevents percolation. Thus, we need to understand what is a dispersion that gives high electrical conductivity, and how to achieve it by tuning the parameters of the technique used. Possible methods to disperse nanoparticles in a thermoplastic matrix include solvent-casting, rod- and spin-coating, which are solvent-based techniques, and melt-mixing, which consists in mixing the fillers with the melted polymer in an extruder. In this work, several of these were employed to create nanocomposites, which ones to explore further being guided by the result of their integration in thermally drawn fibers. In the next sections, the experimental details of the solvent-casting and melt-mixing techniques and resulting properties will be explained. Moreover, we will present the state of the art in the topics the most relevant, illustrated by a selection of references. Fortunately, since carbon nanotubes in particular have attracted a lot of attention, substantial research has been done on conductive nanocomposites on which we can build on.

### 2.1.2 General ideas and theoretical background on relevant properties

Before going into the details of the experimental work realized, we present here some general background on the notions employed and the measurement of properties of nanocomposites.

#### Electrical properties

The ability of a material to conduct electricity is given by its conductivity  $\sigma$  or its resistivity  $\rho$  – the conductivity being simply the inverse of the resistivity:

$$\sigma \left[ \frac{S}{m} \right] = \frac{1}{\rho [\Omega \cdot m]} \quad (1)$$

These properties are independent of the dimensions of the material, but experimentally we can only determine an electrical resistance. For a resistance  $R$  measured through a piece of material of length  $L$  and uniform cross-sectional area  $S$ , the following relationship is then used to calculate the material properties:

$$R [\Omega] = \rho [\Omega \cdot \text{m}] \frac{L [\text{m}]}{S [\text{m}^2]} = \frac{1}{\sigma \left[ \frac{\text{S}}{\text{m}} \right]} \frac{L [\text{m}]}{S [\text{m}^2]} \quad (2)$$

The electrical resistance is the coefficient of proportionality between the applied tension  $U$  and current  $I$  flowing through the piece of material in the well-known Ohm's law:

$$U [V] = R [\Omega] \cdot I [A] \quad (3)$$

Due to the contacts used to connect the material to the multimeter through electrical wires, the tension across the material may not correspond to the one applied by the multimeter. The contacts may indeed bring an additional electrical resistance that cause a drop of potential, or even create a non-ohmic junction [30]. In this case the same wires are used both for the measurement of the tension and the current, and this is called a "2-wire" configuration. One way to circumvent this problem is to apply silver paint at the contact points. Another way, especially useful when measuring small values of resistance where the resistance of the silver paint is not negligible, is to employ a "4-wire" configuration. In this configuration, two pairs of wires are used to measure separately the current flowing through the piece of material and the voltage across it. Almost no current is allowed to flow in the wires for the tension measurement, preventing any drop of potential due to contact resistance, therefore the tension measured is the actual tension across the material.

Different factors influence the electrical conductivity of nanocomposites. One of them is the nanoparticle type, which includes the material and crystallographic structure and the associated intrinsic properties, and the geometry, with for example the diameter, length and resulting aspect ratio for rod-like particles.

The electrical conductivity understandably increases monotonically with the weight percentage of conductive nanoparticles if all the other parameters are fixed, but the increase is not smooth over the whole concentration range. An insulator-conductor transition can be observed, with a sharp increase of the electrical conductivity or equivalently a sharp decrease of resistivity, in a small range of concentration, as shown in Figure 3 for carbon black [31] and carbon nanotube composites. Although real nanocomposites are very complex, their conductivity is often well described by fitting the following simple percolation law derived from a percolation theory based on simplified materials [32], [33]:

$$\sigma(p) = \sigma_0(p - p_c)^c \quad (4)$$

This equation is valid for concentrations  $p$  above the so-called percolation threshold or critical concentration  $p_c$ . More detailed models of insulator-conductor transition have been developed [34], [35] but are not relevant in this work. Tunneling has been put forward as a mechanism that allows for electrical conduction between particles [36]. The exponential dependence on distance can then explain the large range of conductivities and percolation thresholds observed even for a given materials composition due to differences in the particle dispersion.

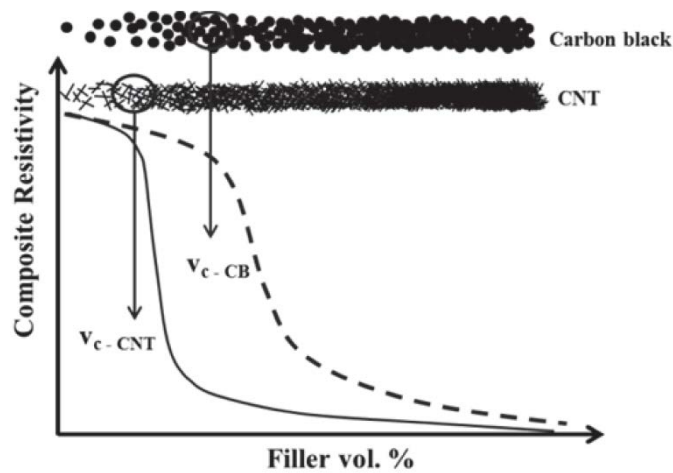


Figure 3. From reference [31]. Schematic of the dispersion of carbon black particles and carbon nanotubes against vol%, showing that elongated particles tend to create a percolation network at a lower concentration  $v_c$ . The typical curve of the logarithm of resistivity versus vol% for carbon nanotube (CNT) and carbon black (CB) composites has a sharp drop of resistivity around  $v_c$ .

A very important factor for the conductivity of such nanocomposites is indeed the state of dispersion of the particles, which itself depends on many factors, such as the way the composite is made and processed, the host matrix material or the potential chemical or physical functionalization of the nanoparticles [32]. Experimental results show a huge range of electrical conductivities and percolation thresholds in nanocomposites, depending on the filler and matrix types, the processing technique used and the resulting dispersion. Critical concentrations as low as 0.0025 wt% have been reported for carbon nanotubes in epoxy thanks to their high aspect ratio [37]. For carbon nanotubes in thermoplastics it can be a fraction of percent to a few percent thanks to their high aspect ratio, but for carbon black a few percent to more than 10 wt%. The problem of the distribution of fillers in a nanocomposite is complex. To obtain a conductive network at a low concentration, the nanoparticles have to be dispersed in the matrix to avoid large agglomerates, but the methods used can also lead to breaking and bundling. However, a dispersion with highly distributed fillers can also prevent percolation, and some degree of agglomeration is required as illustrated in Figure 4. The fabrication or processing technique can cause a decrease and anisotropy of electrical conductivity, for example because shear or alignment during fiber spinning or extrusion [26], [38]–[40]. A thermal annealing treatment can partly counteract this effect by facilitating filler agglomeration and recovery of a conducting network, the temperature needed being higher for lower loadings [26], [41], [42].

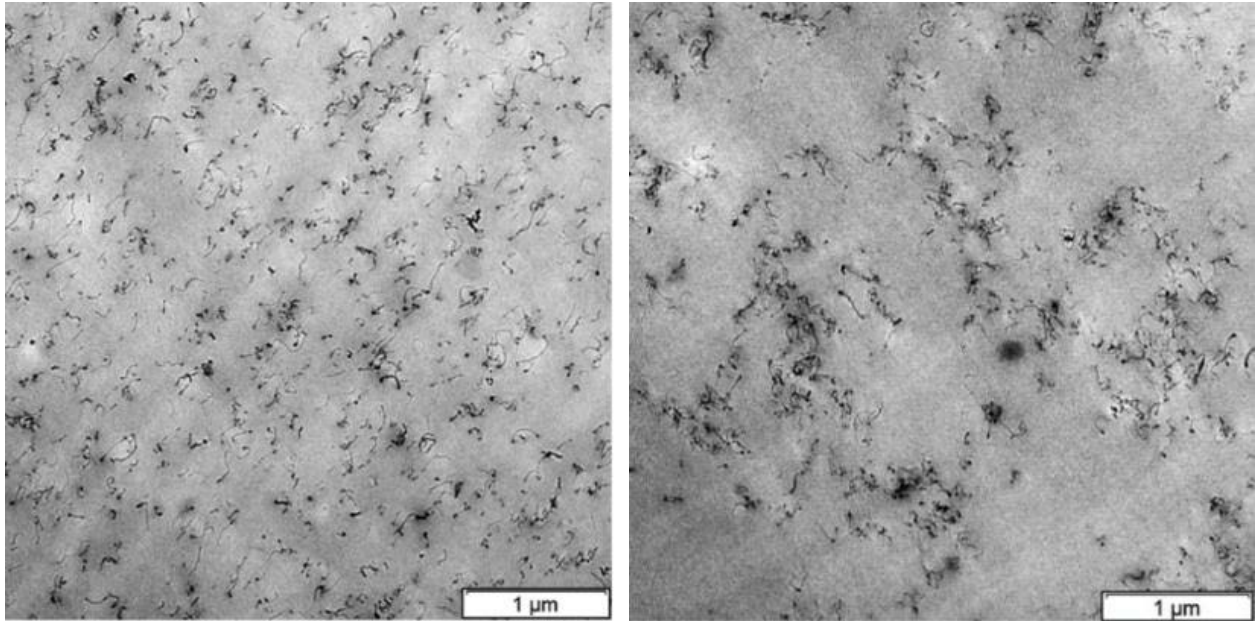


Figure 4. From [43]. Transmission Electron Microscopy images of polycarbonate/multi-wall carbon nanotube samples with the same loading of 0.875 wt%. The left sample has too well dispersed nanotubes and is insulating, whereas the right sample has loosely packed agglomerates and is conducting.

Computing the conductivity of nanocomposites has been done using simplified models of the material to evaluate the influence of various parameters and shear deformation [44]–[48]. The models are not sufficiently complete to predict the properties of real materials and the trends obtained are expected, therefore not useful for our work.

### Rheological properties

The viscoelastic behavior of a material is described by its rheological properties, the most intuitive of them being its viscosity. However, other properties and complicated mechanisms can be evaluated, and rheology is a vast field of study. We will present here some measurable properties that help to understand better how to fabricate and process thermoplastic nanocomposites for the thermal drawing of multimaterial fibers including them. Various types of devices have been invented to measure rheological properties, for example extensional capillary rheometers and parallel plate rheometers, such as the one shown in Figure 28.

The shear viscosity  $\eta$  of a fluid material is defined as the ratio between the shear stress  $\tau$  and the shear rate  $\dot{\gamma}$  applied during a shear deformation. The corresponding law is:

$$\tau [\text{Pa}] = \eta [\text{Pa} \cdot \text{s}] \cdot \dot{\gamma} [\text{s}^{-1}] \quad (5)$$

The material behavior is called Newtonian when the viscosity  $\eta$  is independent of the shear rate  $\dot{\gamma}$ , otherwise Non-Newtonian. Thermoplastics usually have a Newtonian regime for low shear rates and are Non-Newtonian above a limit. Nanocomposites have a much more complex behavior and their viscosity, as well as the other properties presented below, depend on their history of heating and deformation since it can modify the filler dispersion.

The temperature dependence of the viscosity of thermoplastics is described by an Arrhenius law, with  $E_a$  (in J/mol) the activation energy,  $\bar{R} = 8.314$  J/K/mol the gas constant and  $T$  in K:

$$\eta(T) = \eta_0 \exp \frac{-E_a}{\bar{R} \cdot T} \quad (6)$$

The elongational viscosity  $\eta_e$  of a viscous material is defined as the ratio between the tensile stress  $\sigma$  and the elongation rate  $\dot{\epsilon}$  applied during a tensile deformation. The corresponding law is:

$$\sigma [\text{Pa}] = \eta_e [\text{Pa} \cdot \text{s}] \cdot \dot{\epsilon} [\text{s}^{-1}] \quad (7)$$

For Newtonian fluids, the ratio  $\eta_e / \eta$ , called Trouton ratio, is equal to 3.

Elastic solids follow the laws  $\sigma = E \cdot \epsilon$  in tensile deformation, and  $\tau = G \cdot \gamma$  in shear deformation, where  $E$  is the Young's modulus and  $G$  the shear modulus (both in Pa).

Real fluids are actually viscoelastic, which means they have both a viscous and an elastic behavior. Simple measurements under constant shear rate for example only probe the viscous behavior, but it is possible to quantify both behaviors at the same time. One way to achieve this is dynamic shear rheometry: to characterize the viscoelastic response of a material, a sinusoidally time-varying shear is applied:

$$\gamma(t) = \gamma_0 \sin(\omega \cdot t) \quad (8)$$

with amplitude  $\gamma_0$  [ $\text{s}^{-1}$ ], angular frequency  $\omega = 2\pi f$  [rad/s] and frequency  $f$  [Hz]. Then the shear rate is:

$$\dot{\gamma}(t) = \omega \gamma_0 \cos(\omega \cdot t) = \dot{\gamma}_0 \sin(\omega \cdot t + \pi/2) \quad (9)$$

with  $\dot{\gamma}_0 = \omega \gamma_0$ . From the formulas we can observe that there is a phase shift of  $90^\circ$  between the shear  $\gamma(t)$  and shear rate  $\dot{\gamma}(t)$ .

The time-varying response stress  $\tau(t)$  is simultaneously measured. For perfectly viscous fluid,  $\tau(t)$  would be in phase with  $\dot{\gamma}$ , whereas for a perfectly elastic solid  $\tau(t)$  would be in phase with  $\gamma(t)$ . For a real material the response will lie in between, and the measurement quantitatively tells the relative viscous and elastic contributions. For this, the shear stress is written:

$$\tau(t) = \tau_0 \sin(\omega \cdot t + \delta) \quad (10)$$

$$\tau(t) = \tau_0 (\sin(\omega \cdot t) \cos \delta + \cos(\omega \cdot t) \sin \delta) \quad (11)$$

$$\tau(t) = G' \gamma_0 \sin(\omega \cdot t) + G'' \gamma_0 \cos(\omega \cdot t) \quad (12)$$

This allows to define the phase shift  $\delta$ , the storage (elastic) modulus  $G'$  (in phase with  $\gamma(t)$ ) and the loss (viscous) modulus  $G''$  (in phase with  $\dot{\gamma}(t)$ ). We have the following relationships:

$$G' = \cos \delta \frac{\tau_0}{\gamma_0} \quad (13)$$

$$G'' = \sin \delta \frac{\tau_0}{\gamma_0} \quad (14)$$

$$\tan \delta = \frac{G''}{G'} \quad (15)$$

The complex modulus and complex viscosity are defined as

$$|G^*| = \sqrt{G'^2 + G''^2} \quad (16)$$

$$\eta^* = \frac{|G^*|}{\omega} = \frac{\tau_0}{\omega\gamma_0} = \frac{\tau_0}{\dot{\gamma}_0} \quad (17)$$

The value of  $\tan \delta$  is a relative measure of the viscous and elastic components of the complex viscosity. A high value of  $\tan \delta$  means a dominantly viscous material, whereas a low value means a more elastic one. Therefore, this measure is useful to evaluate how much more elastic a polymer becomes with addition of fillers or under annealing for example.

Nanoparticles indeed have an effect on the rheological properties of their host matrix due to the huge interfacial area that cause substantial particle-matrix and particle-particle van der Waals interactions even at relatively low loadings [32]. This is crucial for use in processing techniques that require the materials to be deformed in the melt, such as fiber thermal drawing. For instance the complex viscosity was measured to rise quickly with the concentration of carbon black or carbon nanotubes in thermoplastic composites (Figure 5, Figure 6), with an increase of one order of magnitude at 10 wt% for carbon black and at 2 wt% for carbon nanotubes, at low frequencies [49], [50]. The increase of complex viscosity comes from an increase in both  $G'$  and  $G''$ , but  $G'$  increases much more, corresponding to a decrease in  $\tan \delta$  and meaning the material is becoming more elastic.

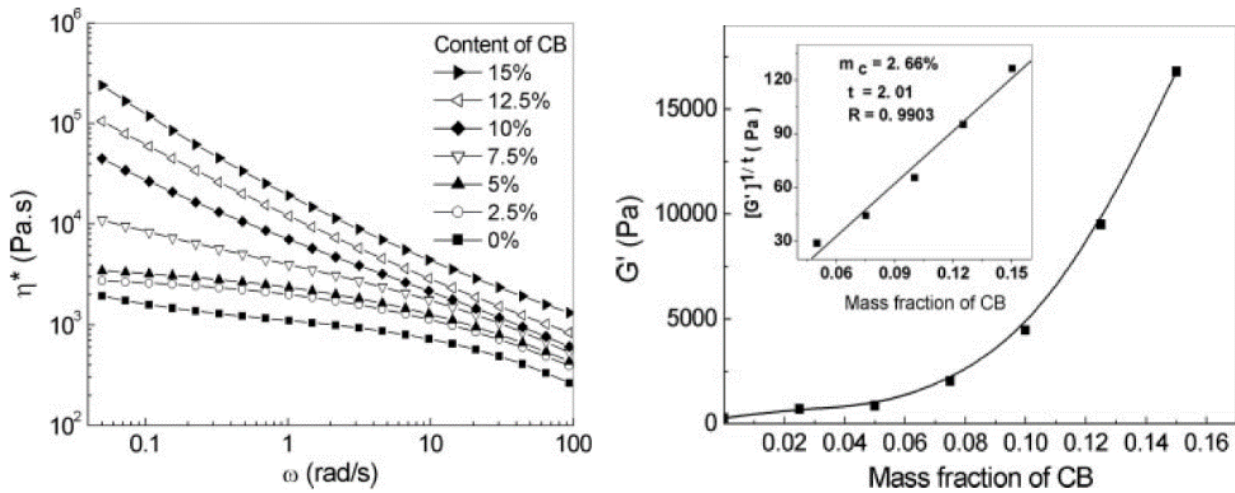


Figure 5. From [49]. Left: Complex viscosity  $\eta^*$  versus Angular frequency  $\omega$  of Carbon Black polymer (PP/LDPE blend) composites for different concentrations, at 190°C, indicating a solid-like behavior from 7.5%. Right: Storage modulus  $G'$  versus mass fraction of the same composites, at 180°C with  $\omega = 1$  rad/s. Inset: fit with a percolation law with  $G'$  instead of the conductivity  $\sigma$  (equation (4)). The fitted rheological threshold (2.66 wt%) is lower than the conductivity threshold (4.9 wt%).

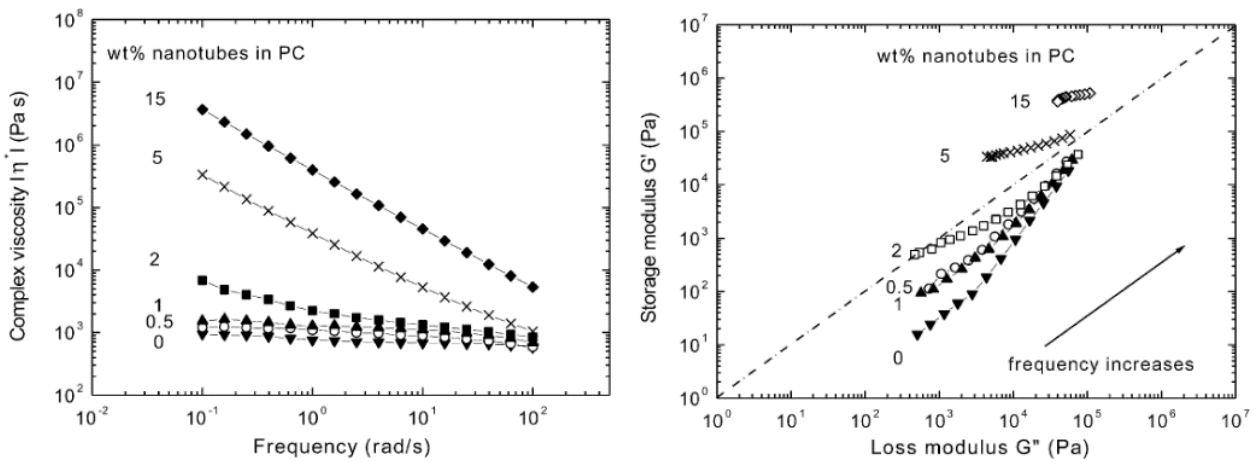


Figure 6. From [50]. Left: Complex viscosity  $\eta^*$  versus Angular frequency  $\omega$  of Carbon nanotube polycarbonate composites for different concentrations, at 260°C. Right: Storage modulus  $G'$  versus Loss modulus  $G''$  for the same composites and the same range of angular frequencies, at 260°C. Both plots indicate a solid-like behavior from 2%.

Various studies on the rheological properties of conductive thermoplastic nanocomposites against concentration have defined a rheological threshold, similarly to the electrical threshold described above. One way is to fit the measurement of  $G'$  versus concentration with the same type of percolation as for the electrical conductivity:  $G' = G'_0(p - p_c)^t$ , as shown in Figure 5 (right), which in this case leads to a lower rheological threshold than electrical threshold [49], [51]. Another way is to watch for a change of frequency dependence in the plot of  $\eta^*$ ,  $G'$ ,  $G''$  or  $\tan \delta$  against  $\omega$  [52]–[56], which can be an indicator of gelation: a liquid-solid transition from flow regime to rubber like plateau. With this type of criterion, Figure 5 (left) suggests a change of behavior from 7.5% for the carbon black composite studied, whereas it is from 2% in Figure 6 for a nanotube composite. This can also be observed on a plot of  $\delta$  versus  $|G^*|$ , called van Gurp-Palmen plot [53], [57]–[59]. The values of the rheological thresholds reported are relatively close to the electrical thresholds, and both are typically between 0.25% and 10% for high aspect ratio nanoparticles (CNT, metallic nanowires such as AgNW), and a few to tens of percent for carbon black.

The rheological properties of nanocomposites are difficult to model, since the nanoscale dimension can cause the properties to be dominated by the molecular interactions and entanglement of fillers with polymer chains. Continuous models developed for composites with micron-sized fillers do not match experimental results for the viscosity of polymer nanocomposites filled with nanotubes [60], therefore it is necessary to take into account the behavior of polymer chains and nanotubes at the molecular level. Modelled rheological properties of a silica nanospheres/polymer nanocomposite considering polymer-particle interactions and chain entanglement proved to match well experimental data, using fitting parameters [61]. However, predictive models for the rheological properties of polymer nanocomposites with high aspect ratio fillers seem to be far from mature [62], [63].

## Evaluation of fillers dispersion and alignment

To understand why certain fabrication parameters lead to higher properties than others and further improve them, studying the nanocomposite microstructure is necessary. Visualizing the dispersion of nanoparticles indeed allows to determine whether they are agglomerated, aligned or if their aspect ratio was decreased due to breaking for instance. Differences in dispersion can be visible to the eye when large agglomerates are present in transparent samples, or by dissolving samples and observing the color of the solution and the amount of sediment [50]. Light transmission microscopy can be employed to observe micron-sized agglomerates in thin sections of samples [64] and compare them quantitatively by measuring the area occupied by such agglomerates [65], [66]. Individual nanoparticles and how they are dispersed at the sub-micron scale can be observed by Transmission Electron Microscopy, as in the example shown in Figure 4 [43]. Then, several measurements techniques indirectly enable to analyze the dispersion and alignment of fillers, such as dynamic light scattering [67], X-ray scattering [39], [40], [64], [68] or Raman spectroscopy [38], [40], [69].

## Properties of transparent conducting films

The electrical properties of a material can be given in terms of conductivity or resistivity and the optical properties in terms of the absorption coefficient, but these correspond to bulk properties. To have an idea of the performance of a transparent conductive film, it is more convenient to give the sheet resistance  $R_s$  (in  $\Omega/\text{sq}$ ) and the transmittance  $T$  (in %) of a film of a specific thickness, which is not required to be known.

The sheet resistance  $R_s$  is defined as follows: the resistance measured along the length of a rectangular film of uniform thickness  $t$ , width  $w$ , length  $L$  and resistivity  $\rho$  is

$$R = \rho \frac{L}{wt} = R_s \frac{L}{w} \quad (18)$$

where  $R_s = \frac{\rho}{t}$ . Therefore if  $R_s$  is known, the resistance  $R$  is obtained from the ratio  $\frac{L}{w}$ , and is equal to  $R_s$  if the sheet is a square ( $L = w$ ), hence the unit ohms per square ( $\Omega/\text{sq}$ ).

The relationship between the absorption coefficient  $\alpha$  and transmittance  $T$  is given by the Beer-Lambert law, for a film of uniform thickness  $t$  [70]:

$$T = e^{-\alpha t} \quad (19)$$

It is then possible to use a figure of merit that combines the sheet resistance and the transmittance: the ratio of the electrical conductivity  $\sigma_{DC}$  to the optical conductivity  $\sigma_{op}$  [70], [71]. The relation between  $T$ ,  $R_s$  and  $\sigma_{DC} / \sigma_{op}$  is (with  $Z_0 = 377 \Omega$  a constant called impedance of free space):

$$T = \left(1 + \frac{Z_0 \sigma_{op}}{2R_s \sigma_{DC}}\right)^{-2} \quad (20)$$

A material with a high conductivity ratio  $\sigma_{DC} / \sigma_{op}$  can form films with high  $T$  and low  $R_s$ , and in principle tuning the thickness can lead to a range of values for  $T$  and  $R_s$ . In practice the electrical and optical properties may depend on the thickness of the films, but this figure of merit is still very useful. A typical value of  $\sigma_{DC} / \sigma_{op}$  for ITO is 150, and films of 15  $\Omega/\text{sq}$  with 85% transmittance in the visible range or 10  $\Omega/\text{sq}$  with 80%

transmittance can be made [15]. Highly concentrated nanocomposites and films made purely of carbon nanotubes or metallic nanowires have been demonstrated to exceed the value required for high-performance transparent electrodes [15], [71]. Thermoplastic nanocomposites with relatively low concentrations and larger thicknesses are more likely to be useful for thermal drawing. For example an 20  $\mu\text{m}$  PMMA film with 0.5 wt% carbon nanotubes and a 16 microns polycarbonate film with 1.4 wt% silver nanowires respectively resulted in 45.7% transmittance and 1064  $\Omega/\text{sq}$  [72], and 80% transmittance and 35  $\text{k}\Omega/\text{sq}$  [20]. These properties correspond to relatively low values of  $\sigma_{DC}/\sigma_{op}$  (0.370 and 0.0456), but such films can still be used in functional optoelectronic devices even if the efficiency is lower [29]. Table 1 summarizes some typical properties of ITO and various transparent films employing high aspect ratio conductive nanoparticles reported in the literature.

Property	Thickness	Refractive index	Sheet resistance	Transmittance in the visible	Figure of merit $\sigma_{DC}/\sigma_{op}$	Transmittance at 3 $\mu\text{m}$
Unit	nm	-	$\Omega/\text{sq}$	%	-	%
<b>ITO [15], [73]</b>	50 - 120	2.0	10 - 300	80 - 88	10 - 300	20
<b>Carbon nanotube network [15]</b>	$\leq 50$	1.5 - 1.6	20 - 400	70 - 95	10 - 65	
<b>Carbon nanotube network [73]</b>	25	1.03 - 1.5	200	80	8	90
<b>Graphene network [15]</b>	6 - 28		600 - 2000	70 - 90	$\leq 1$	
<b>Graphene network [73]</b>	10	1.57	1800	70	0.5	75
<b>Ag nanowire network [15]</b>	40 - 600		1 - 100	75 - 90	25 - 500	
<b>Ag/Au nanowire network [73]</b>	10	-	22	88	130	10
<b>PMMA/CNT composite (0.5 wt%) [72]</b>	$20 \times 10^3$		1064	45.7	0.370	
<b>PC/AgNW composite (1.4 wt%) [20]</b>	$16 \times 10^3$		$35 \times 10^3$	80	0.0456	

Table 1. Optoelectronic properties of ITO and examples of transparent conductive films made of carbon nanotube, graphene or metal nanowire network and thermoplastic nanocomposites with carbon nanotubes or silver nanowires as fillers.

### 2.1.3 Properties to optimize for thermal drawing

The current strategy to identify materials that can be thermally drawn is to look for rheological properties that are similar to that of thermoplastics and was successfully employed to thermoplastic elastomers [8]. As illustrated with polycarbonate in Figure 7, this means a viscosity that slowly decreases with temperature down to  $10^3 - 10^4$  Pa.s over tens of degrees, and a cross-over between  $G'$  and  $G''$ , with a faster decrease of  $G'$ . Such behavior seems necessary for cladding materials, but other materials that do not meet this criterion have been employed in multimaterial fibers: for instance, encapsulated liquid metals even if their viscosity is of the order of 1 mPa.s [74]. On the other end, thermoplastic nanocomposites tend to have increased viscosity and elastic modulus compared to their pure polymer counterpart, but carbon black and more recently carbon nanofiber composites have been successfully drawn [5], [7], [12]. However, to our knowledge, such fillers have not been reported to be suitable for making transparent conducting films. Therefore, our focus is on nanocomposites using carbon nanotubes or metallic nanowires. We consider different fabrication techniques and aim at optimizing the compromise between high electrical conductivity and an effect on the rheological properties that does not prevent thermal drawing. The optical properties of nanocomposites do not seem to depend significantly on the dispersion and we are not aware of studies mentioning such an effect. In contrast, experimental results show a large range of electrical conductivities and percolation thresholds in nanocomposites, depending on the filler and matrix types, the processing technique used and the resulting dispersion. Therefore, we focus on optimizing the conductivity of the nanocomposites and making them thin enough to be transparent after thermal drawing, the thickness required simply depending on the concentration.

The next two sections present the experiments realized for the fabrication and characterization of nanocomposites for thermal drawing, along with literature relevant to the specific techniques employed.

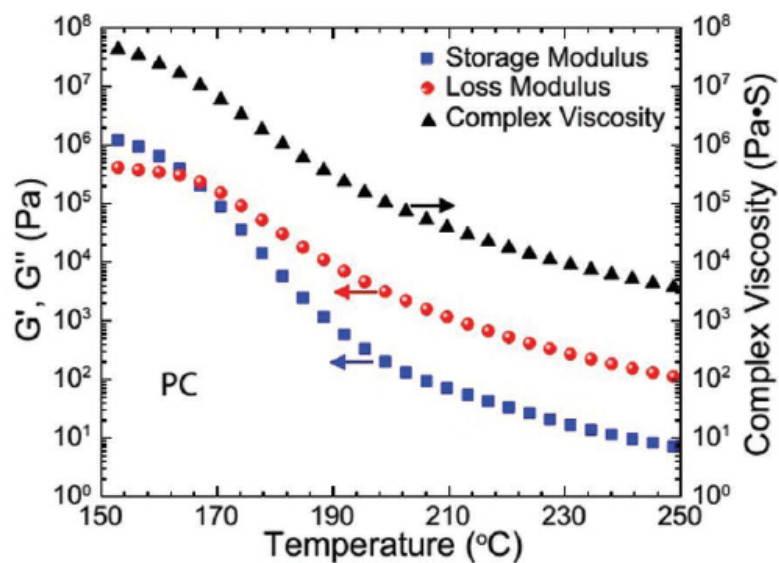


Figure 7. From [8]. Complex viscosity  $\eta^*$ , Storage modulus  $G'$  and Loss modulus  $G''$  versus Temperature of a polycarbonate.

## 2.2 Solution casting

In order to fabricate nanocomposites for thermal drawing, we considered and tested several solvent-based techniques, including rod- and spin-coating, but casting was found to work the best. It consists in pouring a solution on a substrate and letting the solvent dry - possibly accelerated by heating - to create a sheet made of the solid materials that were dispersed or dissolved [75]. Various combinations of solvents, thermoplastic polymers, and high aspect ratio conductive nanoparticles were employed to try to find the most suitable.

### 2.2.1 Materials and preliminary experiments

#### Materials

The first nanoparticles used in this work are Single-Wall Carbon NanoTubes (SWCNT), provided already dispersed in solution. According to the specifications from the manufacturer (OCSiAl), they can be used to make transparent conducting films that have a sheet resistance of 100  $\Omega$ /sq and a transmittance of 87%, and when incorporated in a polymer matrix the resulting nanocomposite can be conducting with a loading of less than 0.1 wt%. Silver nanowires (AgNW) have a larger diameter (by up to two orders of magnitude) and have been shown to reach better performance as transparent conductors [71], thus may be a good alternative to carbon nanotubes. Therefore, they were chosen to be the second type of nanoparticle to study. When cast without modification of the solution composition but after bath ultrasonication, both types of nanoparticles performed well. For example, we could make slightly transparent films with a sheet resistance of 10  $\Omega$ /sq with silver nanowires or 20  $\Omega$ /sq with carbon nanotubes.

We quickly realized that pure films of SWCNT or AgNW could not be thermally drawn in fibers, even if encapsulated between layers of a thermoplastic polymer, as will be shown in Chapter 3. However, conductive thermoplastic nanocomposites based on carbon black (spherical carbon nano-spheres) have been used in thermally drawn fibers for years [5], [7]. Therefore, we then turned towards fabricating nanocomposites in which the nanoparticles considered are dispersed in a thermoplastic polymer.

In fact, the films cast directly from the solutions provided are not pure SWCNT, but also contain the polymer present to stabilize the dispersion. The solvent used is either water or N-Methyl-2-pyrrolidone (NMP), and the stabilizer is either polyvinylpyrrolidone (PVP) or polyvinylidene fluoride (PVDF). The polymer PVP has indeed been reported to stabilize SWCNT dispersions in water [76] and NMP [77]. Such solutions were developed by the manufacturer to improve Li-ion battery electrodes. More details on the composition can be provided: according to the technical data sheets, the specified SWCNT concentration refers to a material that is not purely SWCNTs but has metallic and carbon impurities, and in which the SWCNT dimensions and concentration are estimated (by TGA, EDX, TEM, and Raman spectroscopy) and slightly vary from batch to batch. Thus, the calculated SWCNT concentration in the nanocomposites fabricated includes these impurities. In all batches used, this material is specified to have a carbon content over 85 wt%, a SWCNT content over 75 wt% and a metal impurities content under 15 wt%. The SWCNTs have a mean diameter between 1 and 2 nm, given for each batch with a possible error of at least 0.4 nm, and a length over 5  $\mu$ m, hence an aspect ratio likely over 2500.

Two types of silver nanowires were employed, with either a diameter of 35 nm and a length of 15  $\mu\text{m}$  (hence an aspect ratio above 400) or a diameter of 150 nm and a length of 50  $\mu\text{m}$  (aspect ratio above 300). They were dispersed in water solutions. As SWCNTs have a much smaller diameter and even if they are grouped in bundles in a thermoplastic nanocomposite, the interfacial area with the thermoplastic matrix is huge, which can be presumed to be detrimental to the ability to be drawn in fibers. In that aspect, AgNWs may be more suitable thanks to their larger diameter.

### The solvent casting process

In the fabrication process of solvent-cast thermoplastic nanocomposites based on SWCNT or AgNW, many parameters influence the resulting film. Two thermoplastic polymers that are known to be compatible with thermal drawing were considered: polycarbonate (PC) and poly(methyl methacrylate) (PMMA). A range of different solvents (DMAc, THF, acetone, NMP, chloroform, DMSO) that dissolve either PC or PMMA were tested. This could require the nanoparticles to be transferred from the original solution by evaporating the solvent, then dispersing them again in the tested solvent, assisted by ultrasonication. The resulting solution was then mixed with a solution in which the polymer considered is dissolved, the proportions being guided by the targeted concentration of nanoparticles in the dry composite. Several substrate materials (PTFE, silicone-coated PET, polysulfone, glass) were also compared. To accelerate the drying in air, the substrate was placed on a hot plate. Using a vacuum oven was also considered but led to bubbles in the nanocomposites even when kept at room temperature. To obtain a uniform material, the nanoparticles should not form large agglomerates in the solution or during drying. This can be prevented by performing ultrasonication and adjusting the solution viscosity through polymer concentration and drying temperature. An example of a cast film in which the nanotubes agglomerated during drying is given in Figure 8, whereas uniform films are shown in the next subsection (Figure 12).

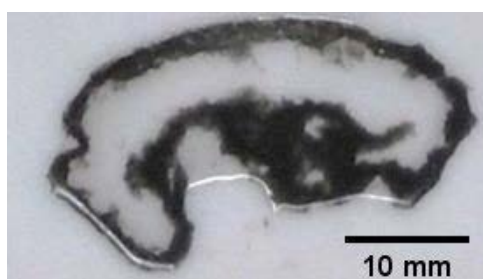


Figure 8. Example of a PMMA/SWCNT nanocomposite with extensive agglomeration of the nanotubes during drying, when the casting parameters are not appropriate.

One combination could achieve a stable dispersion of the nanoparticles both in the solvent and in the dry composite, and a detachable, free-standing nanocomposite sheet: PMMA dissolved in NMP and cast on a non-stick substrate, either silicone-coated PET (polyethylene terephthalate) or Teflon (PTFE or Polytetrafluoroethylene). The PMMA (polymethylmethacrylate) used was purchased from Goodfellow in powder form to facilitate dissolution. As NMP (N-Methyl-2-pyrrolidone) has a high boiling point (202°C) and a low vapor pressure, the substrate was placed on a hot plate set to temperatures between 50°C and 150°C

so that the solvent dries. The drying time was still very long (several weeks), but a higher temperature would cause deformation or agglomeration. A stable dispersion means here that there are no agglomerates visible to the eye, however the conductivity of the nanocomposites depends on how the particles are dispersed at the nanoscale. The AgNW nanocomposites were indeed conductive only from a relatively high loading (about 3 wt%) whereas the SWCNT nanocomposites were conductive even at a very low loading (down to 0.002 wt% - more details in the next subsection). Using scanning electron microscopy (SEM) we could explain this by observing the dispersion under the surface of the nanocomposites: AgNW were grouped in agglomerates that were connected only at high loadings (Figure 9, Figure 10), but SWCNTs form a network even at low loadings (Figure 17, Figure 18). Because of the solvent transfer from water to NMP required for the silver nanowires we could not estimate precisely their concentration in PMMA/AgNW composites.

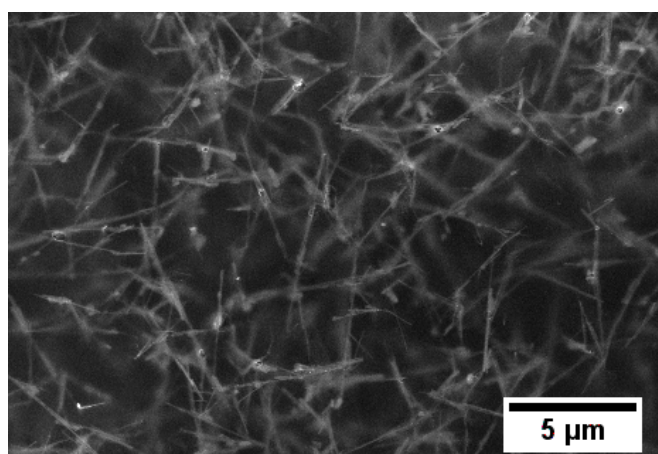


Figure 9. Scanning electron micrograph of a highly concentrated, conductive PMMA/AgNW nanocomposite showing that the nanowires are connected together.

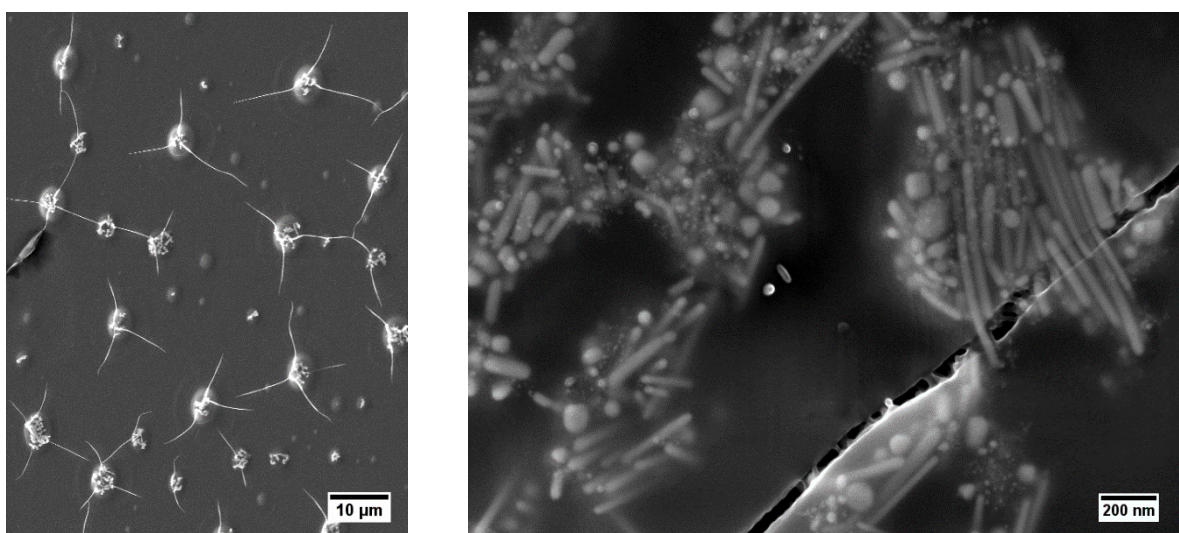


Figure 10. Scanning electron micrographs of a low concentrated, non-conductive PMMA/AgNW nanocomposite showing that the nanowires are grouped in small agglomerates that are not connected together. The white lines in the left image are cracks in the polymer due to the electron beam. It looks like the nanowires have a lower aspect ratio than what is specified, but it may be due to the SEM technique only allowing for an observation of a thin layer under the surface. Ultrasonication could also have broken the nanowires.

Since the solvent casting technique enabled to create PMMA/SWCNT composites with well-dispersed nanotubes, we performed more work of optimization to improve the conductivity at a given loading and probe the lowest concentration at which they are still conductive. This study is presented in the next subsection.

As for PMMA/AgNW composites, they did not give interesting results when thermally drawn in multimaterial fibers, as shown in Chapter 3. They were not studied further, mainly because of the high cost of acquiring them in a larger quantity required for a more extensive study. Metallic nanowires could still prove interesting for the purpose, but a way to disperse them better in the thermoplastic matrix would be required. For example, adding a stabilizing compound in the solution or melt-mixing the dry nanocomposite could be considered. Graphene is another nanoparticle that may be of interest, and hybrid nanocomposites containing two types of nanoparticles could also be investigated.

### 2.2.2 PMMA/SWCNT nanocomposites: Fabrication, measurements and properties

In this subsection, we give more details on the experimental procedure, parameters and experimental results on PMMA/SWCNT nanocomposites made by solvent casting. By doing some work of optimization of the different steps of the process, we tried to improve their conductivity and the lowest concentration at which they are conductive. In particular, one parameter that was not mentioned above is the age of the NMP/SWCNT solution used, i.e. the time between the manufacture and the casting. Three different batches of SWCNTs dispersed in NMP (provided in 250 mL or 1L bottles) were successively used for this study, corresponding to two different formulations: 0.1 wt% SWCNT and 0.3 wt% PVP for the two first ones (called A and B) or 0.2 wt% SWCNT and 2 wt% PVDF (batch C). The SWCNTs are not perfectly individualized but bundled, as determined from TEM images such as the ones shown in Figure 11. The BET surface area is around 500 m<sup>2</sup>/g. Due to gradual agglomeration of the SWCNTs in the suspensions, the manufacturer recommends usage within three months of manufacture and refresh the dispersion before use by ultrasonication. The batch A was used one year after manufacture, whereas the batches B and C were used within 3 months of manufacture.

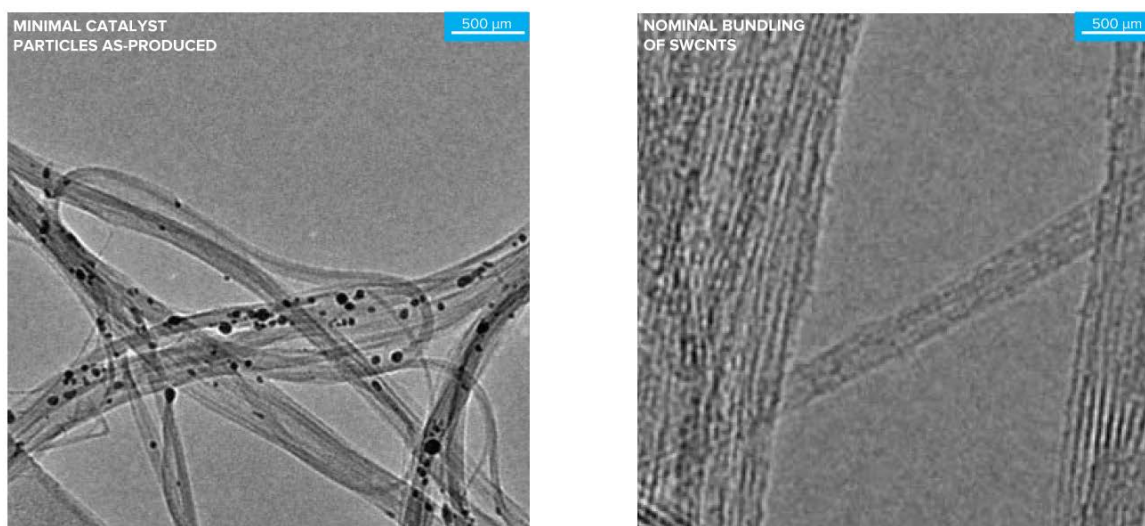


Figure 11. Typical TEM pictures used to estimate the specifications of the SWCNT product by the manufacturer OCSiAl (from the brochure of the product).

### Experimental procedure

Based on calculations from [78], SWCNTs with a diameter between 1 and 2 nm have a density between 1.5 and 3.0 g.cm<sup>-3</sup>. Given that the SWCNTs have an unknown distribution of diameters and the mean diameter is not accurate either, it would only be possible to estimate the volume percentage of SWCNTs in the suspensions and the PMMA nanocomposites made from them with a large inaccuracy. Therefore, in the following we will simply refer to concentrations of the impure SWCNT product given in weight percentages - exactly as for the solutions provided - knowing that the numerical values for volume percentages would be lower since the density of the solvent or PMMA matrix is lower (1.19 g.cm<sup>-3</sup>).

The NMP solutions for casting were prepared by mixing two solutions in 10 mL vials, one containing the dissolved PMMA, the other the dispersed SWCNTs, in proportions calculated to achieve a target loading of SWCNTs in the dry PMMA/SWCNT nanocomposite. The first solution was prepared by dissolving PMMA powder in NMP and homogenized by magnetic stirring; concentrations of 10, 20 and 30 wt% of PMMA in NMP were considered. The second solution was from one of the original formulations provided, either as received or diluted 10 times to allow for a precise measurement of the SWCNT content for the lowest concentrations. Prior to casting, the solutions were sonicated in an ultrasonic bath.

The three batches of the NMP/SWCNT suspensions described above were successively used to improve the fabrication process of the PMMA/SWCNT nanocomposites and the resulting properties. An important factor was indeed found to affect the SWCNT dispersion and the nanocomposite properties: the amount of time passed between manufacture and use of a suspension. This is due to slow agglomeration of the SWCNTs, and the reason why the manufacturer recommends using them within three months. Because of this, optimal conditions found at a particular time may not apply later. Moreover, due to variations in the specifications of the SWCNTs coming from the manufacturing of the different batches, two batches cannot lead to strictly identical results, even if used in the exact same conditions and after the same time since manufacture. For these reasons, for batches A and B then for batch C, the procedure hereafter was followed. First, some work of optimization was done for some of the parameters of the process, which include the concentration of

PMMA in the NMP/PMMA solution, the sonication time of the NMP/PMMA/SWCNT solution, the substrate material and the hot plate temperature. Then a set of parameters was chosen, and a series of samples of different concentrations was made by pouring the corresponding solutions on the flat substrates on which they slowly dried to form a nanocomposite sheet. The samples made typically had a thickness of 200 to 500 microns and a diameter of 3 to 4 cm (Figure 12).

For all three batches the concentration of PMMA in the NMP/PMMA solution was chosen to be 20 wt%. The other values tested were 30 wt% which meant a too high viscosity that prevented uniform mixing, and 10 wt% which led to a too low viscosity that enabled nanotube agglomeration during drying. The same casting parameters were used for the two first batches to evaluate the effect of solution aging. They were bath-sonicated for 2h before mixing and cast on a silicone-coated PET substrate attached on a metallic plate, placed on a hot plate at 60°C for one week. For the third batch the sonication time was increased to 3h, the substrate was Teflon and the hot plate temperature was 100°C. This temperature was chosen after studying the drying time by measuring the weight of a sample regularly over more than a month with these drying conditions (Figure 13). Indeed, even if a sample seemed dry and could be handled and characterized, this measurement showed its weight could still decrease as it could be further dried. Teflon was chosen to replace silicone-coated PET because the latter deforms on a hot plate set to 100°C. None of the samples fabricated were therefore perfectly dry when their electrical and optical properties were measured, but the ones made from batch C were slightly drier.

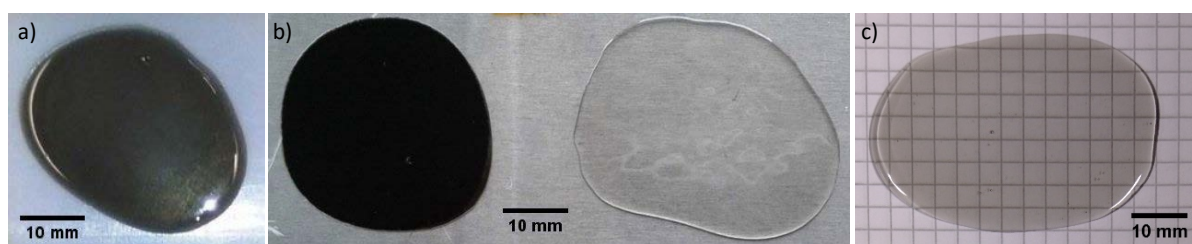


Figure 12. Pictures of solvent-cast PMMA/SWCNT nanocomposites:

a) Sample before drying, on a non-stick white Teflon substrate.

b) Opaque (0.5 wt%) and transparent (0.002 wt%) samples on a silicone-coated PET non-stick substrate (transparent, on a metallic plate).

c) Dry, free-standing, transparent sample placed on a notebook page.

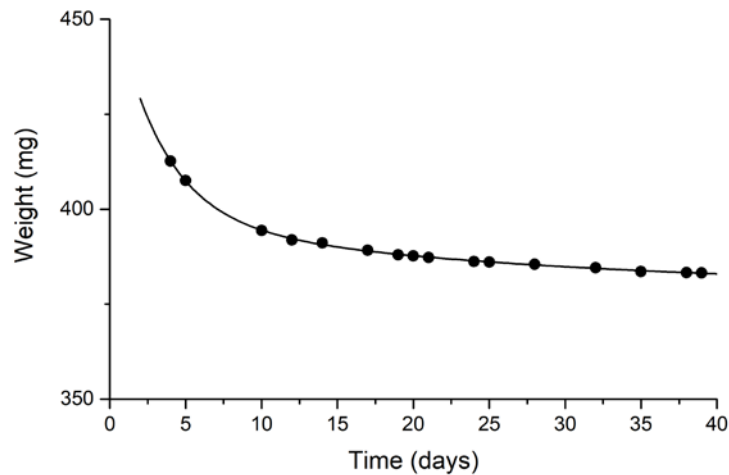


Figure 13. Plot of the weight of a cast sample versus drying time, when placed on a hot plate at 100°C. The line is a guide to the eye - it comes from a fitting with a double exponential decay, which gives the best fit.

### Electrical properties

The electrical conductivity of the samples was measured using a Keithley digital multimeter (DC mode) and a Zürich Instrument Lock-in Amplifier (AC mode, for batch C only). Due to non-perfect electrical contacts, using a 2-wire configuration led to a non-ohmic behavior, i.e. I-V curves that do not form a straight line. To bypass this issue, either a 4-wire configuration or silver paint, which eliminated the contact resistance and enabled to observe the ohmic behavior of the material, was employed. The resistance  $R$  (in DC mode) or impedance  $|Z|$  (in AC mode) of the samples could therefore be measured. After quantifying the geometrical dimensions of the samples cut to a rectangular shape and with uniform thickness, the values of  $R$  or  $Z$  (in Ohm) could be converted to conductivity using equation (2). This correspond to the in-plane conductivity of the samples, but the conductivity across the thickness of the samples could also be evaluated for some samples and was typically 20 times lower for a concentration of 0.1 wt%, showing the anisotropy of the material resulting from the solvent casting process.

Even though samples were also made at concentrations of 0.001 wt, 0.0005 wt% and 0.0002 wt%, the lowest values at which the DC conductivity was measurable were 0.005 wt% for batch A and 0.002 wt% for batches B and C. To our knowledge, 0.002 wt% is lower than the lowest previously reported value for a conducting polymer nanocomposite, which is 0.0025 wt% [37] – and the conductivity is more than 3 orders of magnitude higher.

Figure 14 shows the DC conductivity versus concentration of the samples made from the three batches, along with the corresponding fit obtained using the classical percolation law of equation (4). The fitted values of  $p_c$  and  $c$  and the standard deviations are the following:

- Batch A:  $p_c = 0.002\ 07 \pm 0.000\ 99$  wt%,  $c = 2.099 \pm 0.076$
- Batch B:  $p_c = 0.001\ 89 \pm 0.000\ 07$  wt%,  $c = 1.706 \pm 0.097$
- Batch C:  $p_c = 0.001\ 55 \pm 0.000\ 21$  wt%,  $c = 1.785 \pm 0.107$

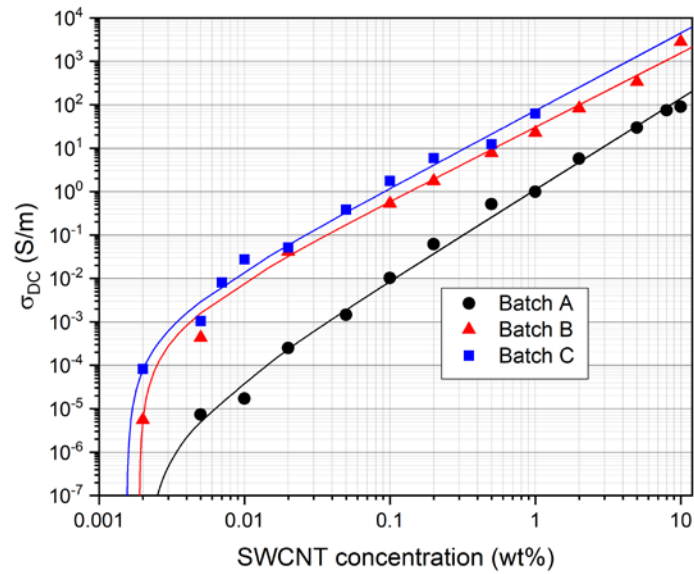


Figure 14. Log-log plot of the DC conductivity versus nanotube concentration of PMMA/SWCNT nanocomposites from the three batches A, B and C (described above). The lines correspond to the fitting with the classical percolation law (equation (4)).

Figure 15 shows the AC conductivity versus frequency of samples of Batch C at different concentrations. The conductivity at low frequencies matches the DC conductivity. For the samples that exhibit a region of frequency-independent conductivity at low frequencies followed by a region of frequency-dependent conductivity, we can extract a critical frequency  $f_c$  which is, according to Alig et al. [79], related to the time that charge carriers take to explore percolation clusters. However, it does not seem to provide any quantitative information.

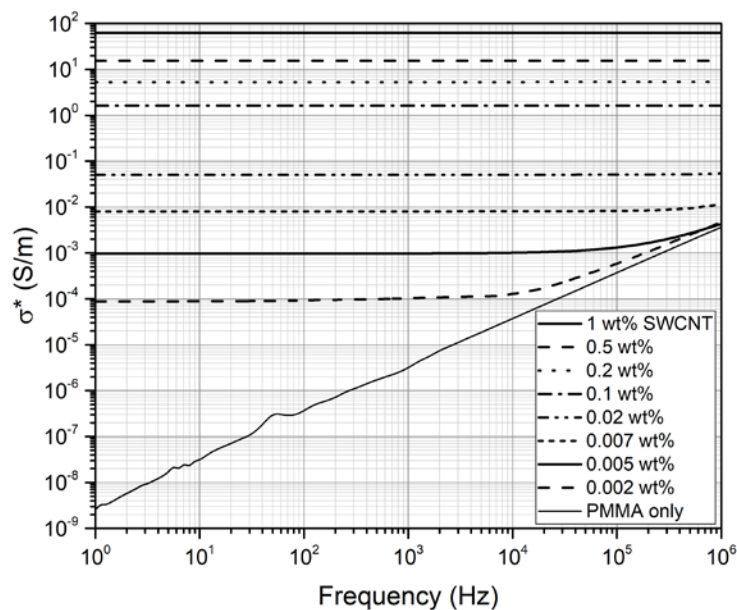


Figure 15. Log-log plot of the AC conductivity versus frequency for the nanocomposites of Batch C and pure PMMA.

### Light and electron microscopy

The samples were then observed using optical and electron microscopy. First, the nanotubes dispersion in transparent samples from batches A and B could be compared using transmitted light microscopy (Figure 16). This shows that for solutions with the same composition and cast under the same parameters, the age of the batch likely has a large influence on the nanotube dispersion and agglomerates in the resulting nanocomposites. The solution used one year after manufacture (batch A) indeed leads to many more large agglomerates than the one used within three months (batch B), which means there was a gradual formation of agglomerates that were not well dispersed by ultrasonication. As observed in Figure 16, more agglomerates mean here a much less efficient electrical conduction at a given concentration. Strictly speaking, we cannot rule out that the difference between the samples from batches A and B does not come from the aging of the solution, as it could also be due to differences in the batches from their manufacture. An ideal experiment would evaluate aging with samples made from the same batch, but then air temperature and humidity should be monitored as they may have an impact on the drying step. Directly evaluating aging of a batch would also be possible by optical techniques that consider the transmission of light through the solution.

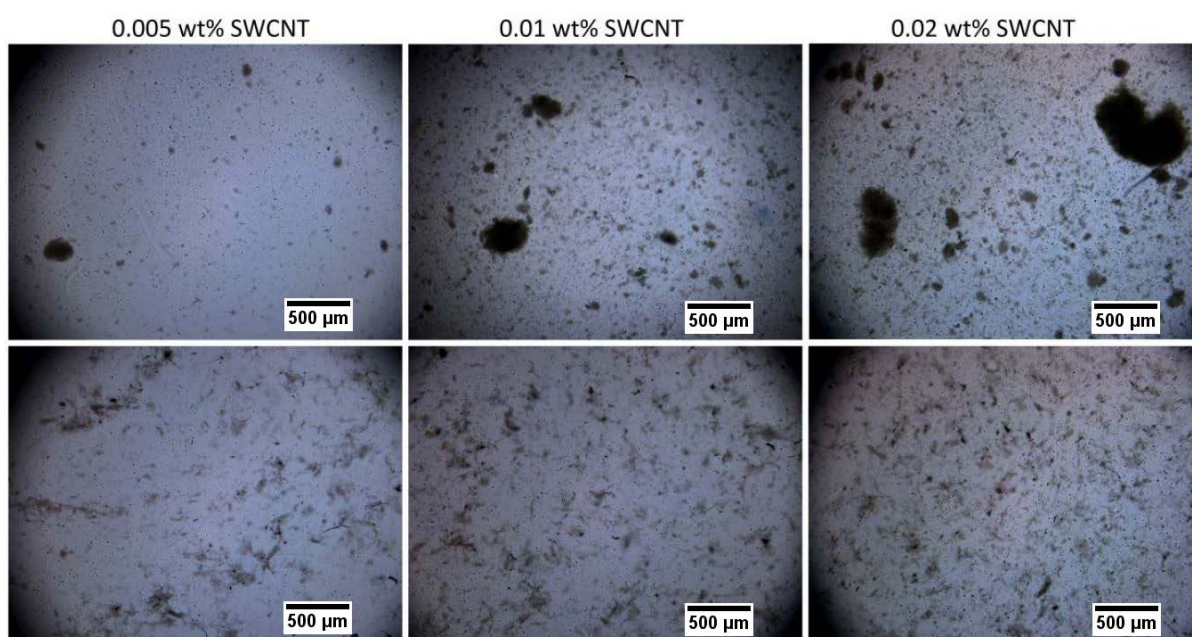


Figure 16. Comparative optical micrographs of 0.005, 0.01 and 0.02 wt% PMMA/SWCNT nanocomposites made using two different NMP solutions with the same formulation: 0.1 wt% SWCNT stabilized with 0.3 wt% PVP. To make the samples in the first row (Batch A), the solution was used one year after manufacture, whereas for the samples in the second row (Batch B), it was within three months.

We could not observe visible differences between the batches B and C, therefore it seems that the cumulative effect of replacing PVP by PVDF and using slightly different casting parameters only incrementally improved the nanotube dispersion and the resulting conductivity.

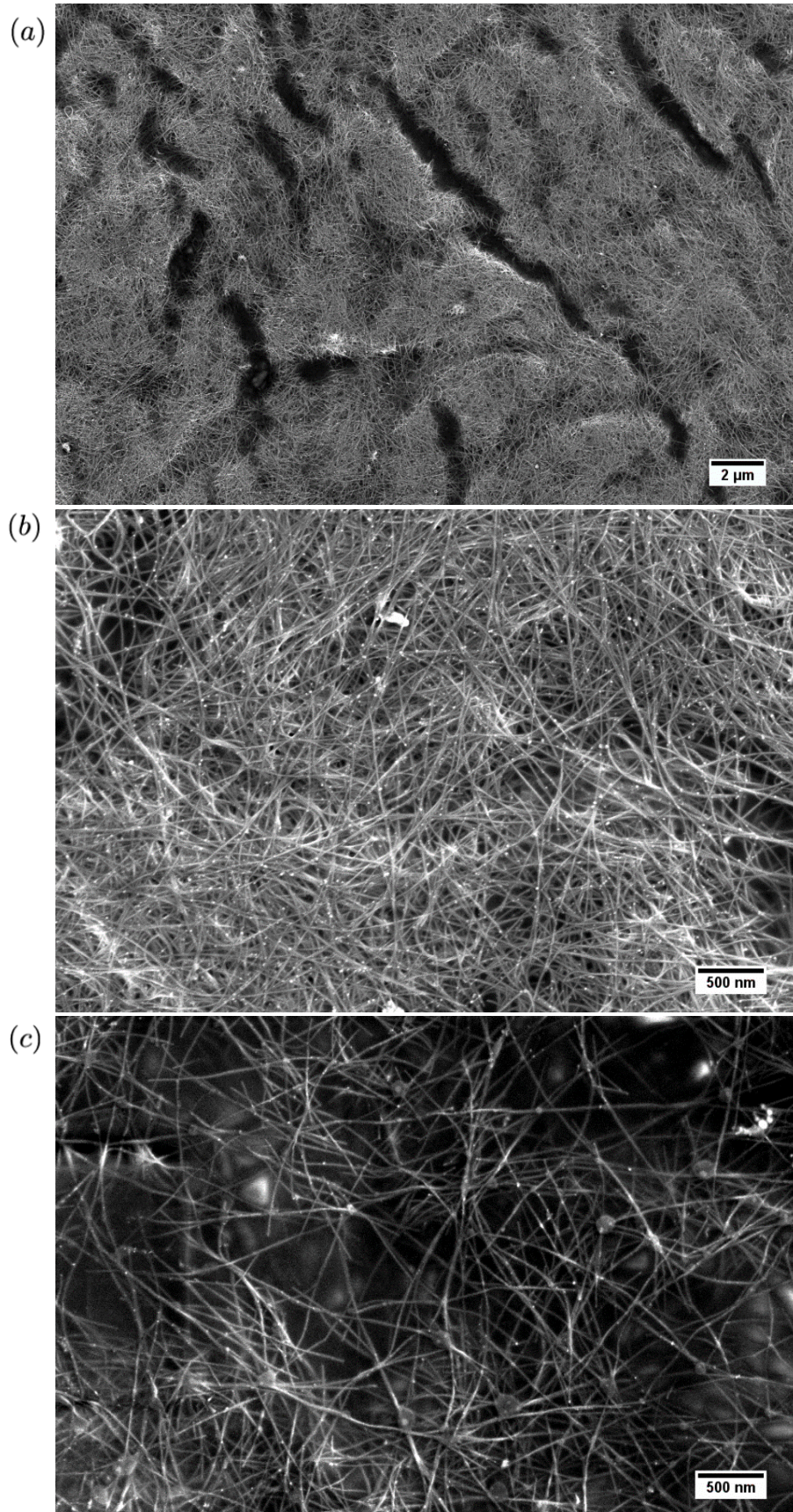


Figure 17. Scanning Electron Micrographs of the surface of PMMA/SWCNT nanocomposites with a concentration of 5 wt% for a) and b), and 0.5 wt% for c). This shows the array of nanotubes is dense at the high concentration of 5 wt%, and sparser but still well interconnected at 0.5 wt%. Metallic impurities are also visible as white dots.

Transmitted light microscopy was found to be the tool that reveals the differences in dispersion between batches A and B thanks to the relatively large scale at which it operates, which is larger than the feature size of agglomerates, and the fact that it takes into account the whole thickness of the samples. By contrast, Scanning and Transmission Electron Microscopy (SEM and TEM) only enable to examine a shallow layer of material over a surface that is too small to evaluate agglomeration quantitatively. However, these techniques allow for an observation of individual nanotubes, how they bundle and form a network. In Figure 17, SEM pictures of the surface of nanocomposites show that this network is well interconnected with long nanotubes or bundles oriented in all directions – at least in the plane perpendicular to the viewing direction. This can also be observed in the left TEM picture of Figure 18, whereas the higher magnification of the right picture enables to observe the atomic layers and notice that there are individual single-wall carbon nanotubes, and mostly bundles of a few nanotubes.

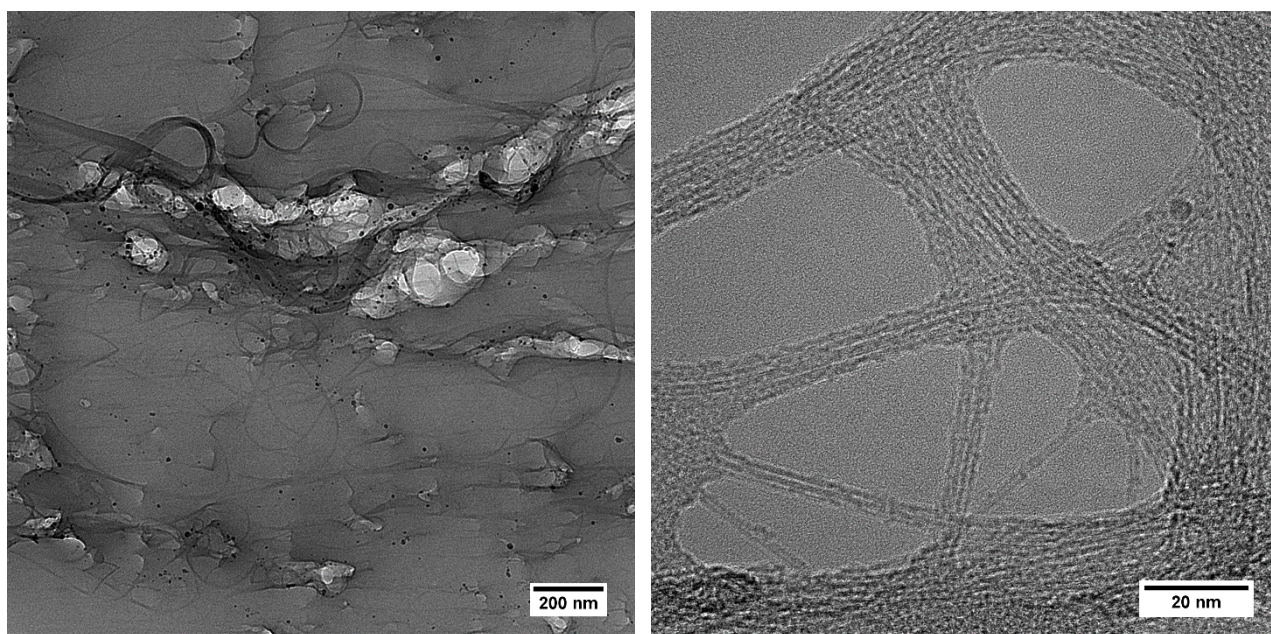


Figure 18. Transmission Electron Micrographs of a PMMA/SWCNT nanocomposite with a concentration of 1 wt%. The sample was prepared by ultramicrotomy.

Overall, these microscopy techniques enable to understand why this technique to fabricate nanocomposites efficiently led to conductive samples down to the very low concentration of 0.002 wt%: a low proportion of nanotube is grouped in large agglomerates, and the nanotubes or bundles have a very high aspect ratio that allows for an interconnected network even at very low concentrations. Every step of the process participates in keeping the nanotubes dispersed until they are in the dry nanocomposite. First, the nanotube solutions were industrially made, therefore the manufacturer likely carefully chose the solvent (NMP) and stabilizer (PVP then PVDF) and optimized the fabrication so that the nanotubes are well individualized with only a relatively slow agglomeration over several months. Then, the solutions were sonicated to refresh and improve the nanotube dispersion. Finally, the concentration of PMMA in the cast solutions was tuned so that their viscosity prevents extensive agglomeration during drying and keeps the nanotubes or bundles well

individualized by limiting their motion. Attractive forces [80] between nanotubes still bring them close enough for electrical contact and a percolating network at the sample scale.

### Optical properties

The optical transmittance in the visible range of the samples from batch C was measured using a white light source, an integrating sphere and a detector (Figure 19). From a concentration of 0.2 wt%, the samples were opaque. For the lowest concentrations, we estimated the absorption coefficient using equation (19). Combining the results on optical transmittance and electrical conductivity we calculated the figure of merit  $\sigma_{DC}/\sigma_{op}$  with equation (20). The values (Figure 20) are low compared to the best transparent conductors, for which it is above 100, but increase with concentration and could not be estimated for loadings higher than 0.05 wt%. However, this result is interesting since the trend suggests that to obtain the best transparent conducting nanocomposite possible in fibers, we should employ the highest loading compatible with thermal drawing.

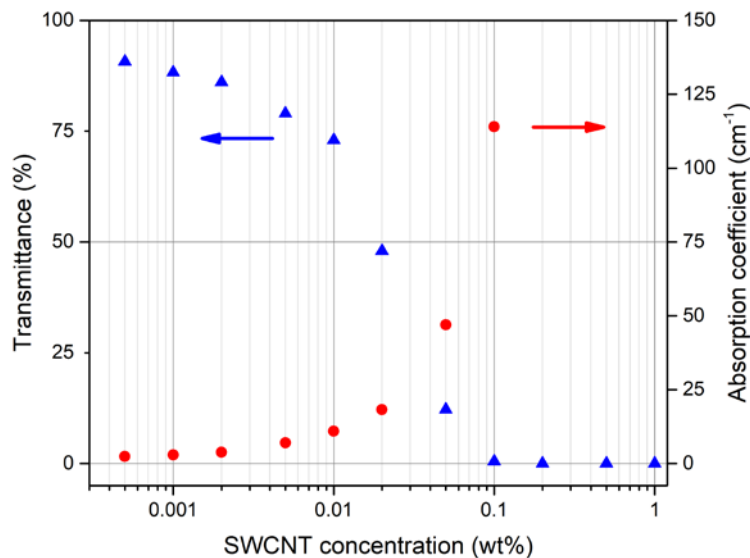


Figure 19. Transmittance (averaged for wavelengths between 650 nm and 750 nm) and absorption coefficient versus SWCNT wt% for the nanocomposites of Batch C. The absorption coefficient was calculated from the transmittance and thickness of the samples; this is an estimate assuming no reflection (which is low, likely below 5%). From 0.2 wt% the nanocomposites are opaque and the absorption coefficient cannot be obtained.

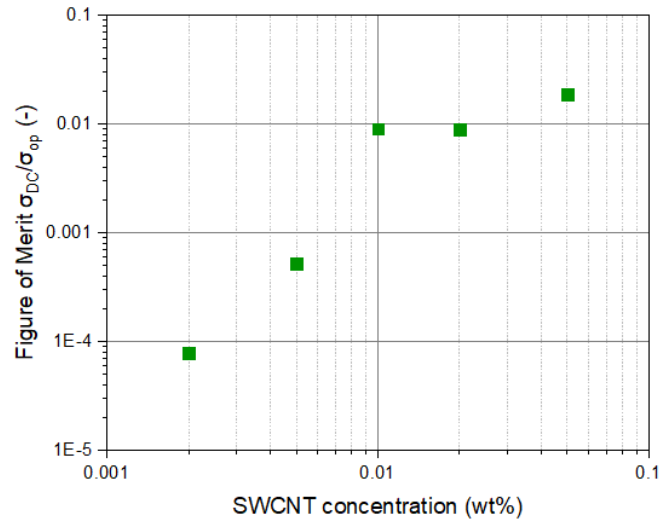


Figure 20. Figure of merit  $\sigma_{DC}/\sigma_{op}$  versus SWCNT wt% for the nanocomposites of Batch C. The values are much lower than that of high-performance transparent conductors, but sharply increases with concentration.

Due to the solvent used, NMP, which has a high boiling temperature, there was an important drawback to this casting technique: residual solvent could not be extracted from the nanocomposite samples and seemed to react with the PMMA matrix when heated above 150°C, making it look brown. We verified that this effect did not occur when heating the PMMA before dissolution in NMP but happened with pure PMMA cast without nanotubes to single out its cause. First, this was an issue when considering improving the conductivity of transparent nanocomposite samples by annealing, since they would then lose their transparent attribute. Moreover, we thought about hot pressing to decrease the thickness of more highly concentrated, opaque samples to make them transparent, but the issue mentioned makes this unusable. Finally, rheological studies were also impacted, as the viscosity at fixed temperature (180°C) of cast PMMA was found to increase with time while it was constant for the PMMA before dissolution.

## Conclusion

We developed a process based on the solvent casting technique that enabled to make a PMMA/SWCNT nanocomposite conductive at concentrations down to 0.002 wt% - or 20 ppm by weight - which is the lowest concentration reported for a bulk thermoplastic to our knowledge. The required conductivity for electrostatic dissipation applications is 10<sup>-3</sup> S/m [30], which is reached by the nanocomposite we fabricated from a concentration of only 0.005 wt%, and at which light transmittance is above 75% for a thickness of 0.4 mm. Therefore, this material may be interesting for being antistatic and transparent even in bulk, as it suppresses the need for coating a non-conductive transparent bulk material. At the time of writing, an article presenting the results of this section is in preparation for submission to a scientific journal.

The NMP solvent employed is however not ideal since it dries slowly and leaves residues that make any treatment that heats the material unusable. This could be solved if an alternative solvent that enables the same process without this drawback was found.

For use in thermally drawn fibers, the fact that the figure of merit  $\sigma_{DC}/\sigma_{op}$  increases drastically with concentration suggests that we should employ the highest loading possible. However, neither the SWCNT nor AgNW nanocomposites made by solvent casting led to interesting results when trying to thermally draw them in multimaterial fibers, as will be shown in Chapter 3. The melt-mixed nanocomposites presented in the following section turned out to work better in fibers, therefore solvent casting was not further studied.

## 2.3 Melt mixing of CB and CNT thermoplastic nanocomposites

The second technique that was used to fabricate nanocomposites is called melt mixing. It consists in mixing a melted thermoplastic with fillers in an extruder, in which shear forces induced by rotating screws (Figure 27) cause the separation of the nanoparticles from bundles to achieve the dispersion required for high electrical conductivity at low concentration. Being able to tune the temperature, screw rotating speed and duration of mixing allow for a better control compared to ultrasonication [81]. Moreover, no solvent is involved in the process, eliminating the possible issues with residual solvent and making the handling of the samples simpler. The melt mixing of carbon nanotube composites has been extensively researched for more than a decade, thus the results of many studies can help understand the mechanisms at stake. The most relevant ones will be presented in this section. Interestingly, both melt mixing and thermal drawing are techniques in which a thermoplastic polymer or nanocomposite is processed in the melt and undergoes large deformation and shear. Therefore, existing literature on melt mixing can not only provide useful knowledge for the fabrication step, but also for the thermal drawing process itself.

### 2.3.1 State of the art

#### **Melt mixing parameters and resulting properties**

Synthesized carbon nanotubes in dry powder form are entangled and attractive interactions tend to keep them agglomerated. To create a conducting percolating network when mixed in a melted polymer, they have to be de-agglomerated and dispersed by applying sufficient shear forces, which is the role of a mixing machine [80], [82] such as the twin-screw micro-extruder shown in Figure 27. This can be done in a single step, or in two steps by masterbatch dilution. This second method consists in mixing a masterbatch of concentrated carbon nanotube composite with pure polymer to achieve the desired concentration. Masterbatches are commercially available in the form of pellets and typically have a loading of 10 to 20 wt% of carbon nanotubes that are already dispersed. This method is more convenient since it does not require to deal with dry nanoparticles and the corresponding necessary safety measures.

Lin et al. [82] compared the nanocomposites made from the same materials (a PC/CNT masterbatch and pure PC) with three different miniature mixers under the same conditions (temperature of 265°C, screw speed of 50 rpm for 6 minutes). The resulting percolation thresholds are between 0.5 and 0.75%, which is relatively low and shows how efficient the process is, even if a decrease of nanotubes length was observed by Atomic Force Microscopy. The differences in the dispersion observed by TEM and properties indicate that this technique is system-dependent. An engineering approach is taken when employing this melt mixing method, as the values of applied shear rates are unknown for example. Various studies tested several mixing parameters or materials to optimize the resulting conductivity [43], [65], [83], observed the corresponding dispersion and interpreted the results in terms of the influence of shear and annealing, which we elaborate on in the following.

## Shear and annealing studies

In fact, although shear forces need to be applied to initially disperse the nanotubes, it is also possible to disperse them too much, in the sense that individualizing them completely can prevent a percolating network, since contacts are necessary for electrical conduction. This can be the case in particular at a low concentration close to the percolation threshold, which itself depends on the processing parameters, and can be observed in the TEM pictures of Figure 4, where some degree of agglomeration provides conductivity whereas individualized nanotubes do not [43]. Recovery of electrical conductivity is however possible by annealing or hot pressing a nanocomposite. At a temperature at which the polymer viscosity is low enough to enable the Brownian motion of the nanotubes, attractive interactions indeed promote a local reorganization that forms a conductive network [43], [84]. Such shear-induced destruction and quiescent recovery of the carbon nanotube network have been the subject of various studies. For example, by measuring the conductivity of the nanocomposite inside the mixing chamber, Alig et al. noticed that the polycarbonate loaded with 0.875 wt% carbon nanotubes was insulating when the extruder was running but quickly recovered its conductivity when stopped (Figure 21). Increasing the temperature or the concentration made the recovery faster.

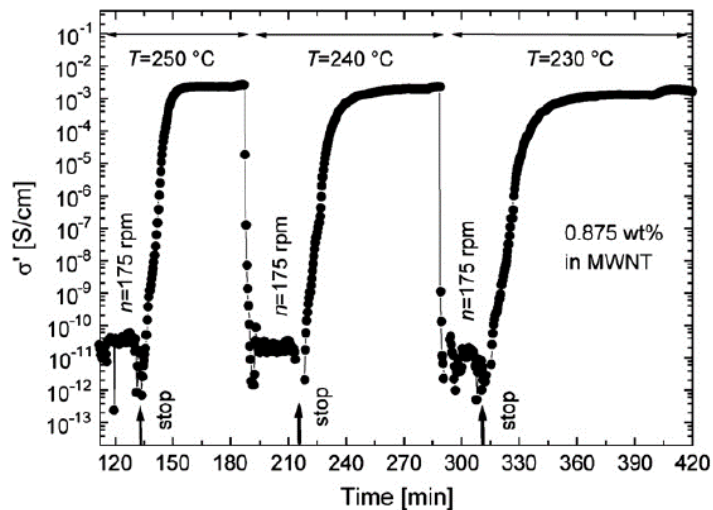


Figure 21. From [84]. Conductivity of a polycarbonate/nanotube composite (0.875 wt%) measured inside a mixing extruder. The nanocomposite has a low conductivity when the twin screws are rotating, and quickly increases when resting at the extrusion temperatures.

The effects of both shear and annealing could be analyzed in more details using a parallel plate rheometer (such as the one in Figure 27), which allows for the application of a known shear rate and simultaneous rheological and electrical measurements [85]–[88]. Annealing induces an increase of the electrical conductivity but also of the elastic modulus and the viscosity after application of shear, as shown in Figure 22. The same effect was present in both carbon nanotubes and carbon black composites [88].

Conversely, application of shear most of the times causes a decrease of the conductivity and viscosity, as shown in Figure 23 [88]. Skipa et al. [86] pointed out that a low shear rate (0.02 rad/s) can actually accelerate

the recovery of conductivity while decreasing  $G'$  and  $G''$ , due to the formation of small connected agglomerates replacing individualized nanotubes.

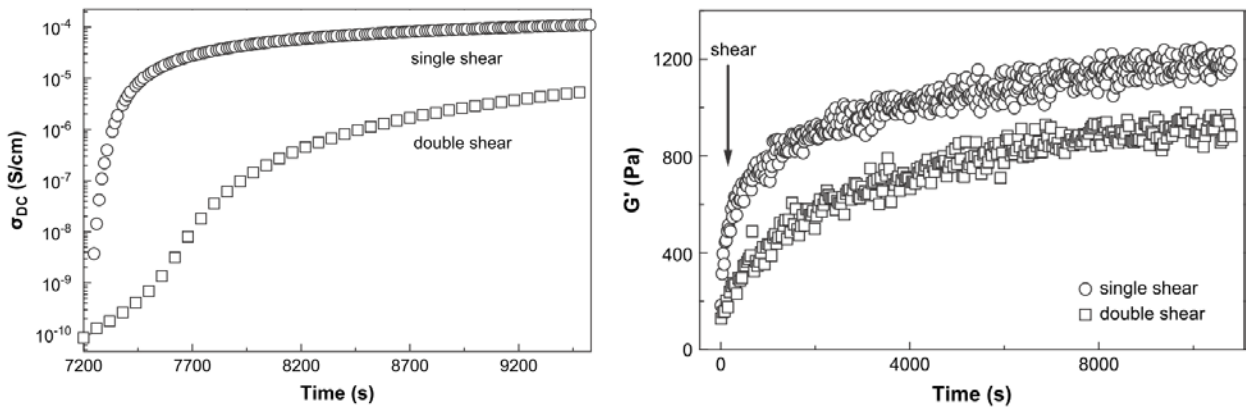


Figure 22. From [85]. Conductivity (left) and Elastic Modulus (right) versus time of annealing of a polycarbonate/nanotube composite (0.875 wt%) after application of shear at a rate of 1 rad/s for 10 seconds (“single shear”) or 10 rad/s for 1 second followed by 1 rad/s for 10 seconds (“double shear”). Note the origin of time of 7200 seconds in the left plot corresponds to 0 seconds in the right plot, and the time scales are different.

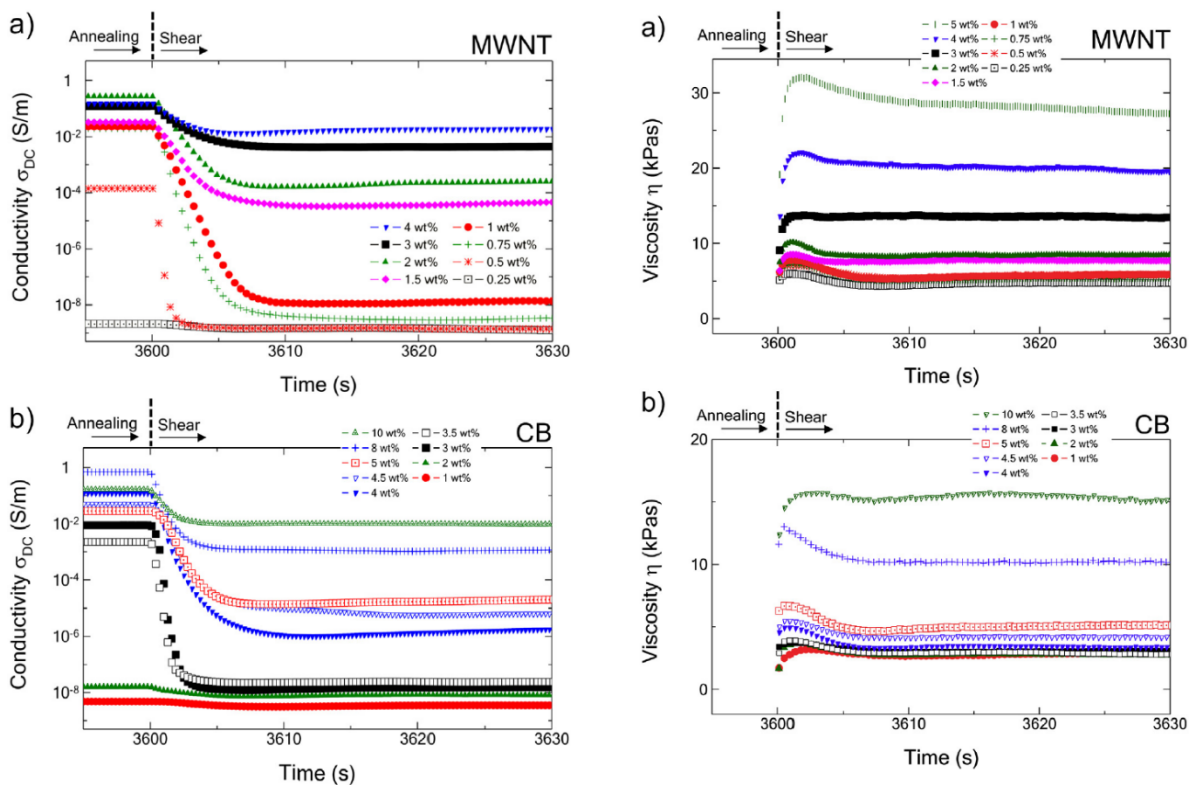


Figure 23. From [88]. Conductivity (left) and Viscosity (right) of nanotube (MWNT) and carbon black (CB) polycarbonate composites at different concentrations, measured simultaneously during application of a steady shear at a rate of 1 rad/s, and after quiescent annealing for 1h at 230°C.

A similar decrease of conductivity was reported for a carbon black composite under elongation instead of shear, as shown in Figure 24 [89]. Since thermal drawing also involves elongation more than shear, this suggests that the studies on sheared nanocomposites can still be considered relevant.

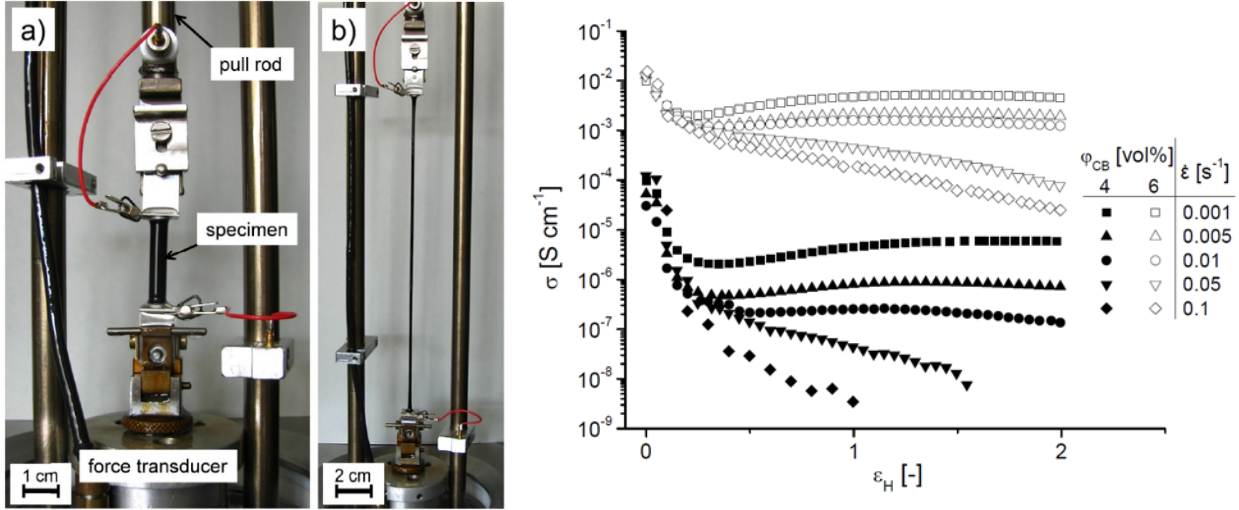


Figure 24. From [89]. Left: Experimental setup based on a Mnstedt tensile rheometer for measurement of electrical conductivity of a polystyrene/carbon black composite, before (a) and after elongation (b). Right: Conductivity versus Hencky strain of two composites (4 and 6 vol%) elongated at different rates at 150°C.

### Modeling the effect of annealing and shear

Models of the behavior of conducting nanocomposites under both annealing and shear were developed along with these experimental studies. First, for recovery of conductivity a kinetic equation was proposed for the concentration  $p_e(t)$  of agglomerated nanotubes that effectively participate in the conduction, the remaining nanotubes being considered individualized and not participating [66]:

$$\partial_t p_e = k_0 \cdot (p_{e\infty} - p_e) \quad (21)$$

Here  $p_{e\infty}$  is the limit for infinite annealing time and  $k_0$  a kinetic coefficient. Then the conductivity is calculated using the percolation law (Equation (4)) replacing the actual concentration  $p$  with  $p_e$ . By fitting the parameters, this model adjusts well to the graphs of conductivity recovery [66], [86], [88]. Adding a second term in the kinetic equation was shown to fit most experimental results for the conductivity of a nanocomposite under constant shear rate [66], [87]:

$$\partial_t p_e = k \cdot (p_{e\infty} - p_e) - k_2 \cdot p_e \quad (22)$$

These kinetic coefficients are fitted for a single value of shear rate. On the other hand, the steady-state (limit for infinite shearing time) viscosity or conductivity can be described by a Carreau equation for shear-thinning, which explicitly shows the dependence on shear rate [54]:

$$\eta(\dot{\gamma}) = \frac{\eta_0}{(1 + (\dot{\gamma}\tau_n)^2)^n} \quad (23)$$

$$\sigma(\dot{\gamma}) = \frac{\sigma_0}{(1 + (\dot{\gamma}\tau_\sigma)^2)^n} \quad (24)$$

Or [87]:

$$\sigma(\dot{\gamma}) = \frac{\sigma_0}{(1 + \dot{\gamma}\tau_\sigma)^m} \quad (25)$$

The dependence on shear rate can also be introduced in the kinetic equation, and enables to fit the results for a large range of shear rates with the same parameter (Figure 25) [24]:

$$\partial_t p_e = -a \cdot \eta \cdot \dot{\gamma}^m \cdot (p_e - p_c) + b \cdot (p_{in} - p_e) \quad (26)$$

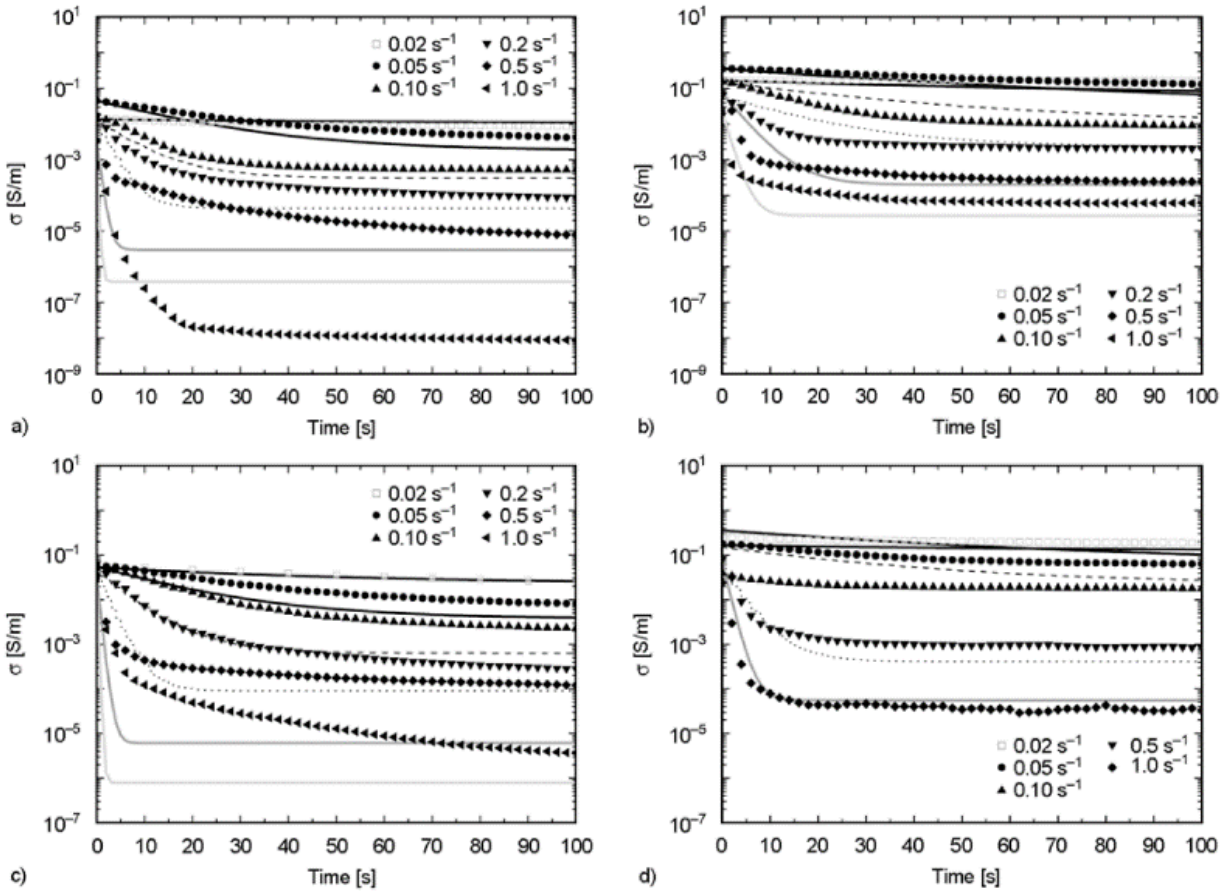


Figure 25. From [24]. Conductivity versus time of polycarbonate/MWCNT composites (a, b: 0.75 wt%. c, d: 1 wt%) under constant shear at different rates and temperatures (a, c: 230°C. b, d: 265°C). The lines correspond to a shared fit of equation (26) with the values  $a = 0.25 \times 10^{-4} \text{ Pa}^{-1} \cdot \text{s}^{-1/2}$ ,  $b = 10^2 \text{ s}^{-1}$  and  $m = 1.5$ . The fit is far from perfect but captures the behavior at different concentrations, temperatures and shear rates simultaneously.

We can notice that in this model, the decrease of effective concentration is proportional to the viscosity. This is consistent with an earlier work conducted in FIMAP that compared the conductivity a carbon black

composite thermally drawn at two different temperatures. The conductivity was indeed much lower after drawing at a lower temperature, therefore with a higher viscosity, whereas the deformation rates are thought to be similar in both conditions. Unlike the studies presented here, thermal drawing is not an isothermal process. The precise temperature profile and deformation undergone need to be known to apply this kinetic equation quantitatively to a nanocomposite during the process. This is the subject of Chapter 4, in which we both model the thermal drawing process and employ a generalized version of this kinetic equation to compute the conductivity of thermally drawn nanocomposites.

### 2.3.2 Experiments: Materials, fabrication process and measurements

The remaining of this section presents the melt-mixing and characterization of conductive nanocomposites we fabricated with the goal of thermally drawing them with optimized post-drawing properties.

#### **Materials**

The first conductive nanocomposite studied has carbon black particles dispersed in polycarbonate (PC/CB), and comes in the form of sheets with a thickness of  $0.010'' = 0.254$  mm. It was employed in previous research on multimaterial fibers and is often referred to as “cPC” for “conductive polycarbonate”. Unfortunately, the carbon black concentration is not known precisely, and the grade of the polycarbonate matrix is unknown. The conductivity of the sheets was measured at 5 S/m in the plane and 0.2 S/m across, the anisotropy being probably due to the manufacturing process.

Then, several types of masterbatch of multi-walled carbon nanotubes (MWCNT) dispersed in a thermoplastic matrix were acquired from the company Nanocyl in pellet form (Figure 26) to prepare nanotube composites by melt-mixing. The matrices were the following: polycarbonate (PC) with 15 wt% MWCNT, high density polyethylene (HDPE, 15 wt%), low density polyethylene (LDPE, 20 wt%), polystyrene (PS, 10 wt%), thermoplastic polyurethane (TPU, 10 wt%) and styrene-ethylene-butylene-styrene (SEBS, 10 wt%). The high loading of already dispersed CNT leads to a high conductivity for these concentrates, for example 300 S/m and 30 S/m respectively for the PC and HDPE masterbatches, which are the ones that were mainly employed due to being the most successful in thermal drawing (see Chapter 3). According to the specifications from the supplier, the MWCNTs have an average diameter of 9.5 nm and an average length of 1.5  $\mu$ m, which corresponds to an aspect ratio of about 150. To dilute the masterbatches and achieve lower loadings, pure polymers in pellet form of either the same grade as in the corresponding masterbatch, also provided by Nanocyl, or from different grades were used. Grades of the same polymer with different viscosities were indeed shown to have a large influence on the rheological and electrical properties of CNT nanocomposites made from them [83], therefore we investigated whether this could help optimizing the ability to draw and properties of the PC and HDPE nanocomposites fabricated.



Figure 26. Pellets of the PC/MWCNT masterbatch (15 wt%).

### Melt mixing

The melt mixing technique was used to prepare PC/MWCNT and HDPE/MWCNT nanocomposites with concentrations ranging from 0.5 wt% to 10 wt% for PC, and 2 wt% to 15 wt% for HDPE. A concentration of 15 wt% means the HDPE/MWCNT masterbatch was mixed without changing its composition, which nevertheless modifies its dispersion and resulting properties. The PC/MWCNT masterbatch was too viscous to be mixed at the original loading of 15 wt%. Pieces of PC/CB sheets were also mixed without changing their composition. The apparatus employed was a DSM twin-screw micro-compounder from the Laboratory for Processing of Advanced Composites (LPAC, previously Laboratory of Polymer and Composite Technology or LTC), as shown in Figure 27. It enables to mix  $5 \text{ cm}^3$  of material per batch, about half of which can be extruded and used, the rest being discarded when cleaning the machine. The screw rotation speed was set to 100 rpm and the mixing time to 5 min. The temperature was however varied as it was found to have a large effect on the properties of the mixed nanocomposites.

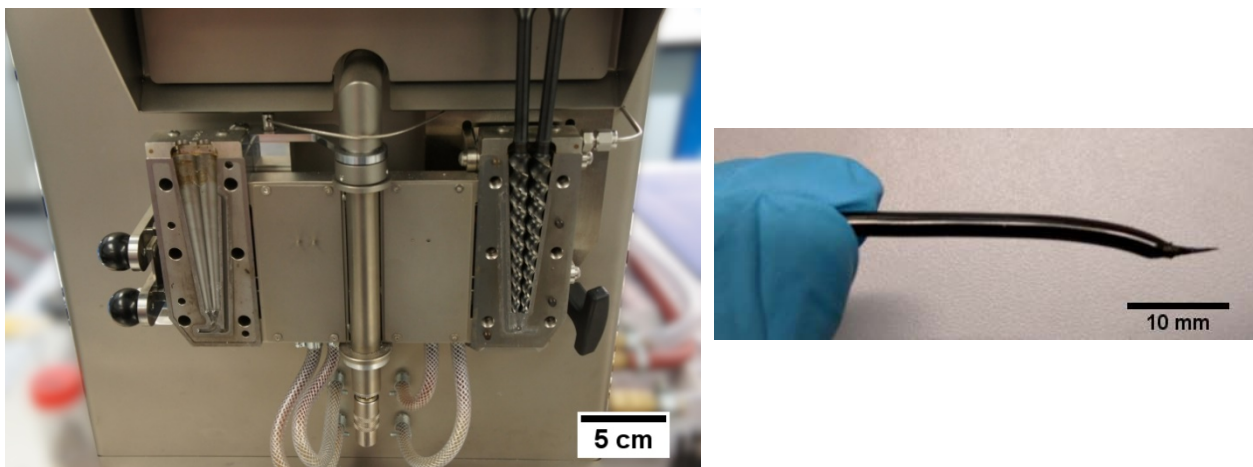


Figure 27. Left: twin-screw micro-compounder employed for the melt mixing of nanocomposites, open to leave visible the screws and the shape of the chamber. Right: piece of a sample extruded using it. From a single batch, a typical sample is 10-20 cm long with a diameter of 2-3 mm.

### **Electrical measurements**

The electrical conductivity of the extruded materials was measured at room temperature using a Keithley multimeter through alligator clips. In 2-wire configuration, a non-ohmic behavior was present, but a 4-wire configuration enabled to remove the effect of contacts and probe the actual properties of the nanocomposites. The resistance, diameter and length measurements were combined to calculate the conductivity with equation (2).

The recovery of conductivity by annealing on melt mixed PC/CB and PC/CNT composites was examined by heating them to 240°C for 30 minutes, then measuring again their conductivity. A higher temperature or duration did not increase the conductivity further.

### **Rheological measurements**

The rheological properties of melt-mixed nanocomposites were studied with the parallel-plate rheometer from LPAC (Model TA Instruments AR2000, Figure 28). It enables to measure the shear viscosity under constant shear rate or the complex viscosity, elastic and loss moduli in oscillatory mode. The shear rate or angular frequency and strain amplitude, and the temperature can be set constant or varied to study their influence. Although this tool does not allow for measurements of elongational viscosity, which would be relevant since thermal drawing mainly consists in elongating the materials, it is very useful to understand the influence of the concentration, mixing temperature, annealing and shear.

The measurements were realized with aluminum discs with a diameter of either 20 mm or 25 mm, and a sample thickness between 0.5 and 4 mm.

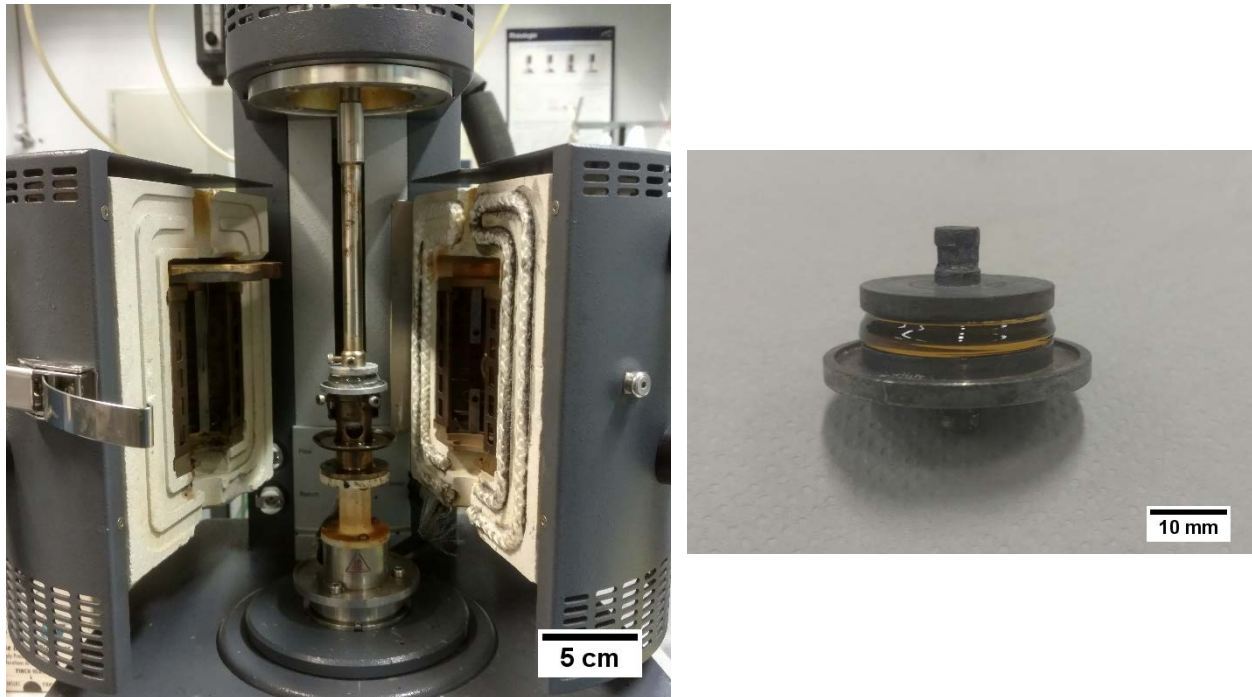


Figure 28. Left: parallel-plate shear rheometer employed for the rheological measurements. Right: 25 mm discs and polymer after a measurement (in this case polysulfone, which is yellow).

### Electron microscopy

The state of dispersion of the fillers in their polymer matrix was studied by Transmission Electron Microscopy (TEM) to understand better the effect of the processing on the structure of the nanocomposites and the resulting properties. For this, the samples were cut to thin slices of 100 to 150 nm by ultramicrotomy, at cryogenic temperatures (using liquid nitrogen) for HDPE nanocomposites since the polymer is too soft at room temperature. The sample preparation and observations were performed in the facilities of the Interdisciplinary Center for Electron Microscopy (CIME)

### 2.3.3 Properties and interpretation

#### Electrical properties

To investigate the effect of shear-induced damaging of the conductive nanoparticle network, we measured the conductivity of the nanocomposites melt-mixed at different temperatures and after annealing. The properties shown in this chapter correspond to HDPE nanocomposites made by mixing the HDPE/MWCNT masterbatch with the same grade of HDPE also provided by Nanocyl, and PC nanocomposites made by mixing the PC/MWCNT masterbatch with pure PC of a different grade, provided by Goodfellow. The reason for this is simply that we did not have the PC grade employed in the masterbatch at the time of the study. The influence of the polymer grade is considered in Chapter 3 where the evolution of conductivity throughout the fiber making process (hot pressing, consolidation and thermal drawing) is examined.

We first show in Figure 29 the conductivity against concentration obtained for PC/CNT and HDPE/CNT mixed at two different temperatures for each type, including the highest temperatures employed, which lead to the highest conductivities. The classical percolation law (equation (4)) was used to fit the results, leading to the following values and standard deviations:

- PC/MWCNT (mixed at 320°C):  $p_c = 0.5 \pm 0.25$  wt%,  $c = 1.45 \pm 0.067$
- HDPE/MWCNT (mixed at 240°C):  $p_c = 2 \pm 1.28$  wt%,  $c = 2.68 \pm 0.364$

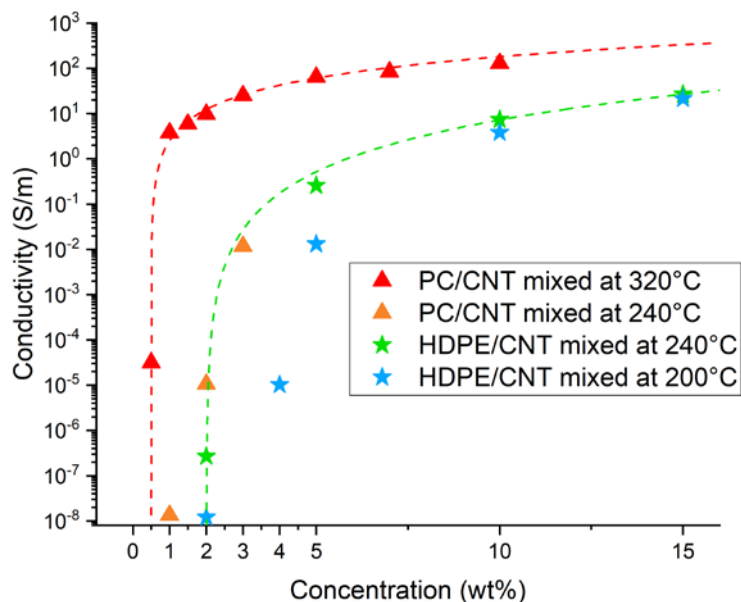


Figure 29. Conductivity of PC/MWCNT (mixing temperature of 320°C or 240°C) and HDPE/MWCNT (240°C or 200°C) composites versus concentration. The fitted percolation law is shown with a dashed line for the highest mixing temperatures.

The conductivity obtained for the melt-mixed PC nanocomposites is on par with the results shown in the literature. Moreover, it can be noticed that at 2 wt% (respectively 3 wt%), the conductivity of the polycarbonate composite we prepared is more than 100 times (resp. 10) higher than the value specified by the masterbatch manufacturer.

The large difference in conductivity between the PC/MWCNT and HDPE/MWCNT at given concentrations can be qualitatively explained by observing the nanotube dispersion thanks to Transmission Electron Microscopy (Figure 30): whereas the nanotubes are well dispersed in the PC matrix, they are found in relatively large agglomerates in HDPE that can be detrimental to bulk conductivity by providing few conduction paths between them. These distinct behaviors were observed at all melt-mixing temperatures and are likely due to the interfacial energy between the nanotubes and the polymer matrix. It was indeed estimated by Pötschke et al. [90] to be two to three times higher for HDPE than PC, thus driving the nanotubes to agglomerate more in HDPE than in PC. This effect may also be the reason why the literature focuses on PC rather than HDPE nanotube composites, the latter being less suitable to provide high conductivity.

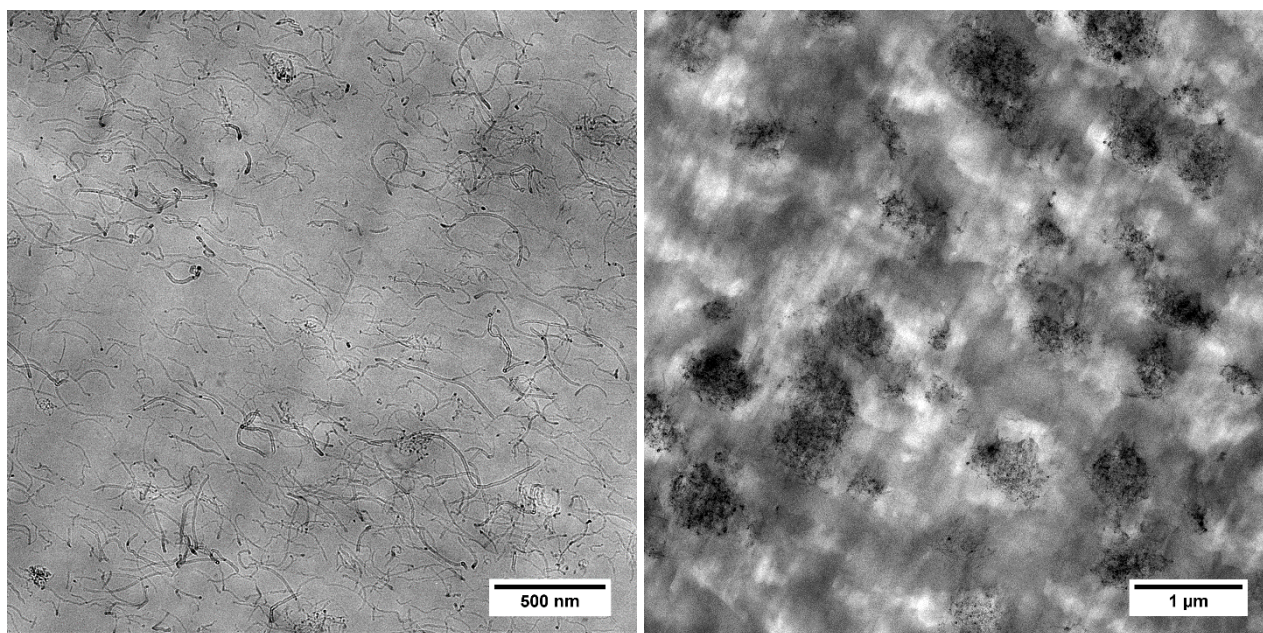


Figure 30. TEM pictures of MWCNT nanocomposites. Left: PC (3 wt%) after melt-mixing at 240°C showing the nanotubes are well dispersed. Right: HDPE (4 wt%) after melt-mixing at 240°C showing the nanotubes are grouped in large agglomerates.

For a given composition, the values of conductivity can span several orders of magnitude depending on the mixing temperature (Figure 31). A curve of conductivity against concentration as in Figure 29 is only valid for given processing parameters and can vary significantly with the temperature and deformation history of the nanocomposite. Since the viscosity of thermoplastics is higher with a lower temperature (equation (6)), the shear stresses are higher (for a given mixing screw rotation speed), and the conductivity decreases more due to the breaking up of conducting pathways between nanoparticles. Moreover, a lower temperature means less annealing during extrusion and cooling. These two effects combined explain why the resulting conductivity of a nanocomposite decreases with decreasing temperature. For all nanocomposites, it seems

therefore preferable to choose the highest mixing temperature. However, the conductivity can also be modified by the thermal drawing process. Thus, optimized pre-drawing and post-drawing conductivities do not necessarily coincide as will be shown in Chapter 3.

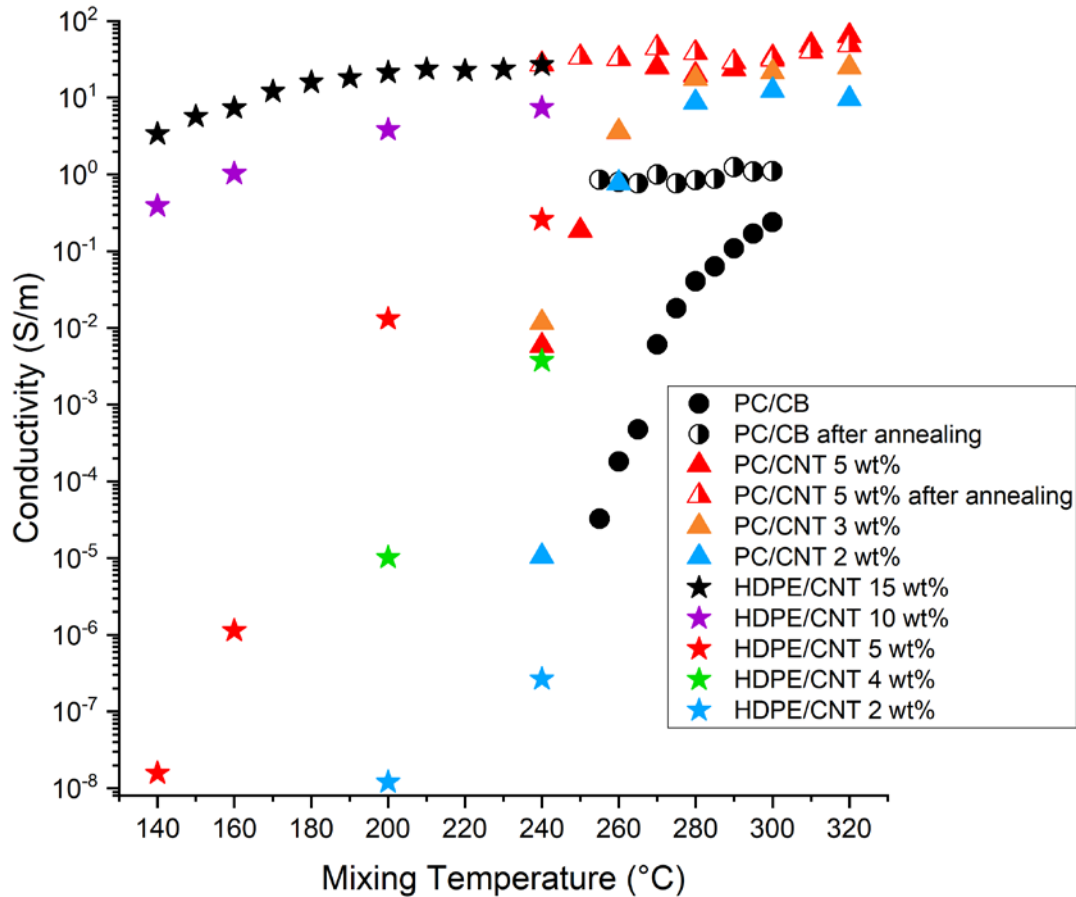


Figure 31. Conductivity versus mixing temperature for PC/CB, PC/CNT (2, 3 and 5 wt%) and HDPE/CNT (2, 4, 5, 10 and 15 wt%) composites after extrusion. For PC/CB and PC/CNT (5 wt%), the effect of annealing at 240°C for 30 minutes is also shown.

The effect of annealing (30 min at 240°C) is also shown in Figure 31 for PC/CNT (5 wt%) and PC/CB composites. It enabled a large recovery of conductivity for the samples mixed at the lowest temperatures, which were the least conductive, but had less effect on the ones mixed at the highest temperatures. The range of conductivities was greatly reduced: whereas it spanned 4 orders of magnitude depending on the temperature of melt-mixing, the highest conductivity after annealing is less than twice the lowest one.

These results again show that carbon black and carbon nanotubes composites have a similar behavior in terms of shear-induced loss of conductivity and recovery by annealing. They are also consistent with the earlier work conducted in FIMAP on PC/CB composites thermally drawn in fibers. They indeed had a lower conductivity after a lower drawing temperature, and annealing also enabled a partial recovery of conductivity, although limited due to possible fiber deformation and shrinkage which are not desired.

## Rheological properties

The rheological properties of PC/MWCNT and HDPE/MWCNT composites were studied by oscillatory shear rheology. Because it can influence the reliability or consistency of any other rheological measurement, the first thing to note is that the rheological properties of nanotube polymer composites changes over time as soon as they are heated to a temperature of interest. It is thus necessary to evaluate how fast they change and whether they stabilize after some time. We first show how the complex viscosity, elastic and loss moduli vary at a fixed temperature, with an angular frequency of 1 rad/s and a strain amplitude of 1% (Figure 32 and Figure 33). Unfortunately, the rheological properties change significantly already in the first minutes of heating and continue gradually for many hours. This means that the rheological properties change during any measurement, which makes it difficult for temperature sweeps to be consistent and prevents a complete picture of the properties before annealing.

In Figure 32 we compare the properties measured over time at 240°C of pure PC and PC composites with 3 wt% CNT mixed at 240, 280 or 320°C. Whereas pure polycarbonate has stable properties, the viscosity of the PC/CNT (3 wt%) is almost 100 times higher and increases with time. Moreover, both effects are mostly due to the elastic modulus which is dominating for the composites, whereas the loss modulus dominates for pure polycarbonate at the measurement temperature of 240°C. As for conductivity, a higher mixing temperature leads to a higher elastic modulus, but the effect on the rheological properties is much weaker.

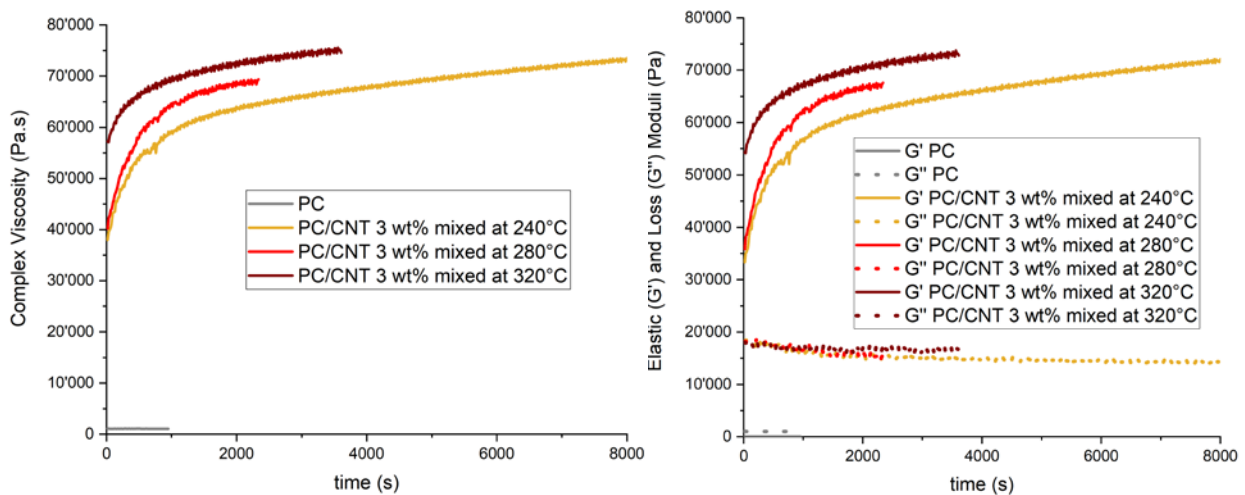


Figure 32. Complex viscosity (left), Elastic and loss moduli (right) versus time at a temperature of 240°C for polycarbonate and PC/CNT composites (3 wt%) mixed at three different temperatures. The measurements were done with an angular frequency of 1 rad/s and a strain amplitude of 1%. Pure polycarbonate is stable with  $\eta^* = 1065$  Pa.s,  $G' = 46$  Pa and  $G'' = 1064$  Pa.

In Figure 33 we compare the properties measured over time at 200°C of pure HDPE and HDPE composites with 4 wt% CNT mixed at 160°C and 15 wt% without processing from the masterbatch. A semi-log plot is used to enable to see the properties of both composites. At the temperature of 200°C, even the pure HDPE does

not have constant properties, but we could verify that it does at 190°C. As for the PC composites, the HDPE composites have a much higher viscosity than pure HDPE, mostly due to a higher elastic modulus and increasing over time.

According to the criteria presented in section 2.3.1, such nanocomposites have the properties of solid-like materials, but as will be shown in more details in Chapter 3, this does not prevent them from being drawn in multimaterial fibers.

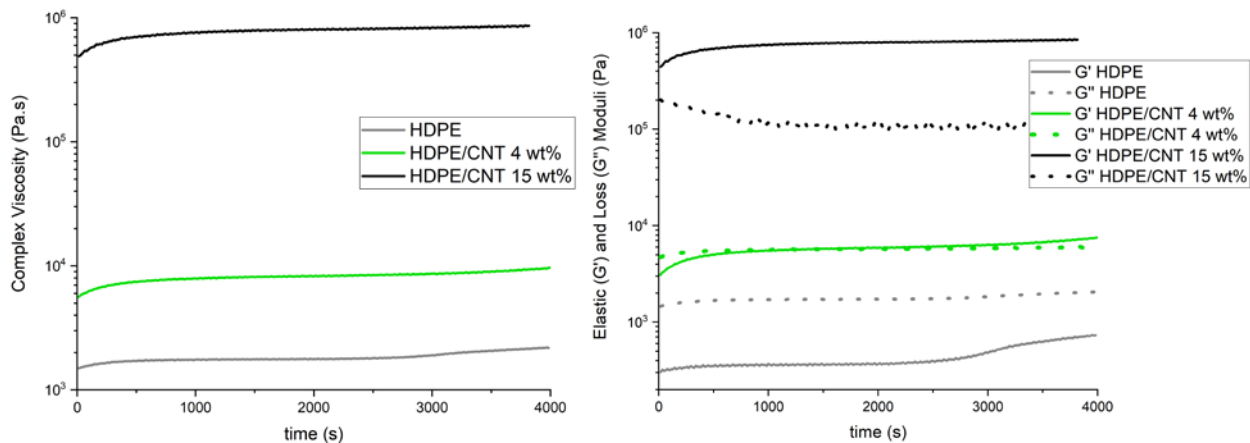


Figure 33. Complex viscosity (left), Elastic and loss moduli (right) versus time at a temperature of 200°C for HDPE and HDPE/CNT composites: 4 wt% mixed at 160°C and 15 wt% (the masterbatch). The measurements were done with an angular frequency of 1 rad/s and a strain amplitude of 1%. Between 1000 and 2000 s, pure HDPE is almost stable with  $\eta^* \approx 1760$  Pa.s,  $G' \approx 360$  Pa and  $G'' \approx 1720$  Pa.

Although the rheological properties of the nanocomposites studied are not stable, we tried to capture their temperature dependence after fabrication by heating them as fast as possible to a starting temperature, then performing a relatively fast temperature sweep with an increase of 10°C per minute (Figure 34 and Figure 35). But the rheological properties increase so fast due to annealing that they seemingly increase with temperature instead of decreasing as for pure thermoplastics.

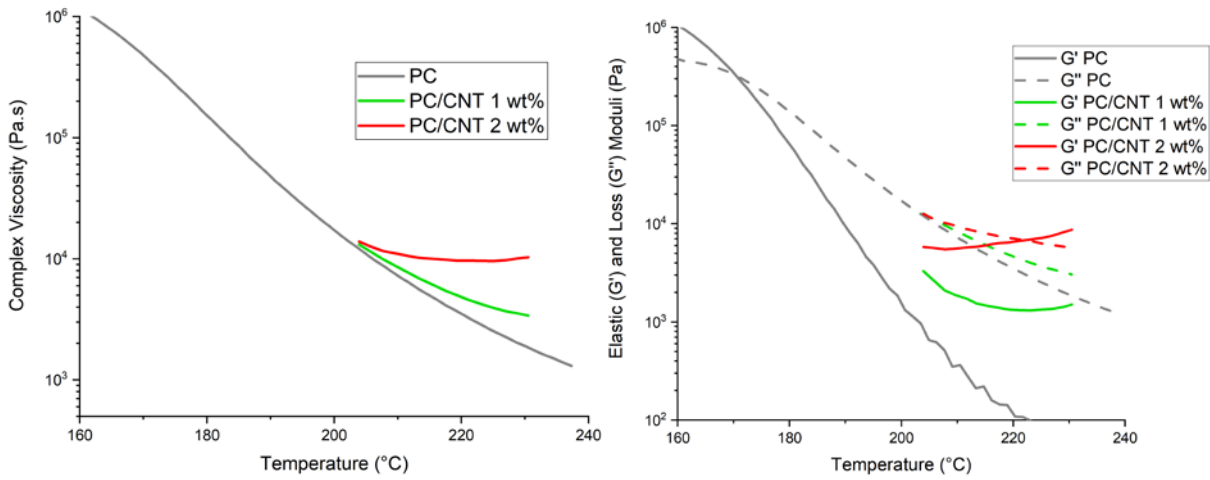


Figure 34. Complex viscosity (left), Elastic and loss moduli (right) versus temperature for polycarbonate and PC/CNT composites (1 and 2 wt%) mixed at  $160^{\circ}\text{C}$ . The measurements were done with an angular frequency of 1 rad/s, a strain amplitude of 1% and a temperature increasing at a rate of  $10^{\circ}\text{C}/\text{min}$ .

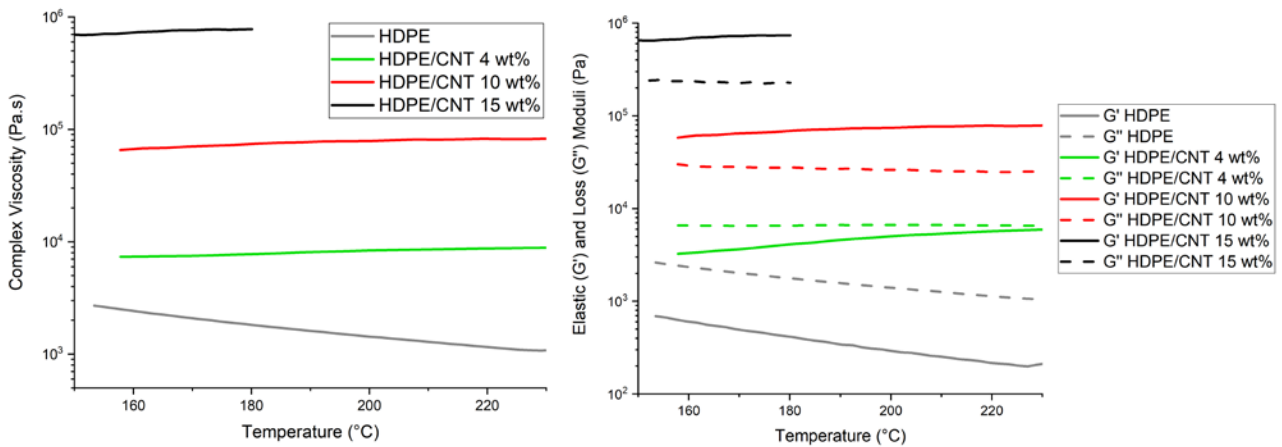


Figure 35. Complex viscosity (left), Elastic and loss moduli (right) versus temperature for HDPE and HDPE/CNT composites: 4 and 10 wt% mixed at  $160^{\circ}\text{C}$  and 15 wt% (the masterbatch). The measurements were done with an angular frequency of 1 rad/s, a strain amplitude of 1% and a temperature increasing at a rate of  $10^{\circ}\text{C}/\text{min}$ .

### 2.3.4 Discussion

We employed concentrated masterbatches and pure polymers in the melt-mixing technique to fabricate polycarbonate (PC) and high-density polyethylene (HDPE) nanotube composites at concentrations between 0.5 and 15 wt%. The mixing temperature was observed to have a relatively small impact on the rheological properties but a large one on the electrical conductivity, which can however be recovered by annealing. For a given composition, mixing conditions or an annealing step that lead to a higher conductivity also mean a higher elastic modulus. Furthermore, a higher conductivity prior to thermal drawing does not necessarily lead to a higher post-drawing conductivity since the materials are both deformed and heated during the process, as will be shown in the next chapter. Both the conductivity and viscosity increase drastically with concentration, which make the nanocomposites interesting and challenging to use in thermal drawing.

The main message from the rheological study is that we should try to heat the nanocomposites as little as possible prior to drawing to avoid increasing the elastic modulus and maximize the chance of successfully draw them in multimaterial fibers. However, rotational rheometry does not probe the properties in a context that mimics thermal drawing accurately. It applies only a pure shear whereas the materials are mostly elongated during drawing, therefore other types of rheometers may be more suitable. A Mnstedt tensile rheometer such as the one used by Stary et al. [89] (Figure 24) could be appropriate since it enables to apply a large elongational strain. However, nanocomposites are sensitive to their deformation and heat history which may be difficult to reproduce. Moreover, knowing this history during drawing is itself challenging, but the modeling work presented in Chapter 4 brings some answers to this problem.

In this thesis, we focused on the MWCNT composites fabricated by melt-mixing because it led to interesting results in thermally drawn fibers, as presented in the next chapter, and raised stimulating questions to solve. The solution cast nanocomposites did not lead to post-drawing conductivity as high as the melt-mixed ones even if SWCNT composites were made conductive at very low concentrations, down to 0.002 wt%. Since both the electrical conductivity and the figure of merit  $\sigma_{DC}/\sigma_{op}$  for transparent conductors increase drastically with concentration, employing the highest concentration possible is preferable in thermally drawn fibers, which makes the melt-mixed nanocomposites more suitable. However, chemical modifications and other types of fillers such as graphene and metallic nanowires or hybrid composites may also be worth considering. Preparing a concentrated masterbatch by solution casting, then using melt-mixing to tune the loading and the filler dispersion would be a valuable way to combine both techniques, since it would enable to employ nanoparticles from any source even if they are not already dispersed in a solution or masterbatch.

The studies of conductivity of nanocomposites under shear and elongation reported in the literature will also prove useful in Chapter 4, in particular the kinetic equation (26) for modeling the post-drawing conductivity according to the deformation that the material is subjected to during thermal drawing.

# Chapter 3 Thermal drawing of conductive nanocomposites

In this chapter, we describe the experimental fabrication of multi-material preforms and their thermal drawing into fibers. We focus on the designs that allow for studying the ability to draw the conductive nanocomposites presented in the previous chapter and their post-drawing properties. The properties of such nanocomposites are modified by each step of the fabrication: preform making, fiber drawing and possible fiber post-treatments. Optimal optoelectronic properties and compatibility with the thermal drawing process can however be contradictory, therefore a work of optimization was necessary to improve the resulting properties.

## 3.1 Description of the experimental process

In this section, we present the technical aspects of the thermal drawing and preform making process. We describe the preform designs employed to study the ability to draw conductive composites in fibers and evaluate their conductivity and performance as transparent conductive electrodes.

### 3.1.1 Thermal drawing and fiber designs

#### **The thermal drawing technique**

The principle of thermal drawing is to heat a macroscopic preform generally made of an amorphous glass or thermoplastic polymer to decrease its viscosity and pull it to create a fiber that is a thinner and longer version of the preform. Different materials can be drawn together with a precise architecture that can provide functionalities to the fiber. The materials are drawn in a viscous state to avoid mixing them and maintain the cross-sectional architecture required depending on the targeted function. This is true at least for the peripheral materials, but low viscosity materials can also be present if they are encapsulated by viscous ones. To be compatible in the same multi-material fiber, all the materials must be viscous or liquid in the drawing temperature range. Exceptions to this rule are possible, for example a solid wire placed in a hollow preform and pulled by the viscous materials, or solid elements placed at discrete positions along the preform [91]. Several compatibility issues can arise in multi-material fiber. Thermal expansion coefficients that are too different and weak adhesion can cause buckling and debonding. Moreover, improper adequacy between

material viscosity and strength can cause fiber breakage or discontinuity of a material in a multi-material fiber, as will be illustrated with carbon nanotube composites in the next section.

In practice, thermal drawing is realized with a so-called draw tower such as the one used for this work shown in Figure 36, controlled by a computer. The preform is attached below the preform holder, a temperature-resistant polyetherimide bar mounted in the feeding system, then lowered in the tubular furnace. To prevent heat from escaping the furnace and keep a stable air temperature, the upper aperture is fitted to the bar diameter and an iris enables to manually adjust the lower aperture.

The temperature in the furnace is not uniform. Instead, the vertical temperature profile is defined by the control of temperature at three positions. The preform, which has an elongated shape, is placed so that its lower end is where the temperature is the highest. A weight is attached at the bottom and enables a necking down of the preform when the materials locally reach a viscosity that is low enough after some heating time. This step marks the start of the draw, and the fiber that comes out of the lower end of the tube furnace is then fed in the capstan that controls the drawing speed. The tension is measured by a three-wheel sensor, and the fiber diameter (or thickness and width in the case of a rectangular section) by a laser gauge.

In steady-state drawing, the diameter of the fiber is defined by the set drawing and feeding vertical speeds. Because of volume conservation, we have the following relation:

$$v_{draw} \cdot S_{fiber} = v_{feed} \cdot S_{preform} \quad (27)$$

$v_{draw}$  is the drawing speed of the fiber in the capstan, and  $v_{feed}$  is the speed of the preform fixed by the feeding system. The cross-sectional areas of the preform and the fiber are  $S_{preform}$  and  $S_{fiber}$ . The draw ratio or draw-down ratio  $Dr$  is the factor by which the preform radius  $R_{preform}$  is decreased, with  $R_{fiber}$  the fiber radius:

$$Dr = \frac{R_{preform}}{R_{fiber}} = \sqrt{\frac{S_{preform}}{S_{fiber}}} = \sqrt{\frac{v_{draw}}{v_{feed}}} \quad (28)$$

In the case of rectangular rather than circular fibers, the same equation applies for the width and thickness instead of the radius.

The tube of the furnace is heated from its external surface and three thermocouples are placed outside. Therefore, the maximum temperature inside the tube is lower than the three temperatures set in the control software, which are chosen empirically depending on the materials to draw. We observed that in a steady draw, closing or opening the iris has a fast effect on the tension measured, which is due to the temperature experienced by the materials drawn. However, the measurement of the furnace wall temperatures does not capture this effect. Moreover, we noticed that after being heated from room temperature, the wall temperatures need to be stable for a relatively long time before a draw could start. This means that there is a large time delay between a change of temperature measured by the furnace thermocouples and the temperature in the tube. To estimate this delay, we inserted a thermocouple in the tube in place of the preform at the vertical position where the temperature is the highest and the necking-down occurs and compared the measurements with the values given by the furnace thermocouples. As shown in Figure 37, the tube wall temperatures reach the values set in a few minutes, except the middle temperature when set to temperatures above 300°C, for which it takes several tens of minutes. However, the temperature of the

air inside the tube rises much more slowly and remains far below the middle wall temperature. Opening and closing the iris leads to a decrease or increase of the air temperature visible within seconds and that can reach tens of degrees in a few minutes, but no effect on wall temperatures is observed at this short timescale.

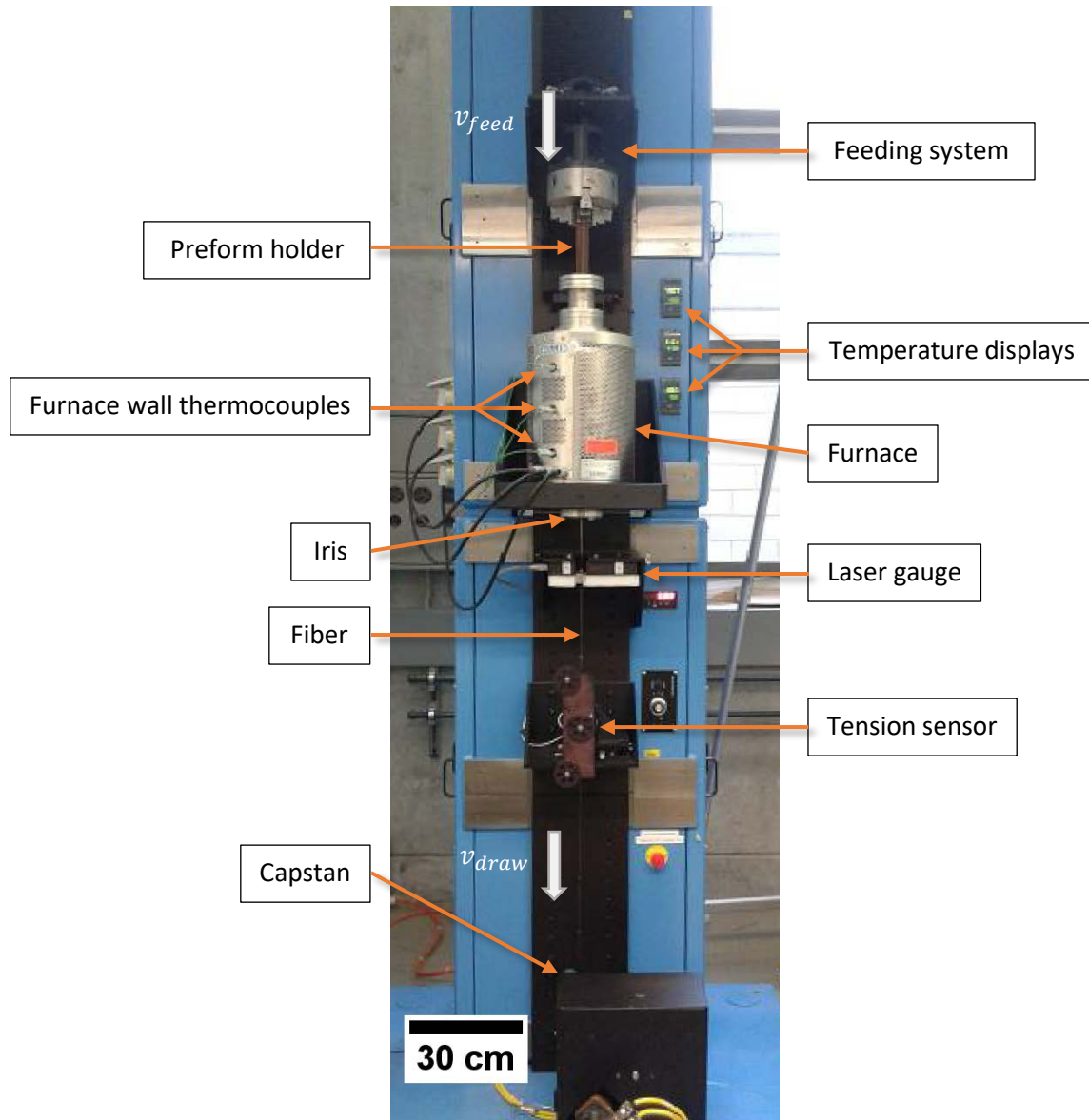


Figure 36. Picture of the drawing tower and legend of the different components.

Even with a fixed stabilization time, we also noticed that it was difficult to rely on the wall temperature measurements to draw the same materials in the same conditions from one fiber to another. It seems that fluctuations can indeed arise, possibly due to the room temperature or stability of the furnace thermocouples. Instead, to ensure a consistent drawing temperature, we rely on the tension measurements and adjust the wall temperature to target a consistent tension for given feeding and drawing speeds. The tension is indeed related to the temperature of the material through its viscosity.

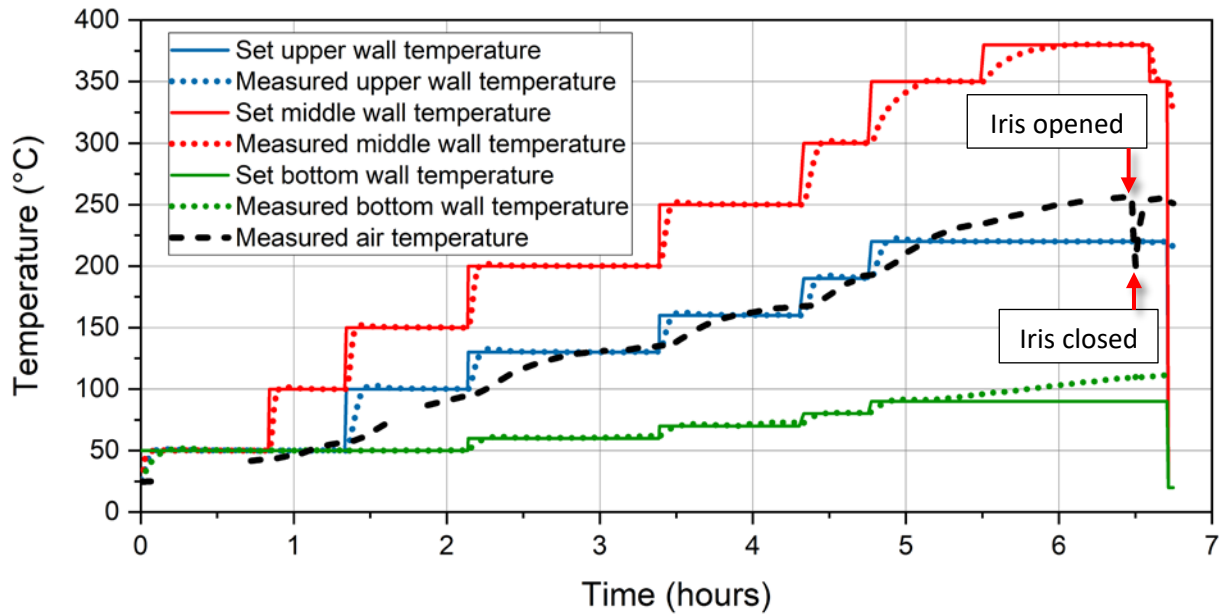


Figure 37. Comparison over time of the three wall furnace temperatures (set and measured) with the air temperature measured with a thermocouple inserted in the tube in place of the preform, at the vertical position where the temperature is the highest and the neckdown occurs. The set temperatures were increased in steps, and near the end of the study the iris was opened and then closed.

### Fiber designs for the study of nanocomposites

The targeted application for carbon nanotube composites is as transparent electrode in multi-material fibers, and more generally as conductive element with improved conductivity compared to carbon black composites, although the knowledge resulting from the study could prove useful for other functions. This means that the nanocomposites studied are not required to be able of being drawn as single material fibers, similarly to metals which cannot form a fiber alone but are compatible when encapsulated, except that nanocomposites can be too elastic for being drawn rather than too liquid.

In order to explore various parameters of fabrication and processing of the nanocomposites, we need to efficiently evaluate their ability to be drawn when encapsulated in a cladding material and measure their conductivity when successfully drawn. Therefore, we employed relatively simple preform designs solely aimed at such studies. The first design, shown in Figure 38, is composed of a sheet of nanocomposite surrounded by a cladding material and was used for assessing their compatibility.

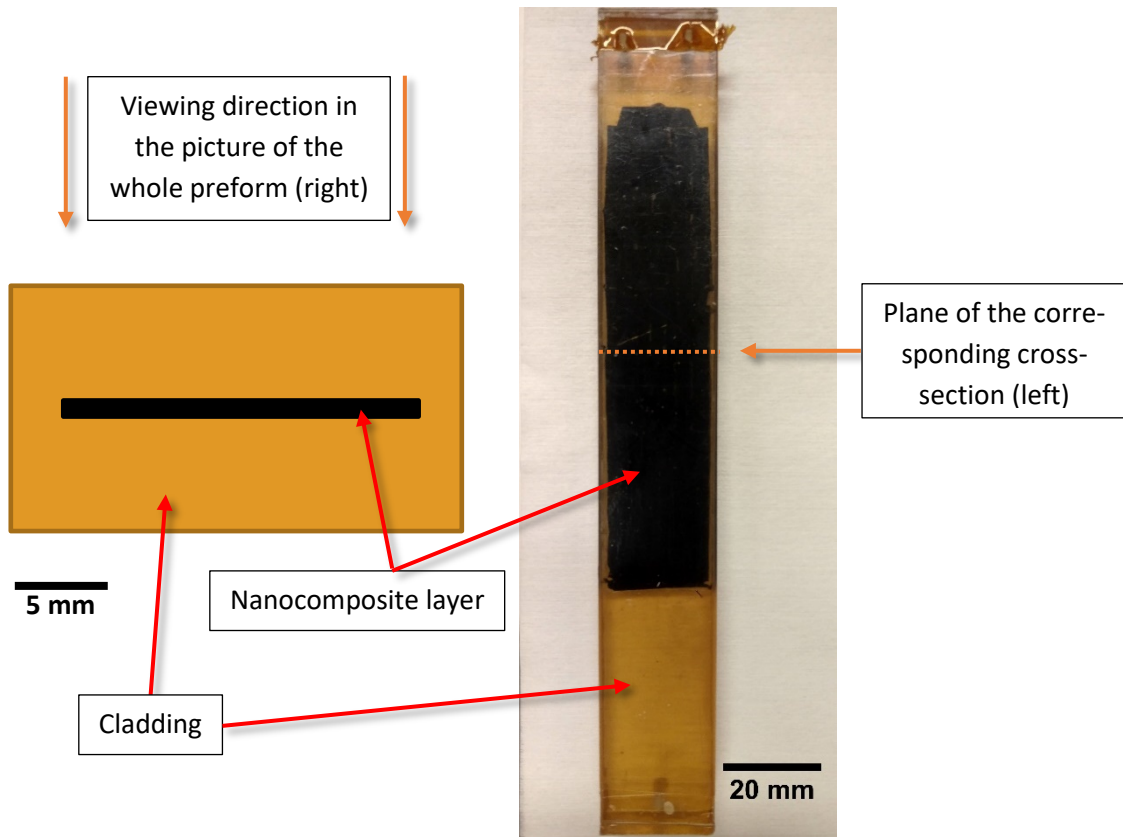
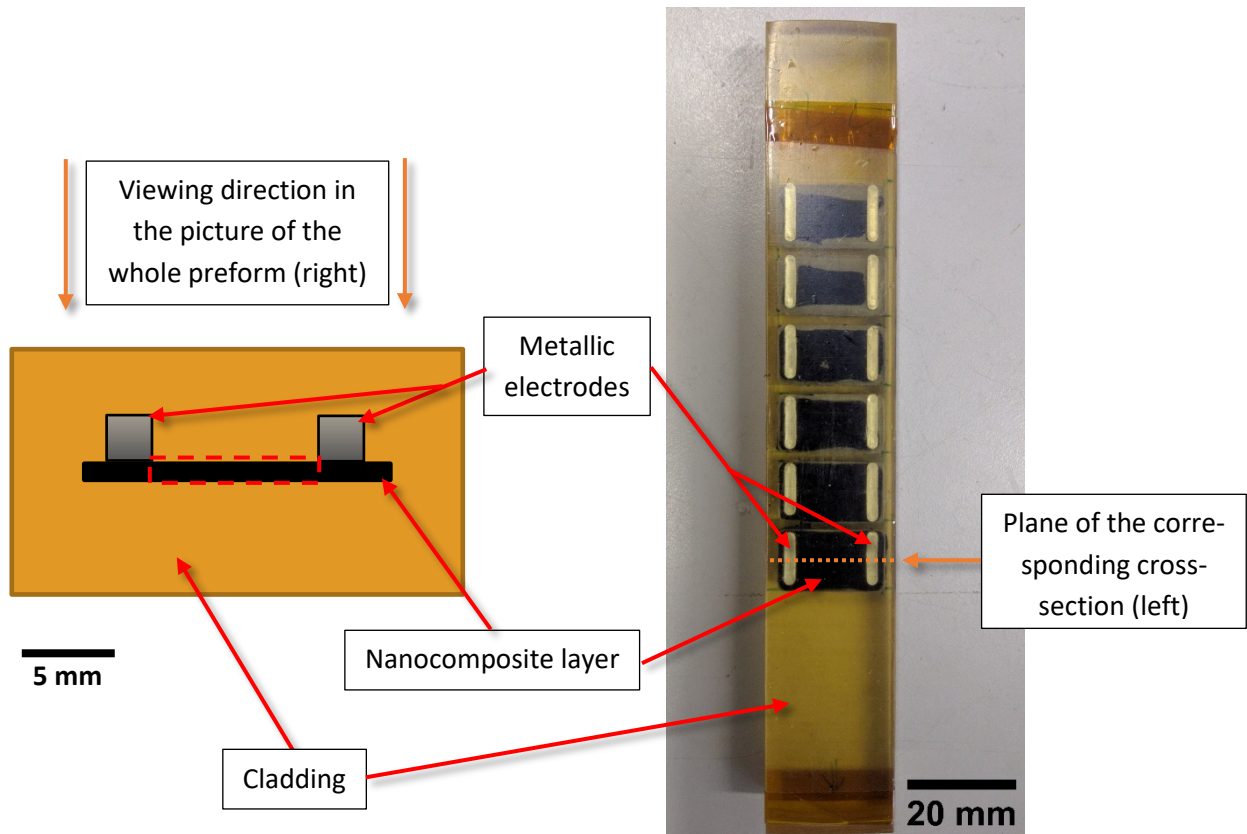


Figure 38. Preform design for assessing the ability to draw a nanocomposite encapsulated in a cladding. This design also enables to measure the conductivity of the nanocomposite in the drawing direction when it is continuous in the fiber.

The second design, shown in Figure 39, has two additional metallic electrodes that enable to measure the conductivity of the nanocomposite in the direction perpendicular to the drawing direction. Connecting the metallic electrodes to a multimeter at any point of a piece of fiber indeed allows for a measurement of the resistance of the nanocomposite material in the entire length of fiber since the resistance of the metallic electrodes is small in comparison. The region of the nanocomposite considered is indicated in the cross section with a dash line and spans the length of the piece of fiber considered. From the resistance measurement, the conductivity of the material is then calculated using the geometrical dimensions of the region considered with equation (2).

Due to the elongation in thermal drawing, the nanocomposites can be expected to have an anisotropic conductivity. Moreover, transparency requires a thin layer that is problematic to connect without the use of metallic electrodes that are thicker and easier to connect. For applications, metallic electrodes would also be used to provide a low resistance along the fiber. For the conductive composites, the conductivity perpendicular to the drawing direction is therefore the most important for electrically contacting other functional materials.

In both designs, only the cladding material is present at the bottom of the preform, which is drawn first. This allows for adjusting the drawing parameters according to the known cladding material and ensure consistency between draws.



*Figure 39.* Preform design for measuring the conductivity of nanocomposites in the direction perpendicular to the drawing direction. In the preform shown in the right, six different materials are examined, which enables to study them in the same draw. However, the short length for each material means little flexibility to explore different draw ratios, and alternating materials causes fluctuations detrimental to the accuracy of the results. Therefore, for most preforms with the cross-sectional design shown in the left we used at most three longer regions.

### Materials and drawing parameters

The nanocomposites studied were the ones presented in the previous chapter, either polycarbonate filled with carbon black (PC/CB) or different polymers filled with carbon nanotube: polycarbonate, high- and low-density polyethylene (HDPE, LDPE) and polystyrene (PS). How they were processed and integrated in the preforms is described further.

The cladding materials employed were thermoplastic polymers: polycarbonate (PC), polysulfone (PSu) or polyetherimide (PEI). They were in the form of large plates cut to the dimensions of the consolidation mold used (170 mm x 24 mm), and for most preforms two layers were used to encapsulate the other materials between them.

The material used for the cladding defines a range of possible drawing temperature profiles. A too low temperature can cause fiber breakage due to very high viscosity and stress, whereas a too high temperature weakens the material which can then break even if the viscosity and stress are low. Moreover, to preserve the cross-sectional shape at the fiber level, a high cladding viscosity is necessary, therefore a temperature in the lower end of the possible range is preferable. Figure 40 shows the cross-section of two fibers drawn at

high and low temperature respectively to illustrate this issue. This is particularly relevant for fibers in which a thin layer is present. A high viscosity was targeted even when studying thick composites since the same materials would then have to be thinner to work as transparent conductive electrodes. For this reason, we fixed the drawing temperature profile for each cladding material to conditions that maintain well the cross-sectional architecture. To study the effect of temperature on a given nanocomposite we changed the cladding material rather than varied the drawing temperature with a given cladding polymer.

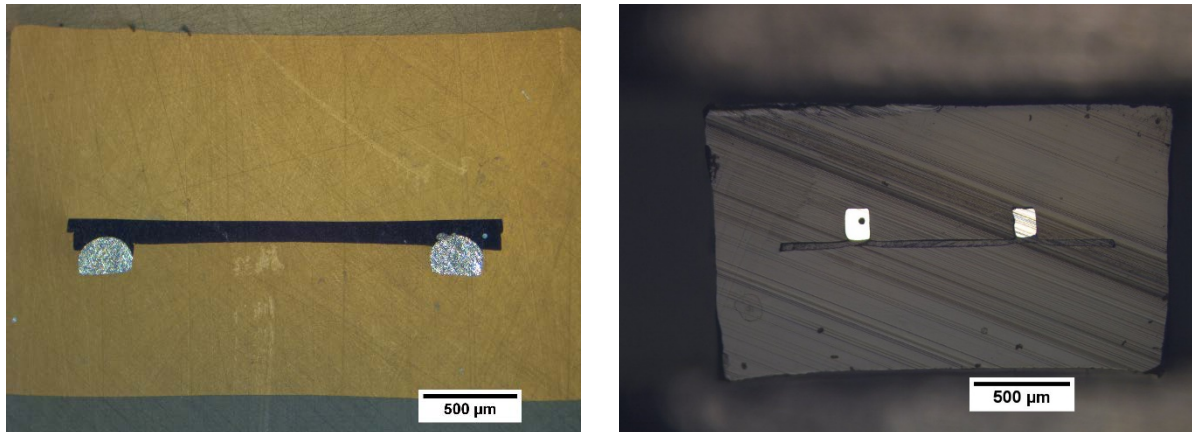


Figure 40. Optical micrographs of the cross-section of fibers drawn from preforms designed as in Figure 39 (left). Left: the drawing temperature was too high and caused a deformation of the cross-sectional architecture, visible with the rounded shape of the metallic electrodes. Right: the drawing temperature was appropriate and enabled to keep their rectangular shape. The lines visible in both pictures are due to the polishing or cutting technique.

The typical top/middle/bottom furnace temperatures employed, which define the temperature profile, were 150/260/100 for PC, 200/320/120 for PSu and 250/340/140 for PEI. Since fluctuations arise as mentioned above, we adjusted the middle temperature to keep a consistent tension between different fibers, corresponding to a sufficient viscosity of the cladding for preserving the cross-sectional shape. In such cases we targeted a tension of 300 grams with a feeding speed of 2 mm/min and a drawing speed of 0.2 m/min.

The cladding material also defines the alloys that can be employed for the metallic electrodes, which were provided in the form of ribbons with a section of 2 mm x 1 mm. The alloy Sn91-Zn9 has a melting temperature of almost 200°C and is compatible with PSu and PEI but not with a PC cladding for which Bi58-Sn42 was used instead since it has a melting temperature of 138°C.

Apart from the temperature profile, the parameters that can be varied are the feeding and drawing speeds, which define the draw ratio. A value of 2 mm/min was used for the feeding speed except when studying specifically its influence, and the drawing speed was usually varied to explore different draw ratios.

### Visualization of the deformation in the thermal drawing process

The fabrication of such preforms and the results of their drawing will be presented in detail further. Prior to this, we would like to mention an effect that we observed and led us to examine the thermal drawing process itself more deeply. We noticed that a flat interface initially perpendicular to the drawing direction in the preform bends and becomes an inverted “V” shape in the fiber, as shown in Figure 41.

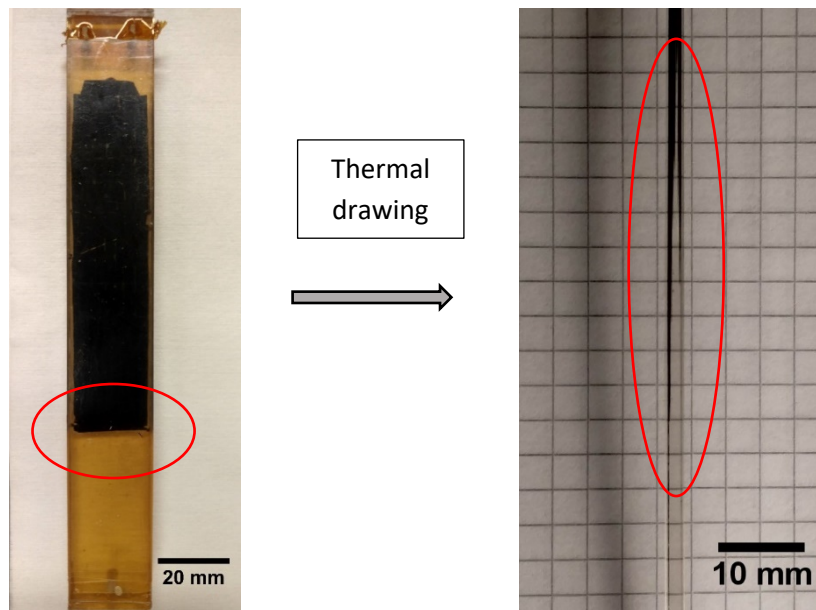


Figure 41. Preform and resulting fiber made with the design shown in Figure 38. The flat interface between the parts of fiber with only the cladding material and with the nanocomposite is strongly deformed and has an inverted “V” shape.

To inspect this effect in more detail, we designed a different type of preform only aimed at studying the process of thermal drawing itself. We placed 1 mm-wide sheets of carbon black-loaded polycarbonate perpendicular to the drawing direction in the preform (Figure 42) and interrupted its draw to visualize the deformation in the preform-to-fiber region. As shown with both a polycarbonate and a polysulfone cladding, the straight sheets clearly deform during the drawing, their edges looking like an inverted “V” in the fiber region. The deformation is not perfectly symmetric, which is likely due to a non-perfect air temperature distribution inside the tube of the furnace.

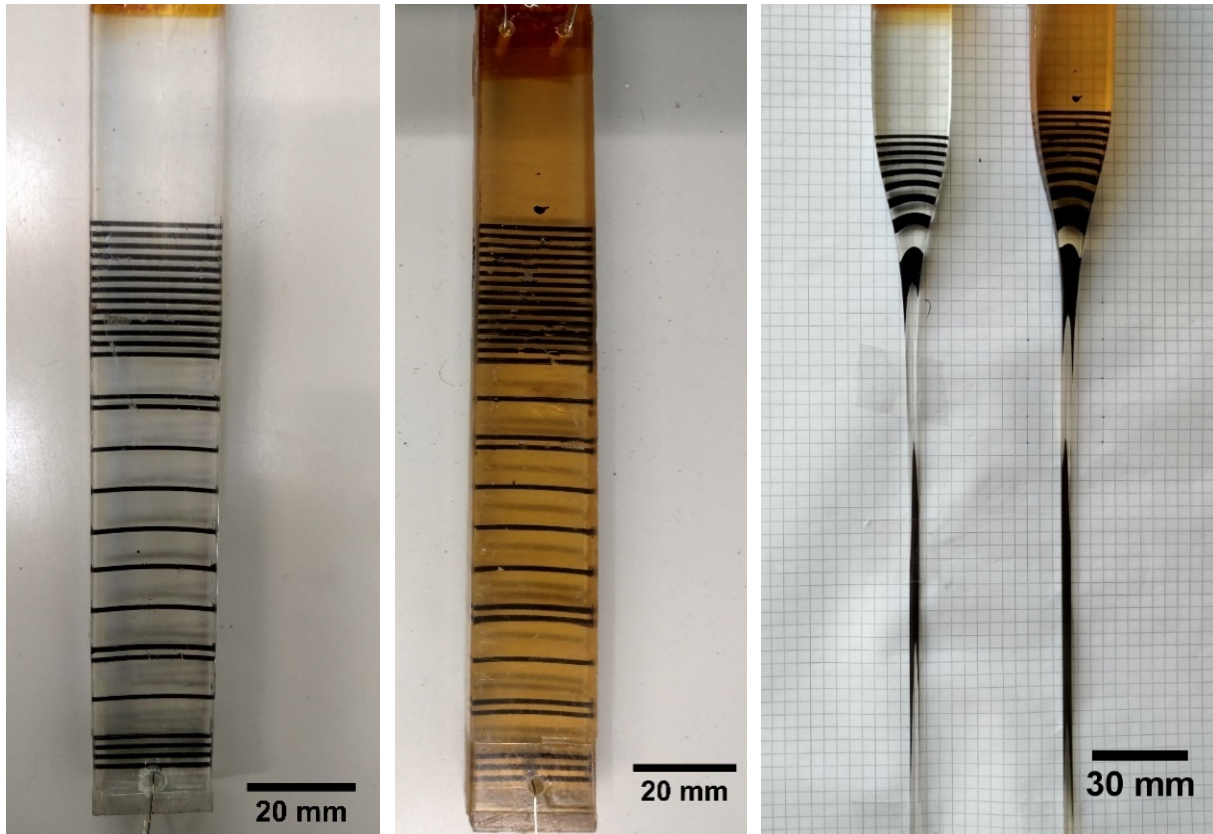


Figure 42. Left and middle: PC and PSu preforms designed to visualize the deformation during drawing. Right: result of their interrupted draw to observe the neckdown (or “preform-to-fiber”) region. Polycarbonate (transparent) and polysulfone (yellow) claddings lead to similar deformations. This allows for illustrating how a flat interface gradually bends during drawing. Due to the consolidation step, there is already some bending visible in the lower part of the preforms, but the region shown in the neckdown picture corresponds to the non-deformed part of the preforms with dense and straight lines.

A fluid dynamic analysis developed to account for this deformation in the thermal drawing process is the subject of Chapter 4. Moreover, since the center and the sides of fibers seem to deform differently, we expanded the preform design of Figure 39 with more than two metallic electrodes to enable to evaluate the conductivity of the nanocomposites at different positions in the cross-section, as will be detailed in the next section.

### 3.1.2 Experimental process for the fabrication of the preforms

The experimental fabrication of the preforms designed to study the drawing of conductive nanocomposites is described here. It includes several steps of processing of the starting materials and a final consolidation. The result of the rheological studies of the carbon nanotube composites shown in the previous chapter suggests that they should be heated as little as possible during these steps to avoid increasing the elastic modulus prior to drawing.

## Hot pressing

In the preform designs presented above, the nanocomposites are in the form of sheets. To shape the extruded materials or masterbatch pellets into the targeted form, we hot pressed them in a Lauffer press. The materials were placed between metallic or glass plates, heated and subjected to a pressing force. The time and temperature of pressing used were up to 30 minutes and 260°C at first, but were later selected to be as low as possible to limit the annealing of the nanocomposites. The amount of material was chosen so that the surface area was 5 to 20 cm<sup>2</sup> (Figure 43). The thickness of the sheets was 100 to 300 μm for studying the ability of the nanocomposite to be drawn and their electrical conductivity. However, to reach a post-drawing thickness sufficiently small to make the material transparent, we had to make the sheets thinner. Using pressing forces of up to 7.5 kN, we could achieve thicknesses down to 30 μm.

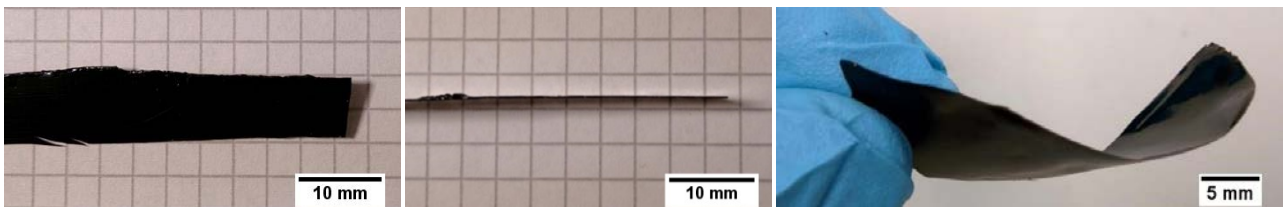


Figure 43. Carbon nanotube composite sheets made by hot pressing the extruded materials. Left and middle: PC/CNT. Right: HDPE/CNT.

## Milling and preform consolidation

To fabricate preforms according to the designs presented above, two cladding plates cut to the dimensions of the consolidation mold (170 mm x 24 mm) were milled with grooves dimensioned to fit the nanocomposite sheets and metallic electrodes. After positioning the materials together, they were thermally welded by hot pressing the preform in a metallic mold. This consolidation step was realized with the Lauffer press. A pressure of 1 N/cm<sup>2</sup> was applied for 1h under a temperature of 220°C for preforms with a polysulfone cladding. This means a relatively long annealing time that could be detrimental to the ability to draw the nanocomposites since it increases their elastic modulus. However, as will be shown in the next section, this did not prevent to draw carbon nanotube composites even at high concentrations and reducing the annealing time and temperature of the sheet pressing step was sufficient. Thermal welding between the cladding and the nanocomposite may be useful since the sheet can then be pulled by the surrounding material during drawing. Moreover, we tried a method in which the nanocomposite sheet is inserted after consolidation in a specially designed preform. The drawing was not successful even if the annealing due to consolidation was avoided, possibly because the encapsulation was not as good as when the materials are thermally welded during the consolidation steps.

We had to develop a strategy to avoid experimental issues that arise when drawing a thin sheet of nanocomposite in contact with metallic electrodes, which we illustrate by showing some examples of fibers drawn from preforms with the cross-sectional architecture of Figure 39. With a relatively thick layer, the deformation that can occur during thermal drawing around the metallic electrodes does not prevent a good contact between the conductive composite and the metal as can be seen in Figure 40. However, the contact can be easily broken or weakened with a thinner composite due to small mismatch and cross-sectional shape

distortion, as illustrated in Figure 44 (left) and Figure 45 (left). We tried to combine an intermediate thick layer with a thin layer of the same nanocomposite, but the contact breakage then happened between the two layers (Figure 44 (right)).

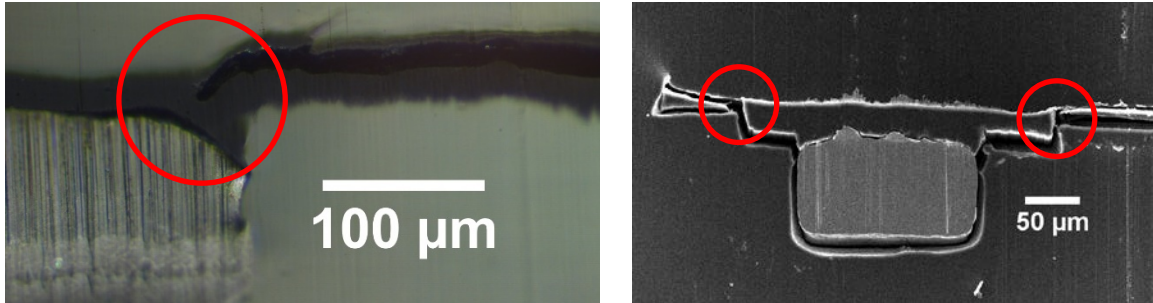


Figure 44. Cross-sectional images of fibers drawn with the design of Figure 39 (left), zoomed-in to examine the interface between a metallic electrode and a thin nanocomposite layer. Left (optical microscopy): the contact is broken. Right (SEM): using an intermediate thick layer of the same material as the thin layer did not prevent contact breaking, which happened between the thick and thin layers.

To prevent this problem, the solution was to first hot press the cladding plate with the metallic electrodes and a layer of Kapton tape in place of the nanocomposite sheet, which created a smooth surface at the transition between the metal and the cladding where the contact issue would arise. Then the nanocomposite sheet and top cladding plate were added and the whole preform was consolidated. The resulting fiber drawn had a good contact between the metallic electrodes and the nanocomposite layer, as shown in Figure 45 (right).

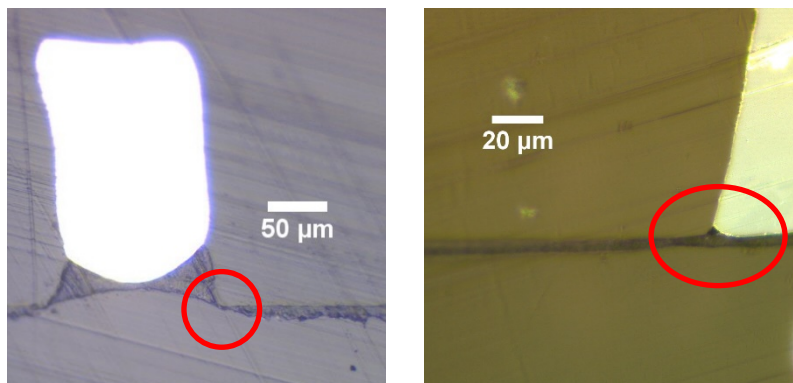


Figure 45. Cross-sectional images of fibers drawn with the design of Figure 39 (left), taken by optical microscopy and zoomed-in to examine the interface between a metallic electrode and a thin nanocomposite layer. Left: The contact is not broken, but the material has a very thin region that can cause the conductivity measured to be higher than the actual value. Right: The nanocomposite and the metallic electrode are well in contact.

## 3.2 Thermal drawing of nanocomposites and resulting properties

### 3.2.1 Solution cast SWCNT composites

We studied the ability of the solution cast films based on SWCNT to be thermally drawn. First, we employed a SWCNT film cast on a PSu sheet from a water solution and placed it in a PSu preform as in the design of Figure 38. The solution, provided by OCSiAl (see Chapter 2), also contained a dissolved stabilizing polymer and was sonicated before casting. As illustrated in Figure 46, the SWCNT film did not remain continuous when the preform was drawn but formed a myriad of cracks. Then we employed films of PMMA/SWCNT made by casting NMP solutions as explained in Chapter 2, but they also cracked or did not flow continuously during drawing even as concentrations as low as 0.3 wt%.

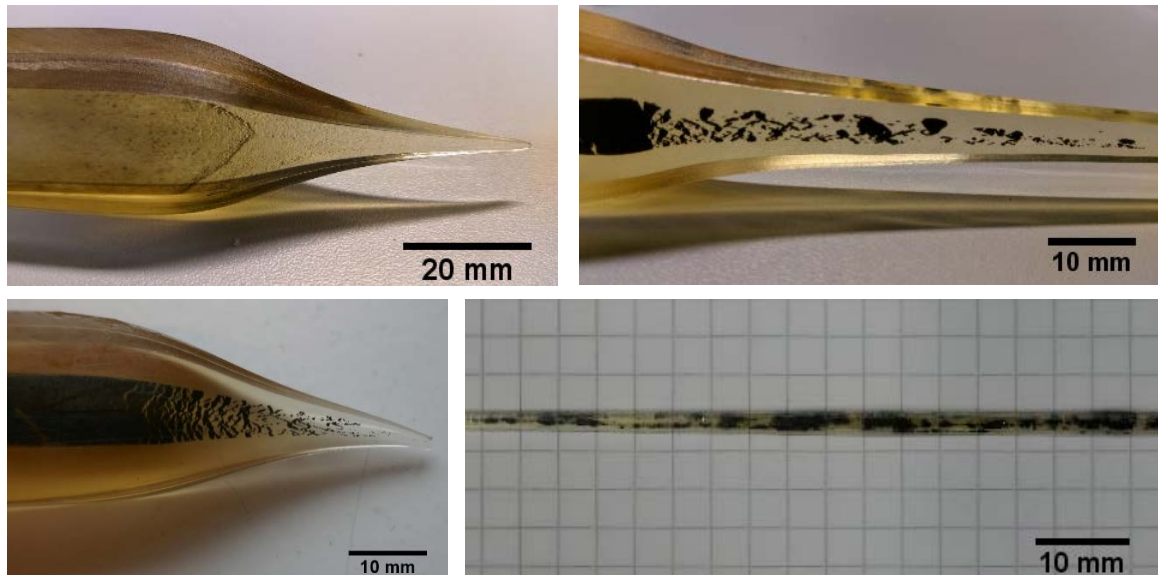


Figure 46. Pictures showing that the drawing of SWCNT polymer composites in polysulfone preforms was not successful with a concentration of 33 wt% (top left), 11 wt% (top right), 1 wt% (bottom left) or 0.3 wt% (bottom right).



Figure 47. Top view picture of a fiber containing a PMMA/SWCNT layer concentrated at 0.1 wt% in a polysulfone cladding. The nanocomposite is transparent but not conductive.

We could draw a continuous and conductive layer of PMMA/SWCNT nanocomposite only at a concentration as low as 0.1 wt%, in a polysulfone or polycarbonate cladding. Figure 47 shows that it was transparent, but its conductivity was too low to be measurable. Since these PMMA/SWCNT nanocomposites were found compatible with thermal drawing only at low concentration and their post drawing properties were poor, they were not studied further.

### 3.2.2 Melt-mixed MWCNT composites

#### Failed and successful drawing of MWCNT composites

The thermal drawing of MWCNT polymer composites prepared by melt mixing was also examined using the designs presented in the previous section. At first, we could not draw continuous PC/MWCNT composites at concentrations of 5 wt% or more in a polysulfone cladding, as shown in Figure 48. However, the results of the rheological studies indicated that heating the nanocomposites less during the preform preparation steps prior to drawing would avoid increasing the elastic modulus. Then, by decreasing the temperature and time of the pressing step that shapes the extruded materials into sheets, we could successfully draw PC/MWCNT composites at concentrations of up to 10 wt% and HDPE/MWCNT composites at 15 wt%, as shown in Figure 49. Instead of pressing the composites at up to 260°C and 30 minutes, employing a higher force allowed to decrease the time and temperature necessary down to 2 minutes at 150°C for the HDPE composites and 200°C for the PC composites.

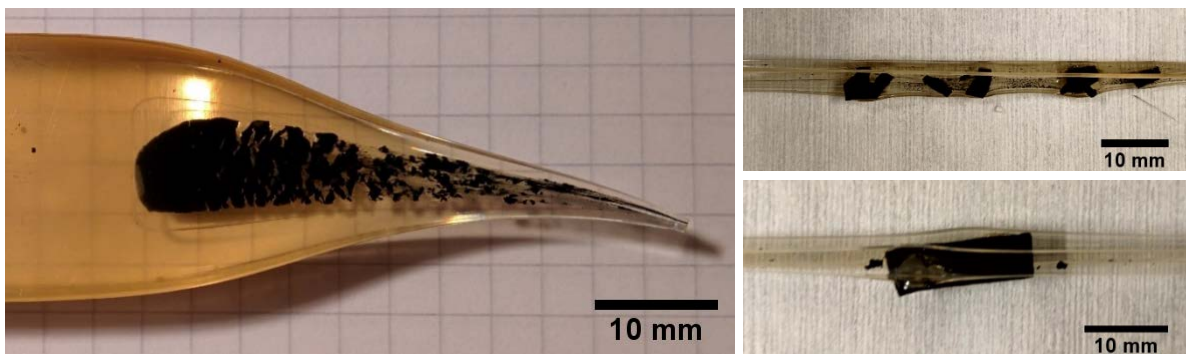


Figure 48. Top-view pictures of fibers in which the nanocomposite was not drawn successfully since it did not flow continuously. The cladding is polysulfone and the preforms were made with the design of Figure 38. Left: preform-to-fiber region of an interrupted draw, for a PC/MWCNT composite with a concentration of 5 wt% that was pressed into a sheet at 260°C for 30 minutes prior to preform consolidation and drawing. Top right: fiber with an HDPE/MWCNT composite (15 wt%) that was pressed into a sheet at 260°C for 2 minutes. Bottom right: fiber with a HDPE/MWCNT composite (15 wt%) that was pressed into a sheet at 260°C for 2 minutes, then annealed at 200°C for 15 hours to observe the effect it would have. The nanocomposite sheet did not deform or even break during drawing but kept the shape it had before placing it in the preform.

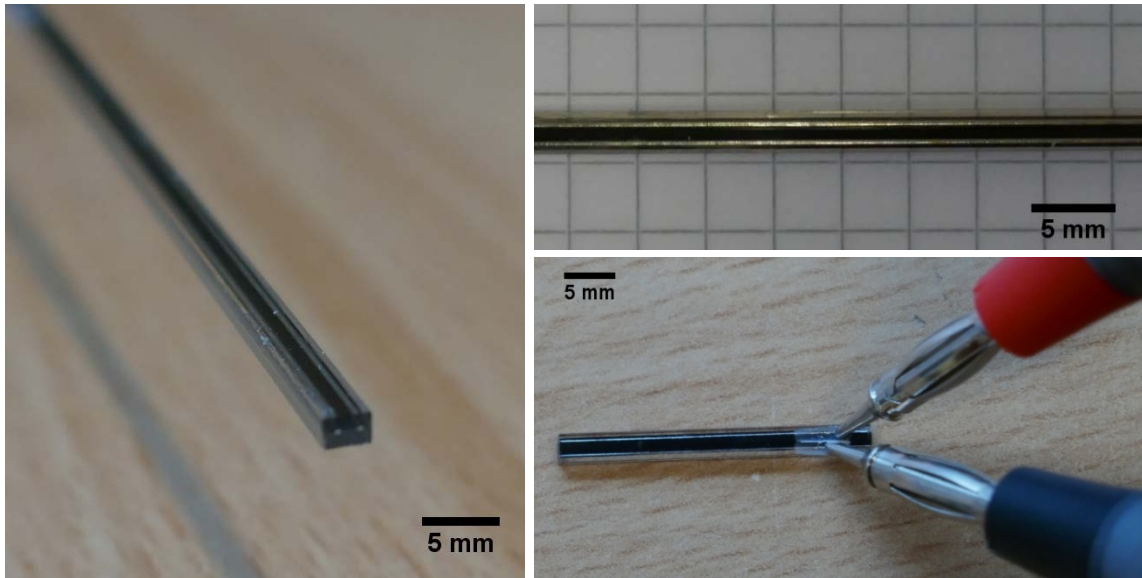


Figure 49. Pictures of fibers in which the MWCNT composite was drawn successfully. The cladding is polysulfone and the preforms were made with the cross-sectional design of Figure 39. The two metallic electrodes appear grey or bright and the nanocomposite is black. Left: perspective view. Top right: top view. Bottom right: top view. The cladding above the metallic electrodes was polished away locally to enable a measurement of the electrical resistance of the nanocomposite layer in between.

We also considered other polymers for which we also acquired a MWCNT masterbatch: low density polyethylene (LDPE) and polystyrene. However, they could not be drawn successfully at a concentration of 5 wt% for LDPE and 10 wt% for polystyrene, as illustrated in Figure 50. Employing a polyetherimide (PEI) cladding material was also considered, but the nanocomposite used did not flow as well as in a PSu cladding. A PEI cladding means a higher temperature profile in the draw tower tube furnace, and this likely causes too much annealing during the preform heating prior to drawing.

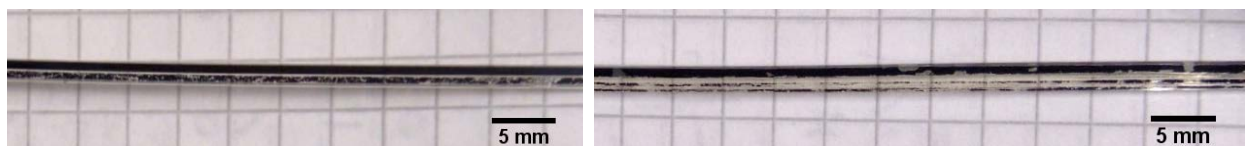


Figure 50. Top view pictures of fibers made with a variant of the design of Figure 38, in which two different MWCNT composites are placed side by side. Left: the HDPE nanocomposite flows well (top) but not the LDPE one (bottom), at concentrations of 5 wt%. Right: the HDPE nanocomposite (15 wt%) flows well (top) but not the polystyrene one (10 wt%, bottom).

The thermal drawing technique decreases the cross-sectional dimensions by a factor equal to the draw ratio  $Dr$ . Values of up to 20 were used in this work, but in most cases, it was around 10 to facilitate the electrical measurements. At first, the nanocomposite sheets employed in the preforms had a thickness of 100 to 300  $\mu\text{m}$ , leading to a 10 to 30  $\mu\text{m}$  layer that is opaque as shown in the figures above or can be slightly transparent for the lowest concentrations. Then, employing very high pressing forces of up to 7.5 kN enabled to shape thinner sheets, with thicknesses below 100  $\mu\text{m}$  and down to 30  $\mu\text{m}$ . Using such sheets in preforms, the

thermal drawing technique made them sufficiently thin to be transparent in the resulting fibers, as illustrated in Figure 51. Interestingly, this reveals that they are not uniform at a scale visible to the naked eye.

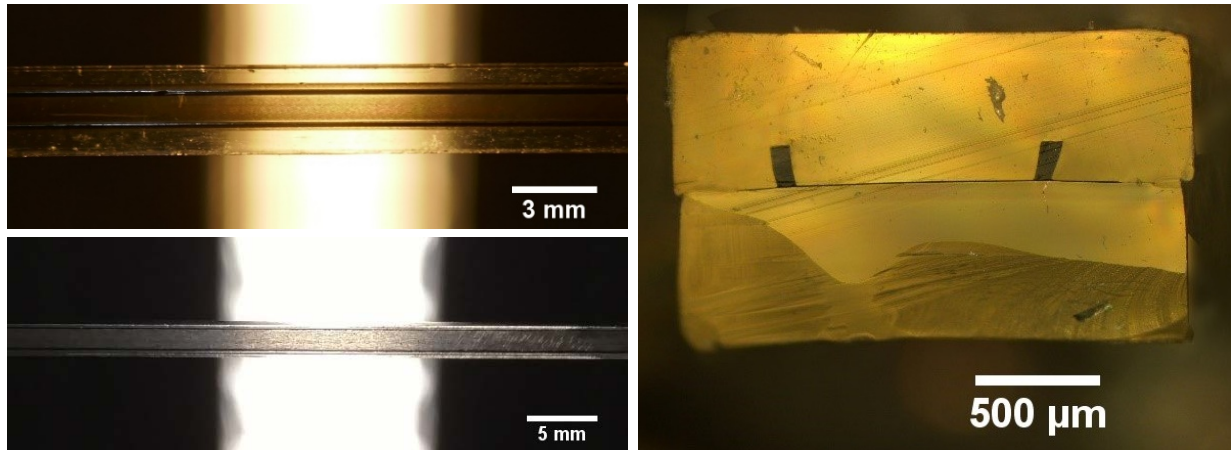


Figure 51. Left: Top view picture of fibers with a transparent HDPE/MWCNT composite layer (top: 5 wt% and about 8.5  $\mu\text{m}$  thick, bottom: 15 wt% and about 3  $\mu\text{m}$  thick) and two metallic electrodes, illuminated from below. Right: Optical microscopy image of the cross-section of a fiber with a 4.5  $\mu\text{m}$ -thick HDPE/MWCNT composite layer (10 wt%) and two metallic electrodes. The sample is the same as in Figure 45 (right) and was prepared via ultramicrotomy by cutting thin slices until the entire nanocomposite layer was polished, which is why the bottom part was not polished entirely. The metallic electrodes are tilted due to the pre-consolidation step realized to ensure a smooth surface at the transition between the metal and the cladding, presented in the previous section. However, thanks to this and a sufficiently high viscosity during drawing, the cross-sectional shapes were well preserved as indicated by the sharp corners of the metallic electrodes, allowing the nanocomposite to be continuous and a good contact with the metal.

We used optical microscopy in transmission to observe the transparent nanocomposite layers more closely, as shown in Figure 52. The concentration of nanotubes in the matrix is known on average but fluctuates at a scale accessible with visible light. In some places, we could observe elongated defects that likely reduce the measured conductivity perpendicular to the drawing direction and contribute to the anisotropy of conductivity. Distinct nanotube composites have microstructures that look different, but we did not identify any feature that would be helpful or predictive for choosing the most effective processing parameters or understanding better their influence. We also studied the drawn nanocomposites by Transmission Electron Microscopy, but did not observe a crucial difference with the melt-mixed ones shown in Chapter 2.

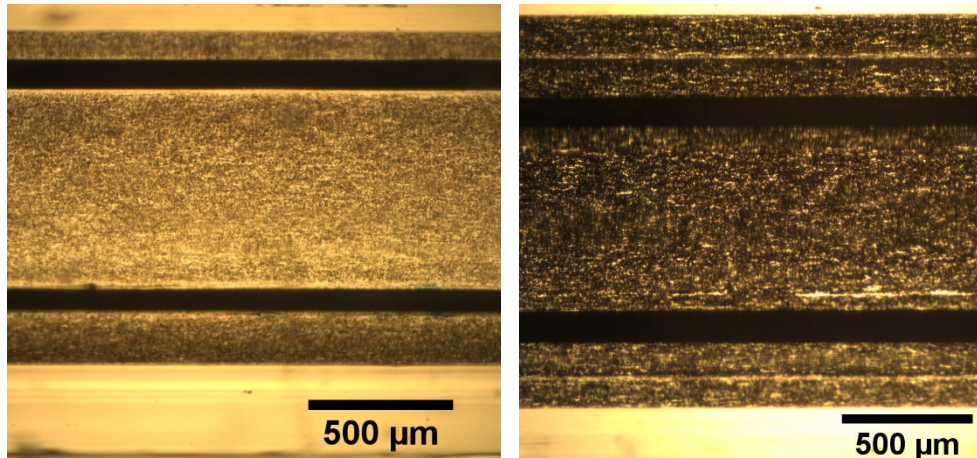


Figure 52. Light transmission microscopy images of fibers (top view) with an HDPE/MWCNT layer with a concentration of 5 wt% (left) or 15 wt% (right) and metallic electrodes in a polysulfone cladding.

### Post-drawing properties of MWCNT composites

The preforms designed as in Figure 39 were thermally drawn into fibers with a scaled-down cross-sectional architecture containing metallic electrodes that enable to measure the nanocomposite conductivity perpendicular to the drawing direction, such as the ones shown in Figure 49. As we observed above, the nanocomposites are not uniform materials, which means that the conductivity measured is an averaged value over the width between the metallic electrodes and the length of fiber considered.

We first show in detail the results obtained using a PC/MWCNT composite with a concentration of 3 wt% made by melt-mixing at 240°C. Sheets made of this material were placed in two different polysulfone preforms with SnZn electrodes and drawn with the same wall temperatures. For the first fiber the feeding speed was set to 2 mm/min, and for the second fiber it was 1 mm/min at first then changed to 2 mm/min. The drawing speed was varied to explore a large range of drawdown ratios. Even though the same wall temperatures were employed, the air temperature was lower when drawing the second fiber, which we infer from a different tension measured. It was typically 150 grams for the first fiber and 300 grams for the second with a feeding speed of 2 mm/min and a drawing speed of 0.2 m/min. In this case we did not adjust the wall temperature to obtain the same tension.

Figure 53 shows that the conductivity perpendicular to the drawing direction depends highly on the draw ratio since it spans almost four orders of magnitude. The loss of conductivity is due to the damage on the nanotube network caused by the deformation of the thermoplastic composite in the molten state, as described in Chapter 2. Such a strong effect can be understood by considering that the total elongation is equal to  $Dr^2$  and ranges from 4 to over 400 for the pieces of fiber considered. In Chapter 4, we explain quantitatively this result thanks to a detailed model of the thermal drawing process and the kinetic equation introduced in Chapter 2 (equation (26)).

At a given draw ratio, the conductivity is lower in the second fiber. This is consistent with the higher tension measured, since the conductivity of nanotube composites decreases more when submitted to shear at a lower temperature and higher viscosity, as explained in Chapter 2. For the second fiber, we can also observe that a lower feeding speed, which also means a lower drawing speed for a given draw ratio, leads to a higher

conductivity. This is also consistent with a lower loss of conductivity when the composite is subjected to a slower deformation.

The dispersion of the results is likely due to the material non-uniformity and the fact that the conductivity of a nanotube network is very sensitive to small fluctuations due to the tunneling nature of conduction in such materials, since the tunneling mechanism depends exponentially on the distance between particles. In comparison, the inaccuracy of the measurements is not significant.

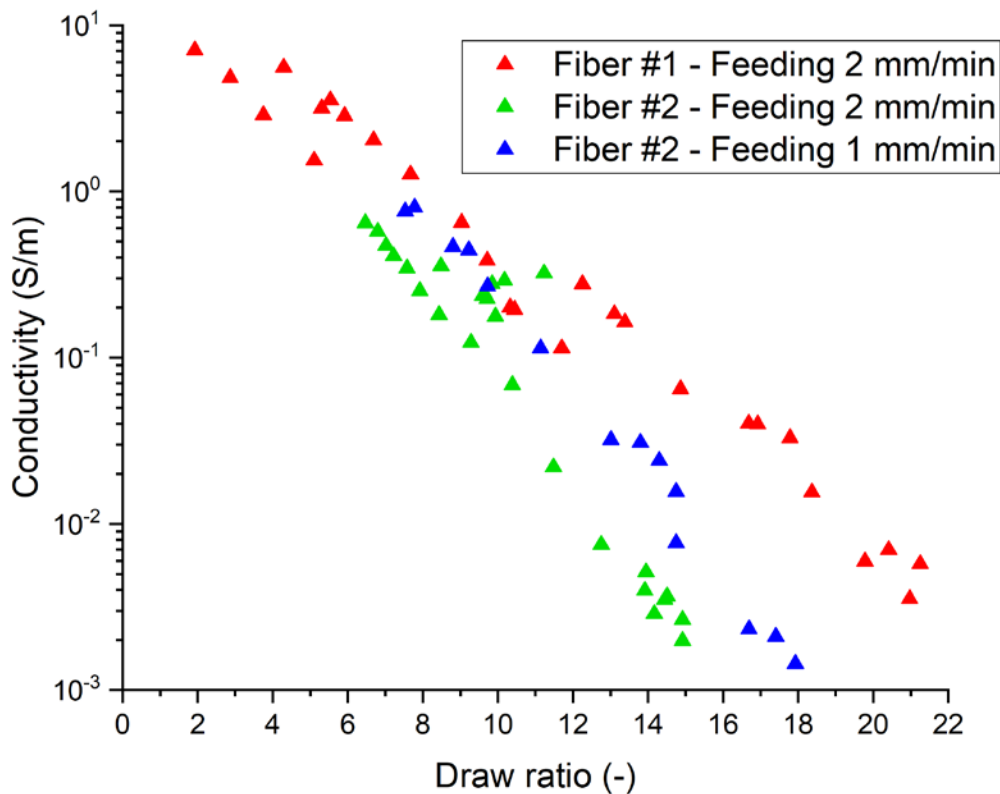


Figure 53. Conductivity versus draw ratio of a 3 wt% PC/MWCNT composite layer in two different PSu fibers. The conductivity is measured in the direction perpendicular to the drawing direction thanks to the two metallic electrodes in contact with the nanocomposite. Each data point is a measurement on a piece of fiber 1 to 10 cm long, the lower lengths being for the smaller draw ratios. The draw ratio is calculated from the measured width and thickness of the piece of fiber.

We also evaluated the anisotropy of conductivity by measuring its value in the fiber direction. The method consists in polishing away the metallic electrodes over a length of a few millimeters and measuring the resistance across the corresponding region in which only the nanocomposite is remaining. The conductivity is then calculated by taking into account the dimensions of the region of nanocomposite considered. This is relatively inaccurate, but we could estimate that the conductivity in the fiber direction is between 1 and 5 times higher than in the perpendicular direction, depending on the piece of fiber considered.

We observed that a flat interface initially perpendicular to the drawing direction bends during thermal drawing, as illustrated in Figure 42. Therefore, we can expect that due to a deformation that depends on the position in the fiber cross-section, the post-drawing conductivity of a nanocomposite also does, but the cross-sectional design used so far enables to measure only an average value between the two metallic electrodes. To evaluate this, we expanded the design with more electrodes placed at different positions, as shown in Figure 54 (left). Four electrodes are placed in the cross-section, with two different configurations along the preform. This enables to measure the conductivity of five different regions indicated with dashed lines of corresponding colors. Since the design is symmetrical, there are three non-equivalent positions termed central, intermediate and side positions. The values of conductivity measured still correspond to an average, but over a narrower width and not necessarily centered as for the simpler two-electrode design. In Figure 54 (right), we present the results obtained with a 5 wt% HDPE/MWCNT composite layer in a PSu fiber, which gives the most visible trend with a MWCNT composite. The conductivity seems to decrease more for the nanocomposite material placed on the sides at least for the higher draw ratios, but there is no clear difference for the lower draw ratios or between the central and intermediate positions.

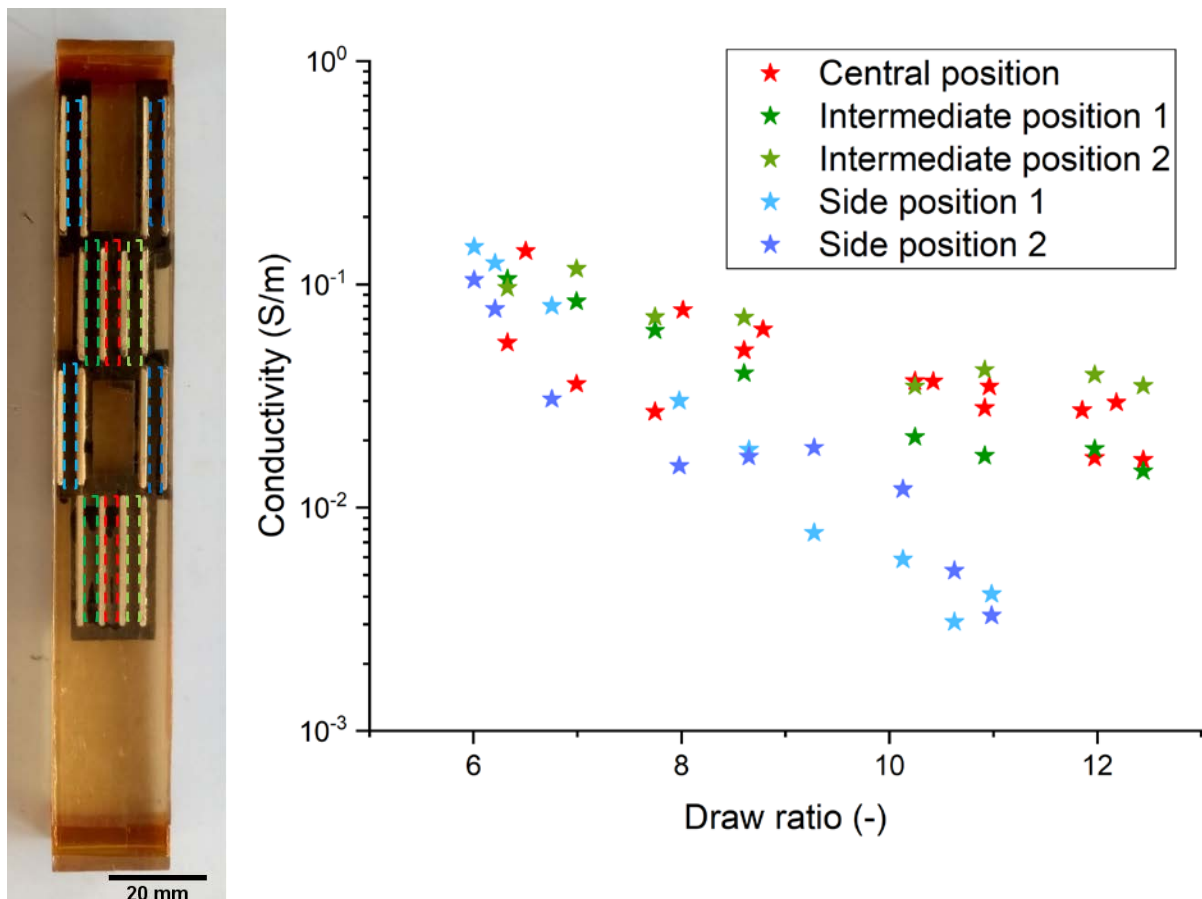


Figure 54. Left: Preform design for evaluating how the conductivity of a nanocomposite layer depends on the position in the cross-section, with five distinct regions indicated with dashed lines of different colors, each between two metallic electrodes. Right: Conductivity versus draw ratio of a 5 wt% HDPE/MWCNT composite layer in a PSu fiber at the five different positions in the cross-section.

We also worked on improving the conductivity obtained by employing MWCNT composites with higher concentrations, up to 10 wt% for PC and 15 wt% for HDPE matrices. Their conductivity was observed to depend less strongly on the draw ratio, with variations of less than an order of magnitude that is not as noticeable in comparison with the dispersion of the results due to material non-uniformity.

To optimize the post-drawing conductivity, we explored various parameters of the entire process: the melt-mixing temperature; the polymer grade mixed with the masterbatch, with either the same polymer as in the masterbatch or one with a different molecular weight and viscosity; and the time, temperature, force applied, and substrate employed for hot pressing the nanocomposites into sheets. Some combinations worked better than others for a given nanocomposite composition, but they were different for distinct polymers (PC or HDPE) and concentrations. We did not identify clear trends that would help choosing the most effective processing parameters, and the conductivity of the nanocomposites after mixing and hot pressing did not seem predictive of the post-drawing conductivity either. We also tried to anneal the fibers to improve the conductivity of the nanocomposite layer but could not improve it significantly at temperatures that do not damage the fiber. The measured conductivity could even decrease, possibly due to a deterioration of the contacts between the nanocomposite and the metallic electrode.

We show in Figure 55 the best conductivity perpendicular to the drawing direction obtained for PC/MWCNT and HDPE/MWCNT nanocomposites of the different concentrations considered, in PSu fibers with draw ratios higher than 6. The nanocomposite layer is opaque for most of them, and we also give the highest conductivity measured for fibers in which the nanocomposite is transparent. For the PC nanocomposites, the conductivity obtained in fibers is one order of magnitude lower than the highest value measured after the melt-mixing step. For the HDPE nanocomposites, the values are closer but lower than that obtained with PC at the same concentration.

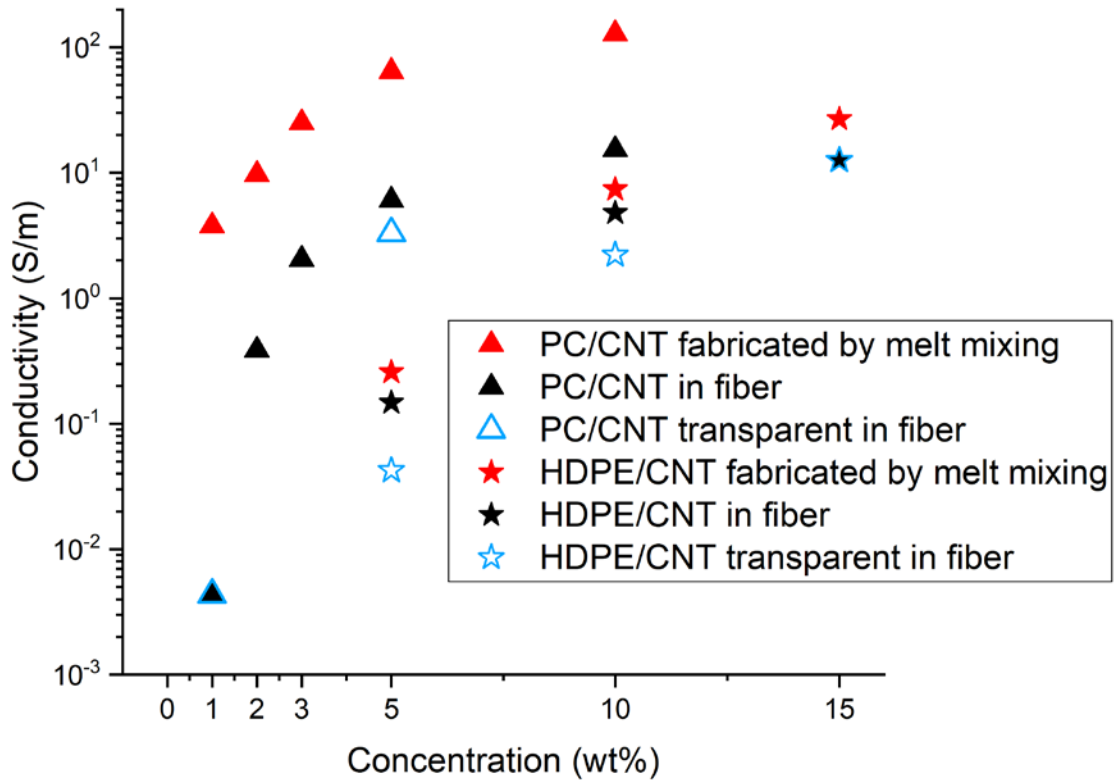


Figure 55. Conductivity against concentration of PC/MWCNT and HDPE/MWCNT composites. We compare the values obtained after melt mixing, in fibers for which the nanocomposite layer can be opaque, and in fibers for which the layer is transparent. We consider fibers with a PSu cladding and a draw ratio higher than 6.

We estimated the optical transmittance in the visible range of the transparent nanocomposite layer in different fibers, such as the ones shown in Figure 51. We used a white light source, an integrating sphere and a detector to measure the transmittance through the fibers and deduced the contribution of the polysulfone cladding. The optical setup was not optimized for examining samples of small width. The measured transmittance, which was between 10 and 40% for the fibers examined, is therefore relatively inaccurate, possibly with a relative error of tens of percent. However, this enables to evaluate comparatively the order of magnitude of the figure of merit  $\sigma_{DC}/\sigma_{op}$  (equation (20)), since it is dominated by the conductivity of the nanocomposite layers considered, which have a relatively similar transmittance but a conductivity that differs by several orders of magnitude. We show in Figure 56 the sheet resistance  $R_s$  and figure of merit  $\sigma_{DC}/\sigma_{op}$  against concentration for several PC/MWCNT and HDPE/MWCNT transparent composites in fibers. For use as transparent electrode in fibers, the highest concentration possible is preferable. The results obtained are relatively far from the value of 35 required for high-performance optoelectronic devices according to De et al. [71], however non-optimal but functional devices are feasible. For example, Wu et al. [29] reported a graphene-based transparent electrode with a sheet resistance of 100 k $\Omega$ /sq and transmission of 95%, corresponding to a figure of merit  $\sigma_{DC}/\sigma_{op}$  lower than  $10^{-1}$  that was used to make a solar cell with an efficiency only halved compared to a reference cell made with high-performance ITO. Therefore, we employed a MWCNT nanocomposite in a simple photodetecting fiber to verify that it can function as transparent electrode in an optoelectronic fiber device, as described in Chapter 5.

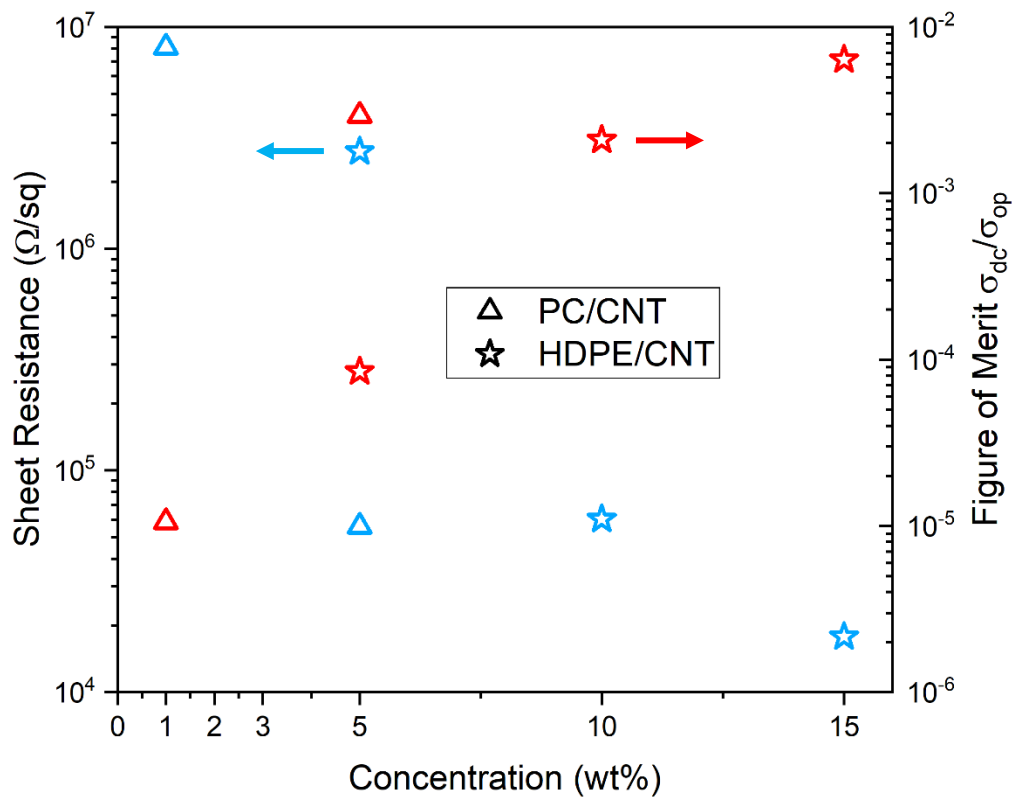


Figure 56. Sheet resistance and figure of merit  $\sigma_{DC}/\sigma_{op}$  against concentration for several PC/MWCNT and HDPE/MWCNT transparent composites in fibers.

### 3.2.3 Carbon Black composites

A study previously conducted in the FIMAP laboratory by Dr. Tùng Nguyen and Inès Richard pointed that the in-fiber conductivity of carbon black composites remained at the pre-drawing value of 5 S/m in a polysulfone cladding but decreased down to  $3 \times 10^{-5}$  S/m in a polycarbonate cladding, which is drawn at a much lower temperature than polysulfone. Since we observed a large decrease of conductivity with MWCNT composites in this work, we studied further the drawing of PC/CB in PC cladding to compare the behaviors of different types of fillers and see if it could help understanding the underlying mechanisms and the thermal drawing technique itself.

We employed a design with six electrodes in the cross section that enables to measure the conductivity of the nanocomposites at five positions, in a similar way to Figure 54. To enable to connect separately the six electrodes, we used relatively low draw ratios. Moreover, rather than spanning a large range of draw ratios, we divided the draw in two draw ratios, close to 5 and 7.

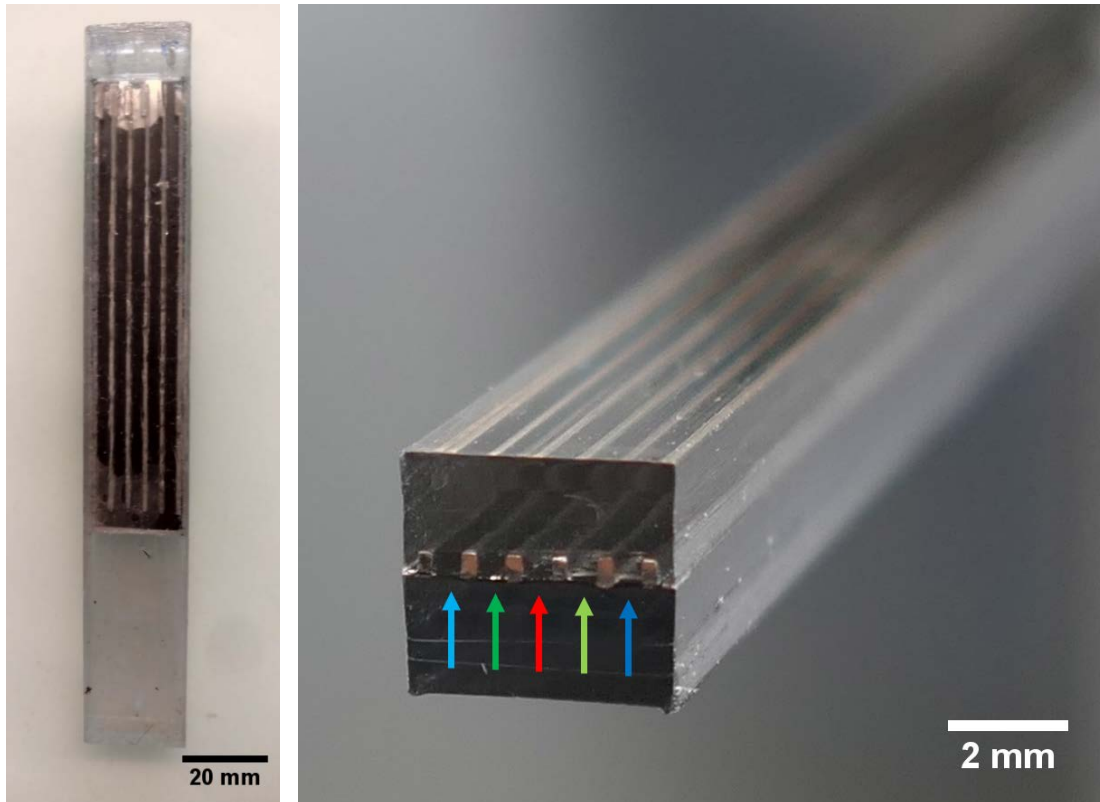


Figure 57. Left: Top view picture of the preform with a PC/CB sheet (0.25 mm thick) and six BiSn electrodes in a PC cladding. Right: perspective view of the resulting fiber, with colored arrows pointing to the five distinct regions of composite between metallic electrodes. The colors correspond to the central, intermediate and side positions as in Figure 58.

We show in Figure 58 the conductivity against draw ratio for the five regions of the fiber. The measurements were done on relatively long pieces of fiber (13 to 27 cm) and show little dispersion compared to the results obtained with MWCNT composites. As for the latter, the conductivity strongly decreases with increasing draw ratio. What appears more clearly, even for such low draw ratios, is that compared to the central position, the conductivity is lower at the intermediate positions and much lower at the side positions.

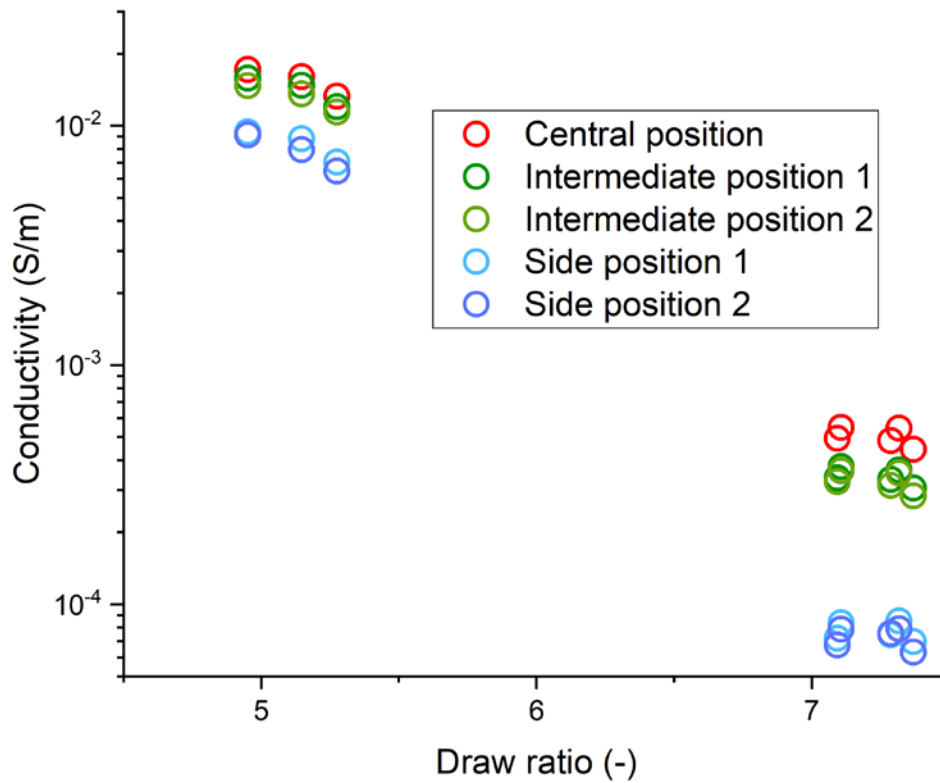


Figure 58. Conductivity against draw ratio for a PC/CB composite in a PC cladding, measured at five positions in the cross-section.

We then grouped the results obtained by draw ratio and position to plot the conductivity averaged over several measurements against the position of the regions in the cross-section. For the two groups of measurements, the average draw ratios are 5.12 (standard deviation 0.16) and 7.24 ( $\pm 0.13$ ). The positions are described by the distance of the center of the corresponding region of nanocomposite to the center of the cross-section, relatively to the half width. Since the design is symmetrical, we grouped the two intermediate positions and side positions. The resulting graph is shown in Figure 59, with error bars corresponding to the standard deviation of the conductivity measurements for which the average is taken. The conductivity decreases strongly with draw ratio but also with distance from the center, which we explain quantitatively through modeling in Chapter 4.

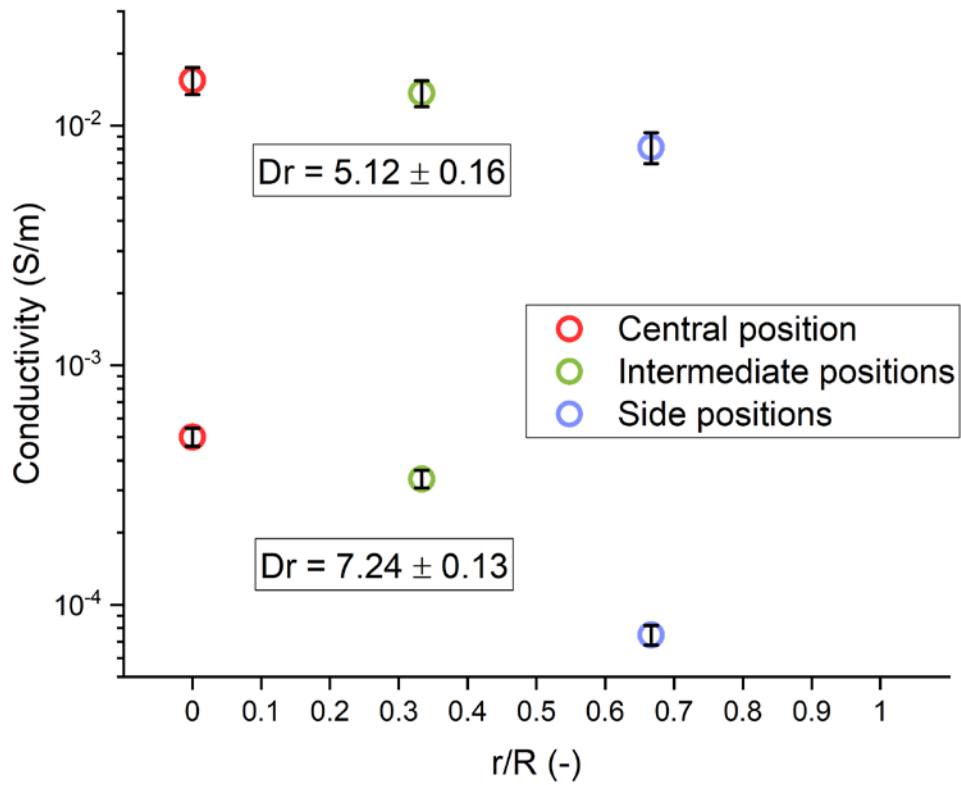


Figure 59. Conductivity against relative distance to the center in the width of the fiber cross-section, for a PC/CB composite layer in a PC cladding. Since the fiber is symmetrical and in anticipation of a cylindrical model in Chapter 4, we use the notation  $r/R$  for the positions relative to the half width. Several measurements were averaged, with the standard deviation written numerically for the draw ratios and shown with error bars for the conductivity.

## 3.3 Discussion

### 3.3.1 Rheology and ability to draw MWCNT composites

Thanks to the rheological studies realized on the carbon nanotube composites considered for thermal drawing, we learned that heating them increases their elastic modulus. By reducing the annealing due to the processing step consisting in hot pressing the melt-mixed materials into sheets, we could increase the concentration at which such nanocomposite sheets could be thermally drawn in polysulfone fibers. To understand more precisely why some composites could be drawn and others could not, we performed rheological measurements during which the heat history due to the pressing and consolidation steps is reproduced. However, we could not identify a criterion that would indicate whether a material can be drawn successfully from the rheological properties measured. Comparing the viscosity of different nanocomposites with that of polysulfone or reviewing the value of their elastic modulus was not sufficient. Moreover, the influence of heat history seemed small compared to that of the MWCNT concentration.

The fact that we did not identify a criterion is not surprising if we compare the shear rheology measurements to the thermal drawing process. Whereas a material is submitted to a pure shear between parallel plates in the shear rheometer, it is hanging in air, pulled and undergoes a large elongational deformation during drawing. Therefore, a type of measurement that reproduces more closely the deformation undergone may provide more adequate information. The fact that the elastic component of complex viscosity dominates in the heated carbon nanotube composites also suggests that yielding may be hindered by the nanotube network. The breakage of the nanocomposite layer observed in unsuccessful draws would mean that the yield stress increased so much that it exceeds the breaking stress at the moment it is pulled in the thermal drawing process. The detailed mechanism is likely more complex, since in the preforms considered the nanocomposite is encapsulated by a thermoplastic cladding which can contribute to prevent its breakage. A more suitable type of measurement may be realized with a Münstedt tensile rheometer such as the one used by Starý et al. [89] (Figure 24). However, the measurement would be isothermal, whereas in thermal drawing the temperature profile goes down to room temperature and nanocomposites have a complex dependence of properties on temperature history.

Since we could draw MWCNT composites even at concentrations far above their rheological threshold, we chose to focus on understanding in more detail the thermal drawing process and how it changes the conductivity, in order to improve it.

### 3.3.2 Properties of MWCNT composites thermally drawn in fibers

We demonstrated the successful integration of conductive and transparent carbon nanotube thermoplastic composites in thermally drawn fibers. We noticed that the values of conductivity measured perpendicular to the drawing direction thanks to metallic electrodes correspond to an average over the region of non-uniform material considered. At a relatively low nanotube concentration and for carbon black composites, we showed that the conductivity strongly decreases with draw ratio. This effect is thought to be due to deformation-induced damage of the conductive filler network. We pointed that the post-drawing conductivity is also influenced by the position of the nanocomposite in the fiber cross-section. This is likely caused by a deformation that is not uniform in the cross section indicated by the bending of initially flat interfaces in the preform. In Chapter 4, we present a model that we developed to explain these mechanisms.

We achieved a conductivity perpendicular to the drawing axis of up to 15 S/m, and for transparent nanocomposites a sheet resistance of  $10^4 \Omega/\text{sq}$  and a value of the figure of merit  $\sigma_{DC}/\sigma_{op}$  approaching  $10^{-2}$ . Such performance is adequate to realize functional optoelectronic fiber devices, even though it is relatively low compared to high-performance materials employed in high-efficiency solar cells. The cladding material used in most cases, polysulfone, is suitable for the integration of semiconducting materials such as Se or  $\text{As}_2\text{Se}_3$ . In Chapter 5, we present a photodetecting fibers that employs a MWCNT composite as transparent electrode and Se as photoconductive material to show that the nanocomposites studied can fulfill their intended function.

In Table 2, we give some properties of the polymers used in this work. Then, Table 3 summarizes the properties of the different types of conducting nanoparticles employed: carbon black, single-wall nanotubes, multi-wall nanotubes and silver nanowires. Finally, Table 4 compares the properties of carbon nanotube composites reported in the literature to those we fabricated and integrated in thermally drawn fibers.

Property	Density	Specific heat capacity	Thermal expansion coefficient	Thermal conductivity	Refractive index	Glass transition temperature
Unit	g/cm <sup>3</sup>	J/(kg.K)	10 <sup>-5</sup> K <sup>-1</sup>	W/(m.K)	-	°C
<b>PMM A</b>	1.19	1400 - 1500	7	0.17 - 0.19	1.49	105 (atactic)
<b>HDPE</b>	0.93 - 0.97	1900	10 – 20	0.46 - 0.51	1.54	- 110
<b>PC</b>	1.20	1200 - 1300	7	0.20	1.59	145
<b>PSu</b>	1.24	1000	5.6	0.25	1.64	190

Table 2. Properties, at room temperature, of the thermoplastic polymers employed in this work: poly(methyl methacrylate), high density polyethylene, polycarbonate and polysulfone. References: product specification sheets from the companies Boedeker, Goodfellow and Nanocyl; Wikipedia and Techniques de l'Ingénieur websites.

Property	Composition	Dimensions	Aspect ratio	Density	Electrical conductivity
<b>Unit</b>			-	g/cm <sup>3</sup>	S/m
<b>Carbon Black</b>	Graphitic Carbon	Sphere-like, 30 - 60 nm (determined by SEM)	≈ 1	Graphite: 2.09 - 2.23	Graphite: 3.3 x 10 <sup>2</sup> to 3.0 x 10 <sup>5</sup> (anisotropic)
<b>SWCNT (OCSiAl Tuball)</b>	Carbon content > 85 wt% CNT content > 75 wt% Iron impurities < 15 wt% BET surface area 500 m <sup>2</sup> /g	Diameter 1 - 2 nm Length > 5 μm	> 2500	1.5 - 3.0 [78]	Single CNT: up to 2 x 10 <sup>7</sup> [15]
<b>MWCNT (Nanocyl NC7000)</b>	Carbon purity 90% Transition metal oxide impurities < 1% BET surface area 250 - 300 m <sup>2</sup> /g	Average diameter 9.5 nm Average length 1.5 μm	≈ 150	0.6 - 2.5 (depending on number of walls) [78]	
<b>Silver nanowires (Yurui)</b>	Silver	Diameter 35 nm & length 15 μm or diameter 150 nm & length 50 μm	300 - 400	Silver: 10.49	Silver: 6.30 x 10 <sup>7</sup>

Table 3. Description and properties of the conductive nanoparticles employed in this work as fillers in thermoplastic composites.

Property	Min. concentration for a conductivity of 10 <sup>-6</sup> S/m	Min. concentration for a conductivity of 10 <sup>-3</sup> S/m	Conductivity	Figure of merit $\sigma_{DC}/\sigma_{op}$
<b>Unit</b>	wt%	wt%	S/m	-
<b>Carbon nanotube composites in the literature</b>	Ref. [37]: 0.0025 in epoxy Ref [92]: 0.4 in PC	Ref [37]: 0.005 in epoxy Ref [92]: 0.4 in PC	Ref [93]: 10 <sup>4</sup> (13.5 wt% in PMMA)	Ref [72]: 0.370 (0.5 wt% in PMMA)
<b>PMMA/SWCNT (as made)</b>	0.002	0.005	2833 (10 wt%), 339 (5 wt%)	0.0189 (0.05 wt%)
<b>HDPE/MWCNT (as made)</b>	4	5	26.7 (15 wt%)	Not transparent
<b>HDPE/MWCNT (in fiber, Dr &gt; 6)</b>	5	5	12.6 (15 wt%)	0.00635 (15 wt%)
<b>PC/MWCNT (as made)</b>	0.5	1	128 (10 wt%)	Not transparent
<b>PC/MWCNT (in fiber, Dr &gt; 6)</b>	1	1	15.3 (10 wt%)	0.00294 (5 wt%)

Table 4. Comparison of some carbon nanotube composites reported in the literature to the ones realized in this work and integrated in thermally drawn fibers, in terms of minimum concentrations required to reach a conductivity of 10<sup>-6</sup> S/m and 10<sup>-3</sup> S/m, high values of conductivity obtained and figure of merit  $\sigma_{DC}/\sigma_{op}$ .

Further improvement of the optoelectronic properties of nanocomposite layers in multi-material fibers is likely possible, for instance by optimizing the experimental process for PC/MWCNT composites at concentrations higher than 5 wt%. Due to anisotropy, the conductivity along the drawing direction could probably reach higher values, which may be of interest for applications in which metals cannot be employed.



# Chapter 4 Modeling thermal drawing and the conductivity of nanocomposites

While the introduction of different materials in the drawing process has triggered much interest to realize innovative fiber-based devices and smart textiles, subtle effects of the fluid dynamics of multi-material co-drawing remain to be investigated to better understand and exploit this approach. In particular, modeling and analytical analysis have mostly relied on fluid dynamics descriptions that assume a velocity in the drawing direction that is independent of the radial position [11], [23], [94]. There exist some numerical studies that are not based on such an assumption, but only in the context of single material, micro-structured optical fibers [94], [95]. The impact of the non-uniform axial velocity in the cross-section in the context of multi-material drawing, however, is essential, albeit yet unexplored. In fact, a radially varying velocity field and hence deformation rate during drawing can influence the targeted architecture and resulting properties of the functional materials at the fiber level. A striking manifestation of this effect is shown in Figure 42 and Figure 60 (a) where initially rectangular domains of polymer nanocomposites deform significantly during drawing. The observed pattern, which we model below, results from a relative displacement of material at different radial positions. Taking this effect into account is primordial to realize advanced fiber-based devices with controlled properties.

In this chapter, we report an in-depth fluid dynamics analysis of the thermal drawing process that takes into account the radial dependency of the axial velocity. We propose a model that includes higher order terms of the velocity field, which enables us to elucidate the observation of line deformation. From this velocity field, we can extract a more accurate distribution of the rate of deformation during drawing, which is crucial for material properties at the fiber level. In particular, we apply the results of our model to precisely account for the dependence of electrical conductivity of polymer nanocomposites on draw ratio and radial position (Figure 53 and Figure 58). This important class of materials widely used in fiber-based devices has a well-known yet so far unexplained dependency of their electrical conductivity on the fiber drawing conditions [7].

The work presented in this chapter was realized through a collaboration with Dr. Mathias Bechert, scientific collaborator at the Laboratory of Fluid Mechanics and Instabilities, directed by Prof. François Gallaire. At the time of writing, an article is in preparation for submission to the journal *Proceedings of the National Academy of Sciences*, the authors being Alexis G. Page, Mathias Bechert, François Gallaire and Fabien Sorin.

## 4.1 Modeling the thermal drawing process

To model the thermal drawing process, we extend the reduced one-dimensional model for elongating fibers widely used in literature [96]–[99]. We follow the derivation as presented by Bechert and Scheid [96] for fiber spinning and film casting and extend the model equations to cover thermal effects, analogue to Scheid et al. [100]. Moreover, we analyze higher order terms to gain information about the radial distribution of the variables. For the sake of simplicity, we consider only the cladding material in the model, as the functional materials represent only a small fraction of the fiber cross-sectional area, and assume a uniform incompressible material. Furthermore, we model an axisymmetric, round fiber in steady state thermal drawing.

### 4.1.1 Presentation of the model

#### Notations and thermal drawing parameters

Figure 60 (b) shows the notations employed in the model. The fiber is considered axisymmetric and we use cylindrical coordinates  $(r, \theta, z)$  with a velocity field  $\mathbf{v}(r, z)$ . We decompose  $\mathbf{v}$  in the radial and axial components  $u(r, z)$  and  $v(r, z)$ , with no  $\theta$  component due to axisymmetry,  $\mathbf{e}_r$  and  $\mathbf{e}_z$  being the unit vectors:

$$\mathbf{v}(r, z) = u(r, z)\mathbf{e}_r + v(r, z)\mathbf{e}_z \quad (29)$$

We consider a domain of modeling, i.e. preform-to-fiber region, of length  $L$ , from  $z = 0$  to  $z = L$ . In this neckdown region, the fiber is delimited by its radius  $R(z)$ , with initial (preform) radius  $R(0) = R_0 = R_{preform}$ . The feeding speed is  $v_{feed} = v_0$  and the drawing speed is  $v_{draw} = v_0 Dr^2$  due to volume conservation as mentioned in Chapter 3 (equation (28)). The draw-down ratio  $Dr$  is the ratio of the preform radius  $R_0$  to the fiber radius  $R(L) = R_{fiber}$ , i.e.  $Dr = R_{preform}/R_{fiber}$ .

We therefore have the following boundary conditions for the velocity field, with  $\langle v \rangle(z)$  the cross-sectional average of  $v(r, z)$ :

$$u(0, z) = 0 \quad (30)$$

$$\langle v \rangle(0) = v_0 \quad (31)$$

$$\langle v \rangle(L) = Dr^2 \cdot v_0 \quad (32)$$

The temperature in the material is  $T(r, z)$ , its viscosity  $\eta(r, z)$  and the stress tensor is  $\boldsymbol{\sigma}(r, z)$ , related with the pressure  $p$  and the extra stress tensor  $\boldsymbol{\tau}$  by the following equation,  $\mathbf{I}$  being the unit tensor:

$$\boldsymbol{\sigma} = \boldsymbol{\tau} - p\mathbf{I} \quad (33)$$

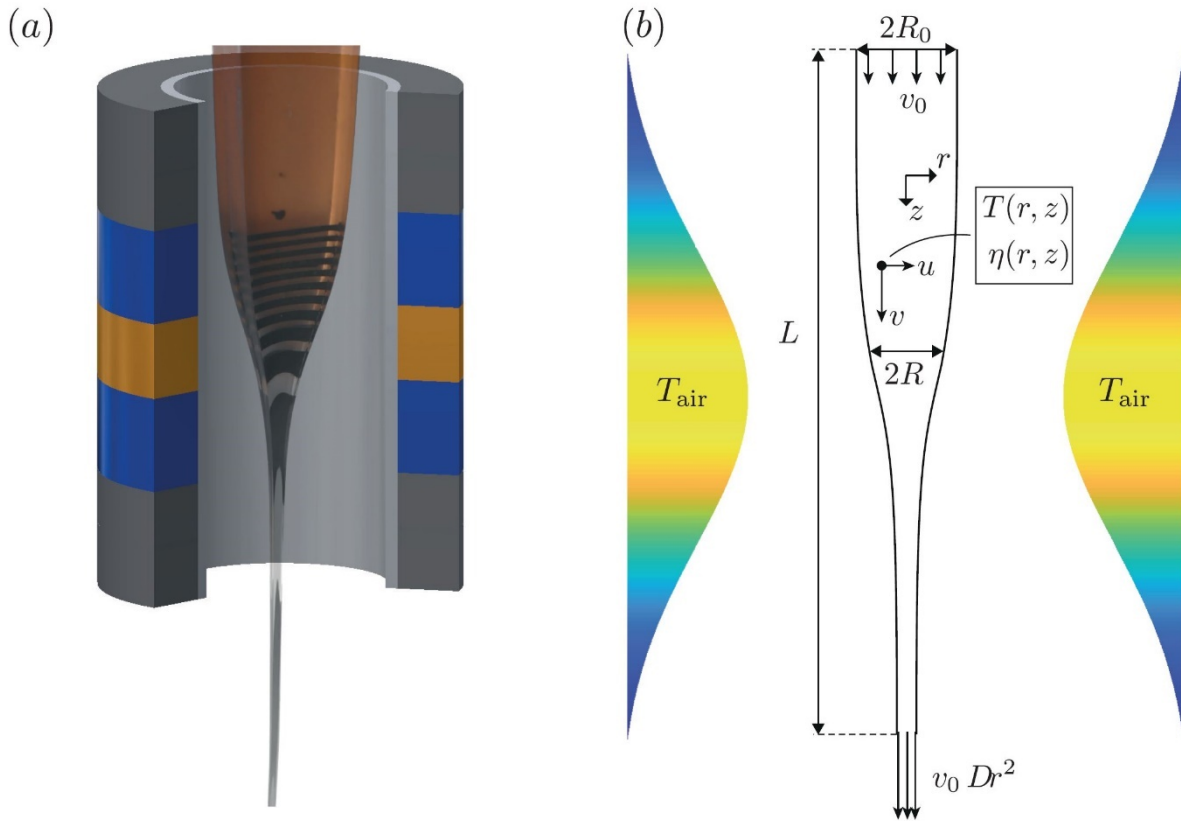


Figure 60. (a) Visualization of the thermal drawing of a fiber in a furnace with three heating zones. We combined a picture of an interrupted draw (as in Figure 42) with a schematic of the furnace. (b) Sketch of the axisymmetric model. The ambient temperature  $T_{air}$  is assumed to have a Gaussian shape along the  $z$ -axis, shown in Figure 61.

We assume a centered Gaussian profile for the description of the surrounding air temperature in the furnace along the drawing axis,

$$T_{air}(z) = \frac{\Lambda \exp\left(-\frac{(z/L - 0.5)^2}{\Delta^2}\right) + 1}{\Lambda + 1} T_{max} \quad (34)$$

The parameters  $\Lambda$ ,  $\Delta$  and  $T_{max}$  are determined using the fiber radius profile measured experimentally, as described further, both for polysulfone and polycarbonate cladding materials. With the choice of a domain length  $L$  of 400 mm, the temperature at the boundaries is small enough so that the resulting high viscosities lead to negligible fiber deformation. The values of the parameters used are listed in Table 5, and the corresponding temperature profile is shown in Figure 61. The preform radius  $R_0$  in the model was chosen to be 12.5 mm so that the diameter corresponds to the width of the preforms used in the experiments.

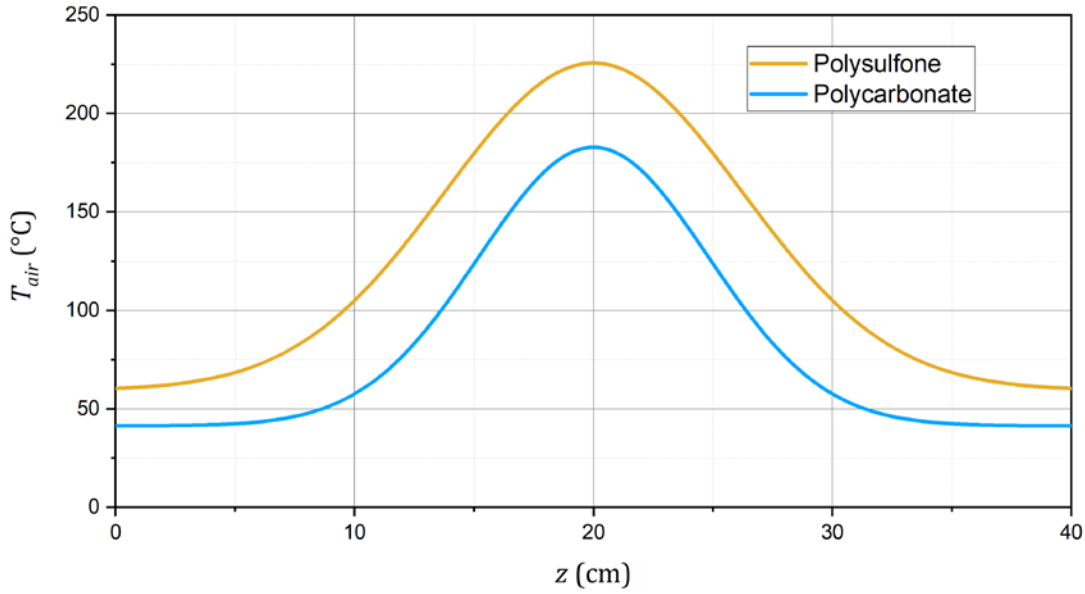


Figure 61. Air temperature against vertical position used for modeling the thermal drawing of polysulfone and polycarbonate fibers.

### Material properties and assumptions

The material is a thermoplastic polymer considered Newtonian with the constitutive equation:

$$\boldsymbol{\tau} = \eta(\nabla \mathbf{v} + (\nabla \mathbf{v})^T) \quad (35)$$

Its viscosity  $\eta$  depends on temperature following an Arrhenius equation:

$$\eta_{polymer}(T) = \eta_{min} \exp \left[ -\frac{E_a}{\bar{R}T_{max}} \left( \frac{T_{max}}{T} - 1 \right) \right] \quad (36)$$

with activation energy  $E_a$  and  $\bar{R}$  the gas constant.  $T_{max}$  is the maximum temperature of the surrounding air and  $\eta_{min} = \eta_{polymer}(T_{max})$  the corresponding viscosity. Note that even though the material does not necessarily reach  $T_{max}$  and  $\eta_{min}$ , it still approaches these values closely during the drawing, which makes them well-suited for scaling. The value of  $E_a$  was determined for polysulfone and polycarbonate by fitting measurements of viscosity versus temperature shown in Figure 62 and realized in the parallel-plate rheometer of Figure 28 under a shear rate of  $0.1 \text{ s}^{-1}$ , which is in the Newtonian regime of these polymers where the viscosity is independent of shear rate. During thermal drawing, the shear rate remains lower than this value.

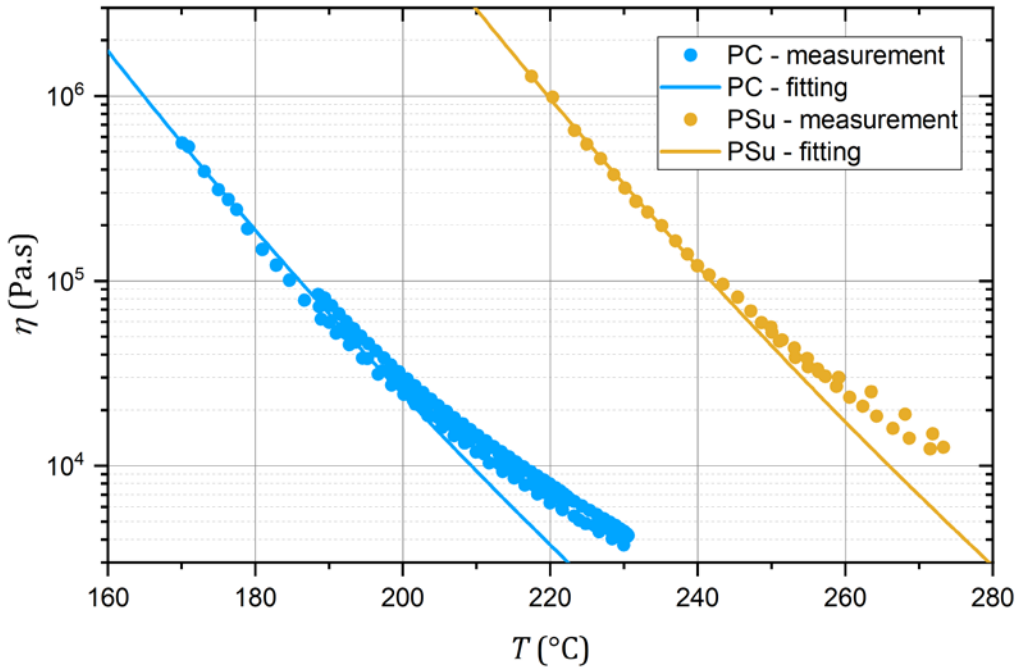


Figure 62. Viscosity against temperature of polysulfone and polycarbonate measured in a parallel-plate rheometer with a shear rate of  $0.1 \text{ s}^{-1}$ .

Thermal expansion is not taken into account. The material density, heat capacity and thermal conductivity are  $\rho$ ,  $c_p$  and  $k$ , respectively, all assumed to be uniform. The values used for the different properties are listed in Table 5. For polysulfone, they are obtained from the material specification sheet of the supplier and correspond to room temperature values. For polycarbonate, we use average values of the properties in the temperature range of drawing from the Comsol Multiphysics material library.

Heat transfer between air and the material and radiative heating are effectively modeled by the heat transfer coefficient  $h$  in Newton's cooling boundary condition (shown further in equation (46)) and the air temperature profile (equation (34)). The value of  $h$  and the parameters  $\Lambda$ ,  $\Delta$  and  $T_{max}$  are determined by fitting the predicted fiber radius profile to the experimental observation. An example is given in the next section.

We then calculate conservative values of dimensionless numbers from the drawing parameters and the materials properties listed in Table 5 to justify more approximations:

- The Capillary number  $Ca = \eta_{min} v_0 / \gamma$  is higher than  $10^2$ .
- The Reynolds number  $Re = \frac{\rho v_0 D r^2 L}{\eta_{min}}$  compares inertial to viscous forces and is smaller than  $10^{-4}$ .
- The ratio of the Reynolds number to the Froude number  $Re / Fr = \frac{\rho L^2 g}{\eta_{min} v_0 D r^2}$  compares the gravitational to the viscous forces and is close to 1.

In our model, we assume negligible effects of surface tension, inertia and gravity.

Symbol	Parameter, material property or dimensionless number	Unit or definition	Polysulfone (PSu)	Polycarbonate (PC)
$R_0$	Preform radius	mm	12.5	12.5
$R_{fiber}$	Fiber radius	mm	1.504	1.502
$L$	Length of neckdown region	mm	400	400
$v_0$	Feeding speed	mm/min	2	2
$v_{draw}$	Drawing speed	mm/min	138.1	138.4
$Dr$	Draw-down ratio	-	8.31	8.32
$\alpha$	Fiber parameter	$R_0/L$	0.03125	0.03125
$\alpha^2$	Parameter for expansion of variables	-	$< 10^{-3}$	$< 10^{-3}$
$T_{max}$	Maximum air temperature	°C	225.7	182.9
$\Lambda$	First parameter for the Gaussian air temperature profile	-	0.5	0.45
$\Delta$	Second parameter for Gaussian air temperature profile	-	0.22	0.17
$\eta_{min}$	Viscosity at $T_{max}$	Pa.s	$5.25 \times 10^3$	$1.38 \times 10^3$
$E_a$	Activation energy for viscosity	kJ/mol	219.8	182.0
$\rho$	Density	kg/m <sup>3</sup>	1240	1200
$c_p$	Specific Heat capacity	J/(kg.K)	1000	1800
$k$	Thermal conductivity	W/(m.K)	0.25	0.25
$h$	Heat transfer coefficient	W/(m <sup>2</sup> .K)	20	30
$\gamma$	Surface tension	N/m	$< 0.05$	$< 0.05$
$Re$	Reynolds number	$\rho v_0 Dr^2 L / \eta_{min}$	$< 10^{-4}$	$< 10^{-4}$
$Ca$	Capillary number	$\eta_{min} v_0 / \gamma$	$> 100$	$> 100$
$Re/Fr$	Ratio of Reynolds to Froude numbers	$\rho L^2 g / \eta_{min} v_0 Dr^2$	$\approx 1$	$\approx 1$
$Bi$	Biot number	$h R_0 / k$	1	1.5
$Pe$	Peclet number	$\rho c_p v_0 R_0 / k$	2.1	3.6
$St$	Stanton number	$2 Bi / (\alpha Pe)$	31	27

Table 5. List of the parameters, material properties and dimensionless numbers used in the implementations of the model.

## Governing equations and boundary conditions

The flow is described by the continuity and momentum conservation equations:

$$\partial_t \rho + \operatorname{div} \rho \mathbf{v} = 0 \quad (37)$$

$$\rho \partial_t \mathbf{v} + \rho (\mathbf{v} \cdot \nabla) \mathbf{v} = \rho \mathbf{g} + \nabla \cdot \boldsymbol{\sigma} \quad (38)$$

We neglect all time derivatives as we are interested in steady solutions only.

Assuming a uniform density  $\rho$ , the continuity equation (37) is simply

$$\operatorname{div} \mathbf{v} = 0 \quad (39)$$

In steady state and neglecting inertia and gravity, the momentum conservation (38) simplifies to

$$\nabla \cdot \boldsymbol{\sigma} = \mathbf{0} \quad (40)$$

At the fiber surface  $r = R(z)$ , the kinematic boundary condition is

$$R' = \frac{u(R, z)}{v(R, z)} \quad (41)$$

The notation  $f'$  means the derivative of  $f$  with respect to  $z$ , and is used for variables and expressions than only depend on  $z$ .

The stress boundary condition is

$$\mathbf{n} \cdot \boldsymbol{\sigma}(R, z) = \mathbf{0} \quad (42)$$

where  $\mathbf{n}$  is the outward vector normal to the fiber surface, given by

$$\mathbf{n} = \frac{\mathbf{e}_r - R' \mathbf{e}_z}{\sqrt{1 + R'^2}} \quad (43)$$

The temperature field is governed by the thermal energy equation, which is, without considering viscous heating as in [100],

$$\rho c_p (\partial_t T + \mathbf{v} \cdot \nabla T) = k \nabla^2 T \quad (44)$$

with  $c_p$  the specific heat capacity and  $k$  the thermal conductivity. It simplifies in steady state to

$$\rho c_p \mathbf{v} \cdot \nabla T = k \nabla^2 T \quad (45)$$

At the fiber surface  $r = R(z)$ , we have the Newton's cooling boundary condition

$$-k \mathbf{n} \cdot \nabla T|_R = h (T(R) - T_{air}(z)) \quad (46)$$

with  $h$  the heat transfer coefficient between the fiber material and the surrounding air, assumed constant.

We also have the boundary condition at  $z = 0$

$$T(r, 0) = T_{air}(0) \quad (47)$$

### Equations in cylindrical coordinates

We write the equations in cylindrical coordinates, neglecting  $\partial_\theta$  due to axisymmetry, and with

$$\nabla = \mathbf{e}_r \partial_r + \mathbf{e}_z \partial_z \quad (48)$$

- Constitutive equation for the Newtonian liquid and relation with pressure (from equations (33) and (35)):

$$\sigma_{rr} = 2\eta \partial_r u - p \quad (49)$$

$$\sigma_{\theta\theta} = \frac{2\eta u}{r} - p \quad (50)$$

$$\sigma_{zz} = 2\eta \partial_z v - p \quad (51)$$

$$\sigma_{rz} = \eta (\partial_r v + \partial_z u) \quad (52)$$

- Continuity equation (39):

$$\frac{1}{r} \partial_r (ru) + \partial_z v = 0 \quad (53)$$

- Momentum equations (40):

$$\frac{1}{r} \partial_r (r\sigma_{rr}) + \partial_z \sigma_{rz} - \frac{\sigma_{\theta\theta}}{r} = 0 \quad (54)$$

$$\frac{1}{r} \partial_r (r\sigma_{rz}) + \partial_z \sigma_{zz} = 0 \quad (55)$$

- Stress boundary conditions (42) and (43):

$$\sigma_{rr}(R) = R' \sigma_{rz}(R) \quad (56)$$

$$\sigma_{rz}(R) = R' \sigma_{zz}(R) \quad (57)$$

- Energy equation (45):

$$\rho c_p (u \partial_r T + v \partial_z T) = k \left( \frac{1}{r} \partial_r (r \partial_r T) + \partial_{zz} T \right) \quad (58)$$

- Heat transfer boundary condition (46):

$$-k \frac{1}{\sqrt{1+R'^2}} (\partial_r T|_R - R' \partial_z T|_R) = h (T(R) - T_{air}(z)) \quad (59)$$

#### 4.1.2 Slender fiber approximation and expansion

##### Fiber parameter $\alpha$ and expansion with orders of $\alpha^2$

In order to go further with the analytical resolution, we introduce the ratio  $\alpha = R_0/L$ , referred to as the fiber parameter, as in previous work on fiber spinning and film casting [96], [100], [101]. To simplify the equations, the slender fiber approximation [96], [102] then consists of an expansion of the variables in the small parameter  $\alpha^2$ , which is about  $10^{-3}$  with an initial radius  $R_0$  of 12.5 mm and a domain length  $L$  of 400 mm.

The parameter  $\alpha^2$  is used to expand the variables  $v, \sigma, p, \eta$  and  $T$  in the following form, with the superscript indicating the order of expansion:

$$f(r, z) = \sum_{i=0}^{\infty} (\alpha^2)^i f^{(i)}(r, z) = f^{(0)}(r, z) + \alpha^2 f^{(1)}(r, z) + \mathcal{O}(\alpha^4) \quad (60)$$

##### Dimensionless variables and equations

We make the variables and equations dimensionless with the following transformations:

$$\begin{aligned} r &\rightarrow R_0 r = \alpha L r, & z &\rightarrow L z, & u &\rightarrow \alpha v_0 u, & v &\rightarrow v_0 v, \\ \eta &\rightarrow \eta_{min} \eta, & \sigma &\rightarrow \eta_{min} \frac{v_0}{L} \sigma, & p &\rightarrow \eta_{min} \frac{v_0}{L} p, & T &\rightarrow T_{max} T \end{aligned} \quad (61)$$

The region considered is then from  $z = 0$  to  $z = 1$ , and the boundary conditions for  $R, u$  and  $v$  become:

$$R(0) = 1 \quad (62)$$

$$R(1) = \frac{1}{Dr} \quad (63)$$

$$u(0, z) = 0 \quad (64)$$

$$\langle v \rangle(0) = 1 \quad (65)$$

$$\langle v \rangle(1) = Dr^2 \quad (66)$$

The equations (47), (49), (50), (51) and (53) remain unchanged in dimensionless form, while the equations (34), (36), (52), (54), (55), (56), (57), (58) and (59) become, introducing  $\sigma_{rz}^* = \alpha \sigma_{rz}$  as in [96]:

$$\eta_{polymer}(T) = \exp \left[ -\frac{E_a}{RT_{max}} \left( \frac{1}{T} - 1 \right) \right] \quad (67)$$

$$T_{air}(r, z) = \frac{\Lambda \exp \left( -\frac{(z - 0.5)^2}{\Delta^2} \right) + 1}{\Lambda + 1} \quad (68)$$

$$\sigma_{rz}^* = \eta^{(0)}(\partial_r v + \alpha^2 \partial_z u) \quad (69)$$

$$\frac{1}{r} \partial_r (r \sigma_{rr}) + \partial_z \sigma_{rz}^* - \frac{\sigma_{\theta\theta}}{r} = 0 \quad (70)$$

$$\frac{1}{r} \partial_r (r \sigma_{rz}^*) + \alpha^2 \partial_z \sigma_{zz} = 0 \quad (71)$$

$$\sigma_{rr}(R) = R' \sigma_{rz}^*(R) \quad (72)$$

$$\sigma_{rz}^*(R) = \alpha^2 R' \sigma_{zz}(R) \quad (73)$$

$$\alpha Pe (u \partial_r T + v \partial_z T) = \frac{1}{r} \partial_r (r \partial_r T) + \alpha^2 \partial_{zz} T \quad (74)$$

with  $Pe = \rho c_p v_0 R_0 / k$  the Peclet number, which compares heat transfer by advection to thermal conduction.

$$-\frac{1}{\sqrt{1 + \alpha^2 R'^2}} (\partial_r T|_R - \alpha^2 R' \partial_z T|_R) = Bi (T(R, z) - T_{air}(z)) \quad (75)$$

with  $Bi = hR_0/k$  the Biot number, which compares the heat exchange between the material and the surrounding air to the heat conduction within the fiber.

### Cross-sectional average

The cross-sectional average  $\langle f \rangle(z)$  of a variable  $f(r, z)$  is

$$\langle f \rangle(z) = \frac{1}{\pi R(z)^2} \int_0^{R(z)} 2\pi r f(r, z) dr \quad (76)$$

As in [23], integrating the axial component of the momentum equation (71) multiplied by  $r$  over the entire radius gives a result that will be useful in the resolution of the model. We take  $\int_0^R r(71)dr$ :

$$\int_0^R \partial_r (r \sigma_{rz}^*) dr + \alpha^2 \int_0^R r \partial_z \sigma_{zz} dr = 0 \quad (77)$$

The first part is, using equation (73):

$$\int_0^R \partial_r (r \sigma_{rz}^*) dr = [r \sigma_{rz}^*]_0^R = R \sigma_{rz}^*(R) = \alpha^2 R R' \sigma_{zz}(R) \quad (78)$$

And the second part is, using the Leibniz integration rule,

$$\alpha^2 \int_0^R r \partial_z \sigma_{zz} dr = \alpha^2 \partial_z \int_0^R r \sigma_{zz} dr - \alpha^2 R R' \sigma_{zz}(R) = \alpha^2 \partial_z \left( \frac{R^2}{2} \langle \sigma_{zz} \rangle \right) - \alpha^2 R R' \sigma_{zz}(R) \quad (79)$$

This gives together:

$$\partial_z (R^2 \langle \sigma_{zz} \rangle) = 0 \quad (80)$$

This corresponds to the fact that the tension in the preform-to-fiber is the same at any axial position.

### Equations at the leading order

At the leading order, the equations (49), (50), (51), (53), (62) to (67), (70), (72) and (80) are not modified, except that the variables  $f(r, z)$  are replaced with  $f^{(0)}(r, z)$ . However, the equations (69), (71), (73), (74) and (75) are simplified and become:

$$\sigma_{rz}^{*(0)} = \eta^{(0)} \partial_r v^{(0)} \quad (81)$$

$$\partial_r (r \sigma_{rz}^{*(0)}) = 0 \quad (82)$$

$$\sigma_{rz}^{*(0)}(R) = 0 \quad (83)$$

$$\alpha Pe (u^{(0)} \partial_r T^{(0)} + v^{(0)} \partial_z T^{(0)}) = \frac{1}{r} \partial_r (r \partial_r T^{(0)}) \quad (84)$$

$$-\partial_r T^{(0)}|_R = Bi (T^{(0)}(R, z) - T_{air}(z)) \quad (85)$$

### Velocity field at the leading order

Using equations (82) and (83), we obtain  $\sigma_{rz}^{*(0)}(r, z) = 0$ . Then from equation (81), we have

$$\partial_r v^{(0)} = 0 \quad (86)$$

This means that the flow is extensional, and we cannot obtain information about the radial dependency of the axial velocity at the leading order.

Since this corresponds the approximation utilized in [23], the resolution can be done in the same way. From the continuity equation (53) integrated over  $r$  and using  $u^{(0)}(0, z) = 0$  (equation (64)), we obtain

$$u^{(0)}(r, z) = -\frac{r}{2} v^{(0)'}(z) \quad (87)$$

Then, from equations (49) and (50):

$$\sigma_{rr}^{(0)} = \sigma_{\theta\theta}^{(0)} = -\eta^{(0)} v^{(0)'} - p^{(0)} \quad (88)$$

Equation (70) gives  $\sigma_{rr}^{(0)} + r \partial_r (\sigma_{rr}^{(0)}) - \sigma_{rr}^{(0)} = 0$  so  $\partial_r (\sigma_{rr}^{(0)}) = 0$ . Then, using equation (72) and (83) we have

$$\sigma_{rr}^{(0)} = \sigma_{\theta\theta}^{(0)} = 0 \quad (89)$$

and

$$p^{(0)} = -\eta^{(0)} v^{(0)'} \quad (90)$$

We also have  $\sigma_{zz} = 2\eta\partial_z v - p$  (equation (51)), which leads to

$$\sigma_{zz}^{(0)} = 3\eta^{(0)}v^{(0)'} \quad (91)$$

Then, we calculate

$$\begin{aligned} (R^2v^{(0)})' &= R^{2'}v^{(0)} + R^2v^{(0)'} \\ &= 2RR'v^{(0)} + R^2v^{(0)'} \\ &= 2R\frac{u^{(0)}(R,z)}{v^{(0)}(R,z)}v^{(0)} + R^2v^{(0)'} \end{aligned}$$

Using equation (87), we have

$$(R^2v^{(0)})' = 0 \quad (92)$$

From the boundary conditions for  $R$  and  $v^{(0)}$ , we have for any  $z$ :

$$R(z) = \sqrt{\frac{1}{v^{(0)}(z)}} \quad (93)$$

From the results in equations (80), (91) and (93) we obtain

$$\partial_z \left( \langle \eta^{(0)} \rangle \frac{v^{(0)'}}{v^{(0)}} \right) = 0 \quad (94)$$

An integration between 0 and  $z$  and the boundary conditions for  $v^{(0)}$  gives

$$v^{(0)}(z) = \exp \left( \frac{\int_0^z \frac{dz}{\langle \eta^{(0)} \rangle(z)} \ln Dr^2}{\int_0^1 \frac{dz}{\langle \eta^{(0)} \rangle(z)}} \right) \quad (95)$$

This result was obtained in [23] and means that the knowledge of  $\langle \eta^{(0)} \rangle(z)$  enables to calculate the velocity field at the leading order since  $u^{(0)}$  can be calculated directly from  $v^{(0)}$  (equation (87)).

### Temperature field at the leading order

We have a partial differential equation for  $T^{(0)}(r, z)$  and a differential equation over the variable  $z$  for the boundary condition at the surface  $r = R(z)$  in equations (84) and (85). To simplify the resolution to a single differential equation over  $z$ , we assume a parabolic profile for  $T^{(0)}$  in the radial direction, analogue to the way Scheid et al. [100] included non-isothermal effects in one-dimensional film casting. It reads, with averaged temperature  $\langle T^{(0)} \rangle$  and fulfilling the boundary condition (85),

$$T^{(0)}(r, z) = \langle T^{(0)} \rangle(z) + Bi \frac{(\langle T^{(0)} \rangle(z) - T_{air}(z)) R(z)}{4 + Bi R(z)} \left( 1 - 2 \frac{r^2}{R(z)^2} \right) \quad (96)$$

The thermal energy equation (84) then becomes, using equation (87) and performing an integration between  $r = 0$  and  $R(z)$ ,

$$v^{(0)}(z)\langle T^{(0)} \rangle'(z) = -St \frac{\langle T^{(0)} \rangle(z) - T_{air}(z)}{R(z) (1 + Bi R(z)/4)} \quad (97)$$

with  $St = 2 Bi / (\alpha Pe)$  the Stanton number, which compares the heat transfer between the fiber and the surrounding air to the heat advected by the polymer flow.

This is a differential equation over  $z$  only. Knowing  $v^{(0)}(z)$ , therefore  $R(z)$  through equation (93), we can calculate  $T^{(0)}(r, z)$  by solving it.

### Velocity field at the first order

We now include the first order in  $\alpha^2$  and write the variables as follows, knowing that  $\partial_r v^{(0)} = 0$  and  $\sigma_{rz}^{*(0)} = 0$ :

$$\begin{aligned} v(r, z) &= v^{(0)}(z) + \alpha^2 v^{(1)}(r, z) \\ u(r, z) &= u^{(0)}(r, z) + \alpha^2 u^{(1)}(r, z) \\ \sigma_{rz}^*(r, z) &= \alpha^2 \sigma_{rz}^{*(1)}(r, z) \end{aligned} \quad (98)$$

The continuity equation (53) is verified by the first order variables:

$$\frac{1}{r} \partial_r (r u^{(1)}) + \partial_z v^{(1)} = 0 \quad (99)$$

Equation (69) becomes

$$\sigma_{rz}^{*(1)} = \eta^{(0)} (\partial_r v^{(1)} + \partial_z u^{(0)}) \quad (100)$$

and the  $z$ -component of the momentum equation (71) is

$$\frac{1}{r} \partial_r (r \sigma_{rz}^{*(1)}) + \partial_z \sigma_{zz}^{(0)} = 0 \quad (101)$$

Replacing the expressions of  $u^{(0)}$  (equation (87)),  $\sigma_{rz}^{*(1)}$  (equation (100)) and  $\sigma_{zz}^{(0)}$  (equation (91)), equation (101) becomes

$$\frac{1}{r} \partial_r \left( r \eta^{(0)} \left( \partial_r v^{(1)} - \frac{r}{2} v^{(0)''} \right) \right) + \partial_z (3 \eta^{(0)} v^{(0)'}) = 0 \quad (102)$$

We then perform successive integrations to calculate  $v^{(1)}(r, z)$ .

Integrating a first time  $(\int_0^r r(102) dr)$ :

$$r \eta^{(0)} \left( \partial_r v^{(1)} - \frac{r}{2} v^{(0)''} \right) + \int_0^r r \partial_z (3 \eta^{(0)} v^{(0)'}) dr = 0 \quad (103)$$

We isolate  $v^{(1)}$ :

$$\partial_r v^{(1)} = \frac{r}{2} v^{(0)''} - \frac{1}{r\eta^{(0)}} \int_0^r r \partial_z (3\eta^{(0)} v^{(0)'}) dr \quad (104)$$

Integrating a second time ( $\int_0^r \dots dr$ ):

$$v^{(1)}(r, z) - v^{(1)}(0, z) = \frac{r^2}{4} v^{(0)''} - \int_0^r \left( \frac{1}{r\eta^{(0)}} \int_0^r r \partial_z (3\eta^{(0)} v^{(0)'}) dr \right) dr \quad (105)$$

Integrating a third time ( $\int_0^R r \dots dr$ ) to obtain  $v^{(1)}(0, z)$ :

$$\int_0^R r v^{(1)}(r, z) dr - \frac{R^2}{2} v^{(1)}(0, z) = \frac{R^4}{16} v^{(0)''} - \int_0^R r \left( \int_0^r \left( \frac{1}{r\eta^{(0)}} \int_0^r r \partial_z (3\eta^{(0)} v^{(0)'}) dr \right) dr \right) dr \quad (106)$$

To solve this equation, we require the condition

$$\langle v^{(1)} \rangle(z) = 0, \quad (107)$$

so as to preserve the fact that at the leading order,  $v^{(0)}(z)$  is equal to the averaged velocity  $\langle v \rangle(z)$ . Since  $\langle v \rangle(z) = v^{(0)}(z) + \alpha^2 \langle v^{(1)} \rangle(z)$ , assuming  $v^{(0)}(z) = \langle v \rangle(z)$  then means  $\langle v^{(1)} \rangle(z) = 0$ .

We then have:

$$v^{(1)}(0, z) = -\frac{R^2}{8} v^{(0)''} + \frac{2}{R^2} \int_0^R r \left( \int_0^r \left( \frac{1}{r\eta^{(0)}} \int_0^r r \partial_z (3\eta^{(0)} v^{(0)'}) dr \right) dr \right) dr \quad (108)$$

And

$$v^{(1)}(r, z) = v^{(1)}(0, z) + \frac{r^2}{4} v^{(0)''} - \int_0^r \left( \frac{1}{r\eta^{(0)}} \int_0^r r \partial_z (3\eta^{(0)} v^{(0)'}) dr \right) dr \quad (109)$$

Then from integrating the continuity equation (99) and using  $u^{(1)}(0, z) = 0$ ,

$$u^{(1)}(r, z) = -\frac{1}{r} \int_0^r r \partial_z v^{(1)} dr \quad (110)$$

This means that knowing  $v^{(0)}(z)$  and  $T^{(0)}(r, z)$ , which is linked with  $\eta^{(0)}(r, z)$  through equation (67), we can calculate the velocity field at the first order.

### 4.1.3 Iterative and simultaneous implementations

#### (a) Iterative computing

The software Mathematica was employed as a tool to develop and test the different elements of the model that we present here. Using it, we did not manage to solve the partial differential equations for the velocity and temperature fields together, which was a drive to derive equations that can be solved successively. The relationships obtained here enable to implement an iterative computing of the velocity and temperature fields which does not require several differential equations to be solved simultaneously.

The iterative resolution is realized as follows:

- (1) We first assume that the average viscosity is given by  $\langle \eta^{(0)} \rangle(z) = \eta_{polymer}(T_{air}(z))$  using equations (67) and (68). From equations (95), (87) and (93) we can then calculate  $v^{(0)}(z)$ ,  $u^{(0)}(r, z)$  and  $R(z)$  without the knowledge of the radial dependency of the viscosity. The temperature and viscosity fields are unknown, and the thermal energy equation is not necessarily respected, but the result serves as a first guess for the velocity field at the leading order.
- (2) The previously calculated velocity field at the leading order is used to solve the differential equation (97) for  $\langle T^{(0)} \rangle(z)$ . The temperature field  $T^{(0)}(r, z)$  is then known from equation (96), with a radial profile assumed parabolic.
- (3) From the previously computed velocity and temperature fields at the leading order and with  $\eta^{(0)}(r, z) = \eta_{polymer}(T^{(0)}(r, z))$  (equation (67)), we calculate  $\langle \eta^{(0)} \rangle(z)$ .
- (4) We obtain  $v^{(0)}(z)$ ,  $u^{(0)}(r, z)$  and  $R(z)$  from  $\langle \eta^{(0)} \rangle(z)$  as in step 1.
- (5) Finally, the velocity field at the first order is computed using equation (109) for  $v^{(1)}(r, z)$ , then equation (110) for  $u^{(1)}(r, z)$ .

After initiating the computation with the first step, the second, third and fourth steps can be repeated successively. Note that the velocity field at the first order (step 5) is not required to be computed to perform the next iteration, but is interesting to examine after each iteration to see how the result evolves between iterations.

Although the governing equations are not verified simultaneously, we observe that the successive iterations quickly converge, as will be shown in the next section.

**(b) Simultaneous computing**

A more rigorous implementation of the model in which the governing equations are verified simultaneously was realized by Dr. Mathias Bechert.

For the cross-section averaged model, equations (92), (94) and (97) coupled with equation (67) are solved by numerical continuation using AUTO97 [103] to obtain  $v^{(0)}(z)$ ,  $u^{(0)}(r, z)$  (through equation (87)),  $R(z)$ ,  $\langle T^{(0)} \rangle(z)$  and  $\langle \eta^{(0)} \rangle(z)$ .

Using these solutions, the radially varying  $T^{(0)}(r, z)$  and  $\eta^{(0)}(r, z)$  are calculated as in the steps (2) and (3) of the iterative resolution.

The  $\alpha^2$ -order of the expanded governing equations (102) and (99) are then solved by numerical integration to obtain  $v^{(1)}(r, z)$  and  $u^{(1)}(r, z)$ .

#### 4.1.4 Analytical solution for the velocity field at the first order

When developing the model, we found that a particular assumption for the viscosity profile enables to obtain an analytical solution for the velocity field at the first order in  $\alpha^2$ . We suppose that the viscosity field is

$$\eta^{(0)}(r, z) = \langle \eta^{(0)} \rangle(z) \sum_{i=0}^{\infty} a_i \left( \frac{r}{R(z)} \right)^i \quad (111)$$

with  $a_i$  independent of  $z$  and normalized to respect the definition of  $\langle \eta^{(0)} \rangle(z)$  (equation (76)). This means that the radial profile has a fixed shape along  $z$  that scales with  $R(z)$ , which is restrictive and does not match the results showed in the next section but leads to an analytical solution.

The shape defined by  $\sum_{i=0}^{\infty} a_i \left( \frac{r}{R(z)} \right)^i$  is a more general function compared to a simple parabolic profile, which would simply be:

$$\eta^{(0)}(r, z) = \langle \eta^{(0)} \rangle(z) \frac{2}{2+A} \left( 1 + A \left( \frac{r}{R(z)} \right)^2 \right) \quad (112)$$

We then calculate  $\partial_r \eta^{(0)}$  and  $\partial_z \eta^{(0)}$  and, using equations (93) and (94), we obtain the following relationship:

$$\partial_z \eta^{(0)} = \left( \frac{v^{(0)'}}{v^{(0)}} - \frac{v^{(0)''}}{v^{(0)'}} \right) \eta^{(0)}(r, z) + \frac{r v^{(0)'}}{2 v^{(0)}} \partial_r \eta^{(0)} \quad (113)$$

The equation (104) for  $\partial_r v^{(1)}$  then simplifies, using an integration by parts, to

$$\partial_r v^{(1)} = \frac{r}{2} \left( v^{(0)''} - 3 \frac{v^{(0)'}^2}{v^{(0)}} \right) \quad (114)$$

Then, by performing integrations over  $r$  as in 4.1.2 we have

$$v^{(1)}(r, z) = \left( \frac{r^2}{4} - \frac{1}{8v^{(0)}} \right) \left( v^{(0)''} - 3 \frac{v^{(0)'}^2}{v^{(0)}} \right) \quad (115)$$

and

$$u^{(1)}(r, z) = \frac{r}{16v^{(0)}} \left( 6 \frac{v^{(0)'}^3}{v^{(0)^2} } - 7 \frac{v^{(0)'} v^{(0)''}}{v^{(0)}} + v^{(0)'''} \right) + \frac{r^3}{16} \left( -3 \frac{v^{(0)'}^3}{v^{(0)^2} } + 6 \frac{v^{(0)'} v^{(0)''}}{v^{(0)}} - v^{(0)'''} \right) \quad (116)$$

In this solution,  $v^{(1)}(r, z)$  depends on  $\langle \eta^{(0)} \rangle(z)$  through  $v^{(0)}(z)$  with equation (95), but not on  $\eta^{(0)}(r, z)$  as it is independent of  $a_i$  or  $A$ . This is true only because we have restricted the radial profile of  $\eta(r, z)$  to be fixed along  $z$ , which enables to obtain this analytical solution but does not comply with the energy equation. A particular case of the assumption of equation (111) is  $\eta^{(0)}(r, z) = \langle \eta^{(0)} \rangle(z)$ , so this result is the solution if we assume a viscosity that is independent of radius.

## 4.2 Results of the model

### 4.2.1 Parameter determination

As mentioned in the presentation of the model, the effective heat transfer coefficient  $h$  and the effective air temperature profile parameters  $\Lambda$ ,  $\Delta$  and  $T_{max}$ , which cover both convection and radiation, are determined by fitting the predicted fiber radius profile to the experimental observation. The experimental profiles are obtained from the interrupted draws of polysulfone and polycarbonate fibers shown in Figure 42. As the fibers fabricated have a rectangular cross-section, we use both the dimensionless width and thickness profiles for fitting. Both profiles exhibit a very similar dimensionless form, which comforts the use of an axisymmetric model.

In addition to that, we make sure that the experimentally measurable tension when drawing the fiber and the theoretical prediction have comparable values, which enables to estimate the temperature distribution in the fiber. Note that by shifting the temperature profile and thus the value of  $\eta_{min}$ , the model can lead to the same results in terms of radius profile and velocity field, regardless of the value of tension. This emphasizes the robustness of the thermal drawing process, which is compatible with a large range of temperature profiles, the boundaries being determined by the emergence of troublesome mechanisms such as fiber breakage, reflow or capillary breakup.

An example of such a fit is shown for polysulfone in Figure 63, and the parameters determined for both cladding materials are given in Table 5.

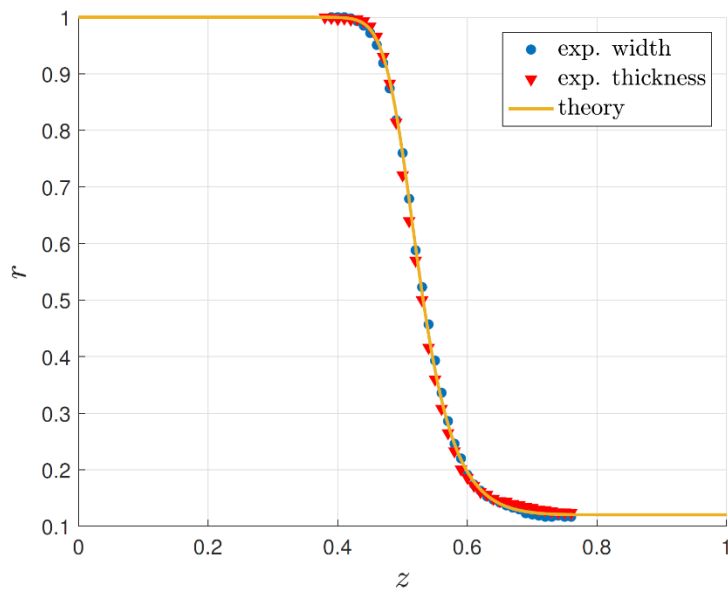


Figure 63. Fit of predicted dimensionless fiber radius profile to the experimentally determined fiber width and thickness profiles for a polysulfone fiber. The result of the implementation with simultaneous computing of the cross-section averaged model, as in 4.1.3(b), is used here. The draw ratio is  $Dr = 8.31$ , the parameters obtained from the fit are  $\Lambda = 0.5$ ,  $\Delta = 0.22$ ,  $h = 20 \text{ W}/(\text{m}^2 \cdot \text{K})$  and  $T_{max} = 225.7 \text{ }^\circ\text{C}$  and the computed tension is 388.9 grams.

## 4.2.2 Deformation of initially straight lines

To demonstrate the importance of taking into account the first order of the velocity field, we calculate the evolution of initially straight lines perpendicular to the drawing direction during the drawing process.

Figure 64 (a) shows the line shape at several axial positions along the fiber within the domain of deformation. If only the cross-section averaged model is considered (black dashed lines), an initially straight line remains straight during the entire process, which is not surprising as the leading order axial velocity does not vary along the radius. However, if the higher order terms  $u^{(1)}$  and  $v^{(1)}$  are included in the calculation (red lines), the lines clearly deform during the drawing, finally looking like an inverted 'V'.

This corresponds to the behavior observed in the experiment, as shown Figure 64 (b). The figure shows the drawing of a PSu preform within which 1 mm-wide sheets of carbon black-loaded polycarbonate are equidistantly placed, perpendicular to the drawing direction. The drawing of this preform was interrupted so that the sheets visualize the deformation of initially straight, horizontal material lines during drawing. The calculated (red) lines coincide very well with the observed shape of the sheets in the PSu fiber. Note that this comparison is nevertheless of some qualitative nature, as the fiber used in the experiment has a rectangular cross-section, while the theoretical model assumes a circular fiber.

Physically, the non-uniform propagation of fluid elements lying on an initially straight line is the result of an interplay between a radially varying viscosity, shown in Figure 64 (c), and the deformation of the fiber due to drawing. In fact, our parametric studies indicated that besides varying  $h$  and by that varying the amplitude of the radial temperature distribution, the fiber radius profile has a strong influence on the deformation of the material lines during drawing. In particular, both increasing  $h$  and the gradient of air temperature, the latter leading to a narrower fiber deformation region, amplify the deformation of material lines.

It is worth mentioning that the significant influence of the higher order velocity terms is a cumulative effect. At one particular position in  $z$ , the change in velocity introduced by the higher order is at most only a few percent. This is expected, as the contribution is scaled by  $\alpha^2$  according to equation (60), with  $\alpha^2$  being small at the basis of the expansion. By following a material point during the drawing, however, we integrate along the fiber length, and by that the order of magnitude increases from  $\alpha^2 = (R_0/L)^2$  to  $R_0^2/L$ . For this reason, the widely used cross-section averaged model is well-suited if one is interested exclusively in the fiber radius and the averaged velocity field, as it is the case for single-material fibers, but insufficient if radially distributed properties come into play, like for multi-material fibers.

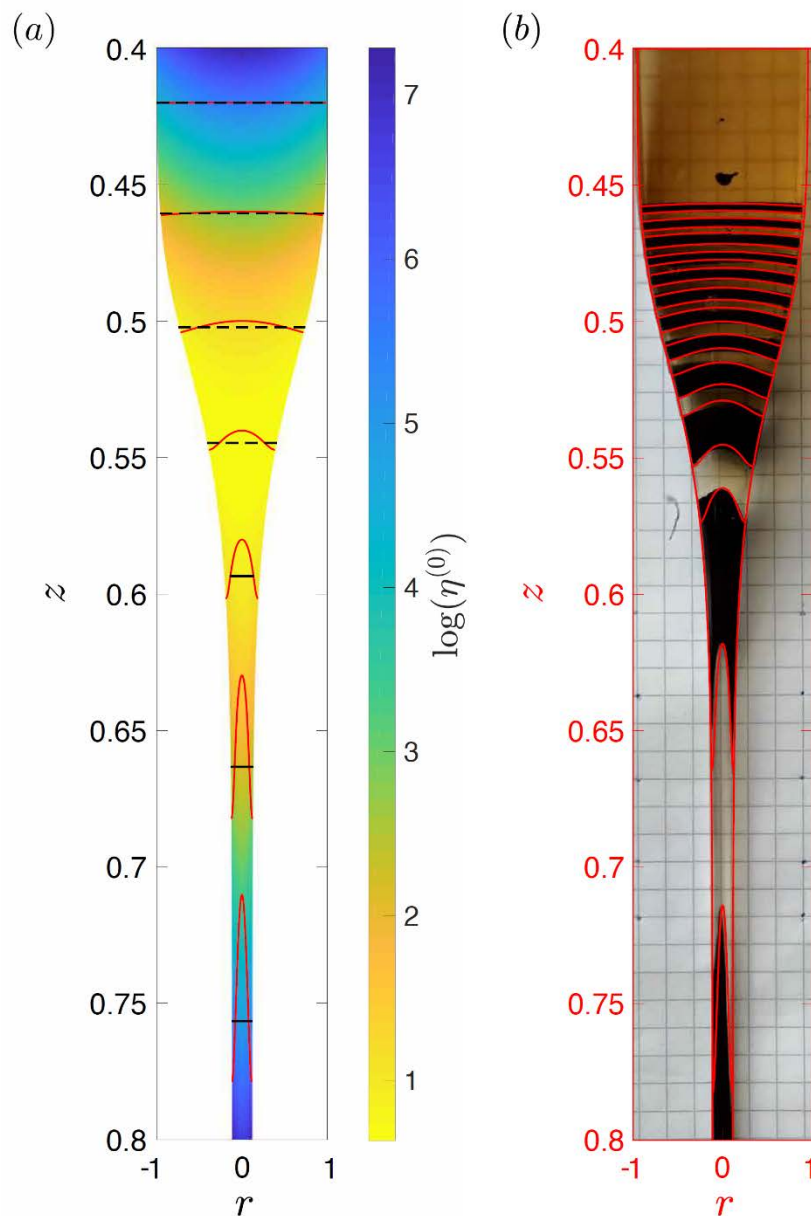


Figure 64. Effect of higher order terms on the evolution of initially straight material lines during the drawing process. The result of the implementation with simultaneous computing of the model, as in 4.1.3(b), is shown here. (a) The black dashed lines are calculated with the cross-section averaged model, while the red lines result from the full model. The color map shows the logarithm of the dimensionless viscosity in the material. (b) Comparison of theoretical prediction (red lines) with experimental observation (picture) for a PSu fiber.

Figure 65 shows the result obtained for polycarbonate, in the same way as Figure 64(b) for polysulfone. We have not found parameters that lead to a result that coincides quantitatively both in terms of radial profile and deformation of the material lines as well as with polysulfone, but there is still a qualitative coincidence. The reason may be that the material properties used do not correspond to the polycarbonate grade employed.

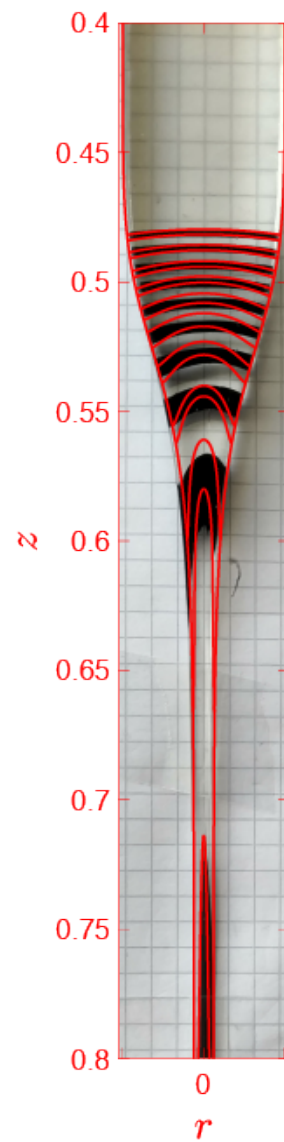


Figure 65. Comparison of theoretical prediction including the higher order terms (red lines) with experimental observation (picture) for a PC fiber. The result of the implementation with simultaneous computing of the cross-section averaged model, as in 4.1.3(b), is shown here.

### 4.2.3 Comparison of the two implementations

We verify here that the two implementations described in 4.1.3 give the same results when using identical parameters, for a polysulfone fiber. For the iterative implementation, we first perform an initiating iteration (indicated with the subscript  $I$ ) with the step (1) only, then three iterations (indicated with the subscripts  $II$ ,  $III$  and  $IV$ ) of steps (2), (3), (4) and (5). The implementation with simultaneous solving of the equation is indicated with the subscript  $S$ .

We first show in Figure 66 the plots of  $r$ -averaged temperature  $\langle T^{(0)} \rangle$  and viscosity  $\langle \eta^{(0)} \rangle$  against  $z$ . For the initiating iteration  $I$ , the temperature is not computed and  $\langle \eta^{(0)} \rangle_I = \eta_{polymer}(T_{air}(z))$ . We also show the air temperature profile. In Figure 67 we show the radius  $R$  and leading order velocity  $v^{(0)}$ .

The result of the iterative implementation converges towards the result of the simultaneous one. While the initiating iteration is far from it, the second iteration is relatively close already and the fourth one almost coincides with the result of the simultaneous computing.

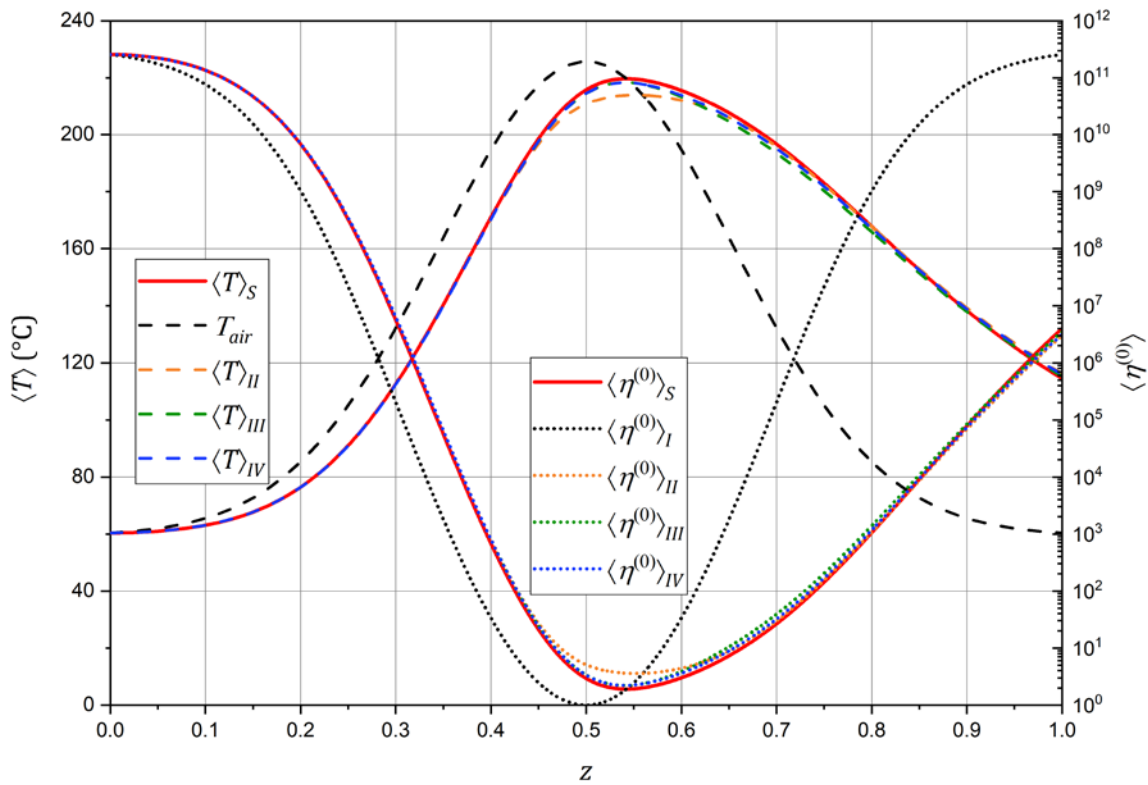


Figure 66. Dimensional  $r$ -averaged temperature  $\langle T^{(0)} \rangle$ , air temperature  $T_{air}$  and dimensionless  $r$ -averaged viscosity  $\langle \eta^{(0)} \rangle$  against axial coordinate  $z$ . The subscripts denote the iterative ( $I - IV$ ) and simultaneous implementations ( $S$ ).

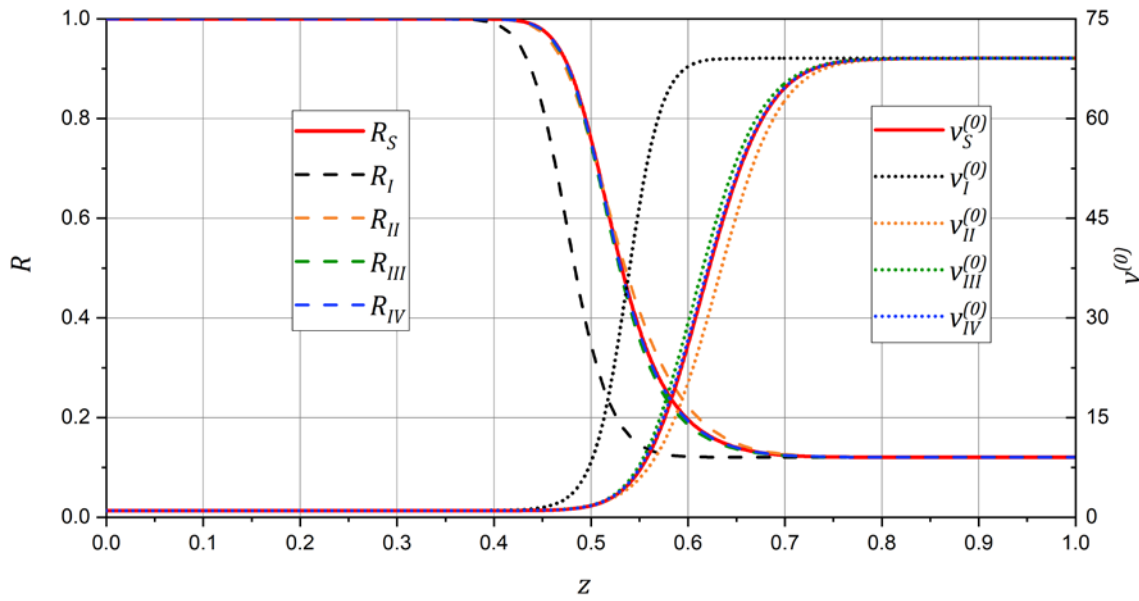


Figure 67. Dimensionless radius  $R$  and leading order velocity  $v^{(0)} = \langle v \rangle$  against axial coordinate  $z$ . The subscripts denote the iterative ( $I - IV$ ) and simultaneous implementations ( $S$ ).

While the maximum temperature  $T_{max}$  is almost reached by the material, justifying the choice of its value as reference, the material temperature exhibits a delayed reaction to the air temperature, which is especially visible in the cooling part ( $z > 0.5$ ). The delay is primarily determined by the Stanton number, which is  $St = 32$  here, as it compares the heat transfer between the fiber and the surrounding to the internal convection. A higher  $St$  thus means  $\langle T \rangle$  approaching  $T_{air}$  closer. Similar to the temperature, the viscosity does not reach its initial value at  $z = 1$ , but is six orders of magnitude higher than its lowest value. As can be seen in the velocity profile, the fiber deformation is already finished at an earlier position and almost all of the deformation occurs between  $z = 0.4$  and  $0.8$ .

We then show in Figure 68 the deformation of lines that are initially straight in the preform and perpendicular to the drawing direction, for the output of the different iterations ( $I - IV$ ). For the initiating iteration, we show the results of both the cross-section averaged model, in which the lines remain straight, and the analytical solution for the velocity field at the first order (Figure 68 (a)). This solution, presented in 4.1.4, is not physical since it does not comply with the energy equation. However, it is easier to compute and compared to the cross-section averaged model, it provides an additional information on deformation that goes towards the result of the full model in Figure 68 (b). In the latter, we observe that there is a significant evolution between iterations  $II$  and  $III$ , then iterations  $III$  and  $IV$  almost coincide. The result of iteration  $IV$  is so similar to that of the simultaneous implementation that the same qualitative comparison with experiment as in Figure 64 (b) can be done, hence we do not show further iterations.

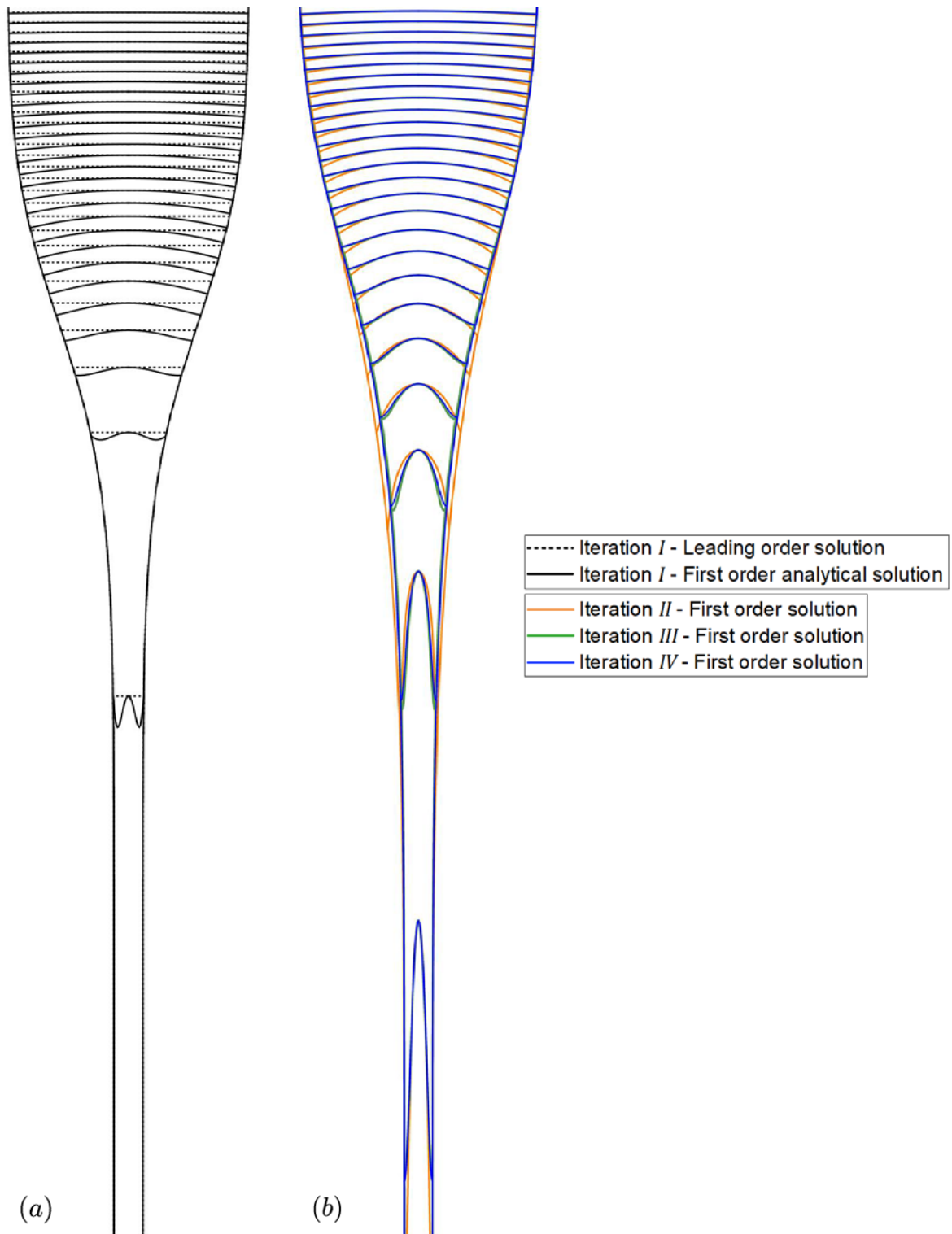


Figure 68. Evolution of initially straight material lines during the drawing process. The results of the implementation with iterative computing, as in 4.1.3(a), are shown here. (a) Initiating iteration *I*, with the leading order solution and the first order analytical solution presented in 4.1.4. (b) Full model including the first order of the velocity field, for iterations *II* to *IV*. Both graphs show regions of equal axial length, which are however shifted to compare them qualitatively: (a) From  $z = 0.39$  to  $0.71$ . (b) From  $z = 0.45$  to  $0.77$ .

#### 4.2.4 Velocity field and deformation rates

Various details on the thermal drawing process can be obtained from the output of the model. We present here some of them, from the result of iteration *IV*. Unlike the graphs shown previously, the following ones do not respect the scaling of the radial and axial axes so that the distributions can be clearly visible.

In Figure 69 we show the distribution of the axial velocity  $v(r, z)$  relative to the value in the center  $v(0, z)$ . While the viscosity exhibits significant changes along the radius over the entire drawing length, as can be seen in Figure 64 (c), the axial velocity varies only in a narrow range. Since the axial and radial velocities are directly linked through the continuity equation, this is also the case for the radial velocity  $u(r, z)$ .

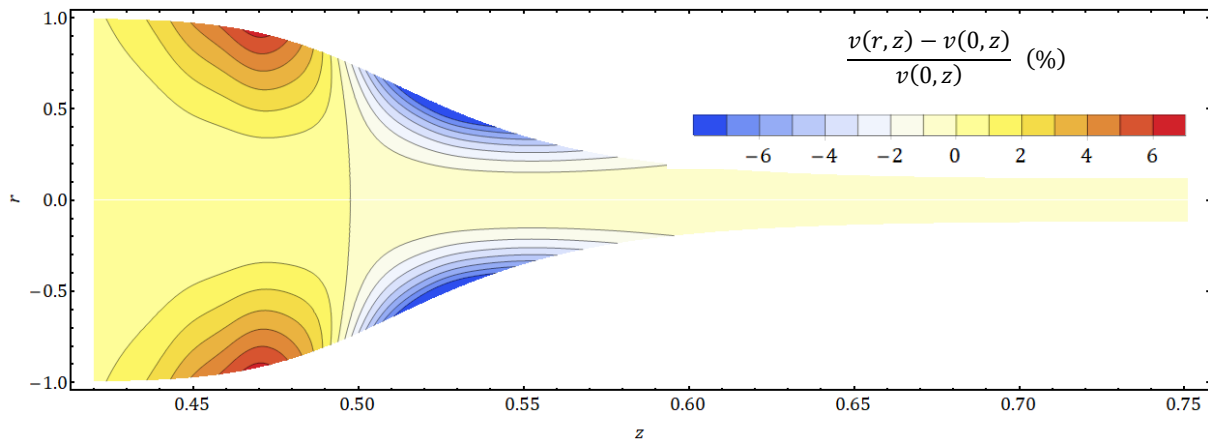


Figure 69. Distribution of the axial velocity relative to the value in the center ( $r = 0$ ), in percent.

Then, we show in Figure 70 the distribution of the strain rates along the  $z$  and  $r$  axes,  $\partial_z v$  and  $\partial_r u$ . As the velocities, the strain rates vary only in a narrow range along the radius. The dimensionless values are multiplied by  $v_0/L = 8.3 \times 10^{-5} \text{ s}^{-1}$  to obtain the dimensional ones. With the parameters employed here,  $\partial_z v$  is smaller than  $0.05 \text{ s}^{-1}$  while  $\partial_r u$  is smaller than  $0.03 \text{ s}^{-1}$  (in absolute value).

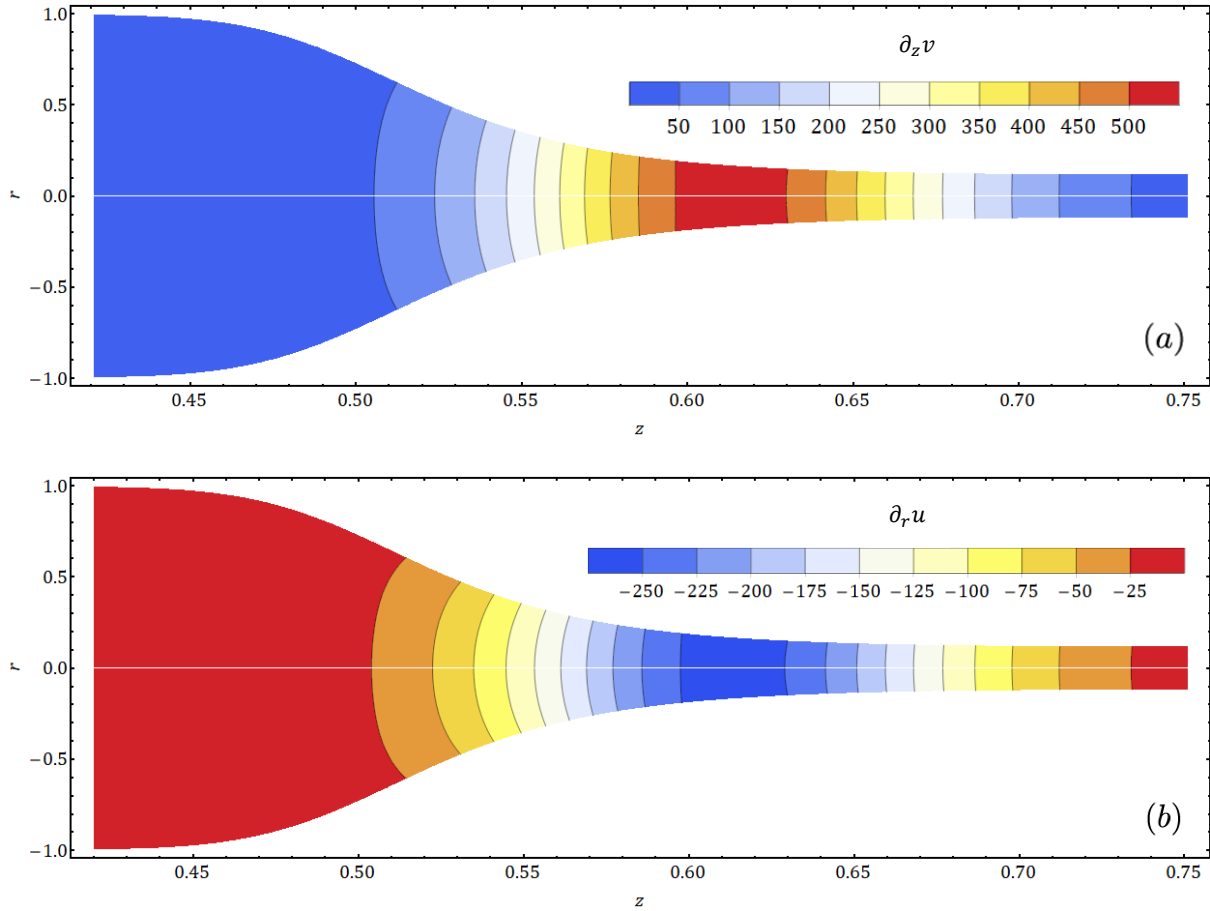


Figure 70. Dimensionless strain rates  $\partial_z v$  and  $\partial_r u$ . Their dimensional values scale with  $v_0/L = 8.3 \times 10^{-5} \text{ s}^{-1}$ .

Finally, we show in Figure 71 the distribution of the shear rate components  $\partial_r v$  and  $\partial_z u$ . Contrary to the velocities and strain rates, they vary significantly along the radius. The dimensionless values are multiplied by  $v_0/R_0 = 2.7 \times 10^{-3} \text{ s}^{-1}$  and  $R_0 v_0/L^2 = 2.6 \times 10^{-6} \text{ s}^{-1}$ , respectively, to obtain the dimensional ones. In this case,  $\partial_r v$  is smaller than  $0.01 \text{ s}^{-1}$  while  $\partial_z u$  is smaller than  $0.003 \text{ s}^{-1}$  (in absolute value).

The dimensional values of deformation rates computed are relatively small and comfort the assumption that the material can be considered Newtonian. With much higher drawing speeds, the deformation rates may be so high that non-Newtonian behaviors become significant.

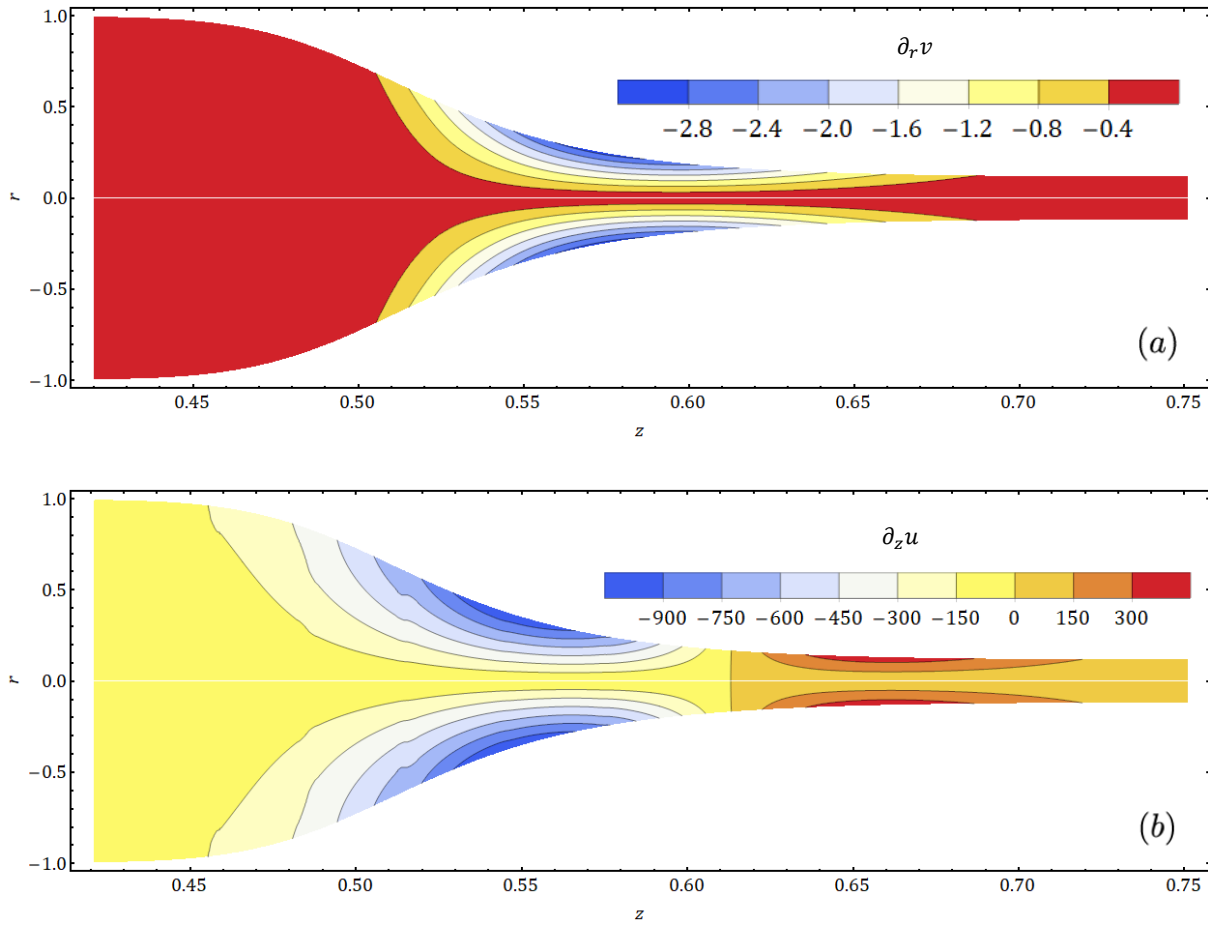


Figure 71. Dimensionless shear rate components  $\partial_r v$  and  $\partial_z u$ . Their dimensional values scale with  $v_0/R_0 = 2.7 \times 10^{-3} \text{ s}^{-1}$  and  $R_0 v_0/L^2 = 2.6 \times 10^{-6} \text{ s}^{-1}$ , respectively.

## 4.3 Modeling the conductivity of nanocomposites

In the following, we model the influence of thermal drawing on the conductivity of nanocomposites in order to account for the dependence on draw ratio and radial position observed experimentally in Chapter 3.

### 4.3.1 Presentation of the model

#### Kinetic equation

To account for the destruction of conductive pathways due to deformation during drawing, we propose to employ a modified version of the empirical kinetic equation shown in Chapter 2 (equation (26)), introduced by Saphiannikova et al. [24] for CNT nanocomposites under simple shear at a rate  $\dot{\gamma}$  (Figure 25). A similar loss of conductivity was observed for a CB nanocomposite under elongation (Figure 24) by Starý et al. [89], which suggests a comparable mechanism. Thus, we generalize the equation to any deformation by replacing the shear rate  $\dot{\gamma}$  with  $\sqrt{II_D}$ , the square root of the second scalar invariant of the rate-of-deformation tensor  $\mathbf{D}$ , which is independent of the choice of coordinate system and therefore physically significant. The kinetic equation is then

$$\partial_t p_e = -a \eta \sqrt{II_D}^m (p_e - p_c) \quad (117)$$

The parameter  $a$  denotes a breakage rate of the percolating network and analogue to Saphiannikova et al. [24], we set  $m = 1.5$ . The part of the equation with the parameter  $b$  is not used since it corresponds to conductivity recovery, which we did not observe.

In our model of thermal drawing, the rate-of-deformation tensor is

$$\mathbf{D} = \begin{pmatrix} \partial_r u & 0 & \frac{1}{2}(\partial_z u + \partial_r v) \\ 0 & \frac{u}{r} & 0 \\ \frac{1}{2}(\partial_z u + \partial_r v) & 0 & \partial_z v \end{pmatrix} \quad (118)$$

and the square root of its second invariant is

$$\sqrt{II_D} = \sqrt{(\partial_z u + \partial_r v)^2 + 2(\partial_r u)^2 + 2(u/r)^2 + 2(\partial_z v)^2} \quad (119)$$

Although Saphiannikova et al. employed the kinetic equation for constant shear rates, to apply it to a nanocomposite during thermal drawing we have to follow the trajectory of a material element subjected to a varying deformation. We assume that when incorporating a nanocomposite sheet, the velocity field is the same as with a single material fiber since the nanocomposite represents a small fraction of the cross-sectional area in the fibers fabricated. We also use the viscosity of the cladding material  $\eta$  in place of that of the nanocomposite. This is a rough approximation, but it is challenging to know the viscosity of a nanocomposite during thermal drawing due to its complex dependence on temperature and deformation history.

A simple percolation law links the effective filler concentration  $p_e$  to the conductivity  $\sigma$ :

$$\sigma(p_e) = \sigma_0 (p_e - p_c)^c \quad (120)$$

As in Saphiannikova et al., we consider the initial conductivity  $\sigma_{in}$  of the undeformed material as a parameter that can be adjusted in the fit. With  $\sigma_{in} = \sigma_0(p_{in} - p_c)^c$ ,  $p_{in}$  denoting the effective concentration in the preform, we then have

$$\sigma(p_e) = \sigma_{in} \left( \frac{p_e - p_c}{p_{in} - p_c} \right)^c \quad (121)$$

Since we employ only steady solutions, we substitute the time derivative with a spatial derivative in equation (117) to follow the trajectory of a material element during drawing:

$$\partial_z p_e = \partial_{tZ} \cdot \partial_t p_e = \frac{1}{v} \partial_t p_e \quad (122)$$

Therefore, the kinematic equation becomes:

$$\partial_z p_e = -a \frac{\eta}{v} \sqrt{II_D}^m (p_e - p_c) \quad (123)$$

### Dimensionless variables and equations

We make the variables and equations dimensionless with the following transformations:

$$\sigma \rightarrow \sigma_0 \sigma, \quad \sqrt{II_D} \rightarrow \frac{v_0}{L} \sqrt{II_D}, \quad a \rightarrow \frac{1}{\eta_{min}} \left( \frac{L}{v_0} \right)^{m-1} a \quad (124)$$

Equations (121) and (123) are unchanged, and  $\sqrt{II_D}$  becomes

$$\sqrt{II_D} = \sqrt{(\alpha \partial_z u + \partial_r v / \alpha)^2 + 2(\partial_r u)^2 + 2(u/r)^2 + 2(\partial_z v)^2} \quad (125)$$

In Figure 72 we show the distribution of  $\sqrt{II_D}$  for a polysulfone fiber with  $Dr = 8.31$ , from iteration *IV* as in the previous section. In this case, its value is smaller than  $0.1 \text{ s}^{-1}$ . Since the shear rate components are smaller than the strain rates,  $\sqrt{II_D}$  only varies slightly more than the strain rates along the radius.

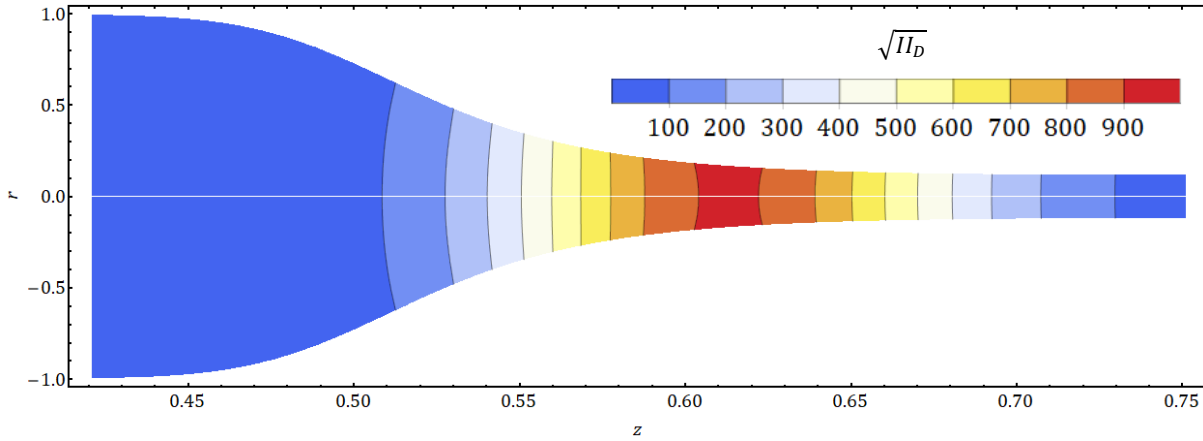


Figure 72. Dimensionless value of  $\sqrt{II_D}$ , the square root of the second scalar invariant of the rate-of-deformation tensor, for a polysulfone fiber with  $Dr = 8.31$  as in the previous section. The dimensional value scales with  $v_0/L$ , equal to  $8.3 \times 10^{-5} \text{ s}^{-1}$  in this case.

To remove the intermediate variable  $p_e$  of the resolution, we substitute the differential equation on  $p_e$  with an equation on  $\sigma$ . For this, we calculate  $\partial_z \sigma$ :

$$\partial_z \sigma = c \partial_z p_e \sigma_{in} \frac{(p_e - p_c)^{c-1}}{(p_{in} - p_c)^c} \quad (126)$$

We then obtain:

$$\partial_z \sigma = -a c \frac{\eta}{v} \sqrt{II_D}^m \sigma(p_e) \quad (127)$$

The trajectory of a material element during drawing identified by its final radial position  $r_f$  is denoted  $\gamma(r_f)$ . It can be parametrized using the axial position  $z$ , the radial position  $r$  being a function of  $z$  defined by the velocity field  $\mathbf{v}(r, z)$ . Integrating equation (127) then yields

$$\sigma(r_f) = \sigma_{in} \exp\left(-a c \int_{\gamma(r_f)} \frac{\eta}{v} \sqrt{II_D}^m dz\right) \quad (128)$$

for the final, post-drawing conductivity. Interestingly, the values of  $p_{in}$  and  $p_c$  do not appear in this result, which depends only on the initial conductivity  $\sigma_{in}$  and exponent  $c$  of the percolation law.

The radial distribution of conductivity in the drawn fiber  $\sigma(r_f)$  can be used to calculate the average conductivity perpendicular to the drawing direction between two electrodes at positions  $r_{min}$  and  $r_{max}$ :

$$\langle \sigma \rangle_{r_{min}, r_{max}} = \frac{r_{max} - r_{min}}{\int_{r_{min}}^{r_{max}} \frac{1}{\sigma(r_f)} dr_f} \quad (129)$$

### 4.3.2 Results of the model for conductivity

We show here that our model is able to account for the dependence on draw ratio and radial position of the conductivity of thermally drawn nanocomposites observed experimentally in Chapter 3. We compute the model of thermal drawing with the simultaneous implementation, using the parameters determined previously except the draw ratio, which is varied as for the fibers fabricated. The product  $a c$  and initial conductivity  $\sigma_{in}$  are determined by fitting the experimental data.

Figure 73 shows the conductivity of a PC/CNT composite in a PSu fiber as in Figure 53 (Fiber #1) for a large range of draw ratios and compares it to the theoretically determined averaged conductivity  $\langle\sigma\rangle$  (red line) between electrodes placed at  $r/R = \pm 0.6$ . The increasing deformation with increasing draw ratio leads to a change in conductivity over several orders of magnitude, which is well reproduced by our model. Also plotted is the theoretical prediction based on the cross-section averaged model (black dashed line). Both models lead to practically identical results, which is not surprising as we average the conductivity over a large part of the total fiber radius.

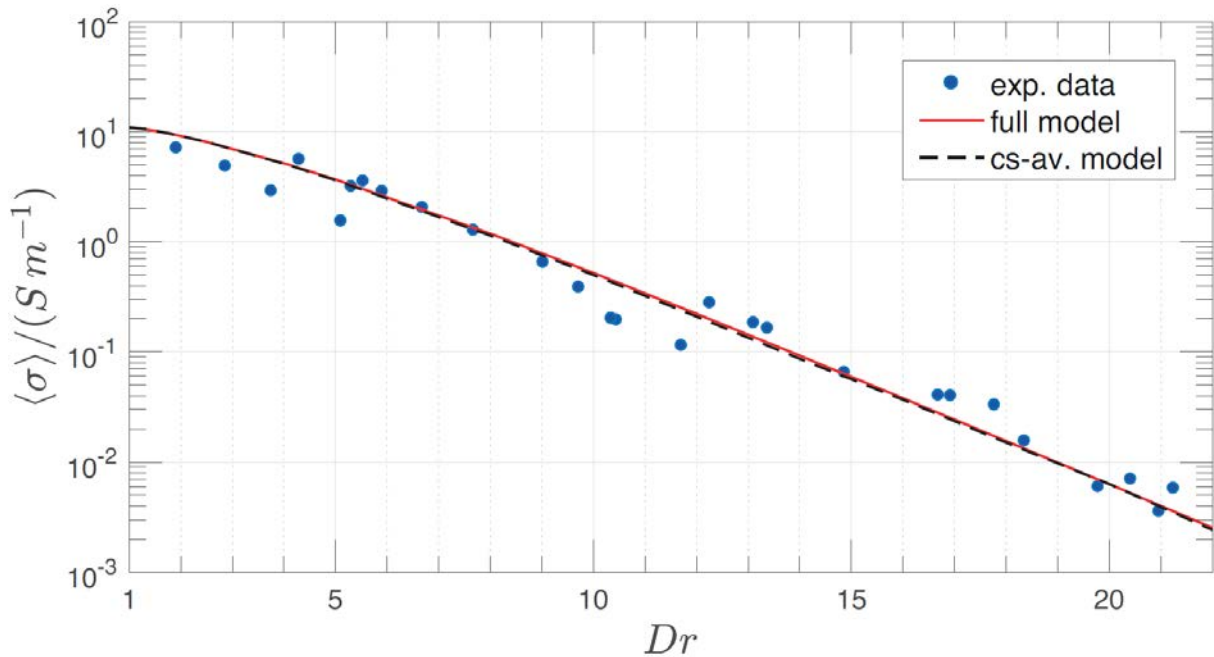


Figure 73. Averaged conductivity  $\langle\sigma\rangle$  of a 3 wt% PC/MWCNT composite layer in a PSu fiber as a function of draw ratio. The blue points correspond to the experimental data of Figure 53 (Fiber #1), while the red and black lines depict the theoretical prediction of the full and cross-section averaged models, respectively, for a composite layer delimited by positions  $r/R = \pm 0.6$ . Parameters:  $m = 1.5$ ,  $\sigma_{in} = 9.7 S/m$ ,  $a c = 3.9 \times 10^{-3}$  (full model),  $a c = 3.6 \times 10^{-3}$  (cross-section averaged model).

In order to access experimentally the conductivity of a nanocomposite as a function of the radial position, we fabricated a PC fiber with a PC/CB composite and six metallic electrodes placed at equal distances along the width, as explained in the previous chapter (Figure 57). Figure 74 shows the conductivity measured for

two different draw ratios. The points are placed in the middle of the domains of average, which have a size of 2.5 mm, i.e.  $0.25 R$ , corresponding to the distance between the electrodes. These measurements are compared to the theoretically obtained distribution of the moving average. Despite its simple approach, our model describes the variation of conductivity along the radial position very well. Note that analogue to the PSu fiber with PC/CNT composite, the values of initial conductivity  $\sigma_{in}$  and product  $a c$  are uniquely set, independent of the draw ratio and radial position. Also shown in Figure 74 is the averaged conductivity distribution resulting from the cross-section averaged model (black dashed line). Clearly, this model is not sufficient for predicting such a large radial variation of the conductivity, emphasizing the need of our extended model.

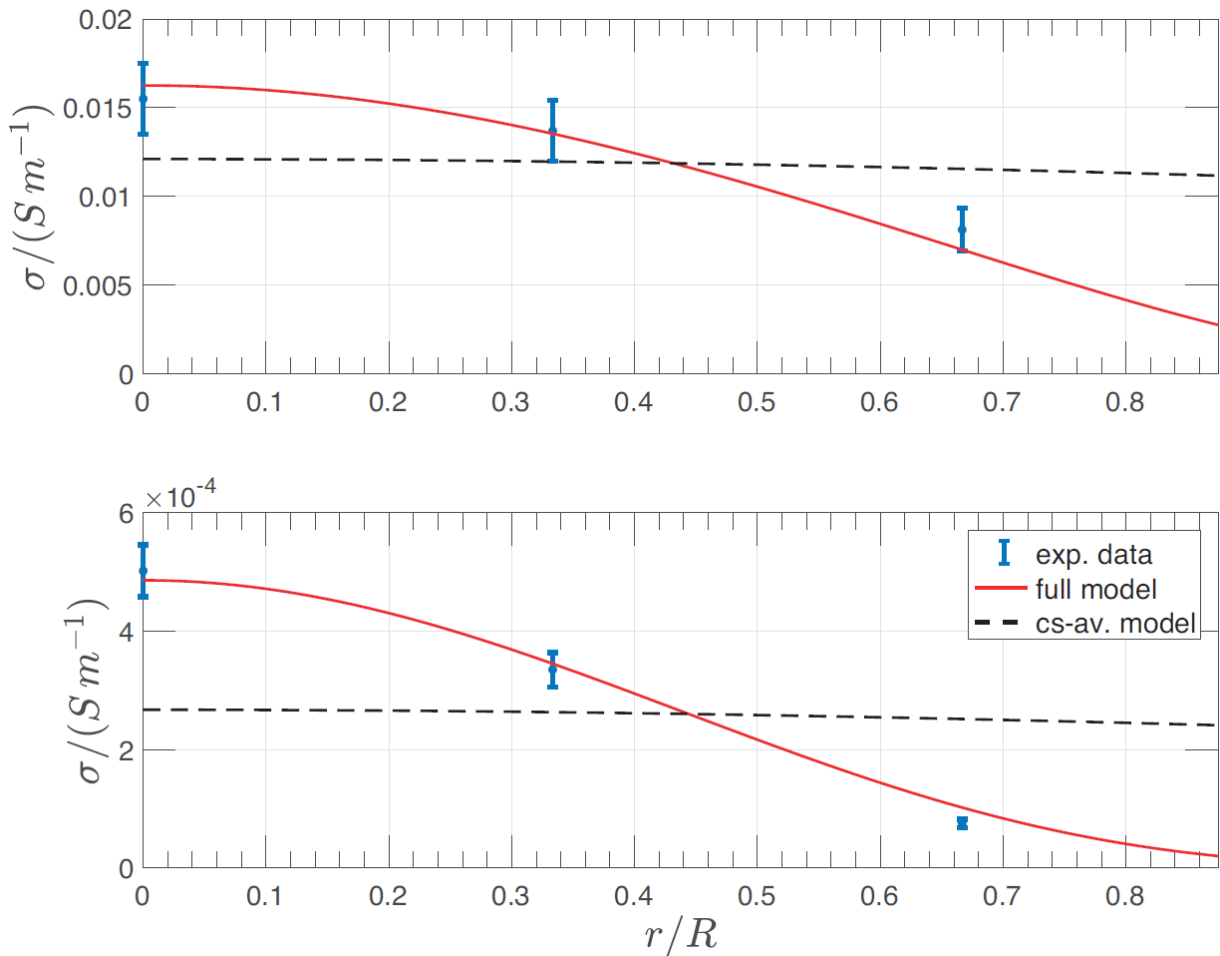


Figure 74. Dependence of the conductivity on the fiber radius for a PC/CB composite sheet in a PC fiber for two draw ratios, (a)  $5.12 \pm 0.16$  and (b)  $7.24 \pm 0.13$ . The blue points depict the experimentally determined averaged conductivities obtained by measuring the perpendicular conductivity between two metallic electrodes. The red line shows the theoretically predicted radial distribution of the averaged conductivity and the black, dashed line depicts the distribution obtained using the cross-section averaged model. Parameters:  $m = 1.5$ ,  $\sigma_{in} = 2 \text{ S/m}$ ,  $a c = 1.1 \times 10^{-2}$  (full model),  $a c = 9.8 \times 10^{-3}$  (cross-section averaged model).

## 4.4 Discussion and summary

### Modeling the conductivity of nanocomposites

Our model for the post-drawing conductivity of nanocomposites enables to account for its dependence on draw ratio and radial position in two different fibers fabricated, but it could be exploited further. We have not yet described the dependence on feeding speed and drawing temperature presented in Figure 53, nor employed the model to predict how to modify the drawing parameters, in particular the temperature profile, to improve the conductivity.

The nanocomposites could be examined separately to determine the product  $a c$  in simpler deformations and estimate the viscosity they have during drawing. Since only the viscosity of the cladding was employed here, the value of the product  $a c$  obtained from the fits is not very meaningful. The anisotropy of conductivity could also be considered, for example with a different value of  $a$  in the model for the  $r$  and  $z$  directions. It may also be possible to model anisotropy by quantifying the alignment of the nanoparticles due to the velocity field. Experimental data could be obtained by fabricating fibers designed in order to allow for accurate measurements of conductivity both along the fiber and in the perpendicular direction.

Then, we could measure the conductivity of a nanocomposite at various axial positions in the neckdown region of an interrupted draw. This would enable to compare the experimental data to the model, based on the kinetic equation, not only in terms of post-drawing conductivity but also against the  $z$  coordinate during drawing.

### Other applications of the model and possible improvements

Besides the electrical conductivity of nanocomposites, it would be possible to apply our model to other types of properties and materials in thermally drawn fibers. It provides an advanced description of the temperature, viscosity and velocity fields in the neckdown region, and could be employed to estimate the alignment of polymer chains or the rotation of solid objects in a fiber during drawing for example. It could also be used to predict the preform design that would be required to obtain a particular shape, rather than an inverted “V” when starting with straight interfaces.

Different refinements may improve the model and make it more accurate. The temperature field could be described without assuming a parabolic radial profile, and radiative heating could be considered explicitly. For the viscosity of the material, the influence of deformation rate and a more accurate temperature dependence instead of a simple fit of the Arrhenius equation could be implemented. The anisotropy and dependence on temperature and deformation of other material properties could be added, and the presence of different materials in multi-material fibers could be taken into account with effective properties.

## Conclusion

To model the thermal drawing process, previous analytical analysis assumed a velocity in the drawing direction that is independent of the radial position. The analytical solution of equation (95) was used in the literature [23], [42] but only considering that the cross-section averaged  $\langle \eta^{(0)} \rangle$  is given directly by the air temperature through the Arrhenius equation, as for the initiating step of our iterative implementation. We then take the thermal energy equation into account in our cross-section averaged model. In our full model we also consider radially dependent temperature  $T^{(0)}$ , viscosity  $\eta^{(0)}$  and velocity field at the  $\alpha^2$ -order  $v^{(1)}$  in order to investigate the radial distribution of fiber properties. The model presented here is capable of describing the thermal drawing process more accurately than the cross-section averaged model previously used, as illustrated with the deformation of initially straight lines. It enables to predict the radial distribution of material properties in multimaterial fibers, while it maintains the simplicity and flexibility of the cross-section averaged one-dimensional model for single-material fibers. Even though assumptions like using a circular cross-section or employing a simple empirical kinetic equation appear to be rather strong, we are able to reach qualitative and quantitative coincidence with our experimental findings. The flexibility of the model enables comprehensive parametric studies to find routes to new experimental designs. Our approach advances the understanding of multi-material fiber drawing and opens novel opportunities for the design of advanced fiber-based devices and smart textiles with optimum control over material microstructure and tailored properties.

# Chapter 5 Applications

In this chapter, we present two types of novel fiber devices that employ conducting nanocomposites based on carbon black and carbon nanotubes.

Through collaborative work with colleagues of the FIMAP laboratory, we could combine our respective skills to create innovative touch sensing fibers. First, the knowledge developed by Dr. Tung Nguyen-Dang on the reflow during thermal drawing and control of cross-sectional architecture enabled us to invent a touch sensing fiber device that relies on a bendable conductive domain. The fiber design allows for detecting but also localizing touch along the fiber. Then, thanks to the expansion of compatible materials to thermoplastic elastomers (TPE) achieved by Dr. Yunpeng Qu, the touch sensing fiber devices could be further improved. We published the results of this work in two publications in *Journal of Physics D: Applied Physics* and *Advanced Materials* [8], [104].

As mentioned in the introductory chapter, the idea driving the development of a conducting and transparent material in multi-material fibers was that it could then be applied in optoelectronic fiber devices made by thermal drawing. Therefore, we employed carbon nanotube composites as transparent electrode in multimaterial fibers that include a layer of semiconductor in a sandwich structure, with a second conductive nanocomposite as back electrode. Due to the photoconductivity of the semiconductor, such fibers are photodetecting. This simple type of optoelectronic device demonstrates the ability of the carbon nanotube composites to be employed as transparent electrodes.

## 5.1 Touch sensing fiber devices

### 5.1.1 Introduction

#### **Multi-material micro-electromechanical fibers with bendable functional domains**

The integration of increasingly complex functionalities within thermally drawn multi-material fibers is heralding a novel path towards advanced soft electronics and smart fabrics. Fibers capable of electronic, optoelectronic, piezoelectric or energy harvesting functions are created by assembling new materials in intimate contact within increasingly complex architectures. Thus far, however, the opportunities associated with the integration of cantilever-like structures with freely moving functional domains within multi-material fibers have not been explored. Used extensively in the micro-electromechanical system (MEMS) technology, electro-mechanical transductance from moving and bendable domains is used in a myriad of applications. In this work we demonstrate the thermal drawing of micro-electromechanical fibers (MEMF) that can detect

and localize pressure with high accuracy along their entire length. This ability results from an original cantilever-like design where a freestanding electrically conductive polymer composite film bends under an applied pressure. As it comes into contact with another conducting domain, placed at a prescribed position in the fiber cross-section, an electrical signal is generated. We show that by a judicious choice of materials and electrical connectivity, this signal can be uniquely related to a position along the fiber axis. We establish a model that predicts the position of a local touch from the measurement of currents generated in the 1D MEMF device, and demonstrate an excellent agreement with the experimental data. This ability to detect and localize touch over large areas, curved surfaces and textiles holds significant opportunities in robotics and prosthetics, flexible electronic interfaces, and medical textiles.

This work, presented in section 5.1.2, was published in the *Journal of Physics D: Applied Physics* on 7 March 2017 in the article titled “Multi-material micro-electromechanical fibers with bendable functional domains” [104]. The other authors are Tung Nguyen-Dang, Yunpeng Qu, Marco Volpi, Wei Yan and Fabien Sorin. I did not fabricate the fiber device shown but contributed through the characterization and modeling of its electrical response to touch and the realization of the piano demonstrator. The publication also discusses how the cross-sectional shape can be maintained with little reflow during thermal drawing even with a cantilever-like design. This understanding of the reflow mechanism is part of the thesis work of Dr Tung Nguyen-Dang.

### **Superelastic Multimaterial Electronic and Photonic Fibers and Devices via Thermal Drawing**

Electronic and photonic fiber devices that can sustain large elastic deformation are becoming key components in a variety of fields ranging from healthcare to robotics and wearable devices. The fabrication of highly elastic and functional fibers remains however challenging, which is limiting their technological developments. Simple and scalable fiber-processing techniques to continuously codraw different materials within a polymeric structure constitute an ideal platform to realize functional fibers and devices. Despite decades of research however, elastomeric materials with the proper rheological attributes for multimaterial fiber processing cannot be identified. In the article published in the journal *Advanced Materials* on 25 May 2018 with the title “Superelastic Multimaterial Electronic and Photonic Fibers and Devices via Thermal Drawing” [8], the thermal drawing of hundreds-of-meters long multimaterial optical and electronic fibers and devices that can sustain up to 500% elastic deformation is demonstrated. From a rheological and microstructure analysis, thermoplastic elastomers that can be thermally drawn at high viscosities (above  $10^3$  Pa.s), allowing the encapsulation of a variety of microstructured, soft, and rigid materials are identified. Using this scalable approach, fiber devices combining high performance, extreme elasticity, and unprecedented functionalities, allowing novel applications in smart textiles, robotics, or medical implants, are demonstrated.

The other authors of this article are Yunpeng Qu, Tung Nguyen-Dang, Wei Yan, Tapajyoti Das Gupta, Gelu Marius Rotaru, René M. Rossi, Valentine Dominique Favrod, Nicola Bartolomei, and Fabien Sorin. In section 5.1.3, we present the results on electronic fiber devices based on conductive composites, which correspond to my contribution and are relevant to this thesis.

## 5.1.2 Multi-material micro-electromechanical fibers with bendable functional domains

### Introduction

The recent development of fiber processing technologies has enabled the fabrication of fibrous structures with increasingly complex functionalities. In particular, the thermal drawing process used to fabricate optical fibers has experienced a series of breakthroughs that have extended the range of cross-sectional architectures and materials that can be integrated in fibers [1], [105], [106]. Thermal drawing traditionally consists of fabricating a macroscopic version of the targeted fiber out of thermoplastic or glassy materials that can be plastically deformed at high viscosities over a relatively large temperature window. The preform is fabricated at the macroscopic scale that enables us to assemble materials and realize architectures with submillimeter feature sizes in straightforward ways. Fiber pulling results in a drastic reduction of cross-sectional dimensions bringing materials together at the microscopic scale, while expanding uniformly along kilometers of fiber length (see Figure 75 (a) and (b)). The first significant breakthroughs in optical fiber processing, which contrasted with conventional step-index solid core silica fibers, were the fabrication of 1D and 2D photonic crystal fibers [107]–[110]. This marked the beginning of a deeper interest, not only in the functionality of the fabricated fibers and in particular the engineering of their optical properties, but also in the materials and the physical processes at play behind the fabrication technique. Photonic crystal fibers integrate hollow micro-channels with diameters down to sub-micrometer in feature sizes that reproduce uniformly along kilometers of fiber length. Bragg mirror fibers exhibit a periodic structure of concentric layers of high index of refraction glasses and low index polymers with thickness down to a few tens of nanometers, again reproduced along extended lengths of fibers. The ability to fabricate such remarkable structures with a simple and low-cost process stems for a large part from a controlled interplay between the viscosity and surface tension. The understanding of the viscous flow and surface science at play in this approach has also led to the design and fabrication of fibers with new materials. It was shown in particular that crystalline materials, if encapsulated well within cavities with high viscosity boundaries, can be integrated and flow as a low viscosity melt during the fiber pulling down to the micrometer scale before capillary breakup [111]. This has been exploited in optics for the fabrication of solid core polycrystalline semiconductor fibers [112], [113]. It has also led to the design of optoelectronic fibers that can not only guide light but also exhibit a variety of novel functionalities, such as optical [9], [14], [114], [115], heat [116] or chemical sensing [117], [118], piezoelectric actuation [5], [119], surface emitting fiber lasers [10], [120], advanced optical probes [121], [122] or field effect and phase change based devices [6], [123]. Polymer fibers with electrically conducting domains can also be used in optical imaging systems [124], or in purely electronic functions, such as touch sensing [7], [125] or capacitors [126].

So far, however, all novel fiber designs have relied on materials organized in intimate contact to deliver a specific functionality. The concept of electromechanical transduction from freely moving functional domains within multi-material fibers has not been exploited. This approach is used in a myriad of configurations in the micro-electromechanical system (MEMS) technology, such as cantilever-based devices for micro-sensors and actuators. The ability to integrate such advanced systems within extended lengths of flexible fibers can bring a breadth of novel opportunities for functional fibers and fabrics. Here, we demonstrate for the first time a micro-electromechanical fiber (MEMF) device that exploits the bending of a freestanding electrically conductive polymer sheet (Figure 75). Under mechanical pressure, the conducting sheet can bend and be brought in contact with another electrically conducting domain, generating an electrical signal that can reveal

the pressure. We show that such fibers enable the detection and localization of a pressure point along the entire fiber length with sub-millimeter resolution. Beyond the simplicity and scalability of the fabrication process, MEMF devices are the first 1D systems that can sense and localize pressure and touch without the need for 2D grids, at a very low energetic consumption, and with such a high resolution. This paves the way towards novel advanced fibers and fabrics capable of functionalizing large area surfaces and textiles with pressure mapping capabilities.

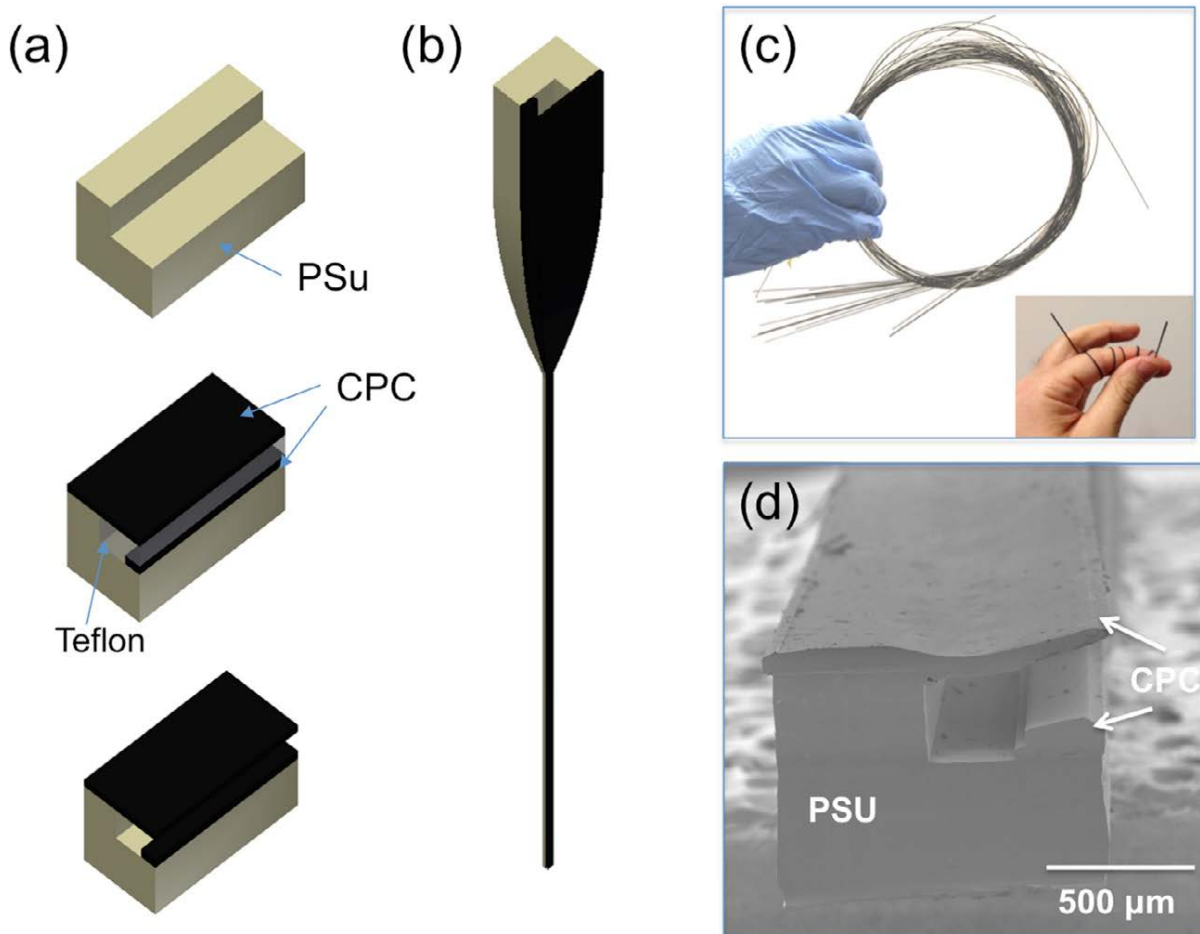


Figure 75. Fabrication of a MEMF device. (a) Schematics of the preform fabrication that starts with the machining of a PSu plate in an L-shape block, the positioning and hot pressing of the PC/CB sheet and bus, with a Teflon domain to transfer pressure to both PC/CB regions, and finally a mechanical removal of the Teflon domain. (b) Schematic of the preform-to-fiber thermal drawing. (c) Photographs highlighting the extended length of fibers fabricated in a single draw and their flexibility. (d) SEM micrograph of the cross-section of a MEMF fiber.

## Methods

### *Preform and fiber fabrication*

The fabrication approach and fiber architecture of the MEMF device are shown in Figure 75. We start by machining a thermoplastic plate, here polysulfone (PSu), in an L-shape cross-sectional structure (Figure 75 (a)). For the conducting material that will deliver the desired electronic function, we choose a carbon black

loaded polycarbonate (PC/CB) composite. PC/CB has been exploited for its electrical conductivity and in particular its linear resistance, and for its compatibility with the thermal drawing process [3]. Indeed, the thermoplastic matrix ensures the compatibility with the thermal drawing process at a glass transition temperature close to the one of PSu, while the carbon black filler provides a percolated path for a sufficient electrical conductivity. A PC/CB bus is placed on the long edge of the L-shaped PSu, while a thin PC/CB sheet is positioned above it on the short edge as shown in Figure 75 (a). A Teflon plate is at the same time machined and positioned so as to support both PC/CB domains during their hot pressing against the PSu construct to fabricate the preform. Hot pressing is performed in a vacuum and at a temperature of 220 °C in a specially designed laboratory press (Lauffer Pressen UVL 5.0, Maschinenfabrik Lauffer GmbH & Co. KG, Germany).

After the preform is consolidated, the Teflon part is mechanically removed (Figure 75 (a)). The assembly is subsequently thermally drawn in a custom-made draw tower at a set temperature of 260 °C that enables the co-drawing of both PSu and PC/CB (Figure 75 (b)). A feeding speed of 1 mm/min and a drawing speed between 0.1 m/min and 1 m/min were used. As shown in Figure 75 (b) and (c), and as discussed below, the thermal drawing results in an extended length of the flexible ribbons that maintain the exact cross-sectional shape of the initial preform.

### ***Fiber structure characterization***

Scanning electron microscopy (SEM) was used to image the fiber cross-sectional architectures. The sample was coated with a 10 nm carbon film before being transferred into the vacuum chamber. The SEM images were taken with a Zeiss Merlin field emission SEM (Zeiss, Göttingen, Germany) equipped with a GEMINI II column operating at 2.0 kV with a probe current of 150 pA.

### ***Electro-mechanical fiber response***

The fiber response to touch was characterized by measuring the electrical response to the local application of pressure. An Electromechanical universal testing machine (UTS) from Walter + Bai AG (Series LFM-125 kN) was used to vertically move a flat rod (4-mm wide) that was placed in contact with the top side of the fiber. The testing machine enabled down to 1 μm steps for this vertical motion. The PC/CB bus and sheet were individually connected to a metal wire at both ends of the 85 cm long fiber piece using silver paint. An Agilent E3612A DC power supply was used to apply a tension of 10 V, and the currents  $i_0$  and  $i_L$  were measured as shown in Figure 76 and explained in more detail below, with a Keithley 2450 Sourcemeter and a Keithley 6517B Electrometer.

Noise current was measured by recording over one hour the highest current measured between  $i_0$  and  $i_L$  for a pressure point close to the contact, at a DC applied voltage of 10 V. From a statistical analysis we could extract the standard deviation of the current fluctuations, which we defined as our noise current. For the conservative assessment of the device spatial resolution we derive below, the highest noise we could measure was around  $i_N = 0.1$  nA.

To measure the time response of the device and obtain a first assessment on its robustness under many bending cycles, we adapted a Dynamic Mechanical Analysis set-up (TA Instrument DMA Q800) to apply a pressure at 200 Hz on the fiber. We used the DMA in compression mode with a 25 μm amplitude, fixing the

fiber between two soft PDMS plates of 1 mm in thickness. The fiber was connected to an oscilloscope with a 1 V DC applied.

### *Fiber piano device*

To demonstrate the ability of the fiber to be employed as a 1D touch sensor, a ‘piano device’ was fabricated by connecting a fiber piece to a voltage divider circuit to extract the electrical resistance, hence the position of the touch. This circuit was combined with an Arduino Leonardo microcontroller, which was programmed to match different positions of touch on the fiber to pitches played by a piezo buzzer. The piece of music ‘Ode To Joy’ (Beethoven) was played and a video recorded (<http://iopscience.iop.org/0022-3727/50/14/144001/media/Piano%20fiber%20device.mp4>).

## **Results**

### *Fiber fabrication*

In Figure 75 (c) and (d) we show that an extended length of highly flexible ribbons is produced with a cross section that remarkably maintains the initial architecture of the preform. All dimensions have rescaled following the same draw down ratio  $Dr$ , a quantity defined as the ratio between the width (or height) of the initial preform to the width (or height) of the ribbon. Note that by a simple mass conservation principle, the ribbon length scales as  $Dr^2$  times the length of the initial preform, highlighting the scalability of the process. The particular microstructure of the ribbon cross-section is shown in Figure 75 (d) with a SEM micrograph of the MEMF cross-section. The two PC/CB domains are clearly visible, separated by a micro-cavity that allows the thin upper PC/CB sheet to bend when pressure is applied, and recover its initial horizontal position upon removal of the mechanical excitation. This mechanical behavior enables us in turn to exploit such architecture for pressure sensing. As the PC/CB layer touches the PC/CB bus underneath, an electrical connection can occur and a current can flow from one PC/CB domain to the other, signaling the local pressure.

### *Pressure localization*

In Figure 76 (a) and (b) we show a schematic of such a deformation as well as the equivalent electrical circuit for consideration. When a potential difference is applied at one fiber end, one quickly realizes that the current generated will depend upon the position along the ribbon axis ( $x$ -axis in the schematic). Indeed, the PC/CB film and bus act as linear resistors and the further away from the applied potential, the higher the equivalent resistance of the circuit. If the potential is applied at a position  $x = 0$  as shown in Figure 76 (b), the resistance of the PC/CB top film  $R_f(x)$  and bottom bus  $R_b(x)$  are simply given by  $R_f(x) = \frac{\rho_{PC/CB} \cdot x}{S_f}$  and  $R_b(x) = \frac{\rho_{PC/CB} \cdot x}{S_b}$  where  $\rho_{PC/CB}$  is the resistivity of PC/CB and was measured to be quite uniform along the fiber length and equal to around 1  $\Omega \cdot m$ .  $S_f$  and  $S_b$  are the cross-sectional surface areas of the PC/CB film and bus respectively. Note that we consider that the width of the pressure applied along the fiber axis is very small compared to the fiber length, so that the position  $x$  of an applied pressure is well defined.

This measurement would not however be sufficient to extract both the presence and position of any pressure applied to the electro-mechanical ribbon. Depending on the pressure intensity, the contact resistance  $R_c$  between the PC/CB film and bus can vary. We hence propose another circuit configuration that enables us to measure two different currents out of which the position can be specified regardless of the applied pressure. In Figure 76 (c), we show the equivalent circuit for this approach where we add a connection to the PC/CB bus at the other extremity from the applied voltage. We can measure independently the two currents flowing in parallel  $i_0(x)$  and  $i_L(x)$ . Taking their ratio  $\beta = \frac{i_0}{i_L}$  eliminates the unknown voltage drop (unknown because it depends on both the position  $x$  and  $R_c$ ) and is simply given by the ratio of the two resistance  $R_b(x)$  and  $R_b(L - x)$ . Using the expressions of  $R_b$  as a function of  $x$  given above immediately gives:

$$x = \frac{L}{1 + \beta} \quad (130)$$

To verify our reasoning that the ratio  $\beta$  is indeed independent of the applied pressure, we plotted in the graph of Figure 76 (c) the measured  $i_L$  current and the ratio  $\beta$  as a function of the position of the probe that pushes down on the ribbon. At a position of 0  $\mu\text{m}$ , the pressure is just high enough for the two PC/CB domains to touch each other. This lower limit of pressure sensing corresponds to a Force of around 0.3 N, or a pressure of around 50 kPa, considering a surface area of 4 mm (probe width) times 1.5 mm (fiber width). As the probe is brought down and its position increases from 0 to 4  $\mu\text{m}$ , a higher pressure results and hence a lower  $R_c$ , increasing the current  $i_L(x, R_c)$  as seen in the graph. Measuring  $i_0(x, R_c)$  at the same time and plotting the ratio  $\beta$  shows, however, that this ratio remains unchanged as the pressure is increased. The measured position  $x$  from our model is therefore only a function of the position of the applied pressure. In Figure 76 (d) we show a plot of the measured position versus the actual position of the probe along an 85 cm long MEMF device. The straight line represents the actual position of the probe during the experiment, while the blue squares are the values of the positions obtained from equation (130) and the experimental measurements of the  $\beta$  ratio, for a length  $L$  of 85 cm. An excellent agreement is obtained, with a slight shift due to the size of the contacts at the fiber edge and the fact that they are not exactly situated at  $x = 0$  and  $x = L$ . Note that, from an engineering point of view, this slight shift can be suppressed by calibrating the response of the fiber, since each pressure location is indeed associated with a single  $\beta$  ratio. The error on the position can then only come from the noise current associated with the measure. Moreover, knowing the location now enables us to find  $R_b(x)$  and  $R_f(x)$ , and to extract the contact resistance  $R_c$  from the value of  $i_0(x)$  for example:  $R_c = \frac{V}{i_0(x)} - (R_b(x) + R_f(x))$ . The applied pressure, knowing the probe size, can then be evaluated from calibration with the respective  $R_c$ . This can be done over a narrow band of applied pressure, between around 0.3 N and 0.6 N for the particular fiber tested, as it saturates quickly with the increasing force applied (see Figure 76 (c)).

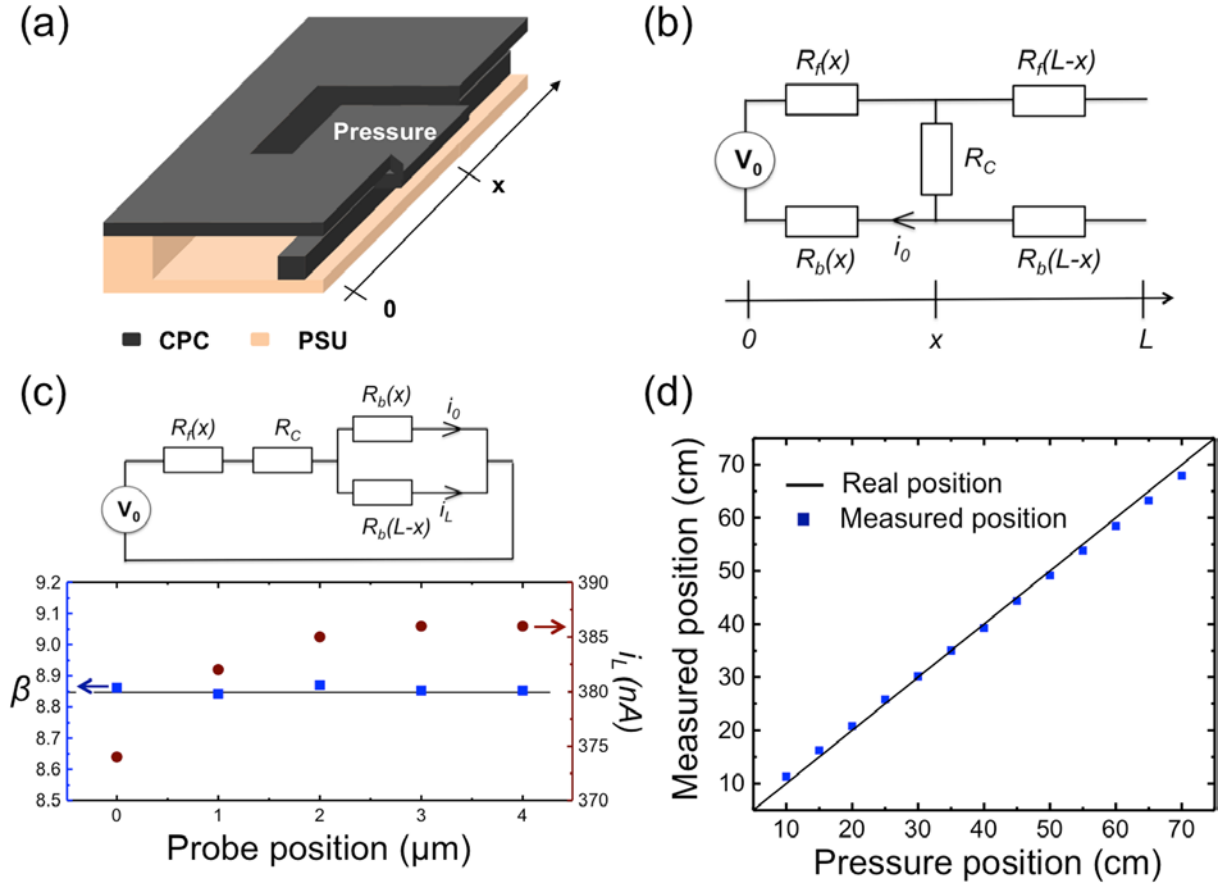


Figure 76. Pressure detection and localization: (a) schematic of a pressure sensing ribbon with local pressure bending the PC/CB film at position  $x$ ; (b) schematic of the equivalent circuit when a potential is applied at one fiber end and pressure is applied at a position  $x$  along the fiber length. (c) Top: schematic of the equivalent circuit used to localize pressure. Bottom: graph of the measured  $i_L$  (scale to the right) that raises as the probe is brought down on the MEMF device. The current ratio  $\beta$  is also shown (left scale) that reveals that it is independent of the pressure applied. (d) Measured position versus real position extracted from the measurement of  $\beta$  for pressure applied along an 85 cm long fiber.

### Spatial resolution

To assess the spatial resolution of our device, we adopt a very conservative approach to define the noise current as the highest noise measured (worst case scenario) of  $i_N = 0.1$  nA and consider this the maximum fluctuation for both  $i_0$  and  $i_L$  for all the measurements made at each pressure position. The uncertainty over the ratio  $\beta$  is again assessed conservatively by considering that it would be comprised between the maximal

$\beta_{max} = \frac{i_0 + i_N}{i_L - i_N}$  and minimal values  $\beta_{min} = \frac{i_0 - i_N}{i_L + i_N}$  given the associated noise. The resolution over  $x$  being given by  $\Delta x = \frac{L}{(1+\beta)^2} \Delta\beta$ , we can write neglecting the terms in  $i_N^2$ :

$$\Delta\beta = \frac{i_0 + i_N}{i_L - i_N} - \frac{i_0 - i_N}{i_L + i_N} = \frac{2 \times i_N (i_0 + i_L)}{i_L^2 - i_N^2} \approx \frac{2 \times i_N (1 + \beta)}{i_L} \quad (131)$$

So

$$\Delta x \approx \frac{L}{(1 + \beta)^2} \times \frac{2 \times i_N(1 + \beta)}{i_L} \quad (132)$$

and gives  $\Delta x \approx \frac{2i_N}{i_L}x$ . Considering the maximum noise value ( $i_N$ ), and the data collected for  $i_L$  at every position  $x$ , we find the value of  $\Delta x$  always below 0.5 mm. This conservative evaluation of the resolution can be experimentally verified by recording the currents over an extended period of time (10 min in this case) for two positions of the probe spaced by a distance above this conservative value, say 0.75 mm. In Figure 77 (a) we plotted the histogram of such a measurement that shows the number of counts for a certain value of the current versus the position of the pressure applied. The standard deviation of each measurement gives the noise of the system. Clearly, the distance between the average current for the two different positions is much greater (around 40 times greater) than their standard deviation, meaning that the two positions can be separated. This means that the position of the center of an excitation can be known with such precision, if the width of this excitation is very small compared to the fiber length, or if the type of excitation is known (such as the touch of a finger, see the discussion part below). If the excitation has a large unknown width, the system can be adapted to measure both the center position and width of the excitation, very similarly to the reconstruction of two different pressure points, as we discuss below. Note also that simple noise management techniques could lead to even better resolutions, potentially in the sub-hundred micrometer range.

#### *Dynamic response*

The inset of Figure 77 (b) shows the voltage response over time for a fiber exposed to a cyclic load in compression, as described in the method section. In the main graph we plotted the experimental recording for part of the cycle (black squares) and the exponential fit (red curve). We could extract a response time of 57  $\mu$ s. We also noted no drift, change of response or damage to the fiber after  $10^4$  cycles, highlighting the robustness of the fiber device.

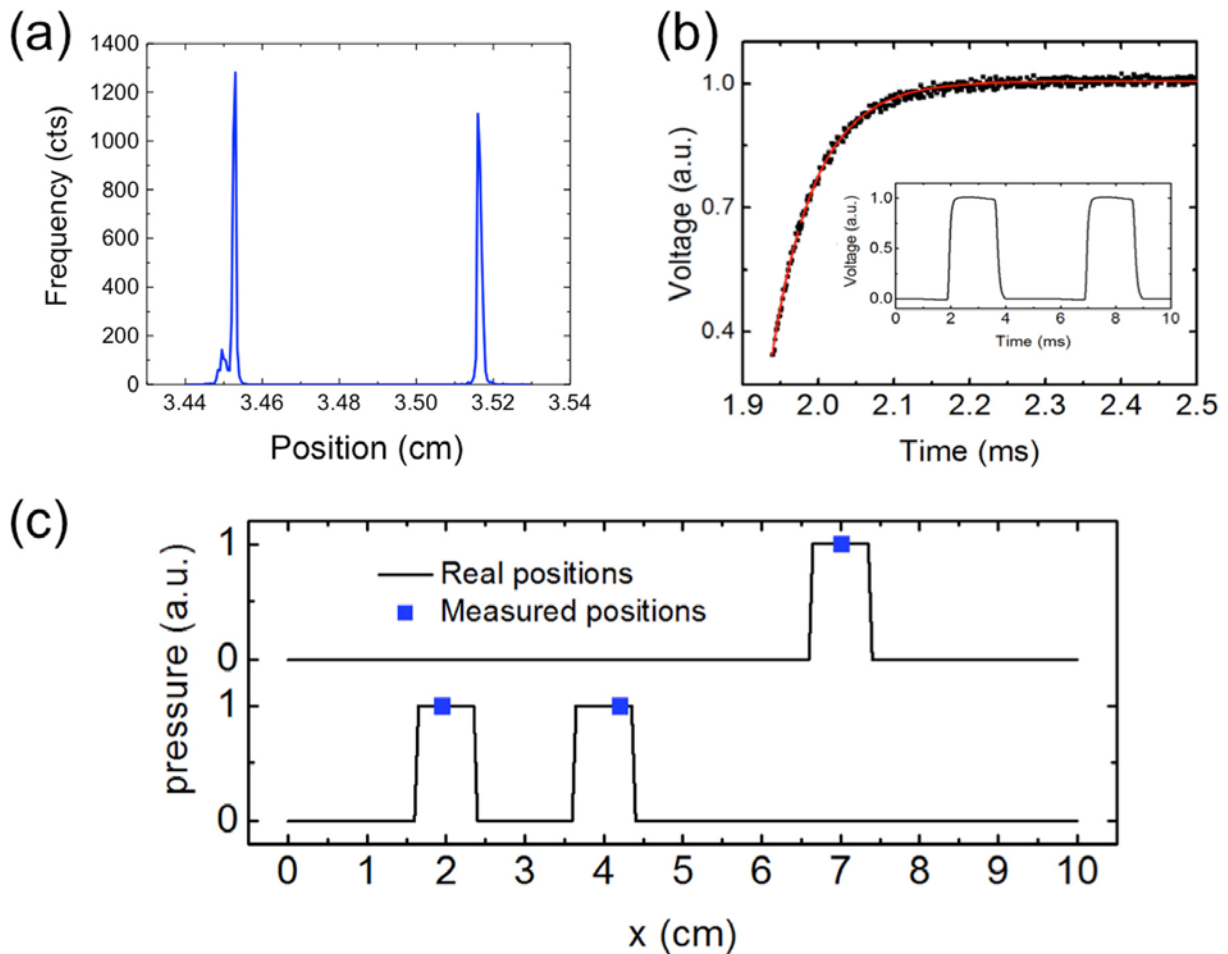


Figure 77. (a) Frequency counts of the generated current values recorded over 10 min versus position of the applied pressure at two different locations. (b) Voltage response versus time under oscillating mechanical excitation at 200 Hz. The main graph shows the experimental data (black squares) and the exponential fit (red curve) for part of the cycle, while the inset shows two full cycles. (c) Graph representing the reconstruction of two pressure points applied along a 12 cm fiber. The black line represents the pressure distribution in an arbitrary unit while the blue dots correspond to the extracted measurements.

### Multiple pressure points

The analysis we performed to localize a pressure point revealed that, assuming a small pressure area, localization is simply performing the measurement of independent currents that can resolve an equation with two unknowns, namely the pressure value (linked to the contact resistance) and the position. It is straightforward to expand this approach to multiple excitations when the pressure is high enough so that the contact resistance saturates and affects the measurement less than the probe size. In such a configuration, two pressure points bring only two unknowns to the system (their positions) that the two current measurements can be used to resolve. Instead of deriving the simple circuit analysis done previously, here we take the approach of calibrating a 12 cm long fiber subjected to one or two simultaneous pressure points. We measured and recorded the currents generated  $i_0$  and  $i_L$  for one and two pressure points spaced by 5 mm (mimicking an application with a finger touch of around 10 mm in width). After this calibration, we subjected the fiber to two events represented in Figure 77 (c) by black curves with an arbitrary pressure value of 1 at the contact point. On top, we show an excitation by a single pressure point, and below an event with

two pressure points. In blue we indicated the reconstructed localized pressure on the fiber for these two events using the calibrated values. The system could sense if one or two touches were present, and the detected positions correspond very well with the excitation to be resolved. We performed a series of similar experiments and found that the calibration was robust and a resolution of  $\pm 3$  mm could be achieved to resolve the position of the center of two excitations.

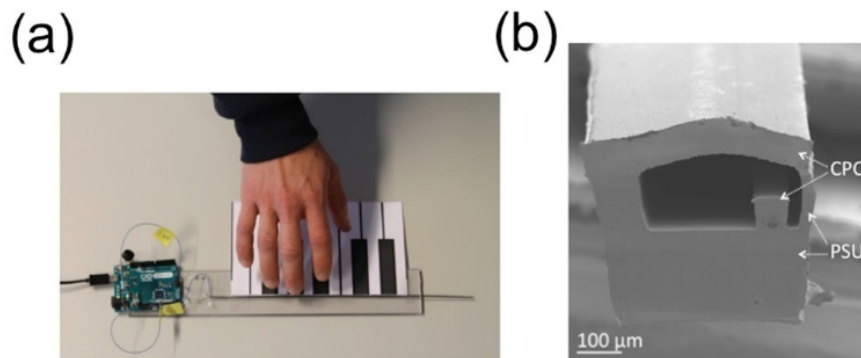


Figure 78. Application. (a) Picture of the fiber piano device (see the video available at <http://iopscience.iop.org/0022-3727/50/14/144001/media/Piano%20fiber%20device.mp4>). (b) SEM micrograph of an enclosed microelectromechanical fiber design.

## Discussion

The ability to realize a fiber device with such a complex microstructure is firstly a result of the particular attributes associated with the drawing process. To maintain the cross-sectional shape during thermal drawing, it is essential to pull the fiber at a high viscosity to avoid any thermal reflow, deformation or capillary break-up of the thin PC/CB sheet and square bus. The thermal drawing of such complex structures enables us for the first time to detect and localize pressure along a single functional fiber. Previous work has reported a capacitive approach that requires a conductive probe (or a finger) to press and then slide on the fiber to extract a location [125]. Other approaches have relied on fiber grids to localize an excitation [7], [115], [127]. The approach we demonstrate here has several advantages compared to existing configurations. First, it does not require a conducting probe to sense and localize pressure, nor does it require a fiber mesh. This drastically reduces the number of contacts to be made to the fibers, hence improving integration. The accuracy with which one can localize pressure is far beyond what is needed in most practical applications, given the very low noise of the system. Moreover, we showed that a single fiber can sense and localize two pressure points simultaneously applied along its length, which was not possible to do with previous configurations. By integrating more electrodes or more contacts along the fiber length, a greater number of independent currents could be measured and hence complex pressure distributions could be extracted. It is also interesting to note that if we could localize two pressure points of small width, it would also be possible to extract the center and location of an excitation with a large width. This could be very interesting for medical applications, such as pressure ulcer prevention discussed below, where large area pressure on the body could be sensed and localized precisely using a system simple to fabricate, integrate and use. Moreover, the device

is an open circuit at rest, consuming very little energy for its functioning to the contrary of other capacitive or piezoresistive based devices.

The ability to have a single fiber capable of detecting and localizing pressure in a straightforward and easy to interface way can have an impact in many fields of applications, such as in healthcare, smart textiles and entertainment. Note that we refer to 'detecting' pressure, even though over a small range of applied pressures we showed that we could also measure its intensity. This range is however relatively small in the current configuration, but could be improved with more advanced designs discussed below. For several applications, such as flexible and foldable keyboards, or ergonomic textile-integrated electronic interfaces, however, detecting pressure points regardless of the intensity is sufficient. In the medical field, the ability to cover a very large surface area, such as hospital bed sheets or chairs, enabled by the fiber format, could be very useful for the prevention of diseases, such as pressure ulcers. These are hard to treat diseases associated with extended periods of immobility and pressure against the skin that fabric-integrated MEMF devices could monitor and help prevent. In Figure 78 (a) we show a picture of a device that highlights an example of the advanced functionality that a single all-polymer MEMF can do. As we show in the movie provided (<http://iopscience.iop.org/0022-3727/50/14/144001/media/Piano%20fiber%20device.mp4>), we can assign to a location on the fiber different notes via different frequencies from a piezoelectric buzzer, fabricating the first 'piano fiber'. With the ability to sense more than one pressure point, more complex operations could be realized in the field of flexible electronic interfaces.

The mechanical behavior of the PC/CB film in MEMF ribbons has proven to be very robust. More accurate characterization of the mechanical robustness to a large number of bending cycles is underway, as well as the use of thinner freestanding sheets to further improve the MEMF response to pressure, its bandwidth and resilience. One difficulty that can be envisioned is the open structure of the cantilever-like design. An encapsulated system with a thin membrane that would protect the fiber from external debris or liquid (when washed if integrated in a textile, for example) could ensure a better protection for the functional parts. In Figure 78 (b) we show the cross-section of a fabricated fiber with an encapsulated design where a thin PSu wall was left to enclose the fiber cross-section. Tens-of-meters of such fiber were produced with a height down to 300  $\mu\text{m}$  and a PSu enclosing layer as thin as 5  $\mu\text{m}$ . This fiber can perform exactly the same functionalities as the cantilever-like fiber, but due to the rigidity of the PSu film and the mechanical excitation, the structure failed after a few thousands of cycles. We are looking into the thermal drawing of softer materials as the next generation of touch sensing fiber devices, which could exhibit the same advanced pressure localization capabilities but with an encapsulated design.

Finally, given the flexibility of the design at the preform level, many other configurations with thinner films, smaller gaps between the two conducting domains, or the integration of several pressure sensing elements in a single fiber or ribbon can be realized. This could result in advanced and robust fibers capable of measuring, with high sensitivity, the intensity but also the location, direction and nature (shear versus compression) of an arbitrary mechanical excitation.

## Conclusion

In conclusion, the thermal drawing process was used to fabricate a polymer based micro-structured ribbon with domains that can move upon mechanical excitation. This movement can bring two conducting composites in contact and trigger an electrical signal that is exploited to sense and localize the applied

pressure. We established a configuration and a model to extract not only the presence but also the position along the fiber axis of the applied pressure regardless of its intensity, and at a submillimeter resolution. We showed that these fiber devices were unaltered after  $10^4$  loading cycles at 200 Hz, that they could recognize and localize two pressure points, and that they exhibited a response bandwidth close to 20 kHz. An important aspect of the thermally drawn MEMF devices is the scalability at which fiber length and hence also surface area can be produced. While several strategies have been proposed to sense and sometimes map pressure using piezo-resistive, piezo-electric or capacitive approaches, very few share the attributes of the simplicity and low cost of the thermal drawing process. This is key for applications that require the functionalization of very large area surfaces. Ongoing research further investigates the mechanical attributes of MEMF devices. Other designs highlighted in the discussion part with thinner freestanding sheets, softer materials or encapsulated architectures are also under investigation, paving the way towards novel functionalities, such as a controlled release from partly closed cavities, or advanced functional surfaces for electronic skin applications.

### 5.1.3 Elastic multimaterial electronic fibers and devices via thermal drawing

#### Introduction

Electrode arrays [128]–[133] and optical fibers [134]–[136] that can sustain large elastic deformations, as well as elongated strain and pressure sensors, [130], [137]–[139] are becoming key components in robotics [128], [129], [140], [141], medical and wearable devices [128], [132], [141], [142], bioengineering [131], [143], [144], and in advanced textiles [138], [145], [146]. To realize the technological promises of elastic and functional fibers, however, novel fabrication strategies that are simple, scalable, and more versatile must be developed. The current processing approaches rely for a large part on extruding an elastomer and use it as a substrate onto which functional materials are applied in a way to comply with various mechanical constraints. These include coiled rigid metallic wires [147], elastic strains with deformable gold thin-films [131], prestretched fibers onto which carbon nanotube based nanocomposites are deposited [130], or hollow elastomeric fibers into which liquid metals are introduced over tens-of-centimeters [133], [139]. While impactful fiber devices could be demonstrated, these approaches involve several steps, have remained restricted to simple device geometries and functionalities, and it is still challenging to fabricate extended lengths of functional fibers. Surprisingly, simple and scalable fiber processing methods to make fibers directly encapsulating various functional materials have remained unexploited for elastic fiber devices. Traditional extrusion or spinning techniques offer interesting opportunities to make elastomeric fibers [148], [149], but remain difficult to adapt to realize fibers with complex multimaterial architectures. The thermal drawing process on the other hand, initially developed for optical fibers, has evolved as a powerful tool to fabricate rigid multimaterial fibers with advanced electronic and photonic functionalities [1], [9], [22], [121], [124], [150], [151]. Despite persistent efforts and growing interests [11], [105], [144], however, this process has never been successfully applied to elastomeric materials. Here, we alleviate this limitation and demonstrate that some thermoplastic elastomers (TPEs) can be compatible with the multimaterial thermal drawing process. We also identify functional materials such as thermoplastics, polymer nanocomposites, or liquid metals that can be codrawn within such TPEs matrices in 3D microstructured architectures of unprecedented complexity. We finally show examples of advanced fibers that can act as robust pressure sensors, combining high performance and multiple embedded functionalities. This novel fabrication platform enables to make superelastic fiber devices with unprecedented structures and functionalities, at industrially relevant length scales, paving the way toward new applications in functional textiles, robotics, or medical implants.

#### Stretchable multimaterial electronic fibers

To provide stretchable fibers and ribbons with electronic functionalities, we need to identify compatible materials with good electrical conductivities. In Figure 79, we demonstrate the codrawing of SEBS with an electrically conducting thermoplastic composite, carbon-black-loaded polyethylene (PE/CB), a family of composites compatible with the thermal drawing process [3], [104] and that can be drawn in a similar temperature range. The fiber architecture shown in the perspective and cross-sectional images reveals a gap between the two nanocomposite domains that was manufactured at the preform level and remained unaltered during drawing.

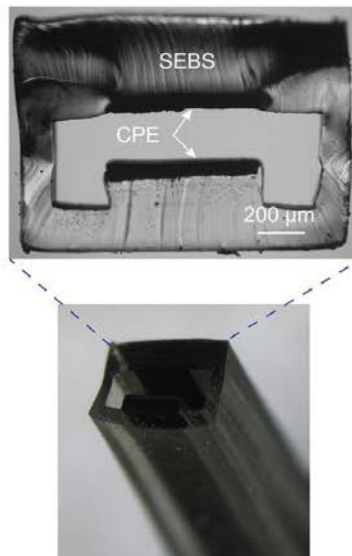


Figure 79. Stretchable multimaterial electronic fiber. Optical microscopy images of the perspective view (bottom) and cross-section (top) of a ribbon integrating two PE/CB electrodes separated by a gap within an SEBS cladding.

Then, we show an example that highlights the complexity of the functionalities that can be achieved with the multimaterial thermal drawing platform. In Figure 80 (a) we schematically represent the thermal drawing of a microstructured fiber that integrates a 3D assembly of a liquid metal electrode and four PE/CB domains encapsulated in a hollow-core SEBS matrix with a rectangular cross-section. Such a complex fiber, shown in the optical microscopy images in perspective and in cross-section in Figure 80 (a), possesses the unique ability to measure pressure, localize it along its axis, and discriminate its direction in a plane perpendicular to the fiber axis. The deformation of the metallic electrode can inform on the pressure locally applied along the fiber, as we discussed above. To localize this pressure position along the fiber length, a particular strategy must be adopted that circumvent a limitation of thermally drawn fiber devices that patterns to their axial uniformity that makes it difficult to extract information along their length. Here, a potential is applied between the top PE/CB electrode and one of the three PE/CB electrodes in the bottom. PE/CB has a resistivity of around  $1 \Omega \cdot \text{m}$  but at rest, the microcavity in the fiber center insulates both PE/CB domains. When a pressure is applied locally, the two conductive domains can get in contact, allowing for a current to pass. The current depends on the pressure location since this location determines the resistance of the overall circuit. A detailed analysis of a similar localization concept within an all-rigid yet bendable configuration is presented in section 5.1.2 and the corresponding publication [104]. In Figure 80 (b) we show the resistance versus the pressure position measured between the top PE/CB electrode and one of the three bottom electrodes, respectively. The fiber can hence be calibrated to localize position along its length, with a submillimeter spatial resolution. A keyboard relying on a fiber with one top PE/CB electrode and one bottom electrode is shown in a movie (available on the following website: <https://onlinelibrary.wiley.com/action/downloadSupplement?doi=10.1002%2Fadma.201707251&file=adma201707251-sup-0003-S3.mp4>) to highlight such capability. The first part of the movie shows a keyboard made out of three pressure sensing fibers, which have one PE/CB electrode in the top and one in the bottom (see Figure 79). The letters are matched to a resistance range using a voltage divider circuit connected to an Arduino Leonardo microcontroller board.

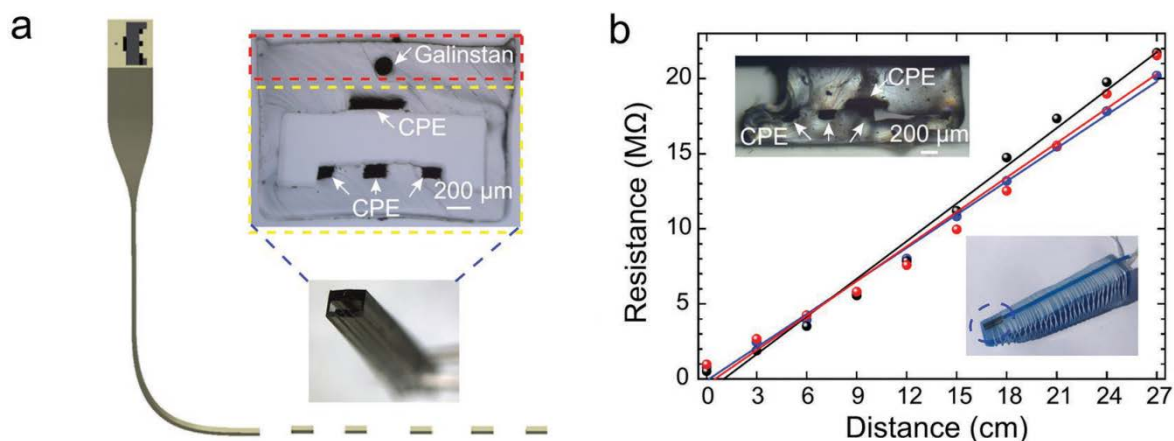


Figure 80. Pressure sensing fiber and various applications of stretchable electronic fibers. a) Schematic of a preform-to-fiber process of a microstructured multimaterial soft electronic fiber. We also highlight the possibility of cutting such fibers and ribbons into small devices. Optical microscopy images of the cross-section and perspective view of a fiber with four PC/CB electrodes and one liquid metal electrode. b) Position and direction sensing function. It relies on four PE/CB electrodes as shown in the optical microscopy image of the fiber cross-section (yellow-dashed rectangle in inset (a)). The graph represents the resistance measured versus the distance where the pressure is applied along the fiber axis. The black, blue, and red solid spheres are experimental data when the top electrode touches the left, middle, and right electrodes, respectively. The solid lines are corresponding fitting curves. The top left inset is an optical microscopy image of the fiber cross-section when the top PE/CB electrode touches the right PE/CB electrode under load. The bottom right inset shows a small fiber device positioned at the tip of a robotic finger to sense pressure.

The microstructured architecture of the ribbon cross-section can also inform on the direction of the pressure applied. Indeed, depending on the direction of the pressure in the plane perpendicular to the fiber axis, the top PE/CB electrode touches one of the three bottom ones. In Figure 80 (b), we show an optical microscopy image of such a fiber experiencing a pressure with a shear in one direction, leading the top electrode to touch one of the side bottom electrodes. The three integrated circuits enable to discriminate five ranges of pressure directions with a single thin fiber (Figure 81). Several well-positioned electrodes could achieve a better angular resolution and map the pressure direction with higher accuracy, which highlights the complexity of the achievable functionalities with the superelastic multimaterial fiber platform. The second part of the movie mentioned above shows that five pressure directions can be sensed by a device integrating a pressure sensing fiber and three different color LEDs. The finger pressing directions are indicated by arrows. The green arrow represents that the pressure is directed to the right. The pressure can close the circuit of the green LED and make it emit. The other relationships are as follows:

- (1) Yellow arrow, pressure directed to the left, yellow LED;
- (2) Red arrow, pressure directed vertically, red LED;
- (3) Two blue arrows, pressure directed between the right and the vertical, green and red LEDs;
- (4) Two orange arrows, pressure directed between the left and the vertical, yellow and red LEDs;

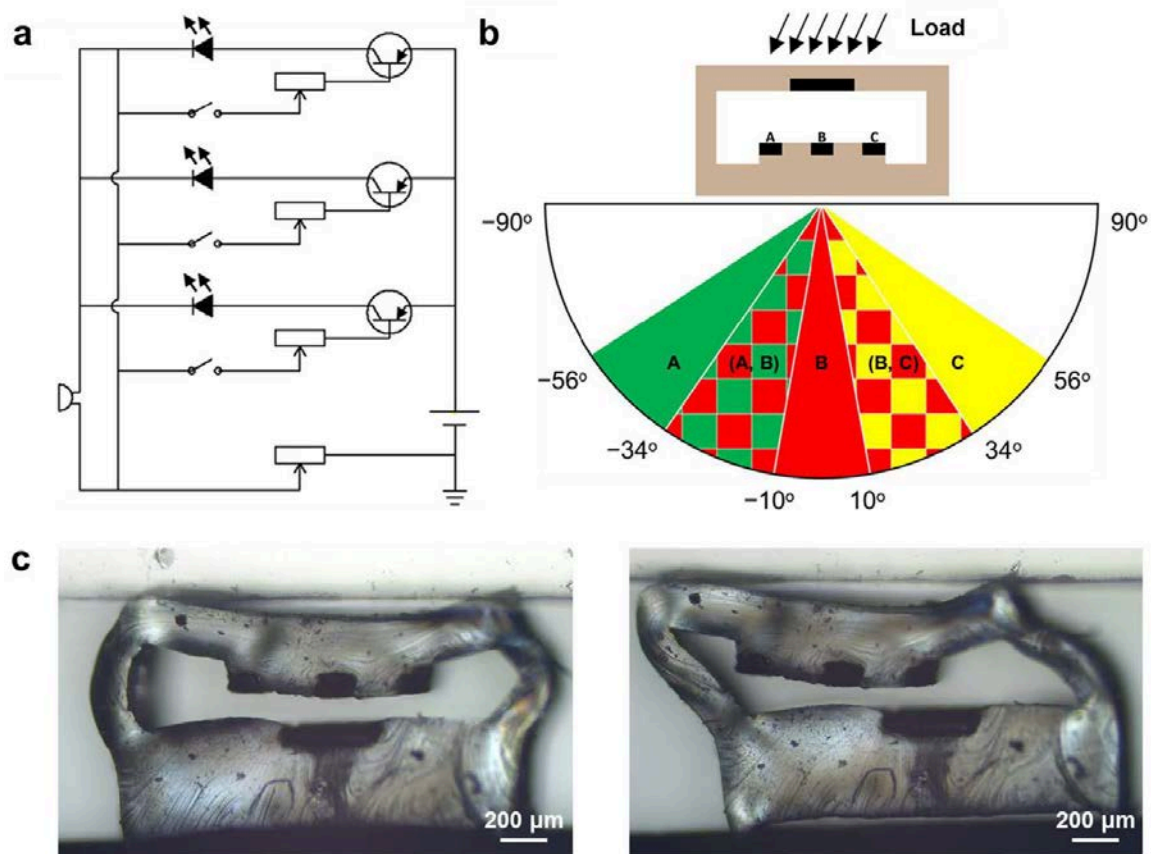


Figure 81. Pressure sensing fiber (pressure direction sensing function). a) Equivalent circuit of the device used in the movie mentioned above. A group of a variable resistor and a switch represents a couple of one bottom PE/CB electrode and the top PE/CB electrode. b) (Top) Schematic fiber cross section for pressure direction sensing function by using three PE/CB electrodes (A, B, C) in the bottom and one PE/CB electrode in the top. (Bottom) Corresponding pressure direction sensing result, for example, the (A, B) sector composed by green and red blocks means that the red and green LEDs are activated when a load is coming from a direction between roughly  $-34^\circ$  and  $-10^\circ$ . c) Optical microscopy images of cross sections of fibers under loads highlighting the shearing effect that can be detected.

## Discussion

Such fibers can be used as long and soft interconnects, or can be cut into several short pieces for smaller networks. In our schematic of Figure 80 (a) indeed, we also highlight the fact that thermal drawing generates long fiber lengths that can be used as is or can be cut into smaller OD devices. A typical 10 km long multimaterial fiber can generate one million 1 cm long devices in a single, continuous process in-line with the thermal drawing. With the properly engineered connections, such devices could be positioned on the tip of robotic fingers [152] for example, to sense pressure as we show in the picture in the bottom right inset of Figure 80 (b).

The scalable production of continuous fibers also opens novel applications where long fiber length (kilometer range) is required like in the textile industry. Our process has the other advantage of directly encapsulating the required functional materials, making the fibers robust mechanically but also against washing or other wear mechanisms. This, combined with the scalability of our approach, allows envisioning novel applications in advanced fabrics and medical textiles such as soft prosthesis, supporting gears, or fabrics monitoring physiological parameters.

The unique ability to integrate several electrodes in a single thin fiber also enables to generate multifunctional devices with several inputs to separate different mechanical excitations. Fibers with two electrodes presented above could rely on both capacitive and resistive devices to differentiate pressure from strain, and compensate thermal or other drifts. It is also possible to envision increasingly complex architectures, combining optical waveguides and electronic configurations, capable of mapping and monitoring complex deformation including twist, shear, strain, pressure, and failure. The peculiar curved surface of the fiber could also be exploited to improve device sensitivity by optimizing the location and geometry of the functional materials to increase or tune their deformation upon various mechanical constraints. Such functional fibers, thin and conformable, can provide a long searched connecting support for advanced robotics and soft skin. They could also be used as biological implants and probes owing to their softness and advanced functionalities.

## **Conclusion**

In conclusion, we have demonstrated an alternative, simple, and scalable platform for the fabrication of elastic functional electronic fibers. Based on the fundamental understanding of the thermal drawing of novel materials, we could realize elastic fibers with unprecedented functionalities. While not applied to the same materials, such fiber devices could be fabricated at scalability and cost comparable with optical fibers processing. This novel methodology can bridge the gap between concepts of stretchable electronic and photonic systems, and large-scale production, while opening new device opportunities. It enables new applications in robotics, medical devices and implants, sensing and monitoring, and smart textiles.

## 5.2 Fiber devices employing a nanocomposite transparent electrode

The reason for introducing transparent conductive films in thermally drawn fibers was that they could in principle enable new types of fiber devices and more performant devices for existing types. In this work, we did not study very advanced optoelectronic fiber devices but realized a simple type to verify the ability of carbon nanotube composites to fulfill their intended function.

### 5.2.1 Working principle

Utilizing a transparent electrode in an optoelectronic device enables to employ a sandwich structure as illustrated in Figure 82. In the cross-sectional architecture shown, a functional layer is placed between the transparent and back electrodes, which are made of conductive nanocomposites. They are supplemented by metallic electrodes to provide electrical conduction along the fiber and facilitate the connections to an external circuit. The detailed composition of the functional layer is not given here to explain the general principle, and it could be made of one or several semiconducting layers depending on the functionality targeted. Incident light can transmit through the cladding and the transparent electrode to interact with the functional layer in the case of light detection or harvesting. Light would transmit in the opposite direction in a light emitting device. Thanks to the sandwich structure, the thickness of the functional layer can be optimized while maximizing the interface area with the electrodes, which could not be done in fiber devices so far since no transparent electrode material was available. The back electrode could be made transparent to allow for light to transmit through both sides of the fiber. A cylindrical design could also be employed for light transmission in all directions.

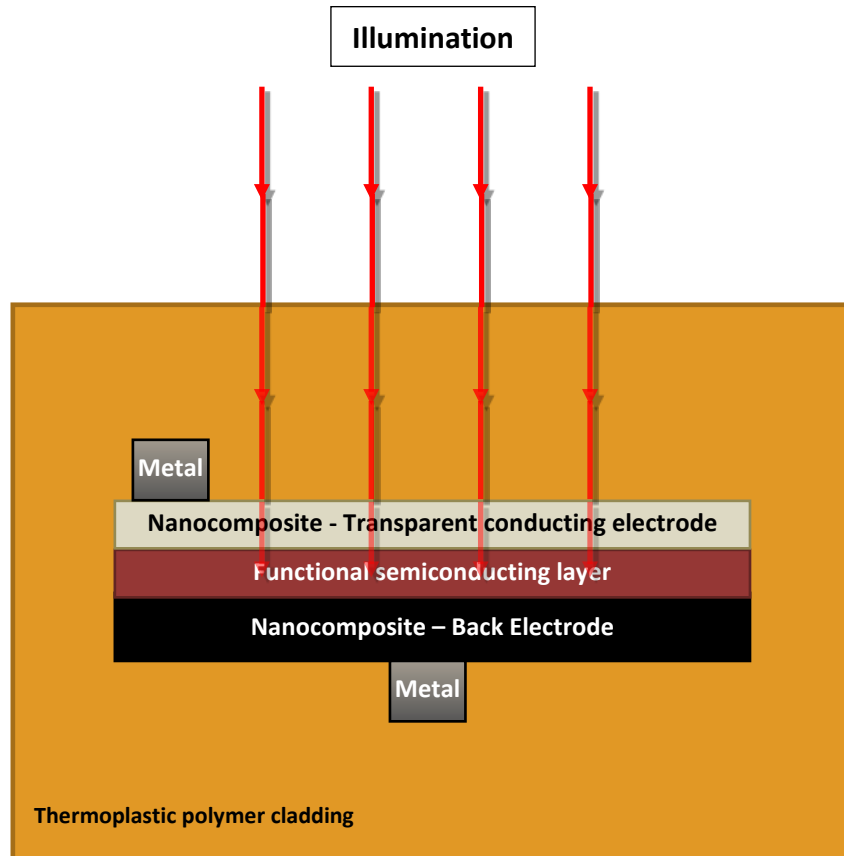


Figure 82. Schematic of the cross-section of an optoelectronic fiber device employing a nanocomposite transparent electrode in a sandwich structure with a functional semiconducting layer and a back electrode. The case of a device that interacts with incident light is shown, with an illumination from the top side of the fiber.

### 5.2.2 Fabrication of a photoconducting fiber device

Optoelectronic devices that rely on junctions between different types of semiconductors are complex to realize in thermally drawn fibers. Therefore, we chose to realize a simpler type of device to assess the ability of carbon nanotube composites to work as transparent electrode. We employed a cross-sectional design that follows the structure shown in Figure 82 with a single semiconducting material as functional layer so that the fiber is photodetecting. The operating principle is to measure the electrical behavior of the semiconductor, which should change when illuminated thanks to its photoconductivity.

Two different techniques were used to fabricate preforms with this type of design. One way is to deposit a film of selenium or  $\text{As}_2\text{Se}_3$  by physical vapor deposition (PVD) on the bottom plate of the preform before its consolidation. However, it is challenging to preserve the architecture with a thin semiconducting layer during the preform consolidation and drawing steps in order to obtain a functional fiber. Too much deformation of the layers inside the fiber indeed creates short circuits or break electrical contacts. The films deposited had a thickness of a few microns, and we did not manage to fabricate functional fibers using this technique, which would require more work of optimization of the experimental process.

The other technique consists in consolidating the preform with a slab of Teflon in place of the semiconductor, then removing it and manually inserting selenium powder in the channel before drawing. The layer is then 4 mm thick in the preform, which means it remains a thick film of several hundred microns in the fiber. In Figure 83 we show an optical microscopy image of the corresponding cross-section.

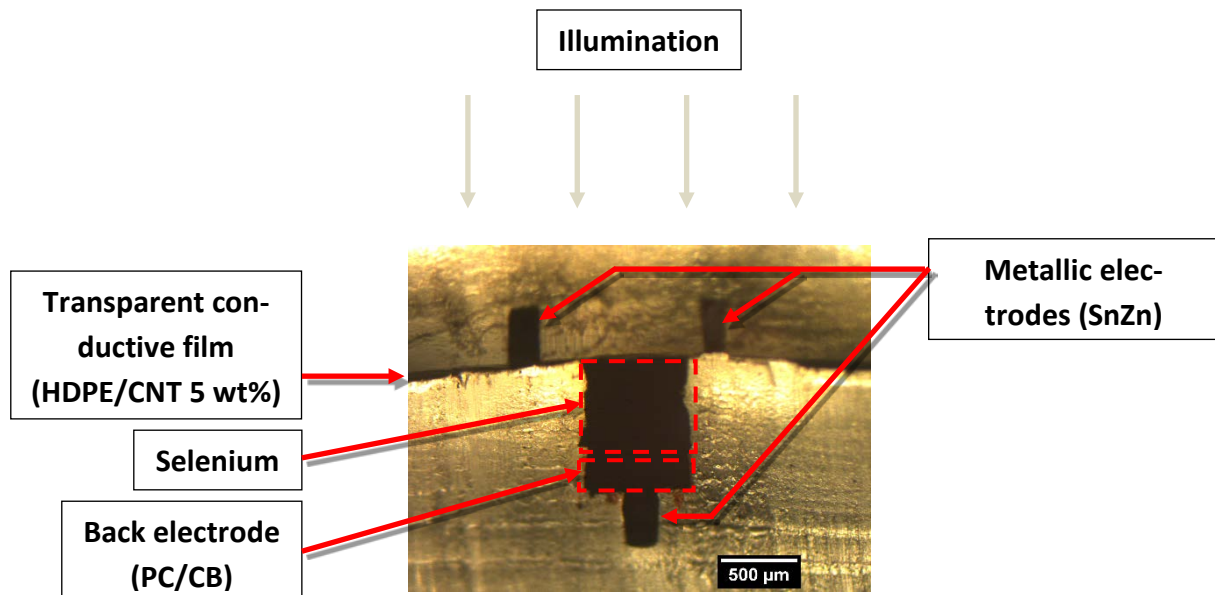


Figure 83. Image of the cross-section of a photoconducting fiber obtained by transmission optical microscopy. The cladding material is polysulfone. The electrical measurements shown below are realized between one of the top metallic electrodes and the bottom one.

The selenium was not conductive after thermal drawing but became so after an annealing treatment of the fiber on a hot plate at 150°C for 15 minutes, which is thought to make it crystallize from an amorphous phase. We first verified that it was photoconductive by applying a current of 10  $\mu\text{A}$  through the selenium layer and recording the corresponding voltage when the fiber is in the dark or illuminated with ambient light. As shown in Figure 84, the voltage decreases under illumination, indicating that the selenium is more conductive than in the dark.

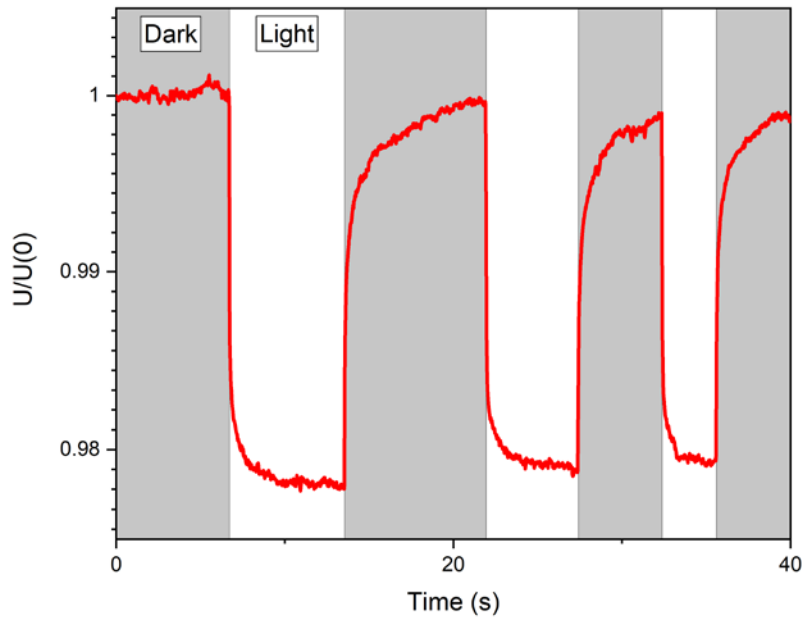


Figure 84. Graph of the time-dependent voltage between the electrodes and across the selenium layer of the fiber shown in Figure 83, when applying a current of  $10 \mu\text{A}$ . The voltage is lower under illumination from ambient light than in the dark, indicating that the selenium layer is photoconductive.

Then, we verified that the photoconductivity is much more pronounced when light is incident on the side of the fiber with the transparent electrode compared to the side with the back electrode, where it can still be present due to light being transmitted to the selenium around the non-transparent electrode.

To characterize further the fiber device, we used a white lamp and recorded the I-V curve in the dark and under illumination on the side of the transparent electrode, represented in Figure 85. The result shows again the photoconductivity of the selenium layer. Moreover, the curve is non-linear, indicating a rectifying behavior, and asymmetrical. This is likely due to junctions at the interfaces between selenium and the two nanocomposite electrodes, which are of different nature, one being based on carbon black and the other on carbon nanotubes.

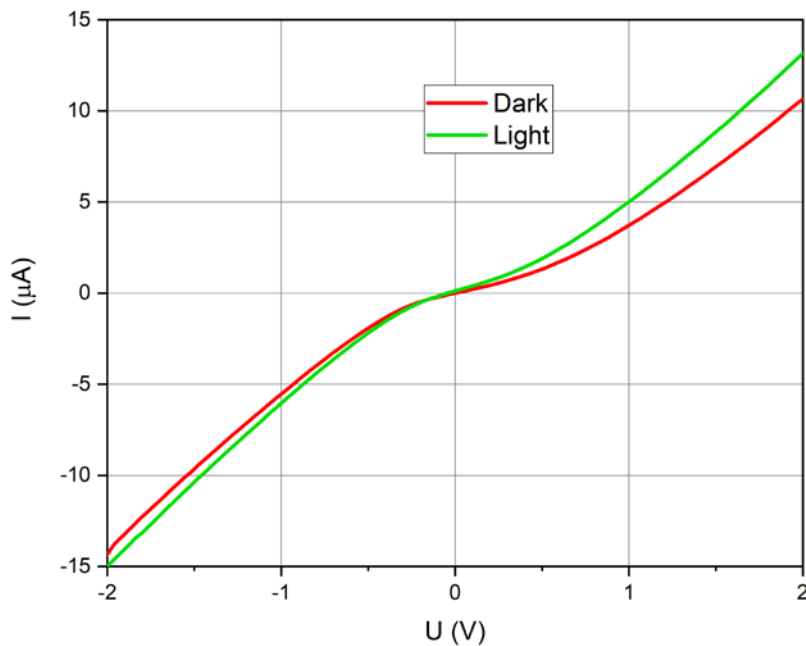


Figure 85. Current against voltage between the electrodes and across the selenium layer of the fiber shown in Figure 83. The fiber was illuminated with a white lamp on the side of the transparent electrode.

In conclusion, we have fabricated a photodetective fiber that demonstrates the ability of a carbon nanotube polymer composite to function as transparent electrode in an optoelectronic fiber device made by thermal drawing. The fiber was not optimized and has a low photosensitivity but represents a proof-of-concept that would be interesting to study further to understand in detail the rectifying behavior observed.

The possibility to integrate transparent electrodes in multi-material fibers made by thermal drawing opens new opportunities of creating optoelectronic fiber devices that are more sensitive, more complex and of new types that have not been realized so far.



## Chapter 6 Conclusion

The possibility to integrate functional materials with various properties at prescribed cross-sectional positions in fibers fabricated by thermal drawing brings wide perspectives for applications. Thus far however, the variety and performance of optoelectronic fibers devices have been limited by the lack of transparent conducting material compatible with the thermal drawing process.

In this work, we extended the range of materials that can be employed to conductive carbon nanotube composites and demonstrated that they can fulfill the role of transparent electrode, which opens up wider possibilities for fiber devices. We achieved this result by examining different techniques used to fabricate nanocomposites and optimizing the different steps of the preform preparation and thermal drawing process. The conductivity perpendicular to the drawing axis reaches up to 15 S/m in thermally drawn carbon nanotube composites, and we integrated transparent conductive films with a sheet resistance of  $10^4 \Omega/\text{sq}$  and a value of the figure of merit  $\sigma_{DC}/\sigma_{op}$  close to  $10^{-2}$  in multimaterial fibers.

As part of this study, we elaborated a solvent casting technique that was employed to produce PMMA/SWCNT nanocomposite sheets that are transparent and conducting at a concentration as low as 0.002 wt%, which is the lowest reported for a bulk thermoplastic that we are aware of.

The use of carbon black nanocomposites was broadened with the creation of a new type of sensing fiber device. We fabricated electronic fibers that rely on freely moving conductive domains to detect a pressure applied. Moreover, such a fiber is able to localize along its length the position of touch with sub-millimeter resolution. For very long fibers, the conductivity of the nanocomposite may be a limiting factor, but this possible issue could be solved by employing carbon nanotubes instead of carbon black. The touch-sensing fibers fabricated are fast and robust, and can be assembled into functional grids and textiles using conventional weaving or thermal welding techniques. They offer perspectives for applications in robotics, prosthetics, flexible electronic interfaces or medical textiles.

Although carbon black nanocomposites have been used for years in multimaterial fibers, little understanding has been developed on the relationship between the thermal drawing conditions and their post-drawing conductivity. Through detailed experimental and theoretical studies of the mechanism, we were able to characterize and model this effect in detail. We developed a fluid dynamic analysis that combines existing models for thermal drawing, fiber spinning and film casting and extends them to cover the effects of non-uniform velocity field in the cross-section. By comparison with the experiment, we showed that our model describes accurately the thermal drawing process. Moreover, we then applied it to compute the conductivity of thermally drawn nanocomposites through a kinetic equation that links the deformation to the conductivity. The result explained quantitatively the impact of thermal drawing on the post-drawing conductivity of nanocomposites in terms of dependency on draw ratio and radial position observed experimentally.

The advanced model of thermal drawing has the potential to be applied to investigate the properties of other materials that are sensitive to the deformation undergone during thermal drawing. Moreover, the knowledge on the integration of nanocomposites in multimaterial fibers can be built upon to exploit other properties that such materials can have, such as high dielectric constant or piezoresistivity, and create further novel functional fiber devices.

## References

- [1] A. F. Abouraddy *et al.*, “Towards multimaterial multifunctional fibres that see, hear, sense and communicate,” *Nat Mater*, vol. 6, no. 5, pp. 336–347, May 2007.
- [2] W. Yan *et al.*, “Advanced Multimaterial Electronic and Optoelectronic Fibers and Textiles,” *Advanced Materials*, p. 1802348, 2018.
- [3] F. Sorin, G. Lestoquoy, S. Danto, J. D. Joannopoulos, and Y. Fink, “Resolving optical illumination distributions along an axially symmetric photodetecting fiber,” *Opt. Express*, vol. 18, no. 23, pp. 24264–24275, Nov. 2010.
- [4] F. Sorin *et al.*, “Multimaterial Photodetecting Fibers: a Geometric and Structural Study,” *Adv. Mater.*, vol. 19, no. 22, pp. 3872–3877, 2007.
- [5] S. Egusa *et al.*, “Multimaterial piezoelectric fibres,” *Nat Mater*, vol. 9, no. 8, pp. 643–648, Aug. 2010.
- [6] S. Danto *et al.*, “Fiber Field-Effect Device Via In Situ Channel Crystallization,” *Adv. Mater.*, vol. 22, no. 37, pp. 4162–4166, 2010.
- [7] J. F. Gu, S. Gorgutsa, and M. Skorobogatiy, “Soft capacitor fibers using conductive polymers for electronic textiles,” *Smart Mater. Struct.*, vol. 19, no. 11, p. 115006, 2010.
- [8] Y. Qu *et al.*, “Superelastic Multimaterial Electronic and Photonic Fibers and Devices via Thermal Drawing,” *Advanced Materials*, vol. 30, no. 27, p. 1707251, 2018.
- [9] M. Bayindir *et al.*, “Metal–insulator–semiconductor optoelectronic fibres,” *Nature*, vol. 431, no. 7010, pp. 826–829, Oct. 2004.
- [10] A. M. Stolyarov *et al.*, “Microfluidic directional emission control of an azimuthally polarized radial fibre laser,” *Nat Photon*, vol. 6, no. 4, pp. 229–233, Apr. 2012.
- [11] T. Nguyen-Dang *et al.*, “Controlled Sub-Micrometer Hierarchical Textures Engineered in Polymeric Fibers and Microchannels via Thermal Drawing,” *Adv. Funct. Mater.*, Jan. 2017.
- [12] Y. Guo *et al.*, “Polymer Composite with Carbon Nanofibers Aligned during Thermal Drawing as a Microelectrode for Chronic Neural Interfaces,” *ACS Nano*, vol. 11, no. 7, pp. 6574–6585, Jul. 2017.
- [13] D. S. Deng, J.-C. Nave, X. Liang, S. G. Johnson, and Y. Fink, “Exploration of in-fiber nanostructures from capillary instability,” *Optics Express*, vol. 19, no. 17, p. 16273, Aug. 2011.
- [14] M. Bayindir, A. F. Abouraddy, F. Sorin, J. D. Joannopoulos, and Y. Fink, “Fiber photodetectors codrawn from conducting, semiconducting and insulating materials,” *Optics & Photonics News*, vol. 15, no. 12, p. 24, Dec. 2004.
- [15] D. S. Hecht, L. Hu, and G. Irvin, “Emerging Transparent Electrodes Based on Thin Films of Carbon Nanotubes, Graphene, and Metallic Nanostructures,” *Adv. Mater.*, vol. 23, no. 13, pp. 1482–1513, Apr. 2011.
- [16] D. S. Hecht *et al.*, “High conductivity transparent carbon nanotube films deposited from superacid,” *Nanotechnology*, vol. 22, no. 7, p. 075201, Feb. 2011.
- [17] S. De *et al.*, “Silver Nanowire Networks as Flexible, Transparent, Conducting Films: Extremely High DC to Optical Conductivity Ratios,” *ACS Nano*, vol. 3, no. 7, pp. 1767–1774, 2009.
- [18] R. H. Schmidt, I. A. Kinloch, A. N. Burgess, and A. H. Windle, “The Effect of Aggregation on the Electrical Conductivity of Spin-Coated Polymer/Carbon Nanotube Composite Films,” *Langmuir*, vol. 23, no. 10, pp. 5707–5712, 2007.
- [19] I. O’Connor, S. De, J. N. Coleman, and Y. K. Gun’ko, “Development of transparent, conducting composites by surface infiltration of nanotubes into commercial polymer films,” *Carbon*, vol. 47, no. 8, pp. 1983–1988, Jul. 2009.

- [20] I. Moreno, N. Navascues, M. Arruebo, S. Irusta, and J. Santamaria, "Facile preparation of transparent and conductive polymer films based on silver nanowire/polycarbonate nanocomposites," *Nanotechnology*, vol. 24, no. 27, p. 275603, Jul. 2013.
- [21] Z. Yu, L. Li, Q. Zhang, W. Hu, and Q. Pei, "Silver Nanowire-Polymer Composite Electrodes for Efficient Polymer Solar Cells," *Adv. Mater.*, vol. 23, no. 38, pp. 4453–4457, 2011.
- [22] W. Yan *et al.*, "Semiconducting Nanowire-Based Optoelectronic Fibers," *Advanced Materials*, vol. 29, no. 27, p. 1700681, Jul. 2017.
- [23] E. Pone *et al.*, "Drawing of the hollow all-polymer Bragg fibers," *Opt. Express, OE*, vol. 14, no. 13, pp. 5838–5852, Jun. 2006.
- [24] M. Saphiannikova, T. Skipa, D. Lellinger, I. Alig, and G. Heinrich, "Superposition approach for description of electrical conductivity in sheared MWNT/polycarbonate melts," Dec. 2011.
- [25] C. Hou *et al.*, "Direct Atomic-Level Observation and Chemical Analysis of ZnSe Synthesized by in Situ High-Throughput Reactive Fiber Drawing," *Nano Lett.*, vol. 13, no. 3, pp. 975–979, Mar. 2013.
- [26] H. Deng, E. Bilotti, R. Zhang, J. Loos, and T. Peijs, "Effect of thermal annealing on the electrical conductivity of high-strength bicomponent polymer tapes containing carbon nanofillers," *Synthetic Metals*, vol. 160, no. 5–6, pp. 337–344, Mar. 2010.
- [27] M. Piao, G. Kim, G. P. Kennedy, S. Roth, and U. Dettlaff-Weglikowska, "Thermoelectric properties of single walled carbon nanotube networks in polycarbonate matrix," *Phys. Status Solidi B*, vol. 250, no. 8, pp. 1468–1473, 2013.
- [28] F. M. Blighe, Y. R. Hernandez, W. J. Blau, and J. N. Coleman, "Observation of Percolation-like Scaling – Far from the Percolation Threshold – in High Volume Fraction, High Conductivity Polymer-Nanotube Composite Films," *Adv. Mater.*, vol. 19, no. 24, pp. 4443–4447, Dec. 2007.
- [29] J. Wu, H. A. Becerril, Z. Bao, Z. Liu, Y. Chen, and P. Peumans, "Organic solar cells with solution-processed graphene transparent electrodes," *Applied Physics Letters*, vol. 92, no. 26, p. 263302, Jun. 2008.
- [30] M. B. Bryning, M. F. Islam, J. M. Kikkawa, and A. G. Yodh, "Very Low Conductivity Threshold in Bulk Isotropic Single-Walled Carbon Nanotube–Epoxy Composites," *Adv. Mater.*, vol. 17, no. 9, pp. 1186–1191, May 2005.
- [31] S.-H. Hwang, Y.-B. Park, K. H. Yoon, and D. S. Bang, "Smart Materials and Structures Based on Carbon Nanotube Composites," *Carbon Nanotubes - Synthesis, Characterization, Applications*, 2011.
- [32] S. Sathyanarayana and C. Hübner, "Thermoplastic Nanocomposites with Carbon Nanotubes," in *Structural Nanocomposites*, Springer, 2013, pp. 19–60.
- [33] D. Stauffer and A. Aharony, *Introduction to percolation theory*. CRC press, 1994.
- [34] F. Lux, "Models proposed to explain the electrical conductivity of mixtures made of conductive and insulating materials," *JOURNAL OF MATERIALS SCIENCE*, vol. 28, no. 2, pp. 285–301, Jan. 1993.
- [35] B. Nigro, C. Grimaldi, M. A. Miller, P. Ryser, and T. Schilling, "Tunneling conductivity in composites of attractive colloids," *J Chem Phys*, vol. 136, no. 16, p. 164903, Apr. 2012.
- [36] E. K. Sichel, J. I. Gittleman, and P. Sheng, "Electrical properties of carbon-polymer composites," *JEM*, vol. 11, no. 4, pp. 699–747, Jul. 1982.
- [37] J. K. W. Sandler, J. E. Kirk, I. A. Kinloch, M. S. P. Shaffer, and A. H. Windle, "Ultra-low electrical percolation threshold in carbon-nanotube-epoxy composites," *Polymer*, vol. 44, no. 19, pp. 5893–5899, Sep. 2003.

- [38] R. Haggemueller, H. H. Gommans, A. G. Rinzler, J. E. Fischer, and K. I. Winey, "Aligned single-wall carbon nanotubes in composites by melt processing methods," *Chemical Physics Letters*, vol. 330, no. 3–4, pp. 219–225, Nov. 2000.
- [39] L. J. Lanticse *et al.*, "Shear-induced preferential alignment of carbon nanotubes resulted in anisotropic electrical conductivity of polymer composites," *Carbon*, vol. 44, no. 14, pp. 3078–3086, Nov. 2006.
- [40] T. D. Fornes, J. W. Baur, Y. Sabba, and E. L. Thomas, "Morphology and properties of melt-spun polycarbonate fibers containing single- and multi-wall carbon nanotubes," *Polymer*, vol. 47, no. 5, pp. 1704–1714, Feb. 2006.
- [41] R. Zhang, A. Dowden, H. Deng, M. Baxendale, and T. Peijs, "Conductive network formation in the melt of carbon nanotube/thermoplastic polyurethane composite," *Composites Science and Technology*, vol. 69, no. 10, pp. 1499–1504, 2009.
- [42] W. Bauhofer *et al.*, "Shear-controlled electrical conductivity of carbon nanotubes networks suspended in low and high molecular weight liquids," *Polymer*, vol. 51, no. 22, pp. 5024–5027, Oct. 2010.
- [43] S. Pegel, P. Pötschke, G. Petzold, I. Alig, S. M. Dudkin, and D. Lellinger, "Dispersion, agglomeration, and network formation of multiwalled carbon nanotubes in polycarbonate melts," *Polymer*, vol. 49, no. 4, pp. 974–984, Feb. 2008.
- [44] J. Li, P. C. Ma, W. S. Chow, C. K. To, B. Z. Tang, and J.-K. Kim, "Correlations between Percolation Threshold, Dispersion State, and Aspect Ratio of Carbon Nanotubes," *Adv. Funct. Mater.*, vol. 17, no. 16, pp. 3207–3215, Nov. 2007.
- [45] A. V. Kyrylyuk and P. van der Schoot, "Continuum percolation of carbon nanotubes in polymeric and colloidal media," *PNAS*, vol. 105, no. 24, pp. 8221–8226, Jun. 2008.
- [46] A. E. Eken, E. J. Tozzi, D. J. Klingenberg, and W. Bauhofer, "A simulation study on the effects of shear flow on the microstructure and electrical properties of carbon nanotube/polymer composites," *Polymer*, vol. 52, no. 22, pp. 5178–5185, Oct. 2011.
- [47] X. Liu, J. Krückel, G. Zheng, and D. W. Schubert, "Electrical conductivity behaviour of sheared poly(methyl methacrylate)/carbon black composites," *Composites Science and Technology*, vol. 100, pp. 99–104, Aug. 2014.
- [48] Y. Gao, D. Cao, J. Liu, J. Shen, Y. Wu, and L. Zhang, "Molecular dynamics simulation of the conductivity mechanism of nanorod filled polymer nanocomposites," *Phys. Chem. Chem. Phys.*, vol. 17, no. 35, pp. 22959–22968, Aug. 2015.
- [49] Q. Zhang, H. Xiong, W. Yan, D. Chen, and M. Zhu, "Electrical conductivity and rheological behavior of multiphase polymer composites containing conducting carbon black," *Polymer Engineering & Science*, vol. 48, no. 11, pp. 2090–2097, Nov. 2008.
- [50] P. Pötschke, T. D. Fornes, and D. R. Paul, "Rheological behavior of multiwalled carbon nanotube/polycarbonate composites," *Polymer*, vol. 43, no. 11, pp. 3247–3255, May 2002.
- [51] F. Du, R. C. Scogna, W. Zhou, S. Brand, J. E. Fischer, and K. I. Winey, "Nanotube Networks in Polymer Nanocomposites: Rheology and Electrical Conductivity," *Macromolecules*, vol. 37, no. 24, pp. 9048–9055, Nov. 2004.
- [52] H. H. Winter and M. Mours, "Rheology of Polymers Near Liquid-Solid Transitions," in *Neutron Spin Echo Spectroscopy Viscoelasticity Rheology*, Berlin, Heidelberg: Springer Berlin Heidelberg, 1997, pp. 165–234.
- [53] P. Pötschke, M. Abdel-Goad, I. Alig, S. Dudkin, and D. Lellinger, "Rheological and dielectrical characterization of melt mixed polycarbonate-multiwalled carbon nanotube composites," *Polymer*, vol. 45, no. 26, pp. 8863–8870, Dec. 2004.

- [54] S. B. Kharchenko, J. F. Douglas, J. Obrzut, E. A. Grulke, and K. B. Migler, "Flow-induced properties of nanotube-filled polymer materials," *Nat Mater*, vol. 3, no. 8, pp. 564–568, Aug. 2004.
- [55] K. Q. Xiao, L. C. Zhang, and I. Zarudi, "Mechanical and rheological properties of carbon nanotube-reinforced polyethylene composites," *Composites Science and Technology*, vol. 67, no. 2, pp. 177–182, Feb. 2007.
- [56] G. A. Gelves, B. Lin, U. Sundararaj, and J. A. Haber, "Electrical and rheological percolation of polymer nanocomposites prepared with functionalized copper nanowires," *Nanotechnology*, vol. 19, no. 21, p. 215712, May 2008.
- [57] M. Van Gurp and J. Palmen, "Time-temperature superposition for polymeric blends," *Rheol. Bull*, vol. 67, no. 1, pp. 5–8, 1998.
- [58] S. Trinkle, P. Walter, and C. Friedrich, "Van Gurp-Palmen Plot II – classification of long chain branched polymers by their topology," *Rheol. Acta*, vol. 41, no. 1, pp. 103–113, Jan. 2002.
- [59] O. Meincke, D. Kaempfer, H. Weickmann, C. Friedrich, M. Vathauer, and H. Warth, "Mechanical properties and electrical conductivity of carbon-nanotube filled polyamide-6 and its blends with acrylonitrile/butadiene/styrene," *Polymer*, vol. 45, no. 3, pp. 739–748, Feb. 2004.
- [60] Z. M. Zhirikova, G. V. Kozlov, and V. Z. Aloe, "A fractal model of melt viscosity of a polypropylene-carbon nanotube nanocomposite," *High Temp*, vol. 50, no. 6, pp. 732–735, Dec. 2012.
- [61] A. S. Sarvestani, "Modeling the solid-like behavior of entangled polymer nanocomposites at low frequency regimes," *European Polymer Journal*, vol. 44, no. 2, pp. 263–269, Feb. 2008.
- [62] D. W. Litchfield and D. G. Baird, "The rheology of high aspect ratio nano-particle filled liquids," *Rheology Reviews*, vol. 2006, p. 1, 2006.
- [63] L. M. Hall, A. Jayaraman, and K. S. Schweizer, "Molecular theories of polymer nanocomposites," *Current Opinion in Solid State and Materials Science*, vol. 14, no. 2, pp. 38–48, Apr. 2010.
- [64] F. Du, J. Fischer, and K. Winey, "A Coagulation Method to Prepare Single-Walled Carbon Nanotube/PMMA Composites and Their Modulus, Electrical Conductivity, and Thermal Stability," *Departmental Papers (MSE)*, Dec. 2003.
- [65] T. Villmow, P. Pötschke, S. Pegel, L. Häussler, and B. Kretschmar, "Influence of twin-screw extrusion conditions on the dispersion of multi-walled carbon nanotubes in a poly(lactic acid) matrix," *Polymer*, vol. 49, no. 16, pp. 3500–3509, Jul. 2008.
- [66] I. Alig *et al.*, "Establishment, morphology and properties of carbon nanotube networks in polymer melts," *Polymer*, vol. 53, no. 1, pp. 4–28, Jan. 2012.
- [67] U. Staudinger, B. Krause, C. Steinbach, P. Pötschke, and B. Voit, "Dispersability of multi-walled carbon nanotubes in polycarbonate-chloroform solutions," *Polymer*, vol. 55, no. 24, pp. 6335–6344, Nov. 2014.
- [68] F. Du, J. E. Fischer, and K. I. Winey, "Effect of nanotube alignment on percolation conductivity in carbon nanotube/polymer composites," *Phys. Rev. B*, vol. 72, no. 12, p. 121404, Sep. 2005.
- [69] E. J. Siochi *et al.*, "Melt processing of SWCNT-polyimide nanocomposite fibers," *Composites Part B: Engineering*, vol. 35, no. 5, pp. 439–446, Jul. 2004.
- [70] B. Dan, G. C. Irvin, and M. Pasquali, "Continuous and Scalable Fabrication of Transparent Conducting Carbon Nanotube Films," *ACS Nano*, vol. 3, no. 4, pp. 835–843, Apr. 2009.
- [71] S. De and J. N. Coleman, "The effects of percolation in nanostructured transparent conductors," *MRS Bulletin*, vol. 36, no. 10, pp. 774–781, Oct. 2011.
- [72] U. Dettlaff-Weglikowska *et al.*, "Conducting and transparent SWNT/polymer composites," *physica status solidi (b)*, vol. 243, no. 13, pp. 3440–3444, 2006.

- [73] L. Hu, D. S. Hecht, and G. Grüner, “Infrared transparent carbon nanotube thin films,” *Appl. Phys. Lett.*, vol. 94, no. 8, p. 081103, Feb. 2009.
- [74] L. Battezzati and A. L. Greer, “The viscosity of liquid metals and alloys,” *Acta Metallurgica*, vol. 37, no. 7, pp. 1791–1802, Jul. 1989.
- [75] Z. Spitalsky, D. Tasis, K. Papagelis, and C. Galiotis, “Carbon nanotube–polymer composites: Chemistry, processing, mechanical and electrical properties,” *Progress in Polymer Science*, vol. 35, no. 3, pp. 357–401, Mar. 2010.
- [76] M. J. O’Connell *et al.*, “Reversible water-solubilization of single-walled carbon nanotubes by polymer wrapping,” *Chemical Physics Letters*, vol. 342, no. 3–4, pp. 265–271, Jul. 2001.
- [77] T. Hasan, V. Scardaci, P. Tan, A. G. Rozhin, W. I. Milne, and A. C. Ferrari, “Stabilization and ‘Debundling’ of Single-Wall Carbon Nanotube Dispersions in N-Methyl-2-pyrrolidone (NMP) by Polyvinylpyrrolidone (PVP),” *J. Phys. Chem. C*, vol. 111, no. 34, pp. 12594–12602, Aug. 2007.
- [78] C. Laurent, E. Flahaut, and A. Peigney, “The weight and density of carbon nanotubes versus the number of walls and diameter,” *Carbon*, vol. 48, no. 10, pp. 2994–2996, Aug. 2010.
- [79] I. Alig, D. Lellinger, S. M. Dudkin, and P. Pötschke, “Conductivity spectroscopy on melt processed polypropylene–multiwalled carbon nanotube composites: Recovery after shear and crystallization,” *Polymer*, vol. 48, no. 4, pp. 1020–1029, Feb. 2007.
- [80] P. Pötschke, A. R. Bhattacharyya, and A. Janke, “Carbon nanotube-filled polycarbonate composites produced by melt mixing and their use in blends with polyethylene,” *Carbon*, vol. 42, no. 5–6, pp. 965–969, 2004.
- [81] S. V. Ahir, Y. Y. Huang, and E. M. Terentjev, “Polymers with aligned carbon nanotubes: Active composite materials,” *Polymer*, vol. 49, no. 18, pp. 3841–3854, Aug. 2008.
- [82] B. Lin, U. Sundararaj, and P. Pötschke, “Melt Mixing of Polycarbonate with Multi-Walled Carbon Nanotubes in Miniature Mixers,” *Macromol. Mater. Eng.*, vol. 291, no. 3, pp. 227–238, 2006.
- [83] R. Socher, B. Krause, M. T. Müller, R. Boldt, and P. Pötschke, “The influence of matrix viscosity on MWCNT dispersion and electrical properties in different thermoplastic nanocomposites,” *Polymer*, vol. 53, no. 2, pp. 495–504, Jan. 2012.
- [84] I. Alig, D. Lellinger, M. Engel, T. Skipa, and P. Pötschke, “Destruction and formation of a conductive carbon nanotube network in polymer melts: In-line experiments,” *Polymer*, vol. 49, no. 7, pp. 1902–1909, Apr. 2008.
- [85] I. Alig, T. Skipa, D. Lellinger, and P. Pötschke, “Destruction and formation of a carbon nanotube network in polymer melts: Rheology and conductivity spectroscopy,” *Polymer*, vol. 49, no. 16, pp. 3524–3532, Jul. 2008.
- [86] T. Skipa, D. Lellinger, M. Saphiannikova, and I. Alig, “Shear-stimulated formation of multi-wall carbon nanotube networks in polymer melts,” *Phys. Status Solidi B*, vol. 246, no. 11–12, pp. 2453–2456, Dec. 2009.
- [87] T. Skipa, D. Lellinger, W. Böhm, M. Saphiannikova, and I. Alig, “Influence of shear deformation on carbon nanotube networks in polycarbonate melts: Interplay between build-up and destruction of agglomerates,” *Polymer*, vol. 51, no. 1, pp. 201–210, Jan. 2010.
- [88] K. Hilarius, D. Lellinger, I. Alig, T. Villmow, S. Pegel, and P. Pötschke, “Influence of shear deformation on the electrical and rheological properties of combined filler networks in polymer melts: Carbon nanotubes and carbon black in polycarbonate,” *Polymer*, vol. 54, no. 21, pp. 5865–5874, Oct. 2013.
- [89] Z. Starý, “Electrical conductivity and rheology of carbon black composites under elongation,” *AIP Conference Proceedings*, vol. 1662, no. 1, p. 040001, Apr. 2015.

- [90] P. Pötschke, S. Pegel, M. Claes, and D. Bonduel, "A Novel Strategy to Incorporate Carbon Nanotubes into Thermoplastic Matrices," *Macromol. Rapid Commun.*, vol. 29, no. 3, pp. 244–251, Feb. 2008.
- [91] M. Rein *et al.*, "Diode fibres for fabric-based optical communications," *Nature*, vol. 560, no. 7717, p. 214, Aug. 2018.
- [92] F. Y. Castillo *et al.*, "Electrical, mechanical, and glass transition behavior of polycarbonate-based nanocomposites with different multi-walled carbon nanotubes," *Polymer*, vol. 52, no. 17, pp. 3835–3845, Aug. 2011.
- [93] V. Skákalová, U. Dettlaff-Weglikowska, and S. Roth, "Electrical and mechanical properties of nanocomposites of single wall carbon nanotubes with PMMA," *Synthetic Metals*, vol. 152, no. 1, pp. 349–352, Sep. 2005.
- [94] S. C. Xue, R. I. Tanner, G. W. Barton, R. Lwin, M. C. J. Large, and L. Poladian, "Fabrication of Microstructured Optical Fibers-Part I: Problem Formulation and Numerical Modeling of Transient Draw Process," *J. Lightwave Technol., JLT*, vol. 23, no. 7, p. 2245, Jul. 2005.
- [95] S. Xue, G. Barton, S. Fleming, and A. Argyros, "Heat Transfer Modeling of the Capillary Fiber Drawing Process," *J. Heat Transfer*, vol. 139, no. 7, p. 072001, Jul. 2017.
- [96] M. Bechert and B. Scheid, "Combined influence of inertia, gravity, and surface tension on the linear stability of Newtonian fiber spinning," *Phys. Rev. Fluids*, vol. 2, no. 11, p. 113905, Nov. 2017.
- [97] J. R. A. Pearson and M. A. Matovich, "Spinning a Molten Threadline. Stability," *Ind. Eng. Chem. Fund.*, vol. 8, no. 4, pp. 605–609, Nov. 1969.
- [98] Y. T. Shah and J. R. A. Pearson, "On the Stability of Nonisothermal Fiber Spinning," *Ind. Eng. Chem. Fund.*, vol. 11, no. 2, pp. 145–149, May 1972.
- [99] R. German and R. E. Khayat, "Interplay Between Inertia and Elasticity in Film Casting," *J. Fluids Eng*, vol. 130, no. 8, pp. 081501-081501–12, Jul. 2008.
- [100] B. Scheid, S. Quiligotti, B. Tran, R. Gy, and H. A. Stone, "On the (de)stabilization of draw resonance due to cooling," *Journal of Fluid Mechanics*, vol. 636, pp. 155–176, Oct. 2009.
- [101] M. Bechert, D. W. Schubert, and B. Scheid, "On the stabilizing effects of neck-in, gravity, and inertia in Newtonian film casting," *Physics of Fluids*, vol. 28, no. 2, p. 024109, Feb. 2016.
- [102] W. W. Schultz and S. H. Davis, "One-Dimensional Liquid Fibers," *Journal of Rheology*, vol. 26, no. 4, pp. 331–345, Aug. 1982.
- [103] E. J. Doedel, A. R. Champneys, T. F. Fairgrieve, Y. A. Kuznetsov, B. Sandstede, and X. Wang, "Continuation and bifurcation software for ordinary differential equations (with HomCont)," *AUTO97, Concordia University, Canada*, 1997.
- [104] T. Nguyen-Dang, A. G. Page, Y. Qu, M. Volpi, W. Yan, and F. Sorin, "Multi-material micro-electromechanical fibers with bendable functional domains," *J. Phys. D: Appl. Phys.*, vol. 50, no. 14, p. 144001, 2017.
- [105] M. Alexander Schmidt, A. Argyros, and F. Sorin, "Hybrid Optical Fibers – An Innovative Platform for In-Fiber Photonic Devices," *Advanced Optical Materials*, vol. 4, no. 1, pp. 13–36, Jan. 2016.
- [106] G. Tao, A. M. Stolyarov, and A. F. Abouraddy, "Multimaterial Fibers," *Int J Appl Glass Sci*, vol. 3, no. 4, pp. 349–368, 2012.
- [107] B. Temelkuran, S. D. Hart, G. Benoit, J. D. Joannopoulos, and Y. Fink, "Wavelength-scalable hollow optical fibres with large photonic bandgaps for CO<sub>2</sub> laser transmission," *Nature*, vol. 420, no. 6916, pp. 650–653, Dec. 2002.
- [108] S. D. Hart, G. R. Maskaly, B. Temelkuran, P. H. Prideaux, J. D. Joannopoulos, and Y. Fink, "External Reflection from Omnidirectional Dielectric Mirror Fibers," *Science*, vol. 296, no. 5567, pp. 510–513, Apr. 2002.

- [109] P. Russell, "Photonic Crystal Fibers," *Science*, vol. 299, no. 5605, pp. 358–362, Jan. 2003.
- [110] A. Argyros, "Microstructured Polymer Optical Fibers," *Journal of Lightwave Technology*, vol. 27, no. 11, pp. 1571–1579, Jun. 2009.
- [111] D. S. Deng *et al.*, "In-Fiber Semiconductor Filament Arrays," *Nano Lett.*, vol. 8, no. 12, pp. 4265–4269, Dec. 2008.
- [112] J. Ballato *et al.*, "Silicon optical fiber," *Opt. Express, OE*, vol. 16, no. 23, pp. 18675–18683, Nov. 2008.
- [113] J. Ballato *et al.*, "Binary III-V semiconductor core optical fiber," *Opt. Express, OE*, vol. 18, no. 5, pp. 4972–4979, Mar. 2010.
- [114] F. Sorin *et al.*, "Geometry and Structure of Multimaterial Photodetecting Fibers: a Comparative Study," in *Conference on Lasers and Electro-Optics/Quantum Electronics and Laser Science Conference and Photonic Applications Systems Technologies (2007), paper CThO4*, 2007, p. CThO4.
- [115] F. Sorin *et al.*, "Exploiting Collective Effects of Multiple Optoelectronic Devices Integrated in a Single Fiber," *Nano Lett.*, vol. 9, no. 7, pp. 2630–2635, Jul. 2009.
- [116] M. Bayindir *et al.*, "Integrated fibres for self-monitored optical transport," *Nature Materials*, vol. 4, no. 11, pp. 820–825, Nov. 2005.
- [117] A. Gumennik *et al.*, "All-in-Fiber Chemical Sensing," *Adv. Mater.*, vol. 24, no. 45, pp. 6005–6009, 2012.
- [118] A. M. Stolyarov *et al.*, "Enhanced chemiluminescent detection scheme for trace vapor sensing in pneumatically-tuned hollow core photonic bandgap fibers," *Opt. Express, OE*, vol. 20, no. 11, pp. 12407–12415, May 2012.
- [119] N. Chocat, G. Lestoquoy, Z. Wang, D. M. Rodgers, J. D. Joannopoulos, and Y. Fink, "Piezoelectric Fibers for Conformal Acoustics," *Adv. Mater.*, vol. 24, no. 39, pp. 5327–5332, Oct. 2012.
- [120] A. M. Stolyarov, L. Wei, F. Sorin, G. Lestoquoy, J. D. Joannopoulos, and Y. Fink, "Fabrication and characterization of fibers with built-in liquid crystal channels and electrodes for transverse incident-light modulation," *Applied Physics Letters*, vol. 101, no. 1, p. 011108, Jul. 2012.
- [121] A. Canales *et al.*, "Multifunctional fibers for simultaneous optical, electrical and chemical interrogation of neural circuits *in vivo*," *Nature Biotechnology*, vol. 33, no. 3, pp. 277–284, Mar. 2015.
- [122] C. Lu *et al.*, "Polymer Fiber Probes Enable Optical Control of Spinal Cord and Muscle Function *In Vivo*," *Advanced Functional Materials*, vol. 24, no. 42, pp. 6594–6600, Nov. 2014.
- [123] S. Danto, Z. Ruff, Z. Wang, J. D. Joannopoulos, and Y. Fink, "Ovonic Memory Switching in Multimaterial Fibers," *Advanced Functional Materials*, vol. 21, no. 6, pp. 1095–1101, Mar. 2011.
- [124] A. Tuniz *et al.*, "Metamaterial fibres for subdiffraction imaging and focusing at terahertz frequencies over optically long distances," *Nature Communications*, vol. 4, p. 2706, Oct. 2013.
- [125] S. Gorgutsa, J. F. Gu, and M. Skorobogatiy, "A woven 2D touchpad sensor and a 1D slide sensor using soft capacitor fibers," *Smart Mater. Struct.*, vol. 21, no. 1, p. 015010, 2012.
- [126] G. Lestoquoy, N. Chocat, Z. Wang, J. D. Joannopoulos, and Y. Fink, "Fabrication and characterization of thermally drawn fiber capacitors," *Applied Physics Letters*, vol. 102, no. 15, p. 152908, Apr. 2013.
- [127] A. F. Abouraddy *et al.*, "Large-scale optical-field measurements with geometric fibre constructs," *Nature Materials*, vol. 5, no. 7, pp. 532–536, Jul. 2006.
- [128] J. A. Rogers, T. Someya, and Y. Huang, "Materials and Mechanics for Stretchable Electronics," *Science*, vol. 327, no. 5973, pp. 1603–1607, Mar. 2010.

- [129] M. L. Hammock, A. Chortos, B. C.-K. Tee, J. B.-H. Tok, and Z. Bao, “25th Anniversary Article: The Evolution of Electronic Skin (E-Skin): A Brief History, Design Considerations, and Recent Progress,” *Advanced Materials*, vol. 25, no. 42, pp. 5997–6038, Nov. 2013.
- [130] Z. F. Liu *et al.*, “Hierarchically buckled sheath-core fibers for superelastic electronics, sensors, and muscles,” *Science*, vol. 349, no. 6246, pp. 400–404, Jul. 2015.
- [131] I. R. Mineev *et al.*, “Electronic dura mater for long-term multimodal neural interfaces,” *Science*, vol. 347, no. 6218, pp. 159–163, Jan. 2015.
- [132] M. D. Dickey, “Stretchable and Soft Electronics using Liquid Metals,” *Advanced Materials*, vol. 29, no. 27, p. 1606425, Jul. 2017.
- [133] S. Zhu *et al.*, “Ultrastretchable Fibers with Metallic Conductivity Using a Liquid Metal Alloy Core,” *Advanced Functional Materials*, vol. 23, no. 18, pp. 2308–2314, May 2013.
- [134] M. Kolle, A. Lethbridge, M. Kreysing, J. J. Baumberg, J. Aizenberg, and P. Vukusic, “Bio-Inspired Band-Gap Tunable Elastic Optical Multilayer Fibers,” *Advanced Materials*, vol. 25, no. 15, pp. 2239–2245, Apr. 2013.
- [135] M. Krehel, R. M. Rossi, G.-L. Bona, and L. J. Scherer, “Characterization of Flexible Copolymer Optical Fibers for Force Sensing Applications,” *Sensors*, vol. 13, no. 9, pp. 11956–11968, Sep. 2013.
- [136] X. Sun, J. Zhang, X. Lu, X. Fang, and H. Peng, “Mechanochromic Photonic-Crystal Fibers Based on Continuous Sheets of Aligned Carbon Nanotubes,” *Angewandte Chemie International Edition*, vol. 54, no. 12, pp. 3630–3634, Mar. 2015.
- [137] D. J. Lipomi *et al.*, “Skin-like pressure and strain sensors based on transparent elastic films of carbon nanotubes,” *Nat Nano*, vol. 6, no. 12, pp. 788–792, Dec. 2011.
- [138] J. Lee *et al.*, “Conductive Fiber-Based Ultrasensitive Textile Pressure Sensor for Wearable Electronics,” *Advanced Materials*, vol. 27, no. 15, pp. 2433–2439, Apr. 2015.
- [139] C. B. Cooper *et al.*, “Stretchable Capacitive Sensors of Torsion, Strain, and Touch Using Double Helix Liquid Metal Fibers,” *Adv. Funct. Mater.*, vol. 27, no. 20, p. n/a-n/a, May 2017.
- [140] C. Bartolozzi, L. Natale, F. Nori, and G. Metta, “Robots with a sense of touch,” *Nature Materials*, vol. 15, pp. 921–925, Aug. 2016.
- [141] A. Chortos, J. Liu, and Z. Bao, “Pursuing prosthetic electronic skin,” *Nature Materials*, vol. 15, no. 9, pp. 937–950, Sep. 2016.
- [142] Z. Bao and X. Chen, “Flexible and Stretchable Devices,” *Advanced Materials*, vol. 28, no. 22, pp. 4177–4179, 2016.
- [143] S. Choi, H. Lee, R. Ghaffari, T. Hyeon, and D.-H. Kim, “Recent Advances in Flexible and Stretchable Bio-Electronic Devices Integrated with Nanomaterials,” *Advanced Materials*, vol. 28, no. 22, pp. 4203–4218, Jun. 2016.
- [144] C. Lu *et al.*, “Flexible and stretchable nanowire-coated fibers for optoelectronic probing of spinal cord circuits,” *Science Advances*, vol. 3, no. 3, p. e1600955, Mar. 2017.
- [145] W. Zeng, L. Shu, Q. Li, S. Chen, F. Wang, and X.-M. Tao, “Fiber-Based Wearable Electronics: A Review of Materials, Fabrication, Devices, and Applications,” *Advanced Materials*, vol. 26, no. 31, pp. 5310–5336, Aug. 2014.
- [146] T. Khudiyev *et al.*, “Electrostrictive microelectromechanical fibres and textiles,” *NATURE*, vol. 8, no. 1435, p. 1, 2017.
- [147] H. Sun, Y. Zhang, J. Zhang, X. Sun, and H. Peng, “Energy harvesting and storage in 1D devices,” *Nature Reviews Materials*, vol. 2, no. 6, p. 17023, Jun. 2017.
- [148] M. Z. Seyedin, J. M. Razal, P. C. Innis, and G. G. Wallace, “Strain-Responsive Polyurethane/PEDOT:PSS Elastomeric Composite Fibers with High Electrical Conductivity,” *Adv. Funct. Mater.*, vol. 24, no. 20, pp. 2957–2966, 2014.

- [149] S. Seyedin, J. M. Razal, P. C. Innis, R. Jalili, and G. G. Wallace, “Compositional Effects of Large Graphene Oxide Sheets on the Spinnability and Properties of Polyurethane Composite Fibers,” *Advanced Materials Interfaces*, vol. 3, no. 5, p. 1500672, Mar. 2016.
- [150] G. Tao, A. F. Abouraddy, A. M. Stolyarov, and Y. Fink, “Multimaterial Fibers,” in *Lab-on-Fiber Technology*, A. Cusano, M. Consales, A. Crescitelli, and A. Ricciardi, Eds. Cham: Springer International Publishing, 2015, pp. 1–26.
- [151] T. Khudiyev, C. Hou, A. M. Stolyarov, and Y. Fink, “Sub-Micrometer Surface-Patterned Ribbon Fibers and Textiles,” *Adv. Mater.*, vol. 29, no. 22, Jun. 2017.
- [152] R. Deimel and O. Brock, “A novel type of compliant and underactuated robotic hand for dexterous grasping,” *The International Journal of Robotics Research*, vol. 35, no. 1–3, pp. 161–185, Jan. 2016.

## Curriculum Vitae

### EDUCATION

- 2014 – 2019 Ecole Polytechnique Fédérale de Lausanne - PhD in Materials Science
- 2013 – 2014 University of Cambridge - Master of Advanced Studies in Materials Science
- 2010 – 2013 Ecole Polytechnique, Paris - Ingénieur - Specialization in condensed and soft matter
- 2008 – 2010 Lycée du Parc, Lyon - Preparatory classes (Mathematics & Physics)
- 2008 Lycée Carriat, Bourg-en-Bresse - Baccalauréat in Science with distinction

### AWARDS

- Prize for the Best Poster at the Research Day of the Doctoral School in Materials Science (EDMX), 2017

### PUBLICATIONS

- T. Nguyen-Dang, [A. G. Page](#), Y. Qu, M. Volpi, W. Yan, and F. Sorin, "Multi-material micro-electromechanical fibers with bendable functional domains", *J. Phys. D: Appl. Phys.*, vol. 50, no. 14, p. 144001, 2017 (highlighted in the journal blog).
- T. Nguyen-Dang, A. C. de Luca, W. Yan, Y. Qu, [A. G. Page](#), M. Volpi, T. Das Gupta, S. P. Lacour, and F. Sorin, "Controlled Sub-Micrometer Hierarchical Textures Engineered in Polymeric Fibers and Microchannels via Thermal Drawing", *Adv. Funct. Mater.*, Jan. 2017.
- Y. Qu, T. Nguyen-Dang, [A.G. Page](#), W. Yan, T.D. Gupta, G.M. Rotaru, R.M. Rossi, V.D. Favrod, N. Bartolomei, and F. Sorin, "Superelastic Multimaterial Electronic and Photonic Fibers and Devices via Thermal Drawing", *Advanced Materials*, vol. 30, no. 27, p. 1707251, 2017.
- W. Yan, T. Nguyen-Dang, C. Cayron, T.D. Gupta, [A.G. Page](#), Y. Qu and F. Sorin, "Microstructure Tailoring of Selenium-Core Multimaterial Optoelectronic Fibers", *Opt. Mater. Express*, vol. 7, no. 4, pp. 1388–1397, Apr. 2017.
- W. Yan, Y. Qu, T.D Gupta, A. Darga, T. Nguyen-Dang, [A.G. Page](#), M. Rossi, M. Ceriotti and F. Sorin, "Semiconducting Nanowire-Based Optoelectronic Fibers", *Advanced Materials*, vol. 29, no. 27, p. 1700681, Jul. 2017.
- W. Yan, [A. Page](#), T. Nguyen-Dang, Y. Qu, F. Sordo, L. Wei and F. Sorin, "Advanced Multimaterial Electronic and Optoelectronic Fibers and Textiles", *Advanced Materials*, p. 1802348, 2018.
- T.D. Gupta, L. Martin-Monier, W. Yan, A. Le Bris, T. Nguyen-Dang, [A.G. Page](#), K.-T. Ho, F. Yesilköy, H. Altug, Y. Qu and F. Sorin, "Self-Assembly of Nanostructured Glass Metasurfaces via Templated Fluid Instabilities", *Nature Nanotechnology*, p. 1, Feb. 2019.
- [A.G. Page](#), M. Bechert, F. Gallaire and F. Sorin, "Unraveling radial dependency effects in fiber thermal drawing", submitted to *Proceedings of the National Academy of Sciences*.

### CONFERENCE TALKS

- [A.G. Page](#), D.T. Nguyen, Y. Qu, M. Volpi, W. Yan, and F. Sorin, "Multi-material Fibers for Electromechanical Touch Sensing", Materials Research Society, Phoenix, U.S.A., Spring 2017.
- [A.G. Page](#), D.T. Nguyen, Y. Qu, M. Volpi, W. Yan, and F. Sorin, "Multi-material Fibers for Electromechanical Touch Sensing", Fiber Society Conference, Aachen, Germany, Spring 2017.
- [A.G. Page](#), Y. Qu, D.T. Nguyen, W. Yan, T.D. Gupta, G.M. Rotaru, R.M. Rossi, V.D. Favrod, N. Bartolomei, and F. Sorin, "Stretchable Optical and Electronic Fibers via Thermal Drawing", IEEE International Flexible Electronics Technology Conference, Ottawa, Canada, August 2018.

## PATENTS

F. Sorin, D. T. Nguyen, Y. Qu, A. Page, and W. Yan, "Fabrication method of functional micro/nano structures over large-area, flexible and high curvature surfaces, by drawing a fiber from a preform", WO2017085323A1, 26-May-2017.

F. Sorin, Y. Qu, M. Volpi, W. Yan, D. T. Nguyen, and A. Page, "Multi-material stretchable optical, electronic and optoelectronic fibers and ribbons composites via thermal drawing", WO2017137945A1, 17-Aug-2017.

F. Sorin, L. Martin-Monier, A.G Page, T.D Gupta, "Fabrication of glass-based nanostructures on large area rigid and soft planar substrates, fibers and textiles", Application N°: US 62/802,725, 2019.

